

TIDES IN THE MARTIAN ATMOSPHERE — AND OTHER TOPICS

by

Paul Gareth Withers

A Dissertation Submitted to the Faculty of the
DEPARTMENT OF PLANETARY SCIENCES

In Partial Fulfillment of the Requirements
For the Degree of

DOCTOR OF PHILOSOPHY

In the Graduate College
THE UNIVERSITY OF ARIZONA

2 0 0 3

FINAL EXAMINING COMMITTEE APPROVAL FORM

Replace this page with the correct approval form.

STATEMENT BY AUTHOR

This dissertation has been submitted in partial fulfillment of requirements for an advanced degree at The University of Arizona and is deposited in the University Library to be made available to borrowers under rules of the Library.

Brief quotations from this dissertation are allowable without special permission, provided that accurate acknowledgment of source is made. Requests for permission for extended quotation from or reproduction of this manuscript in whole or in part may be granted by the head of the major department or the Dean of the Graduate College when in his or her judgment the proposed use of the material is in the interests of scholarship. In all other instances, however, permission must be obtained from the author.

SIGNED: _____

ACKNOWLEDGEMENTS

I came to LPL because everyone I met during my first visit here seemed friendly. Now that I'm ready to leave, I'm sure of it. The welcoming and relaxed environment pervading the department is something that's made my time here a happy one. The faculty, postdocs, and staff are always willing to spend their time, and everyone is willing to spend the faculty's money, encouraging the graduate students.

Hawthorne House has been my home for the past five years. I can't imagine LPL without it. As the host of Bratfests, Science Diet concerts, parties, Thanksgiving Dinners and innumerable gatherings of all sorts, it has been the centre of my social scene. I've shared it with many friends, including Kim Cyr, Joe Spitale, Rachel Mastrapa, Dave O'Brien, Laz Keszthelyi, Gareth Collins, Celinda Kelsey, Matt Chamberlain, Abby Wasserman/Sheffer, Jonathan Fortney, Eric Mamajek, and their lovers. Bratfest and its T-shirt industry have introduced me to absolutely everyone ever associated with LPL, trained me for my backup career in door-to-door sales, and thrown some damn fine fests. The Narcolepsy football team has kept me exercised and entertained. Christmas Skits and April Fools Pranks have cost me many hours of sleep and coincided with my worst day at LPL, but given me much laughter and a list of unprintable LPL pseudonyms. If the editing ever finishes before 6am, then I will know that the end is nigh. My officemates, Ross Beyer, Jen Grier, Ingrid Daubar, and Sally House, have given me office supplies and food. Many friends from other universities and the LPL alumni have made conferences less productive, but much more entertaining. Trading gossip with them has made the idea of leaving LPL less foreboding than it otherwise would be.

Fieldtrips have shown me and most of the Southwest's scenic gems and the true nature of many LPLers. Who can forget Day 4, Kring Narrows, Ralph ralphing, Pete covering himself in glory, Ross stranding us in Death Valley, Pete's stratigraphic monologue, Dave's glaciation speculation, spheroidal weathering, Alfred's vocabulary, or Jay's giant cracks?

I am grateful to staff like Noreen Conarro, Marianne Hamilton, Linda Hickox, and Maria Schuchardt for showing me who really runs any institution; to postdocs like Paul Geissler, Ralph Lorenz, Kevin Richter, Bashar Rizk, and Aileen Yingst for showing me what I have to look forward to after graduation; to my predecessors Betty Pierazzo, Zibi Turtle, Andy Rivkin, David Trilling, Nancy Chabot, Jen Grier, Barb Cohen, Cynthia Phillips, Joe Spitale, Josh Emery, Pete Lanagan, Windy Jaeger, and Rachel Mastrapa for passing their accumulated decades of graduate student lore and wisdom down to me and thus saving me from many mistakes; to my fellow protodoctors Jason Barnes, Ross Beyer, Fred Ciesla, Terry Hurford, and Dave O'Brien for their friendship during every day of my graduate studies; and to the graduate students who follow us, Gwen Bart, Ingrid Daubar, Jonathan Fortney, Celinda Kelsey, Jani Radebaugh, and Matt Tiscareno, Matt Chamberlain, Curtis Cooper, Jim Richardson, and Abby Wasserman/Sheffer, Oleg Abramov, John Keller, and Moses Milazzo for replacing departed old friends with new ones. Section 1.5 contains some professional acknowledgements.

My tongue doesn't have the words to give the most important thanks to those who are always in my heart.

DEDICATION

With love and thanks

To family and friends

TABLE OF CONTENTS

LIST OF FIGURES	13
LIST OF TABLES	16
ABSTRACT	17
CHAPTER 1 INTRODUCTION	18
1.1 Preamble	18
1.2 Introduction to the Martian Atmosphere	21
1.3 Observations of the Martian Upper Atmosphere	24
1.4 Dissertation Structure	26
1.5 Sources of Support	28
CHAPTER 2 TOPOGRAPHICALLY-CONTROLLED THERMAL TIDES IN THE MARTIAN UPPER ATMOSPHERE	30
2.1 Abstract	30
2.2 Introduction	31
2.3 MGS Aerobraking	35
2.4 Sol-to-Sol Variability	41
2.4.1 Introduction to Sol-to-Sol Variability	41
2.4.2 Observations of Sol-to-Sol Variability	42
2.4.3 Discussion of Sol-to-Sol Variability	49
2.5 Observations of the Zonal Structure	53
2.5.1 Introduction to the Zonal Structure	53
2.5.2 Changes in Zonal Structure on Weekly Timescales	56
2.5.3 Changes in Zonal Structure With Altitude	60
2.5.4 Changes in Zonal Structure With Latitude	68
2.5.5 Changes in Zonal Structure With Local Solar Time	76
2.6 Modelling of the Zonal Structure	85
2.6.1 Constraints on Tidal Modes Responsible for Zonal Structure	85
2.6.2 Other Tidal Observations and Theory	94

2.6.3	Effects of the Surface on Zonal Structure	98
2.7	Mars Odyssey and Mars Reconnaissance Orbiter	99
2.8	Future Work	102
2.9	Conclusions	105
CHAPTER 3 DEVELOPMENT OF A NOVEL “BALANCED ARCH” TECHNIQUE FOR MEASURING WINDS		108
3.1	Introduction	108
3.2	Conservation of Momentum in an Atmosphere	113
3.2.1	Simplest Approximation to Equation 3.1	115
3.2.2	Scale Analysis on Equation 3.1	117
3.3	Mars Scale Analysis	122
3.3.1	r component	122
3.3.2	θ component	124
3.3.3	ϕ component	128
3.3.4	Approximate Equations	130
3.4	Venus Scale Analysis	131
3.4.1	r component	132
3.4.2	θ component	132
3.4.3	ϕ component	132
3.4.4	Approximate Equations	133
3.5	Titan Scale Analysis	133
3.5.1	r component	134
3.5.2	θ component	134
3.5.3	ϕ component	135
3.5.4	Approximate Equations	135
3.6	Summary of Simplified Equations	135
3.7	“Balanced Arch” Technique for Estimating Wind Speed	137
3.8	Validation of “Balanced Arch” Technique	140
3.8.1	Test on a Simple Atmosphere	140
3.8.2	MTGCM Testing	142

CHAPTER 4 APPLICATION OF “BALANCED ARCH” TECH-	
NIQUE TO MGS ACCELEROMETER DATA	144
4.1 Introduction	144
4.2 Hemispheric Averages	148
4.3 Northern Hemisphere	150
4.3.1 NH — Effects of Longitude	150
4.3.2 NH — Effect of Latitude	150
4.3.3 NH — Effect of Altitude	152
4.3.4 NH — Summary	152
4.4 Southern Hemisphere	152
4.4.1 SH — Effect of Longitude	152
4.4.2 SH — Effect of Latitude	154
4.4.3 SH — Effects of Latitude and Altitude	156
4.4.4 SH — Summary	158
4.5 Discussion of Results	158
4.6 Comparison to Simulations	159
4.7 Future Work	162
CHAPTER 5 ANALYSIS OF ENTRY ACCELEROMETER	
DATA	164
5.1 Abstract	164
5.2 Introduction	165
5.2.1 Uses of Accelerometers in Spaceflight	165
5.2.2 Fluid Dynamics and Atmospheric Entry	167
5.2.3 Flight Heritage	168
5.3 Equations of Motion	168
5.3.1 Previous Work	168
5.3.2 Alternative Formulation	169
5.3.3 Inertial Cartesian and Spherical Frames	170
5.3.4 Momentary Cartesian and Spherical Frames	170
5.3.5 Transformations between Frames	171
5.3.6 Solution Procedure for the Gravity-only Case	172
5.3.7 The Spacecraft Frame	175

5.4	The Effects of an Atmosphere on Trajectory Reconstructions	176
5.4.1	Addition of Aerodynamics to the Solution Procedure	176
5.4.2	The <i>Head-on</i> Option for Constraining Spacecraft Attitude	177
5.4.3	The <i>Drag-only</i> Option for Constraining Spacecraft Attitude	178
5.4.4	The <i>Acceleration Ratios</i> Option for Constraining Spacecraft Attitude	180
5.4.5	The <i>Gyroscopes</i> Option for Constraining Spacecraft Attitude	183
5.4.6	Summary of Techniques Used to Constrain Spacecraft Attitude	187
5.4.7	Parachute Considerations	188
5.4.8	Error Considerations	189
5.5	Trajectory Reconstruction applied to Mars Pathfinder	192
5.5.1	Programming Details	192
5.5.2	Assembly and Preparation of Pathfinder's Accelerometer Data	193
5.5.3	Entry State Problems	197
5.5.4	Results	203
5.6	Atmospheric Structure Reconstruction	203
5.6.1	Fluid Dynamics During an Atmospheric Entry	203
5.6.2	Generalized Density Reconstruction	210
5.6.3	Generalized Pressure and Temperature Reconstructions	212
5.6.4	Error Considerations	214
5.7	Atmospheric Structure Reconstruction applied to Mars Pathfinder	215
5.7.1	The Importance of an Aerodynamic Database	215
5.7.2	Results	216
5.7.3	$C_D = 2$ Approximation	223
5.8	Conclusions	224

5.9	Acknowledgements	226
CHAPTER 6 SCIENTIFIC USES OF CRUDE TELEMETRY DURING ATMOSPHERIC ENTRY 227		
6.1	Abstract	227
6.2	Deriving Acceleration, Velocity, and Position	228
6.3	Deriving Atmospheric Properties	233
6.3.1	First Technique for Density	234
6.3.2	First Technique for Pressure	234
6.3.3	First Technique for Temperature	235
6.3.4	Second Technique for Temperature	236
6.3.5	Second Technique for Pressure	237
6.3.6	Third Technique for Temperature	237
6.3.7	Third Technique for Pressure	238
6.3.8	Fourth Technique for Temperature	239
6.3.9	Summary	240
6.4	Uncertainties in Transmitted Frequency	240
6.5	Simulated Trajectory and Atmospheric Properties	242
6.6	Derived Trajectory and Atmospheric Properties Using Clean v	249
6.7	Derived Trajectory and Atmospheric Properties Using Noisy v	265
6.8	Conclusions	281
CHAPTER 7 COMPARISON OF VIKING LANDER 1 AND MOLA TOPOGRAPHY 283		
7.1	Abstract	283
7.2	Summary	283
7.3	Introduction	284
7.4	Altimetry from the Viking Landers	284
7.5	Comparison with MOLA Altimetry	285
7.6	Implications for Viking Atmospheric Structure Results	288
7.7	Correcting the Viking Atmospheric Structure Results	288
7.8	Conclusions	289

CHAPTER 8	ENIGMATIC NORTHERN PLAINS OF MARS	292
CHAPTER 9	AGE OF LUNAR CRATER GIORDANO BRUNO	295
9.1	Abstract	295
9.2	Introduction	295
9.3	Meteor Storm	298
9.4	Other Tests of Hartung’s Hypothesis	302
9.5	Conclusions	306
CHAPTER 10	SIMPLE CLIMATE MODELS	307
10.1	Abstract	307
10.2	Two-Box Model	308
10.2.1	Variational Principle	308
10.2.2	Solution for F	311
10.3	Other Simple Climate Models	314
10.3.1	Rodgers’s Model	315
10.3.2	Paltridge’s Model	317
10.3.3	Lin’s Model	318
10.3.4	Restricted Solution	320
10.3.5	Restricted Solution to Rodgers’s Model	320
10.3.6	Restricted Solution to Paltridge’s Model	321
10.3.7	Restricted Solution to Lin’s Model	324
10.3.8	Restricted Solution to Zero and Infinite Heat Transport Models	327
10.3.9	Conclusions	328
CHAPTER 11	CONCLUSIONS	329
APPENDIX A	CHARACTERIZING THE ZONAL STRUCTURE WITH AN HARMONIC FIT	336
APPENDIX B	GENERATING CONSTANT ALTITUDE DATA FROM THE PDS PROFILES	344
APPENDIX C	CURVATURE TERMS IN EQUATIONS 3.6 – 3.7	347

APPENDIX D SIMPLIFYING THE VISCOUS TERMS IN EQUATIONS 3.6 – 3.7	350
APPENDIX E ESTIMATING THE IMPORTANCE OF LATITUDINAL CHANGES IN PRESSURE	353
APPENDIX F UNCERTAINTY ANALYSES FOR SECTION 6.3	366
F.1 Uncertainties for Section 6.3.1	366
F.2 Uncertainties for Section 6.3.2	367
F.3 Uncertainties for Section 6.3.3	367
F.4 Uncertainties for Section 6.3.4	369
F.5 Uncertainties for Section 6.3.5	372
F.6 Uncertainties for Section 6.3.6	372
F.7 Uncertainties for Section 6.3.7	373
F.8 Uncertainties for Section 6.3.8	373
REFERENCES	376

LIST OF FIGURES

2.1	Parameters of periapsis during aerobraking	39
2.2	Examples of density profiles during a resonance	43
2.3	Sol-to-sol variability during the 3:1 — 8:1 resonances	44
2.4	The 11:1 resonance	50
2.5	Fit to outbound densities at 130 km between 10°S and 20°S	55
2.6	As Figure 2.5, but inbound data	59
2.7	Repeat interval between inbound and outbound measurements	61
2.8	Variation in zonal structure with altitude	63
2.9	Variation in normalized harmonic amplitudes with altitude	64
2.10	Variation in phases with altitude	65
2.11	Contour plot of normalized fitted densities	69
2.12	Normalized amplitudes from Figure 2.11	72
2.13	Phases from Figure 2.11	73
2.14	Wave-2 component of Figure 2.11	74
2.15	Wave-3 component of Figure 2.11	75
2.16	Repeat interval between inbound and outbound in polar regions	81
2.17	Polar inbound dayside densities	82
2.18	Polar outbound dayside densities	83
2.19	Polar inbound nightside densities	84
2.20	Meridional structure of the eight lowest order Hough modes with $\sigma = 1, s = -1$	89
2.21	Vertical wavelengths of selected Hough modes	90
2.22	Harmonic decomposition of martian topography	100
2.23	Martian topography	101
3.1	Pressure profiles derived for orbit P679.	114
4.1	MTGCM v_ϕ , $L_s = 30^\circ$, LST = 16 hrs.	160
4.2	MTGCM v_ϕ , $L_s = 90^\circ$, LST = 15 hrs.	161
5.1	Reconstructed latitude using PDS entry state.	198

5.2	As Figure 5.1, but east longitude.	199
5.3	Difference in reconstructed latitudes as a function of time.	201
5.4	As Figure 5.3, but east longitude.	202
5.5	As Figure 5.3, but altitude.	204
5.6	Fractional difference in density versus time.	217
5.7	As Figure 5.6, but pressure.	218
5.8	As Figure 5.6, but temperature.	219
5.9	Fractional difference in density versus altitude.	220
5.10	As Figure 5.9, but pressure.	221
5.11	As Figure 5.9, but temperature.	222
5.12	Fractional difference in temperature versus altitude using $C_D = 2$	225
6.1	Simulated z vs. t	244
6.2	Simulated v vs. t	245
6.3	Simulated a vs. t	246
6.4	Simulated ρ vs. t	247
6.5	Simulated p vs. t	248
6.6	Clean derived z_n vs. t	251
6.7	Clean derived $z_{n+1/2}$ vs. t	252
6.8	Clean derived v_n vs. t	253
6.9	Clean derived $v_{n+1/2}$ vs. t	254
6.10	Clean derived $a_{n+1/2}$ vs. t	255
6.11	Clean derived $\rho_{n+1/2}$ vs. t	256
6.12	Clean derived ρ_n vs. t	257
6.13	Clean derived p_n^* vs. t	258
6.14	Clean derived p_n° vs. t	259
6.15	Clean derived $p_n^\#$ vs. t	260
6.16	Clean derived T_n^* vs. t	261
6.17	Clean derived T_n° vs. t	262
6.18	Clean derived $T_n^\#$ vs. t	263
6.19	Clean derived $T_{n+1/2}^\S$ vs. t	264
6.20	Noisy derived z_n vs. t	267
6.21	Noisy derived $z_{n+1/2}$ vs. t	268
6.22	Noisy derived v_n vs. t	269
6.23	Noisy derived $v_{n+1/2}$ vs. t	270
6.24	Noisy derived $a_{n+1/2}$ vs. t	271

6.25	Noisy derived $\rho_{n+1/2}$ vs. t	272
6.26	Noisy derived ρ_n vs. t	273
6.27	Noisy derived p_n^* vs. t	274
6.28	Noisy derived p_n° vs. t	275
6.29	Noisy derived $p_n^\#$ vs. t	276
6.30	Noisy derived T_n^* vs. t	277
6.31	Noisy derived T_n° vs. t	278
6.32	Noisy derived $T_n^\#$ vs. t	279
6.33	Noisy derived $T_{n+1/2}^\$$ vs. t	280
7.1	Topographic profiles beneath the Viking Lander 1 entry trajectory.	286
7.2	Shaded relief map of MOLA planetary radius data referenced to the Viking Lander 1 landing site.	287
8.1	The northern plains of Mars. (a) Topographic profile near Utopia. (b) Topographic profile near Alba Patera. (c) Viking photomosaic near Utopia. (d) MOLA shaded relief map near Utopia.	294
9.1	Giordano Bruno.	297
9.2	Variation in Meteor Storm properties with ejecta size.	301
9.3	Giordano Bruno close-up.	303
10.1	Simple two-box climate model.	309
B.1	Periapsis altitude versus L_S	345
E.1	Aerobraking Geometry	355

LIST OF TABLES

2.1	Details of the 3:1 – 8:1 resonances	46
2.2	Harmonic amplitudes and phases from Figures 2.5 and 2.6	58
2.3	Comparison of dayside and nightside harmonic fits	80
2.4	Hough modes satisfying the excitation and propagation criteria. . .	92
3.1	Relevant Parameters for Developing “Balanced Arch” Technique . .	123
3.2	Scale Analysis of Equation 3.6	125
3.3	Scale Analysis of Equation 3.7	126
3.4	Dominant Terms in Equation 3.18 for Mars case	127
3.5	Scale Analysis of Equation 3.8	129
4.1	NH — Effects of Longitude	151
4.2	NH — Effects of Latitude	151
4.3	NH — Effects of Altitude	153
4.4	SH — Effects of Longitude	155
4.5	SH — Effects of Latitude	157
4.6	SH — Effects of Latitude and Altitude	157
7.1	Viking Lander 1 Atmospheric Profiles.	290

ABSTRACT

The dynamics of the martian upper atmosphere are not well-understood. I have identified the dominant tidal modes present in the upper atmosphere by comparing density measurements from the aerobraking of the Mars Global Surveyor spacecraft to predictions from classical tidal theory. Other observations and general circulation models have also provided constraints. I have presented a justification for why topography has a strong influence on the tides in the upper atmosphere. I have also studied sol-to-sol variations in density at fixed altitude, latitude, longitude, season, and time of day. I have developed a novel “Balanced Arch” technique to derive pressures and temperature from these density measurements that also estimates the zonal wind speed in the atmosphere. These are the first measurements of winds in the martian upper atmosphere. This technique can also be applied to anticipated data from Titan to measure winds in its upper atmosphere.

I have developed techniques to derive density, pressure, and temperature profiles from entry accelerometer data, used them to investigate the entry of Mars Pathfinder, and discovered that surprisingly accurate temperature profiles can be derived without using any aerodynamic information at all. I have also investigated techniques to derive atmospheric properties from the Doppler shift in telemetry from a spacecraft during atmospheric entry and found that a surprisingly robust estimate of temperature at peak acceleration can be derived.

I have discovered a network of tectonic ridges in the otherwise bland northern plains of Mars and studied their implications for a possible ocean in that area.

I have tested the hypothesis that the formation of lunar crater Giordano Bruno was witnessed in 1178 AD and rejected it due to the lack of any observations of the immense meteor storm that must have followed the crater’s formation.

CHAPTER 1

INTRODUCTION

1.1 Preamble

This dissertation is not a single, monolithic research project. Instead it contains most of the diverse research questions that I have studied during my five years at LPL.

Inasmuch as this dissertation has a central theme, that theme is the analysis of accelerometer data. Back when I began graduate school, Mars Global Surveyor was entering its second phase of aerobraking and returning accelerometer measurements from the martian upper atmosphere on a daily basis (Keating et al., 1998). My first hours of research here at LPL were spent processing and trying to analyse the regular data deliveries from the spacecraft. Five years later, I am still trying.

It seems to me that accelerometer datasets are often collected more for engineering reasons than scientific reasons. Judged purely on their scientific return, other instruments probably have stronger cases for being flown into space. However, since the accelerometer data can be essential for the operation of the spacecraft, accelerometers can fly without needing to compete before review boards and advisory committees against radiometers, spectrometers, magnetometers, and so on. For those who decide to analyse accelerometer data, this has the advantage of regular flight opportunities and the disadvantage of inadequate support for data archiving and scientific activities. To illustrate the regular flight opportunities, in the past five years I have worked with the Mars Global Surveyor, Mars Climate Orbiter, and Mars Odyssey accelerometer teams during their missions and with the Beagle 2

and Mars Exploration Rover (MER) teams before launch. To illustrate the lack of scientific exploitation of the data, only three peer-reviewed publications have analysed significant amounts of the data from the Mars Global Surveyor accelerometer (Keating et al., 1998; Bougher et al., 1999; Wilson, 2002). There have been none from Mars Odyssey. This is an astoundingly low number. The same is currently true for entry accelerometers; there are no scientists planning to analyse the MER entry accelerometer data amongst the forty-strong science team.

Since NASA has gone to all the trouble of collecting the data, someone should at least try to analyse it. As those who are involved with proprietary datasets know, there are often simple discoveries waiting to be made by the first scientists who examine a dataset.

Most of the Mars atmospheric science community is busy analysing huge volumes of lower atmospheric data from Mars Global Surveyor's TES and RS instruments, the first significant martian atmospheric dataset since Viking, and they have not taken a great interest in the behaviour of the upper atmosphere (Smith et al., 2001; Tyler et al., 2001). There are many important questions to be answered with TES, but also many clever people working on them. Accelerometer data from a spacecraft aerobraking around another planet form a new kind of dataset, one that had never been collected before Mars Global Surveyor. As such, there are new phenomena to be discovered and studied, ones that are not present in current models or other datasets. Personally, I prefer working with a simple, novel dataset, not knowing what the big questions it can answer are, to working on a vast dataset, which is similar in its basic properties to those returned from previous missions, where the important questions are already known. To expand on what I mean by not knowing the big questions, two of the most interesting features in the Mars Global Surveyor accelerometer dataset are the possibility of using it measuring winds (Chapter 4) and occasional large changes in density over very short times and distances (Tolson et al., 1999; Tolson et al., 2000). Neither of these features was anticipated before the data were analysed.

Mars Climate Orbiter was unfortunately lost before any data were returned, but Mars Odyssey has aerobraked successfully and I am looking forward to the public release of its accelerometer data. I hope to join in the Mars Reconnaissance Orbiter aerobraking activities as a fully-fledged member of the science team, instead of being mentored by a science team member. Since there are so few scientists working on accelerometer datasets and more flights of accelerometer instruments to come, I hope to have such opportunities in the future.

In an attempt to expand my connections with British and European planetary science, I spent the summer of 2001 working with the Beagle 2 team and developing techniques to analyse accelerometer data from a planetary lander. That snowballed into nearly being funded to join the MER science team to do similar analysis. As a consolation prize, I was invited to join an advisory group for MER, which offers all the data access without any of the funding. I will be in a similar situation with Beagle 2 when it lands — data access without funding. Huygens is also an area of interest. Since Seiff's group at Ames that pioneered this technique has recently dissolved, I am motivated by the chance to establish myself as an expert in the analysis of entry accelerometer data.

One piece of advice I have seen often in career books as I plan my post-PhD future is that scientists should focus on problems, not on techniques. The reasoning behind this advice is that existing techniques, be they experimental or computational, are always superceded by new ones. The same fate befalls the antiquated experts as befalls the antiquated techniques. This dissertation seems to ignore that advice by being dominated by analysis of data collected with a single type of instrument. My feeling on this point is that the advice is good in the long-term, but that I should become established as a competent scientist in one area before I try to move into too many others. I have chosen accelerometer data analysis as this launchpad because of its regular flight opportunities and relative shortage of established scientific leaders. Luckily, it also contains interesting scientific questions that are sufficiently close to those addressed by other instruments or theoretical

models to allow me to develop related research interests elsewhere in the study of planetary atmospheres after I graduate.

Owing to NASA's current focus, this dissertation is heavily weighted toward studies of the dynamics of the martian atmosphere using accelerometer data. In Sections 1.2 and 1.3 I outline the current state of our understanding of martian atmospheric dynamics and how accelerometer data analysis can improve it.

1.2 Introduction to the Martian Atmosphere

My three main sources for this Section are Kieffer et al. (1992), Haberle (1997), and Leovy (2001). I have not referenced these sources explicitly at each appropriate occasion in this Section because that would fill the printed page with citations. Instead it should be understood that information from these sources has been used throughout the entire Section. I make exceptions to that rule when I provide an explicit reference for direct quotations.

The martian atmosphere is predominantly composed of CO_2 . N_2 and Ar are present at the percent level and H_2O is a trace constituent. Suspended aerosols such as micron-sized dust and condensates of CO_2 and H_2O have a large effect on the transfer of radiation within the atmosphere. Mars is farther from the Sun than Earth is; its orbital semi-major axis is about 1.5 AU. A martian year is about twice as long as a terrestrial year. Its orbit is quite elliptical with an eccentricity of nearly 0.1, which causes solar insolation at perihelion to be 40% more than at aphelion. The martian obliquity is very similar to Earth's, which makes the effects of seasons similar. Seasonal effects are complicated by the changing Sun-Mars distance. The martian day is also similar in length to Earth's. The mean column mass of the martian atmosphere is about 20 g cm^{-2} , one fiftieth of Earth's. The martian atmosphere is cold, and its temperature at the surface varies between approximately 145 K and 275 K. The surface pressure is so low, a mean value of 7.5 mbar, that liquid water, pure or contaminated, is short-lived on the martian

surface. Interestingly, the atmospheric pressure is close to that of the triple point of water, the minimum surface temperature is the freezing point of CO_2 at that pressure, and the maximum surface temperature is close to that of the triple point of water. In contrast to the great cycle of H_2O which drives the Earth's climate, the martian climate is driven by the condensation and sublimation of CO_2 at the polar caps. Tens of percent of the atmosphere's mass flows back and forth between the two hemispheres each year. Even in the absence of CO_2 condensation, there would still be an appreciable hemispheric flux due to the extreme pole-to-pole gradient in topography and the changing atmospheric scale height with the seasons. There are many possible past states of martian climate depending on variations in obliquity and other orbital parameters.

The vertical temperature structure of the martian atmosphere differs significantly from the Earth's. Latent heating due to H_2O is negligible and there is no heating from the absorption of solar UV by ozone. The martian troposphere is heated by dust, whereas Earth's is heated by H_2O . On Earth, H_2O freezes out at the tropopause and limits the height of the troposphere to around 10–15 km. On Mars, the dust is not trapped in this way and it can be lifted to several tens of kilometres altitude, so the martian troposphere extends higher than Earth's. The dust content and distribution in the martian atmosphere can vary significantly over the seasons and during a dust storm. This causes variability in the height and temperature gradient of the troposphere. Above the martian troposphere, there is the near-isothermal mesosphere. This is capped by the thermosphere, a region where temperature increases with altitude due to extreme UV heating. The martian atmosphere has a much smaller mass per unit heating than Earth's with which to buffer diurnal and other subseasonal changes in heating. Departures from a mean state are common with many types of atmospheric waves and tides prominent. The main cycles governing martian climate are those of CO_2 , dust, and H_2O . The effects of H_2O are the weakest of the three under current climatic conditions, being limited to its radiative effects as a vapour or a condensate and its potential to trap CO_2 and dust as it condenses.

The lower atmospheric circulation has been well-studied by observations and theory. “The mean meridional atmospheric circulation is nearly zonally-symmetric. At equinoxes, two Hadley cells share a common rising branch near the equator, extending upwards to ~ 30 km altitude and poleward to $\sim 30^\circ$. At solstices, the Hadley cells intensify and merge into one cross-equatorial cell with air descending in the winter hemisphere, moving across the equator, and rising in the summer hemisphere” (Haberle, 1997).

“In the tropics, the winds are westward at all seasons. Winds are also westward in the summer hemisphere at solstices. Winds are eastward in the winter hemisphere at solstices and at extratropical latitudes during the equinoxes. Jet streams can reach speeds on the order of 200 m s^{-1} ” (Haberle, 1997).

Superimposed on this pattern is the seasonal flux of CO_2 to and from the poles. Winds at the edge of the southern polar cap become strongest in springtime, close to perihelion, as CO_2 sublimates off the cap. These strong surface winds can lift significant amounts of dust into the atmosphere, sometimes initiating planet-encircling dust storms.

“Eastward travelling planetary waves with zonal wavenumbers of 1 to 3 occur during winter and spring in mid and high latitudes of both hemispheres. Stationary planetary waves, with zonal wavenumbers 1 and 2, are generated by the interaction of eastward zonal winds and topography. Thermal tides are common in equatorial to mid-latitudes. Most of them migrate westward with the Sun, but some travel eastward. The breaking of these disturbances as they reach the middle and upper atmosphere deposits energy and momentum into the atmosphere and will alter the circulation” (Leovy, 2001). The nature of the circulation in the middle and upper atmospheres has not been well-studied observationally.

Various large-scale wave motions are present in the martian atmosphere. These motions are of interest because of their intrinsic nature, their relationship with the averaged general circulation, and their effects on the transport of aerosols

and trace constituents. They are generated by atmospheric instabilities and external forcings such as solar heating, topography, albedo, and thermal inertia. The long-duration surface pressure records from the two Viking landing sites revealed transient eddies, similar to travelling cyclones and anticyclones at terrestrial mid-latitudes, with periods of a few days and zonal wavenumbers of 2 or 3 travelling eastwards with phase speeds of 10–20 m s⁻¹. Global-scale oscillations, or tides, are also common. Migrating diurnal and semidiurnal tides, modes which have the same phase speed as the Sun, cause regular surface pressure variations of a few percent. The relative strengths of these two modes depends on atmospheric dust loading. The frequencies of some non-migrating tidal modes, modes which are generated by the interaction of solar heating and topography, are close to atmospheric resonant frequencies, which encourages their amplitudes to become relatively large. One of these, the diurnal Kelvin wave (see Chapter 2), has been detected in Viking surface pressure records, vertical temperature profiles in the lower atmosphere measured by orbiting IR spectrometers, and Mars Global Surveyor accelerometer data at 130 km altitude (Wilson, 2002). Many other transient waves are probably present in the martian atmosphere. This paragraph follows Section V of Zurek et al. (1992) closely.

1.3 Observations of the Martian Upper Atmosphere

The martian upper atmosphere has been studied remotely by instruments on flyby and orbiting spacecraft and *in situ* measurements have been made by instruments on landers and aerobraking orbiters (Kieffer et al., 1992). UV spectrometers on the Mariner 6 and 7 (Mars arrival in 1969) flyby spacecraft studied upper atmospheric composition. Mariner 9 (1971) was the first spacecraft to orbit another planet. It studied upper atmospheric composition with a UV spectrometer and ionospheric densities with radio occultations. Mars 4 and 5 (1973) were flyby spacecraft that studied upper atmospheric composition with visible spectrometers and ionospheric densities with radio occultation. Viking 1 and 2 landers (1976) measured *in situ*

ionospheric properties and vertical profiles of upper atmospheric composition, density, pressure, and temperature during their descent. A suite of instruments on the short-lived Phobos 2 orbiter (1989) studied ionospheric properties. Phobos 2 also measured two vertical profiles of upper atmospheric temperature from X-ray occultations of solar flares (Krasnopolsky et al., 1991). Pathfinder (1997) measured a vertical profile of upper atmospheric density, pressure, and temperature during its atmospheric entry. Mars Global Surveyor (1997) measured *in situ* upper atmospheric densities during its aerobraking passes and ionospheric densities from radio occultations. Prior to Mars Global Surveyor, all of these observations apart from Mariner 9 came from landers or flyby spacecraft that did not have extended spatial or temporal coverage. How altitude, latitude, season, longitude, time of day, and the phase of the 11-year solar cycle affect upper atmospheric densities, pressures, temperatures, and winds is not well-known.

Volatile escape rates, and their variation over martian history, play a crucial role in studies of the history of the climate and habitability of Mars. An important loss mechanism for oxygen, dissociative recombination, is controlled by the diffusion of hydrogen through the lower thermosphere. The dynamics of the martian upper atmosphere affect escape rates and so this dissertation contributes indirectly to those important scientific questions. The underdeveloped state of our understanding of the physics and chemistry of the martian upper atmosphere was highlighted by the recent Decadal Survey recommendation for a Mars Upper Atmosphere Observer spacecraft (Belton, 2002).

Mars Global Surveyor accelerometer data can be used to improve our understanding of the dynamics of the martian upper atmosphere. This dataset contains profiles of upper atmospheric density between 100 and 160 km altitude at various latitudes, longitudes, seasons, and times of day (Keating et al., 2001a). These density profiles can, in principle, give pressure and temperature profiles as well. Since the density measurements on each aerobraking pass are made at two different latitudes for every altitude, zonal winds can, in principle, be derived as well, as

discussed in Chapter 3. There have been no previous measurements of winds in the martian upper atmosphere. MGS measured density profiles on 800 aerobraking passes. This dataset is significantly larger and more extensive in its coverage than previous measurements of upper atmospheric properties. An unfocused initial survey of the dataset will probably yield interesting results and can be followed by addressing specific questions such as which tides are present, what mechanisms are dominating the heat transport, what controls the circulation, or how the upper atmosphere responds to solar variability or lower atmospheric dust storms.

In this dissertation I have studied which tidal modes are present in the upper atmosphere and how they relate to observations and simulations of tides in the lower atmosphere. I have also developed and applied a novel technique for measuring winds with the accelerometer data. Many of the other questions posed in the preceding paragraph remain to be answered; I hope to answer them in future work as I delve deeper into this dataset aided by theoretical predictions, lower atmospheric observations, and similar, subsequent datasets like those of the Mars Odyssey and Mars Reconnaissance Orbiter accelerometers.

1.4 Dissertation Structure

Chapter 2 is an expanded version of a paper accepted for publication by *Icarus* (Withers et al., 2003). Steve Bougher and Gerry Keating are coauthors. As my advisor, Steve Bougher provided guidance, oversight, and innumerable comments on draft manuscripts. Gerry Keating is a coauthor because of his role as instrument principal investigator. Several other people are acknowledged in the paper for their assistance. Chapters 3 and 4 will be prepared for publication after I graduate. Chapter 5 has been accepted for publication by *Planetary and Space Science* (Withers et al., 2003). Martin Towner, Brijen Hathi, and John Zarnecki are coauthors. Martin Towner provided insight into real-world issues with instrumentation and commented on many early drafts of this chapter/publication. There are several

short passages in this chapter that are more his words than mine. Brijen Hathi provided helpful discussions on the coordinate frames and aerodynamics. John Zarnecki provided supervision and financial support. Several other people are acknowledged in the paper for their assistance. Chapter 6 is work that I will use as a member of the MER Entry, Descent, and Landing Atmosphere Science Advisory Team when the two MER spacecraft reach Mars in early 2004. Chapter 7 has been published in *Icarus* (Withers et al., 2002). Greg Neumann and Ralph Lorenz are coauthors. Greg Neumann provided expert advice on the MOLA dataset. Ralph Lorenz wrote the *Datathief* program that extracted data from a figure in another publication. Several other people are acknowledged in the paper for their assistance. Chapter 8 has been published in *Nature* (Withers and Neumann, 2001). Greg Neumann is a coauthor. He was my supervisor during my summer internship at Goddard when I began this work. Several other people are acknowledged in the paper for their assistance. Chapter 9 and a subsequent Comment and Reply have been published in *Meteoritics and Planetary Science* (Withers, 2001; Nockolds and Withers, 2002). Several other people are acknowledged in the paper for their assistance. Chapter 10 contains my contribution to Lorenz et al. (2001) and some subsequent work that has not been published. Only one of the projects that I have presented at scientific meetings is not included here — Angle of Repose-limited Shapes of Asteroids. This project, which tried to find how far away from spherical an asteroid could be without requiring strength, has not received enough of my attention in recent years to develop beyond the level of a class project. The question remains interesting and unsolved, but it not discussed further in this dissertation.

I have not tried to keep fully up-to-date with the scientific literature whilst preparing this dissertation. I have not cited any publications that appeared in the LPL library after 2002. Important publications from 2003 will have to wait until my next peer-reviewed publications to be cited appropriately.

1.5 Sources of Support

I have received intellectual support from a great many people in the past five years. Many secretaries, faculty, postdocs, and graduate students at LPL have been generous with their time when I have been seeking help. I single out some of the most important ones here. Don Hunten and Jay Melosh have, in their own inimitable styles, shaped my ideas of what a scientist should be, what problems should be tackled, and how they should be tackled. Their teachings have influenced how I selected and approached the projects included in this dissertation. Ralph Lorenz's enthusiasm for simplicity in science and understanding of what makes a spacecraft mission work are resources that I have called upon often. Chapters 6, 7, and 10 have been influenced by his ideas. Many discussions with those graduate students whom I met when I arrived at LPL have helped guide me safely through the department, conferences, orals, publications, this dissertation, and job-hunting. Outside LPL, the LPL mafia has given me many networking opportunities. Bob Tolson has saved me from several horrendous mistakes with his occasional emails. His comments have influenced Appendix A and my processing of data in Chapter 4. I have been privileged to see how a science team should work through my association with the MOLA team which led to Chapter 8. The Open University welcomed me back to Britain one summer and helped me catch up on planetary science activities in Europe. Finally, Steve Bougher has let me invest my time (and his money) in projects far afield from his research interests that have helped me reach this stage of my career. The freedom he has given me to make mistakes has been invaluable to me.

I have received financial support from a variety of sources. Steve Bougher's NASA grants were my primary source of funding. LPL has supported me with two semesters of quarter-time teaching assistantships and one semester of a half-time research assistantship after Steve Bougher moved to the frozen north. The University of Arizona's College of Science awarded me a Galileo Circle Scholarship that helped me after two summers away from LPL's doubled summer pay. The Goddard

Summer Student Program in the GSFC Earth Sciences Directorate supported me for one summer. The MOLA team supported my travel to several conferences and team meetings. The Open University supported me for another summer. Jonathan Lunine sent me to an LPSC meeting. JPL partially sent me to a Planetary Science Summer School. The European Union sent me to Italy for two wonderful weeks. Finally, the Deep Space 2 E/PO budget supplied me with a fine computer. Sadly, I am barred from entering the MER naming contest.

CHAPTER 2

TOPOGRAPHICALLY-CONTROLLED THERMAL TIDES IN THE MARTIAN UPPER ATMOSPHERE

2.1 Abstract

Mars Global Surveyor accelerometer observations of the martian upper atmosphere have revealed large variations in density with longitude during northern hemisphere spring at altitudes of 130 – 160 km, all latitudes, and mid-afternoon local solar times (LSTs). This zonal structure is due to tides from the surface. The zonal structure is stable on timescales of weeks, decays with increasing altitude above 130 km, and is dominated by wave-3 (average amplitude 22% of mean density) and wave-2 (18%) harmonics. The phases of these harmonics are constant with both altitude and latitude, though their amplitudes change significantly with latitude. Near the South Pole, the phase of the wave-2 harmonic changes by 90° with a change of half a martian solar day while the wave-3 phase stays constant, suggesting diurnal and semidiurnal behaviour respectively. I use a simple application of classical tidal theory to identify the dominant tidal modes and obtain results consistent with those of General Circulation Models. My method is less rigorous, but simpler, than the General Circulation Models and hence complements them. Topography has a strong influence on the zonal structure.

2.2 Introduction

My objectives in Chapter 2 are to understand the nature of large variations in density with longitude observed in the martian upper atmosphere with the Mars Global Surveyor (MGS) accelerometer and to identify the underlying phenomena that cause them. I present a quantitative and detailed analysis of this zonal structure as a function of altitude, latitude, and local solar time (LST). I then use classical tidal theory to identify the dominant mechanisms causing the zonal structure, and finally outline a simple justification for topography having a strong influence on the zonal structure. I begin by quantifying the sol-to-sol (a sol is a martian solar day) variability, or weather, in the martian upper atmosphere and placing some constraints on its causes.

Accelerometer data from MGS's aerobraking phases revealed an unexpected phenomenon: the upper atmospheric density at fixed altitude, latitude, LST, and season varied by factors of 2 or more as a function of longitude (Keating et al., 1998). Corresponding atmospheric variabilities for the Earth, measured by the Satellite Electrostatic Triaxial Accelerometer at its reference altitude of 200 km altitude, are on the order of 10% (Forbes et al., 1999). For reference, typical atmospheric densities at 200 km altitude on Earth in Forbes et al. (1999) are $\sim 0.1 \text{ kg km}^{-3}$ and typical atmospheric densities at 130 km altitude on Mars in this Chapter (Tables 2.2 and 2.3) are $\sim 1 \text{ kg km}^{-3}$. No such variations can be observed on Venus because its similar lengths of day and year do not allow all longitudes to have the same LST on a sub-annual timescale.

This zonal structure must originate in the lower atmosphere; it cannot be created *in situ*. There are no zonal inhomogeneities present in solar heating, which powers the dynamics of the martian atmosphere, or in the upper boundary of the atmosphere. There are many zonal inhomogeneities near the lower boundary of the atmosphere, including topography, surface thermal inertia, surface albedo, and lower atmosphere dust loading, which may influence this zonal structure. Since the

zonal structure must propagate through, and be affected by, the lower atmosphere, observations of the zonal structure in the upper atmosphere may reveal information about the properties of the lower atmosphere. This zonal structure is caused by atmospheric tides, which are global-scale atmospheric oscillations at periods which are subharmonics of a solar day (Forbes, 1995).

Keating et al. (1998) found that the zonal structure intensified during the build-up of a regional dust storm and, based on the constancy of its phasing, suggested that it was caused by topographically forced stationary waves. Several publications have presented theoretical simulations disagreeing with the stationary wave (disturbances which have no variation with time) hypothesis of Keating et al. (1998) for the zonal structure. Instead, nonmigrating tides, disturbances which vary with time but are not locked in phase with the Sun, are suggested (Keating et al., 1999; Keating et al., 2000; Forbes and Hagan, 2000; Joshi et al., 2000; Wilson, 2000a; Forbes et al., 2001). The restricted sampling in LST of the accelerometer data make these two types of disturbances impossible to distinguish observationally. Stationary waves are unlikely because they require an implausible vertical profile of zonal winds in the lower atmosphere if they are to be present in the upper atmosphere. All of these publications responding to Keating et al. (1998) predate the public release of the accelerometer dataset, hence they are based on the limited quantitative data presented in that paper and short conference abstracts discussing the complete accelerometer dataset (Keating et al., 1998; Keating et al., 1999; Keating et al., 2000). Here I present an analysis of the complete accelerometer dataset.

A previous publication has discussed the properties of the zonal structure, including its responses to changes in altitude, latitude, and LST, using the complete accelerometer dataset. Wilson (2002) observed that the zonal structure decreased in amplitude with increasing altitude and did not change in phase with changes in latitude. Wilson (2002) discussed the observation of Withers et al. (2000) that the zonal structure varied with half a sol changes in LST. Wilson (2002) did not present

quantitative results for how altitude or LST affected the zonal structure, nor did he quantify changes in the zonal structure on weekly timescales. Wilson (2002) only presented quantitative results for the strongest 2 components of the zonal structure, wave-2 and wave-3. In this chapter I present quantitative results for all these items, including the first four harmonic components of the zonal structure. Wilson (2002) compared his analysis of the MGS density data to General Circulation Model (GCM) predictions that accurately reproduced some aspects of the zonal structure, such as its amplitude and phase at 130 km and its changes with LST. He used them to identify the dominant tides causing the zonal structure (Wilson, 2002). Unlike Wilson (2002), I use my observations in conjunction with idealized classical tidal theory to identify the dominant tides. In this longer work I am able to go into more quantitative detail about the accelerometer dataset and choose a less rigorous, but simpler, theoretical approach to interpret my observations. I also outline a simple justification for topography, rather than any other surface physical property, being the strongest influence on the zonal structure.

The zonal structure and the tidal modes responsible for it have also been studied by other instruments onboard MGS, including the Thermal Emission Spectrometer (TES), the Mars Horizon Sensor Assembly, and the Radio Science experiment (Banfield et al., 2000; Banfield et al., 2003; Smith et al., 2001; Murphy et al., 2001; Bougher et al., 2001; Hinson et al., 2001; Tracadas et al., 2001).

The dynamics of the martian upper atmosphere are important for several reasons. Firstly, great cost savings are generated when a spacecraft aerobrakes into orbit around Mars, rather than using chemical propellant. Aerobraking is not possible without an understanding of the upper atmosphere, and improvements in this understanding yield great cost savings. Secondly, theoretical models of the upper atmospheres of Earth and Mars, regions which are very sensitive to changes in solar flux, share many key features. Understanding the upper atmosphere of Mars helps develop and verify these models, which can then be used, for example, to monitor changes in solar flux in Earth's upper atmosphere, an important measurement

for terrestrial climate change. Thirdly, as we shall see later in Section 2.6.1, the dynamics of the lower and upper atmosphere on Mars are strongly coupled, so by understanding the upper atmosphere we also learn about the lower atmosphere. The publicly available accelerometer dataset from the MGS spacecraft is a rich resource for studying the martian upper atmosphere (Keating et al., 2001a; Keating et al., 2001b). The results of this chapter contribute to a better understanding of the dynamics of the martian upper atmosphere.

The remainder of this chapter is divided into six parts. The first of these, Section 2.3, provides background information on the MGS accelerometer dataset.

In Section 2.4, Section 2.4.1 introduces the concept of sol-to-sol variability, or weather, *i. e.* changes between repeated density measurements at fixed altitude, latitude, LST, and season at intervals of one martian day, in the upper atmosphere. Section 2.4.2 presents my observations of the sol-to-sol variability and the implications each of them have for the nature of this variability. Finally, in Section 2.4.3, I sum up my constraints on the mechanism responsible for the sol-to-sol variability.

In Section 2.5, Section 2.5.1 introduces the zonal structure. Next, in Section 2.5.2, I examine how the amplitudes and phases of the harmonics making up the zonal structure change on timescales on the order of weeks. Section 2.5.3 continues this theme by examining how the amplitudes and phases of each harmonic in the zonal structure change as a function of altitude and see if this behaviour is affected by latitude. Section 2.5.4 follows by examining changes in the amplitudes and phases of each harmonic in the zonal structure as a function of latitude, discussing whether the cause of the zonal structure is planetary-scale or localized, and quantifying which harmonics are dominant. Finally, in Section 2.5.5, I compare the amplitudes and phases of harmonics in dayside and nightside zonal structures in polar regions.

In Section 2.6, Section 2.6.1 uses only the accelerometer data and classical tidal theory to make preliminary conclusions about which tides are causing the zonal

structure in the upper atmosphere. Section 2.6.2 discusses previous modelling and observational work on tides and the zonal structure and uses it to re-examine the preliminary conclusions of Section 2.6.1. Finally, in Section 2.6.3, I outline a simple justification for topography, rather than any other surface physical property, being the main underlying cause of the zonal structure.

Three short Sections complete this Chapter. Section 2.7 discusses the successful aerobraking of Mars Odyssey and the planned aerobraking of Mars Reconnaissance Orbiter. Section 2.8 discusses opportunities to extend and develop my studies of tides and zonal structure in the martian upper atmosphere. Finally, in Section 2.9, I state my main conclusions.

2.3 MGS Aerobraking

An aerobraking spacecraft, such as Mars Global Surveyor, passes through an atmosphere near the periapsis of its orbit and experiences an aerodynamic force which decreases the energy and semi-major axis of the spacecraft's orbit without the need for significant fuel consumption (French and Uphoff, 1979; Eldred, 1991). Aerobraking has previously been used by Atmospheric Explorer-C and its successors at Earth, the Pioneer Venus Orbiter at Venus, and Magellan at Venus (Marcos et al., 1977; Strangeway, 1993; Croom and Tolson, 1994; Lyons et al., 1995). Aerobraking permits *in situ* atmospheric studies not possible from a typical spacecraft orbit. The ill-fated Mars Observer, designed to use chemical propulsion for orbit insertion, launched on a \$350M Titan III, whereas Mars Global Surveyor (MGS), reflaying 5 of the 7 lost Mars Observer science instruments and designed to use aerobraking for orbit insertion, launched on a \$50M Delta II (Lyons, 1996; Albee et al., 1998; Albee et al., 2001). This was the first use of aerobraking as an operational necessity in planetary exploration. Despite serious structural problems with the spacecraft, which restricted the maximum heating rate it could safely endure, and a severe dust storm raging in the atmosphere, MGS eventually reached its desired orbit and has

completed both its nominal and an extended mission (Tolson et al., 2000; Albee et al., 2001). Aerobraking would have been used by Mars Climate Orbiter, has been successfully used by Mars Odyssey, and is likely to be used by many future missions, including non-Mars missions.

MGS carried an Accelerometer Experiment (Keating et al., 1998; Keating et al., 2001a; Keating et al., 2001b). This accelerometer measured the aerodynamic forces on the spacecraft during an aerobraking pass. The accelerometer readings have been processed to generate a “profile” of atmospheric density along each flight path through the atmosphere (Keating et al., 1998; Cancro et al., 1998; Tolson et al., 1999; Tolson et al., 2000; Keating et al., 2001a; Keating et al., 2001b). This information was used by the spacecraft operations team in the hours immediately after the aerobraking pass to plan modifications to MGS’s trajectory, changing the altitude of the next periapsis in steps of about 2 km by small expenditures of chemical propellant at apoapsis, to achieve the desired drag without exceeding heating rate thresholds, and guide it safely to the desired mapping orbit. MGS’s orbit during aerobraking was near-polar, with an inclination of about 93° , and highly elliptical.

The changing characteristics of MGS’s orbit during aerobraking were quite complicated and controlled the data coverage of the accelerometer. As such, they strongly influence the data analysis that I am able to do in Sections 2.4 and 2.5. I first discuss the orbital characteristics for the case when periapsis is away from the pole.

A typical aerobraking pass through the atmosphere lasted a few minutes and spanned several tens of degrees of latitude with only small changes in longitude or LST; unlike planetary entry probes or landers, the flight path of MGS through the atmosphere on each aerobraking pass is not vertical. On a typical aerobraking pass, latitude has a roughly quadratic dependence on altitude. The maximum altitude at which the accelerometer measured atmospheric density, set by the instrument sensitivity, was approximately 160 km. The minimum altitude at

which the accelerometer measured atmospheric density was that of periapsis, typically 110 km. Periapsis altitude was rarely outside 100–120 km. It often changed from one orbit to the next by a kilometre or so in response to the non-spherically symmetric gravitational field of Mars, in addition to any deliberate trajectory modifications. As aerobraking progressed, MGS’s apoapsis altitude steadily decreased and the parabolic aerobraking pass through the atmosphere became flatter. A given altitude level was crossed twice on each aerobraking pass, once descending towards periapsis at one latitude and longitude, and once ascending after periapsis at another latitude and longitude. To distinguish between these two measurements at the same altitude and same orbit, I refer to the “inbound” and “outbound” legs of an aerobraking pass.

Since the near-polar orbit was close to sun-synchronous, periapsis LST changed only slowly between orbits. Periapsis longitude changed greatly between orbits as the planet rotated every 24.6 hours beneath MGS’s orbit. The change in periapsis longitude per orbit, relative to 360° , was equal to the ratio of MGS’s orbital period to the martian rotational period.

Periapsis latitude changed slowly but steadily between orbits. Due to the oblateness of Mars, the orbit precessed around in its orbital plane (Murray and Dermott, 1999). This caused periapsis latitude to change. The entire parabolic flight path also shifted in latitude as the orbit precessed. Due to this precession, I can analyse densities at a range of altitudes, but fixed latitudes, from the non-vertical aerobraking passes (Section 2.5.3) and analyse densities at a range of latitudes, but fixed altitudes (Section 2.5.4). To summarize, MGS had a slowly flattening, parabolic flight path through the atmosphere, travelled in either a north or south direction with small changes in LST and longitude during a pass, with large changes in longitude due to the planet’s rotation, small changes in LST, and steady changes in latitude between periapses.

The picture is more complicated when periapsis is in the polar regions. This is discussed in Section 2.5.5.

Aerobraking took place in two Phases, 1 and 2, separated by a hiatus containing the Science Phasing Orbits (Albee et al., 1998; Albee et al., 2001). Phase 1 included orbits 1 – 201 from mid-September, 1997, to late March, 1998, and Phase 2 included orbits 574 – 1283 from mid-September, 1998, to early February, 1999. This covers a range of martian seasons. L_S , martian heliocentric longitude, is 0° at the northern spring equinox, 90° at the northern summer solstice, 180° at the northern autumn equinox, and 270° at the northern winter solstice. At the beginning of Phase 1, $L_S = 180^\circ$, periapsis occurred at 30°N and 18 hrs LST, then moved northwards and earlier in the day to reach 60°N and 11 hrs LST at the end of Phase 1, $L_S = 300^\circ$. One “hour” of LST is equal to 1/24th of a sol, not 60 minutes of elapsed time. MGS flew from north to south through the atmosphere on each aerobraking pass during Phase 1. At the beginning of Phase 2, during the next martian year at $L_S = 30^\circ$, periapsis occurred at 60°N and 17 hrs LST, then moved southwards and earlier in the day to cross 80°S at 15 hrs LST. At the beginning of Phase 2, MGS flew from south to north through the atmosphere on each aerobraking pass. Periapsis then reached its farthest south ($\sim 87^\circ\text{S}$) near the south pole, crossed the terminator by drifting through nighttime LSTs, and reached 60°S and 02 hrs LST by the end of Phase 2, $L_S = 90^\circ$. At the end of Phase 2, MGS flew from north to south through the atmosphere on each aerobraking pass. When periapsis was near the south pole, each aerobraking pass’s profile of atmospheric density spanned a large range of LST. The behaviour of periapsis during aerobraking is summarized in Figure 2.1.

In this chapter, I discuss two broad subsets of the accelerometer data, both from Phase 2 of aerobraking. The Phase 1 data are complicated by significant changes in both periapsis latitude and LST between each orbit and by the presence of a regional dust storm, so I leave them for future work. Some work on the Phase 1 data has previously been published (Keating et al., 1998; Bougher et al., 1999). The two subsets of data from Phase 2 are: (1) the southward progression from 60°N to 60°S at almost fixed L_S and LST at the beginning of Phase 2 and (2) the crossing of the south pole from 60°S back to 60°S at almost fixed L_S and two

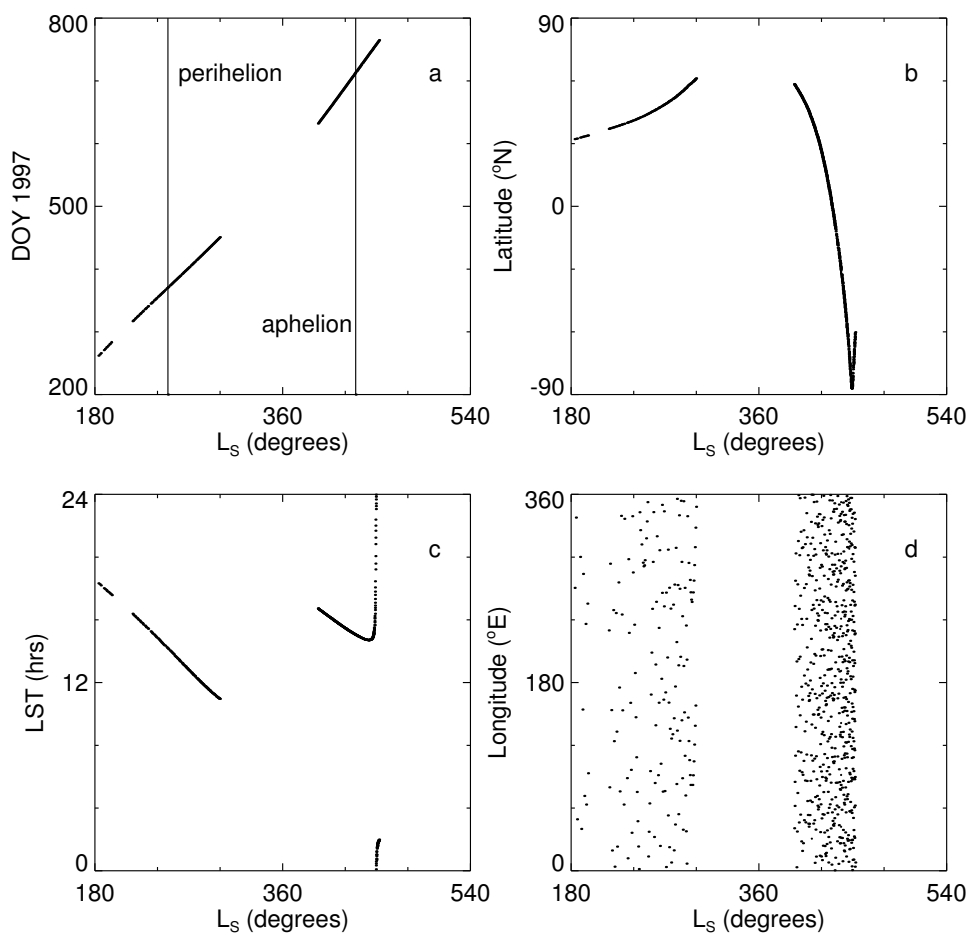


Figure 2.1: Parameters of periapsis during aerobraking: (a) periapsis date in days since Jan 1, 1997 (DOY 1997), (b) periapsis latitude, (c) periapsis LST, and (d) periapsis longitude, all plotted against heliocentric longitude, L_S . Phase 1 of aerobraking occurred before $L_S = 360^\circ$ and Phase 2 afterwards. The change from daytime to nighttime LSTs as periapsis reached its furthest south can be seen at $L_S \sim 450^\circ$. The L_S of perihelion and aphelion are marked on panel (a) for reference.

different LSTs, half a sol apart, at the end of Phase 2. I name these two subsets of data the “Daytime Precession” (subset 1) and the “Polar Crossing” (subset 2). The boundary between these two subsets is defined as when a specified point on the aerobraking pass crosses the 60°S boundary on the dayside part of Phase 2. When discussing, for example, data at 130 km altitude from the inbound leg of aerobraking passes, all aerobraking passes in which the latitude at 130 km on the inbound leg is south of 60°S are classified in the Polar Crossing part of Phase 2. For data at different altitudes, or from the other leg of the aerobraking pass, a slightly different group of aerobraking passes forms the Polar Crossing part of Phase 2. As a rough guide, the first periapsis latitude southward of 60°S occurred on orbit 1095.

Data from the Accelerometer Experiment is archived in the Planetary Data System (PDS) (Keating et al., 2001a). This dataset contains 800 upper atmospheric density profiles. The only previous three are those of the Pathfinder and two Viking landers (Magalhães et al., 1999; Seiff and Kirk, 1977a). Also archived are data extracted from 768 of these profiles at 130, 140, 150, and 160 km altitude on both the inbound and outbound legs of each aerobraking pass (Keating et al., 2001b). The constant altitude data were used for this work. Many orbits between 911 and 961, during the Daytime Precession part of Phase 2 of Aerobraking, do not have density data due to spacecraft computer problems. Data and results affected by this are highlighted in the text.

Previous work on this dataset includes Angelats i Coll et al. (2001), Bougher et al. (1997), Bougher and Keating (1999), Bougher et al. (1999), Bougher et al. (2000), Bougher et al. (2000), Bougher et al. (2001), Bougher et al. (2001), Forbes (1999), Forbes and Hagan (2000), Joshi et al. (2000), Keating et al. (1998), Keating et al. (1999), Keating et al. (1999), Keating et al. (2000), Keating et al. (2001), Tolson et al. (1999), Tolson et al. (2000), Wilson (2000b), Wilson (2002), Withers et al. (1999), Withers et al. (2000), Withers et al. (2001a), Withers et al. (2001b), Withers et al. (2002b), Withers et al. (2002a), and Withers et al. (2002c). There have been few peer-reviewed publications analysing this dataset, so there is

not a comprehensive bibliography anywhere in the literature of existing work on this dataset.

2.4 Sol-to-Sol Variability

2.4.1 Introduction to Sol-to-Sol Variability

In this section I quantify sol-to-sol variability in the atmosphere to test whether I can meaningfully compare density measurements made at different longitudes on different days as if they were made simultaneously. Such comparisons are important in the remainder of this chapter.

During aerobraking, the orbital period of MGS decreased from over 30 hours to less than two hours. Whenever the orbital period was a submultiple of Mars's 24.6 hour rotational period, repeated density measurements were made along essentially the same flight paths, that is longitude/altitude/latitude, at one sol intervals. When the rotational period is n times the orbital period, then I say that MGS is in the $n:1$ resonance. Such a "resonance" typically lasted for several sols as the orbital period decreased through the resonance condition. In the 1:1 resonance, an aerobraking pass traces the same altitude/latitude/longitude path as the one before it. In the 2:1 resonance, there are two different altitude/latitude/longitude paths 180° apart in longitude traced through the atmosphere on each aerobraking pass, each traced by every second one. In the $n:1$ resonance, paths are $360^\circ/n$ apart, each traced by every n th aerobraking pass. If the outbound legs at, say, 130 km are considered, and the latitudes and longitudes of each orbit in the $n:1$ resonance are plotted, then they form n clusters separated by $360^\circ/n$ of longitude. I study the different density measurements taken in these very restricted altitude/latitude/longitude clusters during various resonances. If the atmosphere does not change from one sol to the next, then all the measurements in a given cluster should be the same. My measure of the sol-to-sol variability is the standard deviation of the density measurements

in a cluster, expressed as a percentage of the mean of the density measurements in that cluster. For example, the number “50” implies a standard deviation equal to half of the mean.

This analysis is important for determining how much of the difference between density measurements at different longitudes and sols is due to zonal structure and how much is due to temporal variations. The sol-to-sol variability is an important parameter in mission planning and operations involving aerobraking, such as the current planning for Mars Reconnaissance Orbiter.

Orbits were assigned to the $n:1$ resonance if their periods were within 3% of the appropriate submultiple of the martian sidereal day. With this criterion, the latitudes and longitudes at, say, 130 km on the inbound leg of each orbit in the resonance formed well-defined clusters (typically 10° wide in longitude and somewhat narrower in latitude) with enough orbits in each cluster to measure a meaningful atmospheric sol-to-sol variability.

As an example, I show in Figure 2.2 the four trajectories and density profiles whose periapsis longitudes were within $\pm 5^\circ$ of 135°E during the 7:1 resonance. These are periapses 963, 970, 977, and 984. Periapsis latitude progressed southward as periapsis number increased, so periapsis 963 is the northernmost aerobraking pass in Figure 2.2. Three density profiles are very similar, but the periapsis 977 profile is significantly different.

In summary, occasional repeat measurements at one sol intervals along nearly identical flight paths can constrain the sol-to-sol variability in the martian upper atmosphere at fixed longitude, altitude, latitude, and LST.

2.4.2 Observations of Sol-to-Sol Variability

Figure 2.3 shows the sol-to-sol variability for the 3:1 to 8:1 resonances. These resonances occurred during the Daytime Precession part of Phase 2. Crosses

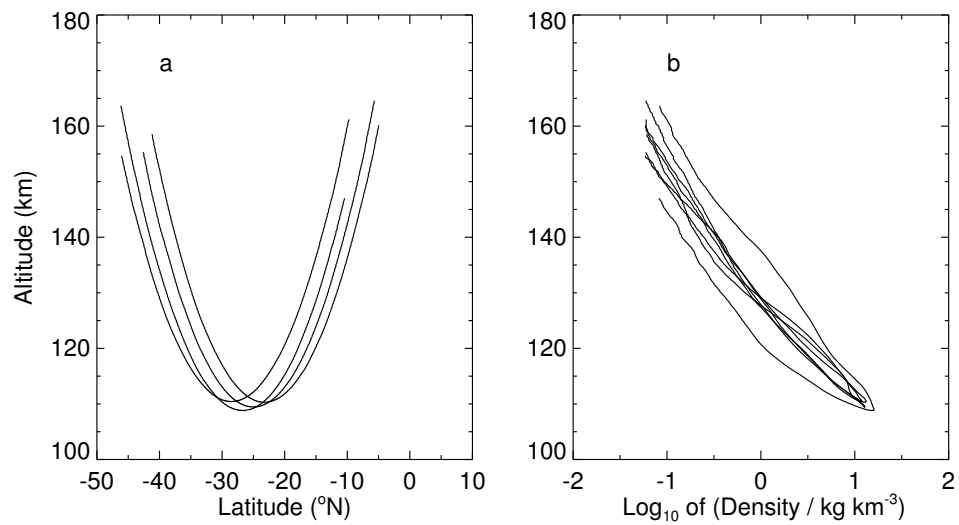


Figure 2.2: Trajectories (a) and density profiles (b) for periapses within $\pm 5^\circ$ of 135°E during the 7:1 resonance. From the north, periapsis numbers are 963, 970, 977, and 984. Periapsis 977's density profile is significantly different from the others.

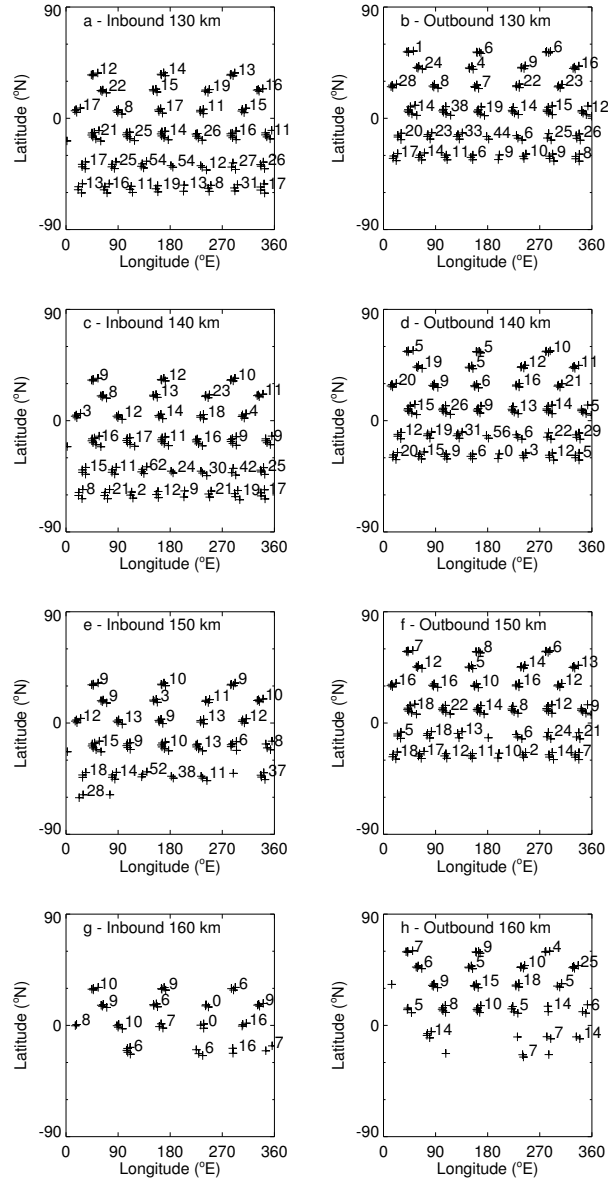


Figure 2.3: Latitudes and longitudes of clustered density measurements made at 130, 140, 150, and 160 km altitude on inbound and outbound legs during the 3:1 — 8:1 resonances, plotted as crosses. The number adjacent to each cluster of crosses is the sol-to-sol variability for that cluster.

mark the latitude and longitude of each density measurement at a certain altitude whose orbital period satisfies my resonance criterion. Fewer crosses are plotted at higher altitudes because many orbits do not have good density measurements at the higher altitudes. This is especially common in the southern (winter) hemisphere, where observed densities were lower than at corresponding northern (summer) latitudes. Each row of crosses on a panel in Figure 2.3 corresponds to a different resonance. The $n:1$ resonance contains n clusters at equally spaced longitudes. By counting the numbers of clusters at a given latitude in a panel of Figure 2.3, n for that resonance can be found. This does not work so well at the higher altitudes where nothing is plotted for some clusters, because none of the orbits which belong to those clusters have valid density measurements at those altitudes. On panel (a), data in the northernmost three clusters were collected over a few days during the 3:1 resonance. During those same few days of the 3:1 resonance, data in the northernmost three clusters on each panel were collected. A couple of weeks later, data in the second row of four clusters were collected for each panel. On each panel, the same orbits contribute to, say, the northernmost and easternmost cluster. The $n:1$ resonance at any altitude is farther north on outbound than inbound. The latitude of the outbound (inbound) $n:1$ resonance at a given altitude is further north (south) than at any lower altitude. The numbers adjacent to each cluster are my measure of the sol-to-sol variability in that cluster. Table 2.1 gives the periapsis latitude, periapsis LST, L_S , and beginning and ending periapsis numbers for each resonance. Periapsis number n was the n th periapsis during the MGS mission.

1σ measurement errors in the individual density measurements are about 3% or less over 130 – 150 km, increasing to 5% at 160 km (Keating et al., 2001b). These are negligible compared to the sol-to-sol variability at 130 – 150 km altitude. At 160 km, the 5% measurement error is smaller than the average sol-to-sol variability of 8 – 10%, suggesting that I am actually observing sol-to-sol variability and not merely errors in individual measurements. The sol-to-sol variability decreases with increasing altitude. It averages 15 – 20% at 130 km and 8 – 10% at 160 km. This is consistent with dissipative processes operating on upwardly propagating

Resonance	L_S (degrees)	Latitude (°N)	LST (hrs)	Beginning Periapsis	Ending Periapsis
3:1	48	45	16	645	656
4:1	57	32	16	710	725
5:1	64	16	15	784	803
6:1	71	-4	15	864	901
7:1	78	-28	15	963	989
8:1	82	-45	15	1030	1057

Table 2.1: L_S , periapsis latitude, periapsis LST, and beginning and ending periapsis number for the 3:1 – 8:1 resonances.

disturbances (Zurek et al., 1992; Forbes et al., 2001).

At a given altitude, latitude, LST, and season, the sol-to-sol variability is not constant from one longitude region to the next. A few hours separates measurements at one longitude region on a given sol from measurements at the neighbouring longitude region on the same sol. The sol-to-sol variability often changes significantly over longitude intervals of only 60° . Either the solar forcing is varying significantly on timescales of a few hours or the sol-to-sol variability is in some way affected by the local properties of the planetary surface far below.

There is no obvious difference between sol-to-sol variabilities in the tropics and in the extratropics, so the sol-to-sol variability cannot be caused by a mechanism that is filtered out beyond certain latitudes, such as inertio-gravity waves with periods of one sol or longer (Houghton, 2002). At the highest northern, but not southern, latitudes the sol-to-sol variability is significantly lower than is typical. This difference between the inbound and outbound legs of the 3:1 resonance could be due to effects from the planetary surface or differences in the atmospheric dynamics between the near-winter polar regions and elsewhere; it can't be due solely to solar flux variations.

Compare, for example, the inbound and outbound 8:1 resonances at 130 km. The inbound example, at 60°S , has its lowest value of sol-to-sol variability at 250°E and its highest at 290°E , yet the outbound example, at 30°S and including the same aerobraking passes, has its lowest value at 150°E and its highest at 20°E . This is one example, and others can be seen in Figure 2.3, of changes in the sol-to-sol variability over meridional length scales of several tens of degrees. This is in contrast to the zonal structure, discussed from Section 2.5 onwards, which has no significant changes over similar meridional length scales.

Compare, for example, the outbound 7:1 resonances at 130 and 140 km. The lower example has its lowest value of sol-to-sol variability at 220°E and its highest at 180°E . So has the other example, 10 km higher up. This is one example, and others

can be seen in Figure 2.3, of sol-to-sol variabilities at one altitude level being related to sol-to-sol variabilities at the neighbouring altitude level. This implies that the vertical length scale for changes in the sol-to-sol variability at one longitude relative to another is greater than 10 km.

The sol-to-sol variability at fixed altitude and latitude is not constant from one observation using inbound data to another observation, a few weeks later at the same altitude and latitude, using outbound data during a different resonance. Neither its pattern of high and low values as a function of longitude nor its zonally-averaged value is constant. For example, the inbound leg of the 6:1 resonance and the outbound leg of the later 7:1 resonance both occurred around $10^\circ - 20^\circ\text{S}$, yet the zonal mean of the sol-to-sol variabilities is significantly higher for the outbound leg of the 7:1 resonance compared to the inbound leg of the 6:1 resonance. The inbound leg of the 6:1 resonance has low sol-to-sol variabilities around 220°E flanked by higher variabilities, yet the outbound leg of the 7:1 resonances has high variabilities around 220°E flanked by lower variabilities. This suggests that the time scale for change in the sol-to-sol variability is less than several weeks, *i. e.* short on seasonal timescales, and that the sol-to-sol variability is not simply a function of properties of the underlying surface.

Sol-to-sol variability as a function of longitude is not correlated with the elevation of the topography below, so the sol-to-sol variability is not significantly affected by a few km difference in the distance propagated through the lower atmosphere.

Later in the mission, during the Polar Crossing part of Phase 2, inbound and outbound legs of an aerobraking pass spanned similar latitudes on opposite sides of the pole. During the 11:1 resonance, inbound measurements at 130 km were made at $70^\circ - 80^\circ\text{S}$ and $\text{LST} = 01$ hours and outbound measurements at the same altitude were made a few minutes later at $60^\circ - 70^\circ\text{S}$ and $\text{LST} = 15$ hours. Data at higher altitudes are not available. In this case, I extended my resonance criterion from periods within 3% of resonance to 4% to have enough measurements

in most clusters. Figure 2.4 shows significant LST dependence in relative sol-to-sol variability as function of longitude, though both dayside and nightside measurements have average sol-to-sol variabilities in the typical 15 – 20% range for 130 km altitude.

High sol-to-sol variabilities do not coincide with high densities in the zonal structure, which can be seen in Section 2.5.4. The sol-to-sol variability is not correlated with the zonal structure, so they have different causes.

In summary, the mechanism(s) responsible for the sol-to-sol variability has a vertical length scale greater than 10 km, a meridional length scale less than several tens of degrees, a zonal length scale less than 60 degrees, and a timescale shorter than several weeks. The sol-to-sol variability weakens with increasing altitude, is affected by changes in LST, and is not restricted in latitude. As discussed later in Sections 2.5.2 and 2.5.4, the mechanism responsible for the zonal structure has different properties, specifically longer time and meridional scales.

2.4.3 Discussion of Sol-to-Sol Variability

In this section I discuss the implications of the previous section and other work for the cause of the sol-to-sol variability. I also make predictions about the sol-to-sol variability to be compared against future observations.

Sol-to-sol variations in density due solely to short-term solar flux variations have been observed in data from Phase 1 of aerobraking. Keating et al. (1998) observed a 50% increase in density at 160 km altitude at both 32°N and 57°N near orbit 90, with no significant change in density at 130 km altitude, at the same time as an increase in the extreme ultra-violet solar flux incident upon the martian atmosphere. The decrease in sol-to-sol variability with increasing altitude in this Section, in contrast to the increase in sol-to-sol variability with increasing altitude in the Keating et al. (1998) example, suggests a mechanism beyond just short-term solar flux variations.

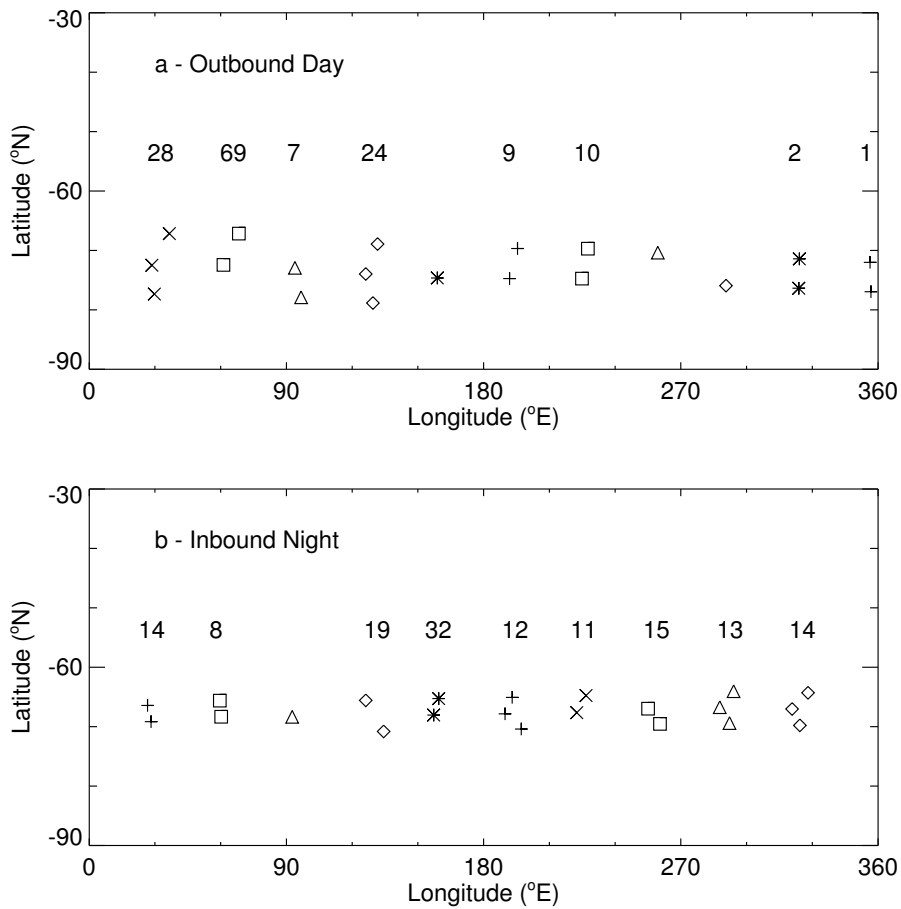


Figure 2.4: Locations of repeat samplings at 130 km during the 11:1 resonance and sol-to-sol variability in each cluster, as discussed in Section 2.4.2. To aid identification of the clusters, all measurements in a given cluster have the same symbol and neighbouring clusters have different symbols.

Several observations from the MGS Radio Science experiment may shed light on this subject (Tyler et al., 2001). Tracadas et al. (2001) studied changes in the orbit of MGS during the Science Phasing Orbits and concluded that at 180 km altitude and latitudes north of 60°N the orbit-to-orbit variability of atmospheric density at $L_S = 300^\circ - 360^\circ$ and LST= 13 hours was 50 – 70%, whereas at $L_S = 0^\circ - 30^\circ$ and LST= 07 hours it was 10 – 20%.

Tracadas et al. (2001) also concluded that no zonal structure was present. Their orbit-to-orbit variability may not be due solely to sol-to-sol variability, since it may be affected by zonal variability that does not have the well-behaved form of the zonal structure. Since zonal variability should asymptote to zero at high altitudes I shall assume that this orbit-to-orbit variability is purely sol-to-sol variability. Their 10 – 20% variability at 180 km altitude near the beginning of the Daytime Precession part of Phase 2 is similar in scale to my 8 – 10% variability at 160 km during the Daytime Precession part of Phase 2. Either the sol-to-sol variability in the upper atmosphere was greater during their observations than mine or the sol-to-sol variability does not decrease monotonically with increasing altitude above the 130 – 160 km region.

Hinson et al. (2001) analysed temperature profiles as a function of pressure from 0 – 50 km altitude at $L_S = 74^\circ - 77^\circ$, 04 hours LST, and latitude = 65°N . They found sol-to-sol variability of less than 2% but significant variability with longitude. These measurements were made between the 6:1 and 7:1 resonances. My measurements, at the earlier L_S of 48° during the 3:1 resonance, of the sol-to-sol variability in the upper atmosphere at $55 - 60^\circ\text{N}$ are the closest to these in latitude. These northernmost measurements have the lowest sol-to-sol variability of any in Figure 2.3. These observations suggest that sol-to-sol variability in the lower and upper atmospheres is low at far northern latitudes during this season. Equivalent southern latitudes have sol-to-sol variability in the upper atmosphere that is typical of Figure 2.3.

Current GCMs are climate, not weather, models, so they cannot directly

simulate the sol-to-sol variability (Murphy et al., 1995; Forget et al., 1999; Bougher et al., 2000; Wilson, 2000a). However, they could be used to place additional constraints on the possible mechanisms causing the sol-to-sol variability. For example, regions that launch strong gravity waves and also permit them to propagate to the upper atmosphere may be correlated with those that have high sol-to-sol variabilities. However, the current focus of my work is on understanding the zonal structure, so I do not address these issues further in this chapter.

The sol-to-sol variability at the highest northern latitudes is consistently below average. There is a wide variation in sol-to-sol variability over changes in longitude of less than 60° . Neither of these observations can be explained by solar flux variations alone. High sol-to-sol variability might be explained by gravity waves preferentially propagating upwards from certain places when atmospheric conditions are favorable. This is just one possible mechanism, but I do not investigate this any further in this chapter.

Preflight estimates of the orbit-to-orbit variability, which includes effects from both sol-to-sol and zonal variabilities, of 35% were realistic (Stewart, 1987; Tolson et al., 1999). The sol-to-sol variability of 15 – 20% accounts for part of this, with variations in density with longitude accounting for the rest. For comparison, the Earth's day-to-day variability at 200 km altitude can be on the order of 50% during magnetic storms, Venus's nighttime density at 150 km can vary by factors of two over 24 hours, yet its daytime density varies by less than 10% over the same period (Forbes et al., 1996; Keating et al., 1979; Lyons, 1999).

An estimate of likely orbit-to-orbit variability is a critical part of JPL's ongoing preparation for the aerobraking of Mars Reconnaissance Orbiter in 2005. What predictions can I make for the sol-to-sol variability that might be experienced by this and other future missions? If the MGS Phase 2 Aerobraking period is representative, then I predict sol-to-sol variabilities of 15 – 20% at 130 km, decreasing with increasing altitude. Periods of significantly above-average and below-average sol-to-sol variability should be expected. I am unable to make any predictions for

how the sol-to-sol variability may vary with LST, longitude, and latitude, I have no evidence to suggest that the sol-to-sol variabilities remain the same from one season to the next. The martian climate has enough inter-annual variability that the characteristics of the sol-to-sol variability could even change significantly from year to year.

New measurements will, of course, be useful in understanding this phenomenon, but they will be most useful if they are designed to allow a thorough sampling of one possible influencing factor whilst keeping the others fixed. Without this level of experimental control, it will be difficult to disentangle the various effects of latitude, longitude, LST, solar flux variations, and so on.

To answer the question posed at the beginning of this Section, it is reasonable to compare density measurements made at different longitudes several days apart as long as differences in density smaller than or similar to the sol-to-sol variability of 15 – 20% are not automatically attributed to zonal variations.

In summary, the sol-to-sol variability appears to require a mechanism beyond just solar flux variations, such as gravity waves, is an important constraint on aerobraking planning and operations, and is very different on Mars from that on Venus or Earth.

2.5 Observations of the Zonal Structure

2.5.1 Introduction to the Zonal Structure

I now move on from studying density measurements at fixed longitude, altitude, latitude, and LST to studying density measurements at varying longitudes and fixed altitude, latitude, and LST. Keating et al. (1998) discovered that large, regular variations in density with longitude exist in the martian upper atmosphere. Similar variations on Earth are significantly smaller (Forbes et al., 1999). Now that I have

constrained how much sol-to-sol variability exists, I can examine this zonal structure in density. In this section I discuss my technique for fitting a model to the observed zonal structures.

When MGS's orbital period is not in resonance with the rotational period of Mars, reasonably complete longitudinal coverage is obtained from a small set of consecutive orbits due to the changes in periapsis longitude between each orbit. As periapsis latitude precesses between each orbit, there is a finite range of periapsis latitude in this subset of the data. The same reasoning applies to building up a picture of the zonal structure at a fixed altitude, say 130 km on the outbound legs of aerobraking passes — reasonably complete longitudinal coverage can be obtained over a narrow range in measurement latitude. Figure 2.5 shows outbound densities at 130 km altitude between 10°S and 20°S from the Daytime Precession part of Phase 2 of aerobraking. This illustrates the zonal structure. LST (14.7 – 14.8 hrs) and L_S (77–80°) are effectively constant for these measurements. Periapsis precessed southward between 10°S and 20°S with large changes in periapsis longitude between each periapsis. The longitudinal sampling is not built up in a regular pattern (*e. g.* from east to west) and measurements that appear to sample the same longitude repeatedly are not from consecutive orbits. During this period, MGS travelled from south to north on each aerobraking pass with its periapsis between 24°S and 33°S at altitudes of between 108 and 112 km. These data were taken during the 7:1 resonance, a period of significant sol-to-sol variability as can be seen in Figure 2.3. Despite the variability in measurements at a given longitude, *e. g.* 90°E, it is immediately apparent that regular variations in density with longitude exist in the upper atmosphere of Mars. Density varies by a factor of two over 90° of longitude, greater than the sol-to-sol variability.

Measurement uncertainties are not shown in Figure 2.5. As discussed in Section 2.4, they do not become comparable to the sol-to-sol variabilities until altitudes greater than 150 km. I use a least-squares fit to a wave-4 model to characterize the zonal structure. This model contains a constant density term, an amplitude

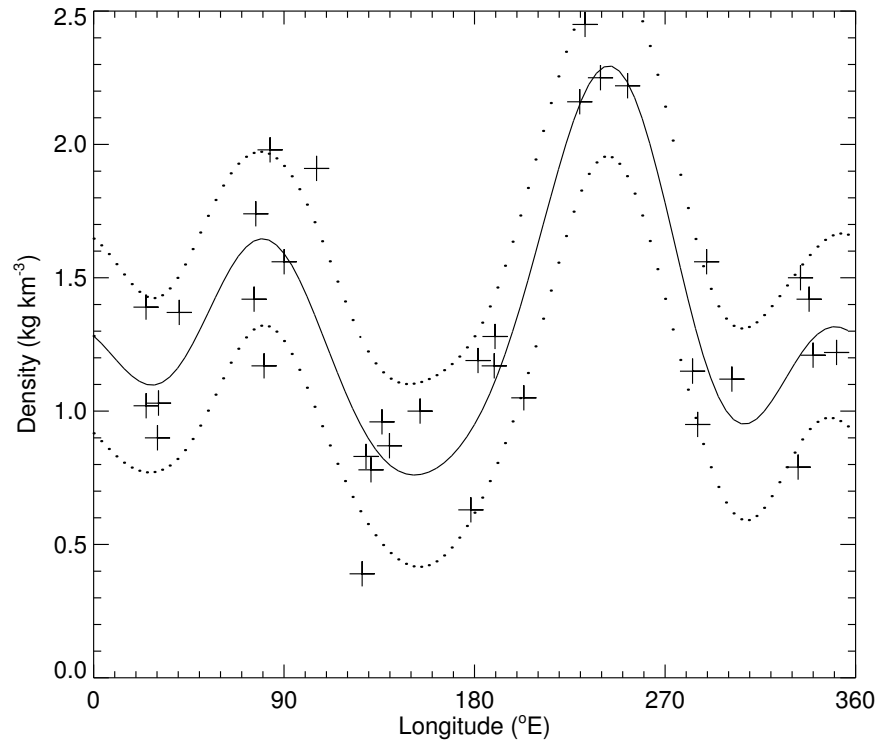


Figure 2.5: All outbound density measurements at 130 km altitude between 10°S and 20°S from the Daytime Precession part of Phase 2, crosses, wave-4 harmonic model fit to the data, solid line, and 1σ uncertainties about the fit, dotted lines. The data were collected over about a week, all at an LST of 15 hrs. Measurement uncertainties (not shown) are much smaller than the range in multiple measurements at any longitude. Zonal structure with large peaks in density at 90°E and 250°E can be seen.

and phase for a sinusoid with one cycle per 360° of longitude, which I label as the wave-1 harmonic, and higher harmonics up to and including wave-4. It has 9 free parameters. Measurement uncertainties are not used to constrain the fit. A wave-4 model was chosen because wave-3 models had significantly worse fits to the data in the Daytime Precession part of Phase 2 of aerobraking and wave-5 models did not have significantly better fits. The details of the model and the fitting procedure are discussed in Appendix A. The error envelope plotted on Figure 2.5 shows a 1σ uncertainty on what a single new observation at a given longitude might be. I define the phase of a given harmonic as the longitude of its first peak east of 0° . The phase of the wave- n harmonic must lie between 0° and $360^\circ E/n$. I generally normalized the zonally-varying terms in each wavefit by their constant density term. This facilitates a comparison of the strength of the zonal structure between different seasons or altitudes.

Throughout this chapter, I only attempted model fits to more than 15 data points and only accepted the fit as good if there was a 90% probability that not all model parameters beyond the constant density term should be zero (Neter and Wasserman, 1974). Bad fits generally occurred in regions where there were significantly fewer data points than usual, which might be due either to data dropouts or to a high rate of periapsis precession through a given latitude range. If fewer than 16 data points were available, then I did not attempt a fit.

In summary, large zonal structures in density are present in the martian upper atmosphere, even during periods of high sol-to-sol variability, and I characterize them with a wave-4 harmonic fit.

2.5.2 Changes in Zonal Structure on Weekly Timescales

As periapsis latitude precessed between orbits, the entire parabolic flight path through the atmosphere shifted with it. This changed the latitude at which MGS passed through, say, 130 km on its outbound leg.

If, as during the Daytime Precession part of Phase 2 of aerobraking, periapsis precesses southward as MGS travels from south to north during each aerobraking pass, then first the 130 km measurement on the inbound leg, and later the same measurement on the outbound leg, occur at a given latitude.

This gives me two separate opportunities, inbound and outbound, a few weeks apart, to study the atmospheric density at a given latitude, altitude, season, and LST. Season and LST are changing much more slowly than periapsis latitude is precessing. Since periapsis longitude (which is the same as the longitude of the rest of the aerobraking pass away from the polar regions) is continuing to change from one orbit to the next, a picture of the zonal structure at a given latitude range and altitude can be built up on these two separate occasions. In this section I examine how the amplitudes and phases of the harmonics making up the zonal structure change between these two samplings and discuss whether data from the two samplings should be combined or kept separate.

Figure 2.5 shows *outbound* densities at 130 km altitude between 10°S and 20°S from the Daytime Precession part of Phase 2 of aerobraking. Figure 2.6 shows *inbound* densities at 130 km altitude between 10°S and 20°S from the Daytime Precession part of Phase 2 of aerobraking. The inbound measurements, taken during the 6:1 resonance, were made about two weeks prior to the outbound measurements. The data in each figure were collected over a period of one week. Changes in the zonal structure in this example are minor. Table 2.2 shows how the amplitudes and phases of the various harmonics change. Only the wave 1 amplitude and wave 2 phase have changed in a statistically significant sense. Recall that the maximum value of the wave- n phase is $360^\circ E/n$.

Figure 2.7 shows the interval between repeated density measurements at 130 km altitude as a function of latitude for the Daytime Precession part of Phase 2. Figure 2.1 shows that changes in LST and L_S are small on these timescales. This allows me to characterize the zonal structure at a given altitude, latitude, LST, and L_S twice — with an interval on the order of several weeks between the

Parameters	Inbound	Outbound
Constant Amplitude (kg km^{-3})	1.324 ± 0.042	1.337 ± 0.051
Normalized Wave 1 Amplitude	0.054 ± 0.045	0.165 ± 0.055
Normalized Wave 2 Amplitude	0.249 ± 0.058	0.345 ± 0.055
Normalized Wave 3 Amplitude	0.204 ± 0.059	0.177 ± 0.071
Normalized Wave 4 Amplitude	0.105 ± 0.058	0.109 ± 0.065
Wave 1 Phase (degrees)	298.7 ± 47.7	260.5 ± 18.3
Wave 2 Phase (degrees)	80.4 ± 6.4	64.1 ± 4.5
Wave 3 Phase (degrees)	103.0 ± 5.1	109.6 ± 7.2
Wave 4 Phase (degrees)	81.5 ± 7.7	74.0 ± 9.7

Table 2.2: Model fit parameters for measurements made between 10–20°S during the Daytime Precession part of Phase 2. Uncertainties are 1σ .

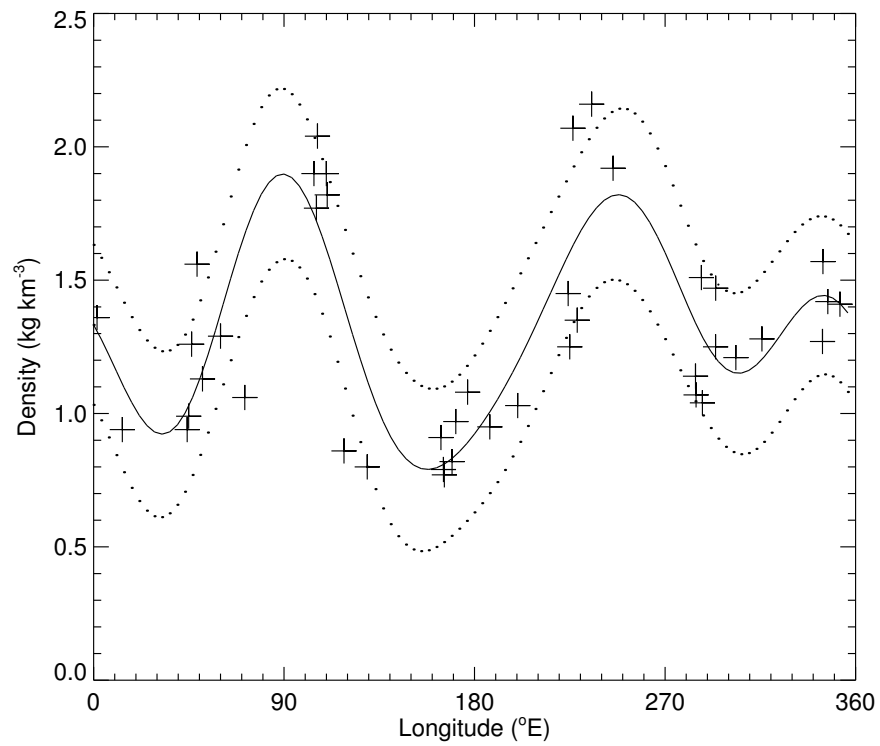


Figure 2.6: As Figure 2.5, but showing inbound data collected in the same latitude range a couple of weeks earlier. The data were also collected over about a week, all at an LST of 15 hrs. The amplitudes of the two large peaks have changed somewhat, but their phases have not. The zonal structure is stable on timescales of a couple of weeks.

two characterizations.

This leaves me with two options: I may either combine inbound and outbound measurements to characterize a given altitude, latitude, LST, and L_S once only or treat these two halves separately. Combining measurements gives more data points but introduces the issue of having half the data collected over a week, a week of no data, then a week of collecting the last half of the data. Wilson (2002) notes that the meridional variation of zonal mean density is the same for inbound and outbound, further notes that there is little difference between the zonal structure observed in inbound and outbound data, and then uses inbound and outbound data together. Until I have carefully investigated the statistical similarity of the inbound and outbound wavefits at a given altitude, latitude, LST, and L_S I keep inbound and outbound measurements separate. Each data collection period is thus continuous.

In summary, the zonal structure during the Daytime Precession part of Phase 2 of aerobraking is stable on timescales of a couple of weeks. This is in contrast to the sol-to-sol variability, which has a shorter timescale.

2.5.3 Changes in Zonal Structure With Altitude

In this section I characterize how the amplitudes and phases of each harmonic in the zonal structure change as a function of altitude and see if this behaviour is affected by latitude.

Density measurements are made at every altitude on each leg of an aerobraking pass. Densities at one altitude can be compared with those at another altitude from the same leg. However, since the two densities are also measured at different latitudes, the comparison does not isolate changes due to altitude alone. Due to the precession of periapsis and with it the entire parabolic flight path through the atmosphere, a density measurement at one altitude and latitude on the outbound leg of an aerobraking pass can be compared to another density measurement

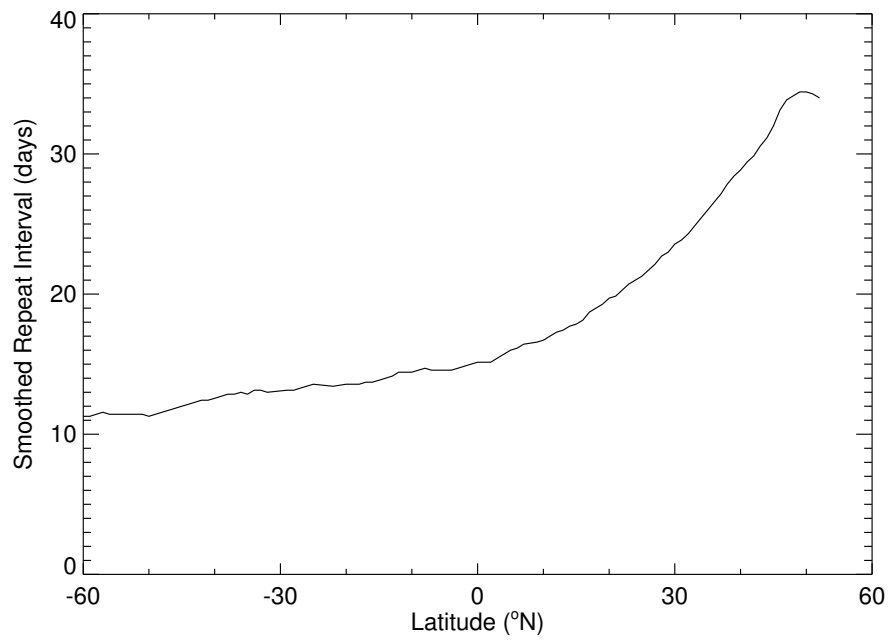


Figure 2.7: Interval between inbound measurements at 130 km altitude at a given latitude and later outbound measurements at the same latitude and altitude from the Daytime Precession part of Phase 2.

at a different altitude, but the same latitude, from the outbound leg of a subsequent aerobraking pass. The precession of periapsis enables me to separate variations due to altitude and latitude despite having non-vertical aerobraking passes. Figure 2.5 shows outbound densities at 130 km altitude between 10°S and 20°S . Orbits whose data are shown in this Figure also measured outbound densities at 140 km, but between 9°S and 18°S . Examining all 140 km outbound data between 10°S and 20°S requires a slightly different set of orbits, and so on for other altitude levels.

Figure 2.8 shows the zonal structure between 10°N and 20°N on the outbound leg during Phase 2 at 130, 140, 150, and 160 km. These data were taken between the 5:1 and 6:1 resonances. I have shifted from $10\text{--}20^{\circ}\text{S}$ to $10\text{--}20^{\circ}\text{N}$ to show the clearest example. The constant density term decreases monotonically as altitude increases, as expected for the background density structure in any atmosphere, and the zonal structure tends to a zonal mean as altitude increases. All the statistically significant peaks and troughs appear fixed in longitude. The trough at 270°E and peak at 330°E are no longer statistically significant at 160 km altitude.

Figure 2.9 shows the normalized harmonic amplitudes, and their uncertainties, from Figure 2.8 as a function of altitude. The normalized amplitudes for the waves-1, 3, and 4 harmonics all decrease as altitude increases. In this example, the normalized amplitude for the wave-2 harmonic does not change in any statistically significant way as altitude increases from 130 km to 160 km. Figure 2.10 shows the phases, and their uncertainties, from Figure 2.8 as a function of altitude. Recall that the maximum value of the phase of the wave- n harmonic is $360^{\circ}\text{E}/n$. When the normalized amplitude of the wave-1 harmonic is very small and indistinguishable from zero, its phase is not well-constrained. The phase is meaningless when the amplitude is not significant. All other phases appear constant with altitude.

At 160 km, the individual normalized harmonic amplitudes are about 10%, but the largest peak in the fitted density is 25% greater than the constant density term. This peak normalized amplitude is greater than the 8 – 10% sol-to-sol variability and the similar uncertainty in each density measurement at this altitude.

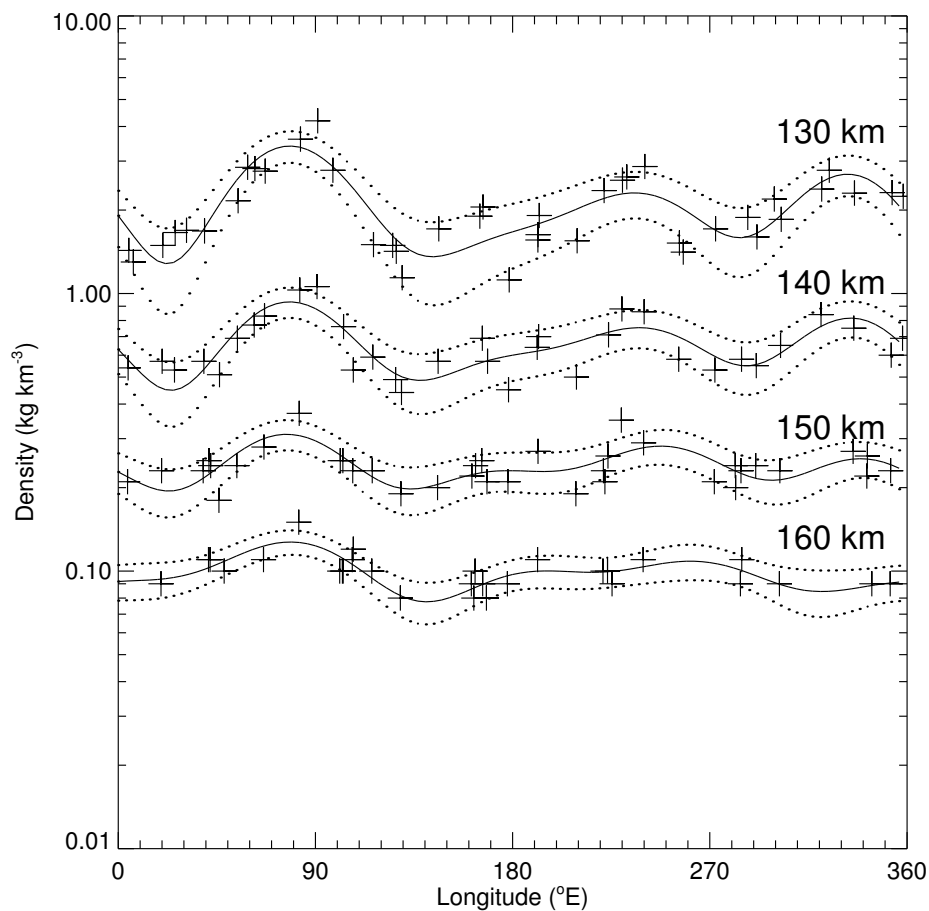


Figure 2.8: Density measurements at 130, 140, 150, and 160 km altitude between 10°N and 20°N for outbound measurements during the Daytime Precession part of Phase 2, plotted as crosses. Model fits to data from each altitude are plotted as solid lines and 1σ uncertainties about each fit as dotted lines. Measurement uncertainties (not shown) are much smaller than the range in multiple measurements at any altitude and longitude. All data were taken at an LST of 15 hrs. Measurements at each altitude level were taken over about a week, but this interval is offset by a couple of days between one altitude level and the next. All density measurements are associated with the obvious altitude level; there are no pathological cases of, say, a 140 km density measurement lurking within the range of the 130 km measurements.

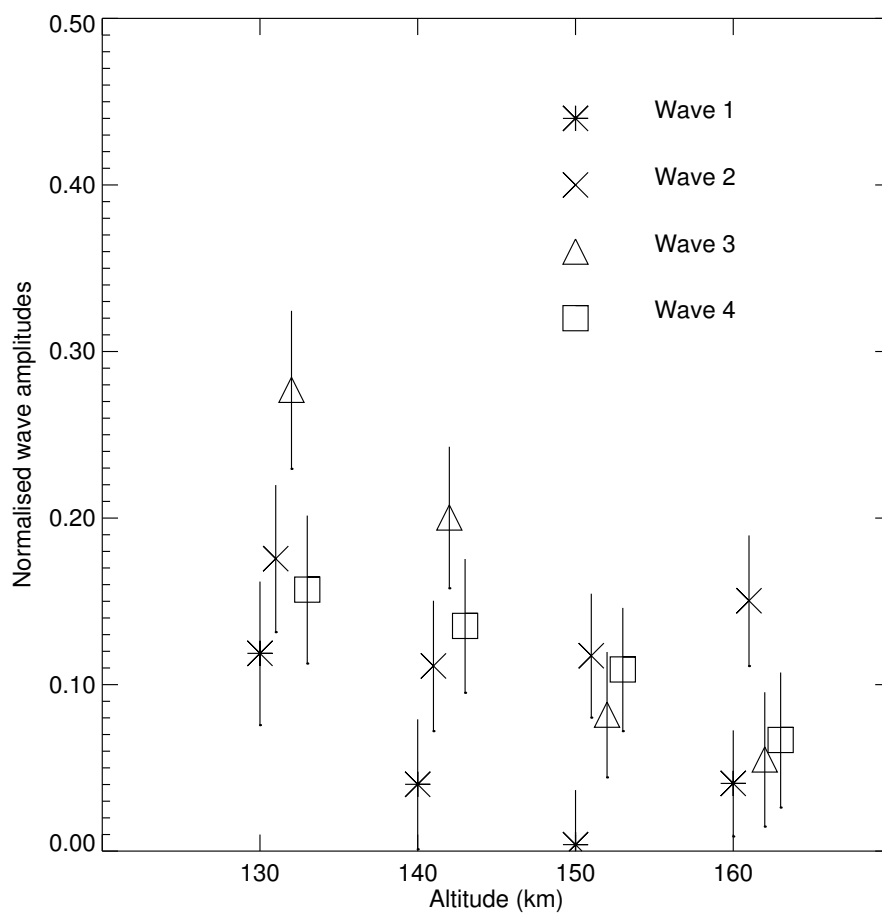


Figure 2.9: Normalized harmonic amplitudes and their uncertainties from Figure 2.8.

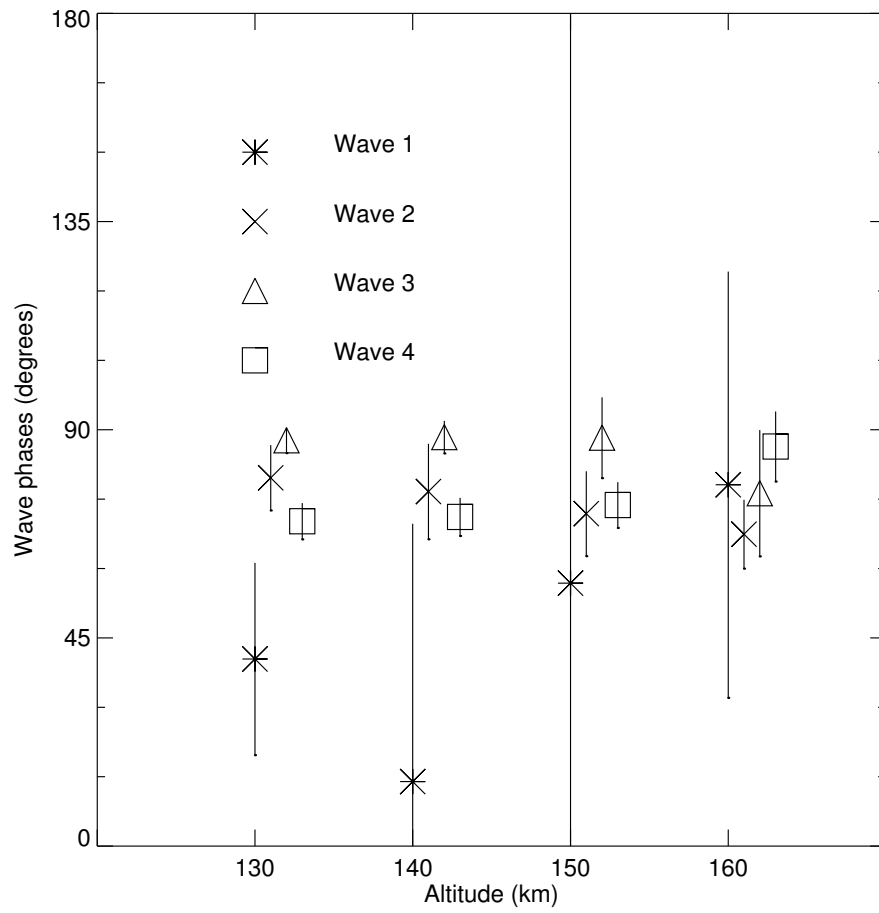


Figure 2.10: Phases and their uncertainties from Figure 2.8.

The similarity of the phases at 160 km to those at lower altitudes supports the contention that I am detecting zonal structure rather than fitting models to noise, but detailed conclusions for this altitude should incorporate the measurement uncertainties and sol-to-sol variabilities in a more formal way. I do not use the 160 km measurements in the remainder of this chapter. At lower altitudes, the zonal structure exceeds the sol-to-sol variability and the measurement uncertainty, both discussed in Section 2.4.1, comfortably.

I have repeated this for other latitude bands between 60°S and 60°N using data from the Daytime Precession part of Phase 2. I generally find that the normalized wave-1 amplitude decreases by about 50% from 130 km to 150 km and those for waves-2, 3, and 4 decrease by about 30%. The rate of change of normalized harmonic amplitude with altitude is influenced by the nature of the atmospheric phenomenon that I observe as zonal structure and are discussed further in Section 2.6.1. Wave-1 normalized amplitudes are small and not very statistically significant at higher altitudes. The phase is meaningless when the amplitude is not significant, which is why its formal value changes erratically with increasing altitude. The wave-2, 3, and 4 phases can change by up to 10–20° with increasing altitude, but are not systematic in an eastward or westward sense within any restricted latitude region and are most consistent with no change in phase with increasing altitude.

Changes in normalized amplitude and phase with increasing altitude are similar at all latitudes. There is no obvious evidence for a shift in behaviour between the northern and southern hemispheres, or between the tropics and extra-tropics. This suggests that the mechanism causing the zonal structure is planetary-scale, rather than localized, and is not restricted to equatorial regions.

Decreases in normalized harmonic amplitude as altitude increases are evidence of dissipation. Classical tidal theory, which assumes a dissipationless medium, predicts that these normalized amplitudes should increase as altitude increases (Chapman and Lindzen, 1970). Possible causes of this dissipation include radiative cooling, wave-wave coupling, shear instabilities, and viscosity (Hooke, 1977;

Forbes, 1995).

Tracadas et al. (2001) modelled the orbit of MGS during the Science Phasing Orbits and found that the zonal structure did not exist in density measurements at 180 km altitude, $L_S = 300^\circ - 30^\circ$, and latitudes north of 60°N at either 07 or 13 hours LST. This is consistent with my observation of decreasing normalized harmonic amplitude with increasing altitude up to 160 km.

Bougher et al. (2001) used data from the MGS Radio Science experiment to find that the altitude of peaks in vertical profiles of electron number density varied systematically with longitude. This zonal structure in electron number density, observed at about 135 km altitude in the primary peak at $64^\circ - 67^\circ\text{N}$, $L_S = 70^\circ$, and LST = 04 hours, closely matches that seen in the neutral atmospheric density at $60^\circ - 65^\circ\text{N}$, $L_S = 30^\circ$, LST = 16 hours (12 hours offset), and 130 km altitude. Bougher et al. (2001) noted that the longitudes of maxima in the electron number density shifted by about 30° over the 20 km altitude difference between the primary peak near 135 km and the secondary peak near 115 km. The amplitude of their zonal structure is greater at 115 km (8 km peak-to-peak) than at 135 km (6 km peak-to-peak), which is consistent with our observation of decaying normalized harmonic amplitude with increasing altitude. The difference between their apparent observation of a phase shift and my absence of one may be due to limited secondary peak data, the different altitudes, or their restriction to one latitude region poleward of 60°N where different tidal modes may be responsible for the zonal structure. This point is addressed further in Section 2.6.2.

Wilson (2002) used a GCM to model atmospheric densities at 130 km altitude and below. His neutral density results reproduced the amplitude and phase and 30° phase shift observed by Bougher et al. (2001) in electron density. His Figure 3 shows that simulated normalized harmonic amplitudes increase with increasing altitude up to the model top at 130 km, inconsistent with the decrease in amplitude in Bougher et al. (2001).

Hinson et al. (2001) analysed temperature profiles as a function of pressure from 0 – 50 km altitude at latitude = 65°N , 04 hours LST, and $L_S = 74^\circ - 77^\circ$. They observed wave-2 zonal structure in the temperature and geopotential height as functions of pressure at their higher altitudes. Banfield et al. (2000) also observed wave-2 zonal structure in the lower atmosphere. Both observations had temperature amplitudes of about 1K, or 1%.

In summary, the zonal structure is present between 130 and 160 km and decays with increasing altitude. The wave-1 harmonic decays the fastest and the remaining harmonics decay less rapidly (but similar to each other). There are no phase shifts with increasing altitude. The similar behaviour of the zonal structure at all latitudes between 60°S and 60°N suggests a planetary-scale cause. Observations at 115 km and 180 km are consistent with a monotonic decay in the zonal structure between those altitudes. Models have some success at reproducing the 115 km observation of the zonal structure.

2.5.4 Changes in Zonal Structure With Latitude

In this section I examine changes in the normalized amplitudes and phases of each harmonic in the zonal structure as a function of latitude, discuss whether the zonal structure is planetary-scale or localized, and quantify which harmonics are dominant.

In Section 2.5.1 I built up a picture of the zonal structure at 130 km using outbound data. In order to sample enough longitudes I had to include data from so many orbits that the measurement latitude precessed from 10°S at the first density measurement to 20°S at the last density measurement. By allowing periapsis latitude (and the latitude corresponding to the measurement altitude) to precess still further, I can see how the zonal structure changes from one latitude range to another.

Figure 2.11 shows the zonal structure as a function of latitude for inbound

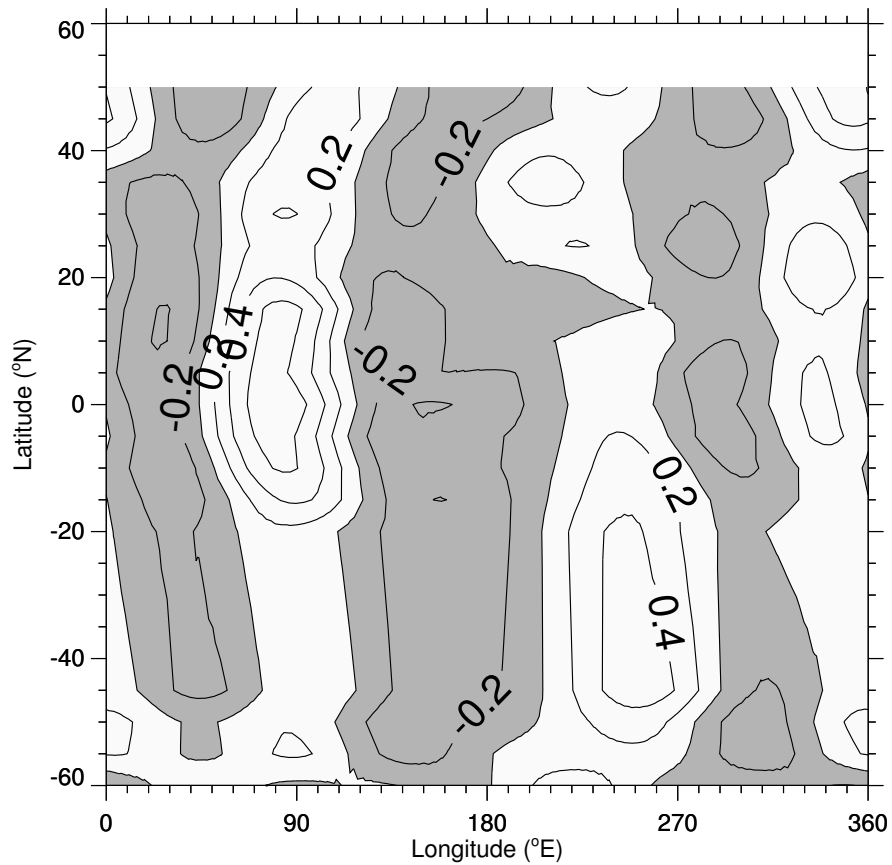


Figure 2.11: Contour plot of $(\text{fitted density} - \text{constant density term}) / (\text{constant density term})$ at 130 km altitude, inbound leg, from the Daytime Precession part of Phase 2. The normalization highlights the zonal structure. The LST of the data is 17 hrs in the north, decreasing to 15 hrs in the south. The L_S of the data is 30° in the north, increasing to 80° in the south. Contour intervals are 0.2 (dimensionless) and negative regions (low densities) are shaded. The peaks and troughs from Figure 2.6 can be seen between 10°S and 20°S .

data at 130 km altitude from the Daytime Precession part of Phase 2. Wavefits similar to Figure 2.6 were constructed at five degree intervals with ten degree windows in latitude. The difference between the wavefit and the constant density term as a function of longitude was then normalized by the constant density term, and these values were then merged into a contour plot. There is overlap between adjacent latitude windows, so adjacent wavefits are not statistically independent. The overlap is included to smooth the contours. Figure 2.11 should be compared to Figure 1 of Wilson (2002) which uses both inbound and outbound data. The two Figures are similar, as they should be according to Section 2.5.2. Only wavefits from latitude ranges which yielded a good fit, as discussed in Section 2.5.1, are included in this plot. Latitude ranges with bad fits, 20–40°S, include orbits 911–961 which have poor or missing data due to spacecraft computer problems. Since zonal fits in this range are poor because of inadequate data, this region in Figure 2.11 is filled by the interpolation of nearby fits. Uncertainties in the fitted density as a function of latitude and longitude are not shown, but the mean 1σ uncertainty is 20% of the constant density term with most values within a few percentage points of this mean. Figure 2.6 shows the uncertainty in the fit in one latitude range.

A contour plot similar to Figure 2.11, but using outbound data, can also be constructed. Measurements at a given altitude and latitude are taken first on the inbound leg and then, a few weeks later, on the outbound leg. A contour plot similar to Figure 2.11, but at a different altitude, can also be constructed. There is also a few days difference in time between measurements at a given latitude and different altitudes. All these similar contour plots have a high density peak at 80°E, most prominent in the northern hemisphere, a high density peak at 250°E, most prominent in the southern hemisphere, and a high density peak at 330°E. The peak at 330°E is always the smallest and the other two peaks are relatively large.

The meridionally broad nature of the zonal structure is immediately apparent. Together with its stability on fortnightly timescales, discussed in Section 2.5.2,

and its consistent behaviour with altitude at different latitudes, discussed in Section 2.5.3, this implies that whatever atmospheric phenomenon is causing the zonal structure operates on a planetary scale. At first glance, given the two large peaks 180 degrees apart, the wave-2 harmonic appears dominant.

Figures 2.12 and 2.13 show the normalized amplitudes and phases of the harmonic fit displayed in Figure 2.11 over a range of latitudes. The situation is more complicated than a mere wave-2 dominance. Wave-3 is dominant in the northern extratropics and no single harmonic is dominant in the southern extratropics or the tropics. Wave-1 is the weakest harmonic over the entire range of latitude. Waves-2, 3, and 4 all have phases, all around 90°E , which stay remarkably constant over a wide range of latitude. This constancy is additional evidence that a planetary-scale mechanism is responsible for the zonal structure. Similar conclusions are reached from the study of outbound data and/or different altitudes.

Figures 2.14 and 2.15 show the wave-2 and wave-3 components of Figure 2.11. They should be compared to Figures 2a and 2b of Wilson (2002). The two pairs of Figures are similar, as they should be according to Section 2.5.2. The constancy of the phases can be seen, as can the way in which these two harmonics interfere to yield the apparent wave-2 dominance in Figure 2.11. Overlaps between peaks in the wave-2 and wave-3 harmonics (*i. e.* constructive interference to give large densities) occur at about 80°E (mainly in the northern hemisphere) and 250°E (mainly in the southern hemisphere). The wave-3 peak at 330°E destructively interferes with the wave-2 trough at the same longitude to give only a small peak in density. The shift in the phase of the wave-3 harmonic with latitude is responsible for the shift of the largest peak in the zonal structure from 80°E in the northern hemisphere to 250°E in the southern hemisphere.

Figure 2.12 shows erratic changes in normalized harmonic amplitude with latitude, in contrast to the well-behaved phases of Figure 2.13. This may represent the individual responses by each tidal mode to whatever surface inhomogeneity is

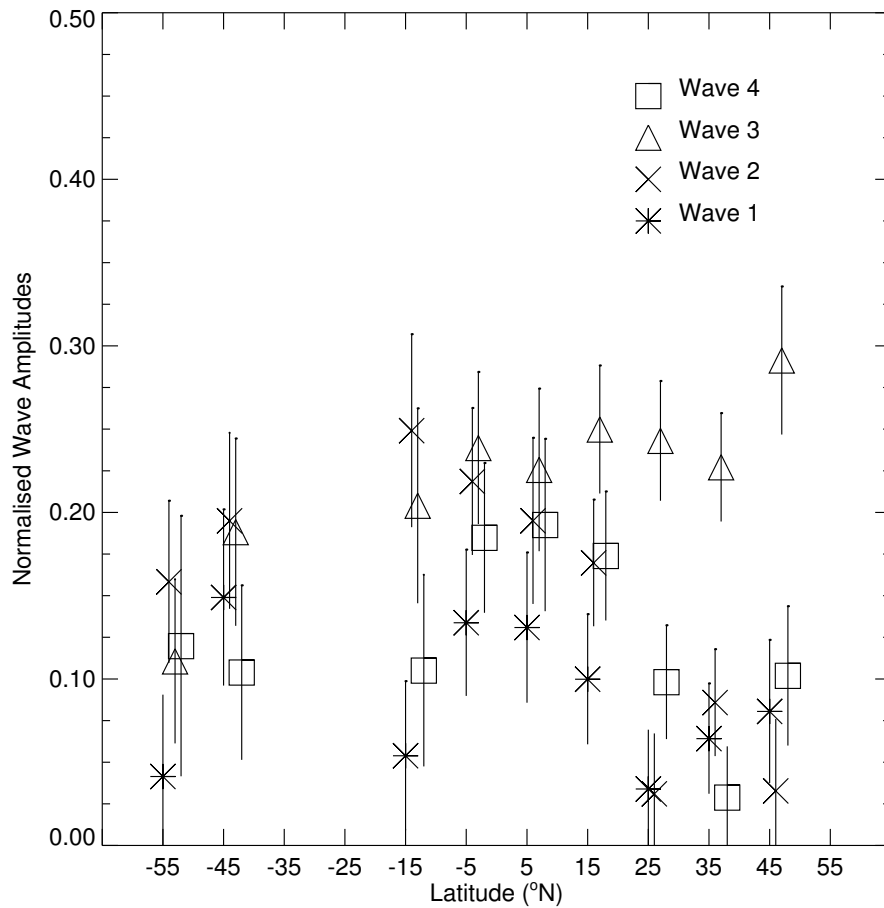


Figure 2.12: Normalized amplitudes from the wave-4 harmonic fits that were merged to create Figure 2.11. The latitude of each set of harmonics is the centre of the 10° wide latitude band from which all the density measurements that contributed to the harmonic fit came. Only every other fit used in Figure 2.11 is shown; including every fit increases the clutter without aiding interpretation. Gaps at 25°S and 35°S are due to bad fits which were not included in Figure 2.11.

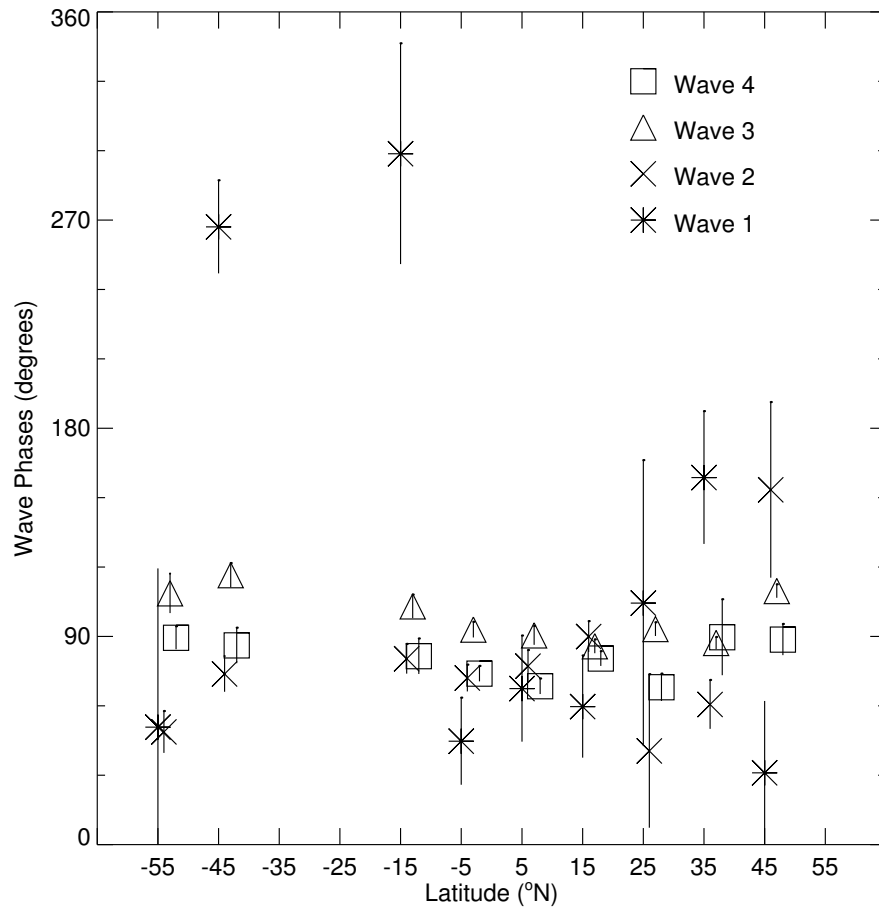


Figure 2.13: Phases corresponding to the amplitudes in Figure 2.12. Recall that the maximum value of the phase of the wave- n harmonic is $360^\circ E/n$.

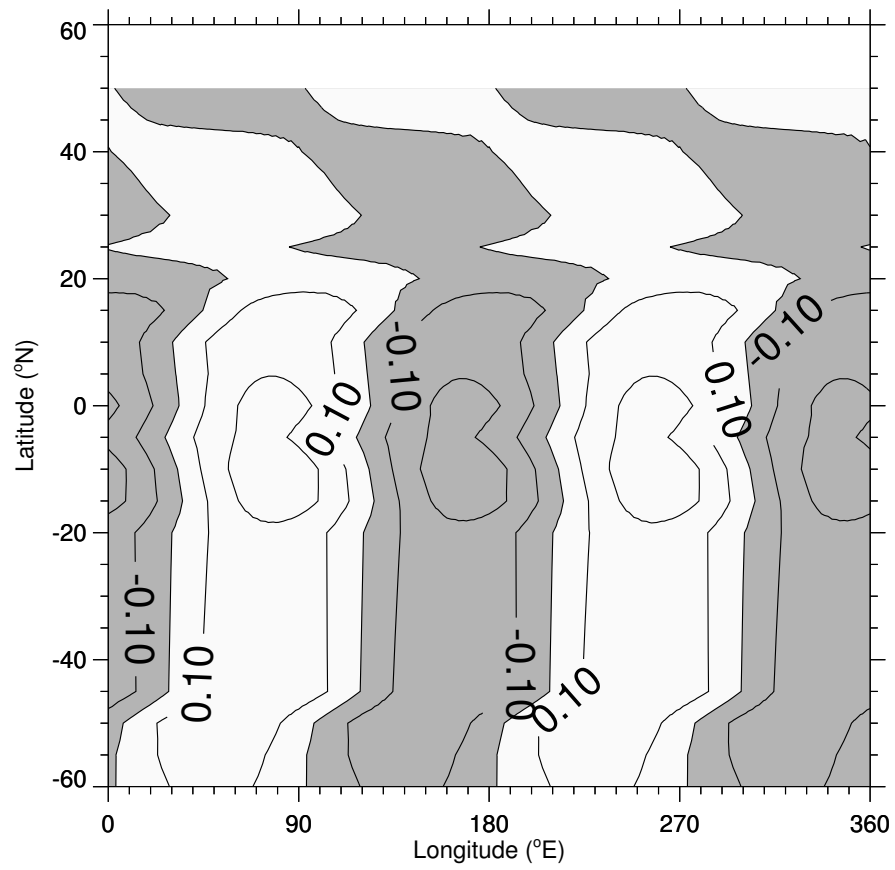


Figure 2.14: As Figure 2.11, but plotting only the wave-2 components. Contour intervals are 0.1 and negative regions (low densities) are shaded.

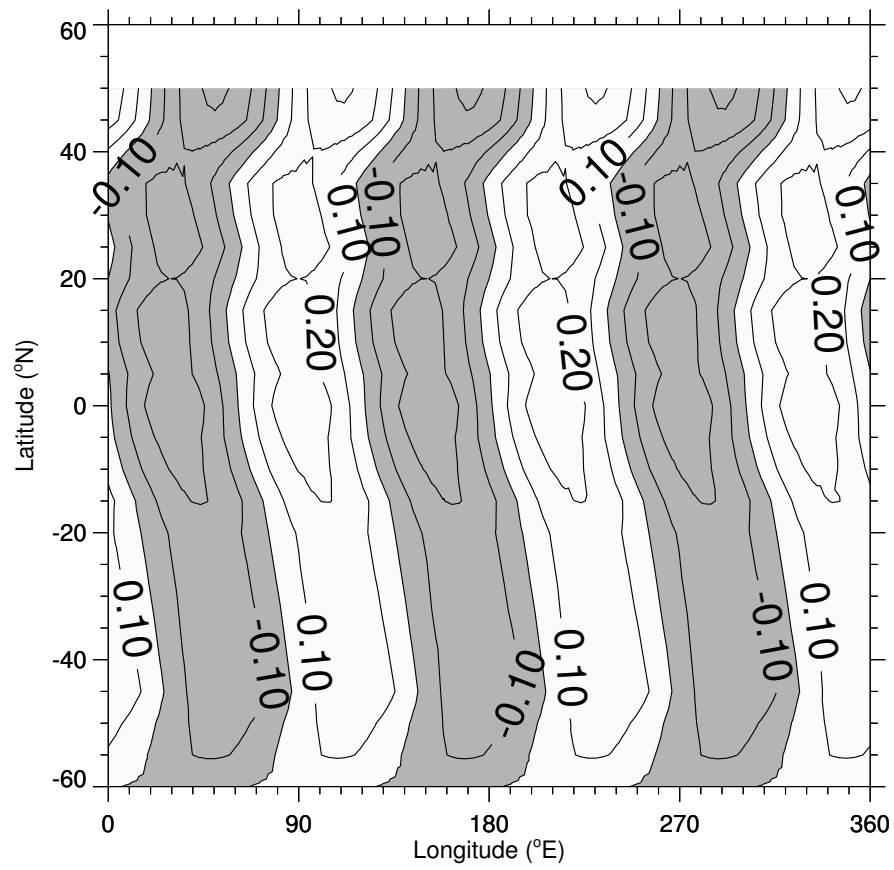


Figure 2.15: As Figure 2.11, but plotting only the wave-3 components. Contour intervals are 0.1 and negative regions (low densities) are shaded.

causing the zonal structure and/or the ease of propagation through the lower atmosphere at this latitude. Insight into this behaviour may come from new surface-to-thermosphere GCMs currently under development (Bougher et al., 2002; Angelats i Coll et al., 2002).

The total energy associated with each harmonic in a given latitude band is proportional to the product of the area of the latitude band and the square of the amplitude. A measure of the global strength of each harmonic is its root-mean-square (rms) normalized amplitude, where the mean-square normalized amplitude has been weighted by the cosine of latitude. Using both inbound and outbound harmonic amplitudes at 130 km altitude, I find that the wave-3 rms normalized amplitude of 22% is greatest. Wave-2 is the next strongest at 18%, followed by wave-4 at 14%, and wave-1 at 12%. The 1σ uncertainties in the rms normalized amplitudes are 1%. Wave-2 is not the most important harmonic in the observed zonal density structures; wave-3 is.

Wilson (2002) used a GCM to model atmospheric densities at 130 km altitude and below. He found wave-2 and wave-3 to be the strongest harmonics at 120 km altitude, with wave-2 stronger than wave-3, and reproduced the lack of phase variation with changes in latitude.

In summary, the zonal structure is meridionally broad, suggesting a planetary-scale cause. This is in contrast to the sol-to-sol variability, which has a smaller meridional length scale. The phases of individual harmonics in the zonal structure are stable, often around 90°E , yet their normalized amplitudes are erratic. Wave-3 is the dominant harmonic, followed by wave-2. Models are broadly able to reproduce the observations.

2.5.5 Changes in Zonal Structure With Local Solar Time

In this section I use data from the Polar Crossing part of Phase 2 of aerobraking to examine the week-to-week repeatability of the zonal structure in polar regions,

then compare the normalized amplitudes and phases of harmonics in dayside and nightside zonal structures in polar regions.

During the Daytime Precession part of Phase 2, periapsis latitude precessed southward with little change in periapsis LST from one orbit to the next, little change in longitude from atmospheric entry to exit during an individual aerobraking pass, and little change in LST from atmospheric entry to exit during an individual aerobraking pass. This is shown in Figure 2.1. Periapsis cannot continue to precess southward indefinitely. As periapsis continued to precess around in the orbital plane, it reached an extreme southern latitude, then precessed northward. Periapsis, which was on the sunward, daytime side of Mars, has shifted to the antisunward, nighttime side of Mars. The extreme southern latitude ($\sim 87^\circ\text{S}$) is set by the inclination of MGS's orbital plane. Since periapsis crossed the terminator during this Polar Crossing, periapsis LST must change from one orbit to the next.

As in the Daytime Precession part of Phase 2, periapsis longitude changes from one orbit to the next during this Polar Crossing. Unlike the Daytime Precession behaviour, the longitude of MGS during an individual aerobraking pass also changes during this Polar Crossing. The longitude of MGS must steadily track through all 360° during one orbit. At polar latitudes, MGS's longitude changes significantly over short arcs of an orbit as MGS crosses the converging lines of longitude. When periapsis occurs close to the pole, MGS's longitude changes significantly over the short arc that is the aerobraking pass. MGS's LST changes significantly during an individual aerobraking pass for exactly the same reason.

As periapsis precesses southwards towards the pole, the 130 km altitude level on the inbound leg occurs to the south of periapsis and periapsis occurs to the south of the 130 km level on the outbound leg. That is, MGS travelled from south to north during an aerobraking pass before reaching its furthest south. The 130 km altitude level on the inbound leg reaches its furthest south, crosses the terminator from day to night, and moves northward before periapsis does. Periapsis, in turn, does so before the 130 km altitude level on the inbound leg. When periapsis was

at its furthest south, MGS travelled from north to south on the inbound leg, then from south to north on the outbound leg.

When periapsis is exactly at its furthest south, the latitudes at which the inbound and outbound legs cross, say, the 130 km altitude level are the same. This is a consequence of the reflection symmetry of an ellipse (such as an orbit) about its semi-major axis. With a near-polar orbit, the LSTs of these two points are about half a sol apart. Density measurements can be made a few minutes apart at exactly the same latitude and altitude, half a sol apart in LST. By considering several orbits close to when periapsis was at its furthest south, a picture of the daytime and nighttime zonal structure at a given altitude and this latitude can be built up.

In practice, to accumulate enough data to build up a picture of the zonal structure at, say, 130 km takes so many orbits to acquire that there is a finite range in the latitude of the measurements (as in Section 2.5.1). I use a 20° wide latitude range, instead of the usual 10° , because there are fewer measurements per degree of latitude at this stage of aerobraking than before.

When periapsis is at its furthest south, the inbound and outbound legs cross the 130 km altitude level at about 70°S . At this time, the 130 km altitude level on the inbound leg is moving north and the same altitude level on the outbound leg is moving south. To build up a picture of the zonal structure at 130 km between 50°S and 70°S , I must use data from the preceding week for the outbound case and data from the following week for the inbound case. Despite this difference of about a week between the two sets of observations at $50\text{--}70^\circ\text{S}$, can I compare them as if they were taken simultaneously? I addressed this problem for non-polar regions in Section 2.5.2 and found that I could do so. Here I should examine the week-to-week repeatability of both the daytime and the nighttime zonal structure. I would like to compare daytime measurements at 130 km between 50°S and 70°S for inbound and outbound legs. I would also like to compare nighttime measurements at 130 km between 50°S and 70°S for inbound and outbound legs. However, aerobraking

ended when the 130 km altitude level on the outbound leg reached its furthest south and repeat nighttime measurements are not available.

There are three relevant subsets of data at 130 km altitude between 50°S and 70°S ; inbound on the dayside with MGS travelling from south to north through the atmosphere, outbound on the dayside with MGS travelling from south to north through the atmosphere, and inbound on the nightside with MGS travelling from north to south through the atmosphere. Due to the cold temperatures and consequently decreased densities, nightside data at higher altitudes are not available in useful quantities. Figure 2.16 shows the intervals between these three sets of measurements at a given latitude. In the $50\text{--}70^\circ\text{S}$ latitude band, the 11 day interval between inbound dayside and outbound dayside measurements is longer than the interval between inbound nightside and outbound dayside measurements. The difference in LST between the nightside measurements at LST = 02 hours and the dayside measurements at LST = 15 hours is very close to half a sol. Figures 2.17, 2.18, and 2.19 show wavefits for the three sets of measurements at 130 km altitude between 50°S and 70°S . Each of the three includes a couple of resonances, the 8:1 and 9:1 for inbound on the dayside, the 10:1 and 11:1 for outbound on the dayside, and the 11:1 and 12:1 for inbound on the nightside. The normalized amplitudes and phases of the various harmonics are shown in Table 2.3. A comparison between the inbound dayside and outbound dayside results is consistent with the results of Section 2.5.2 for more equatorial latitudes — changes in normalized amplitudes and phases are minor.

Assuming that the nightside atmosphere does not change more rapidly than the dayside atmosphere does, I can compare the phases of the inbound nightside and outbound dayside wavefits as if the measurements were effectively simultaneous. There is no way to test this assumption with the MGS accelerometer data. The formal amplitude of each of the four harmonics has increased from day to night, but with little statistical significance. The phase of the wave-1 harmonic changes by approximately 90 degrees, the phase of the wave-2 harmonic changes by

Parameters	Inbound Dayside	Outbound Dayside	Inbound Nightside
Constant Amplitude (kg km^{-3})	0.807 ± 0.023	0.810 ± 0.027	0.383 ± 0.033
Normalized Wave 1 Amplitude	0.069 ± 0.040	0.083 ± 0.047	0.275 ± 0.125
Normalized Wave 2 Amplitude	0.148 ± 0.041	0.168 ± 0.046	0.280 ± 0.115
Normalized Wave 3 Amplitude	0.066 ± 0.040	0.134 ± 0.046	0.202 ± 0.118
Normalized Wave 4 Amplitude	0.051 ± 0.049	0.101 ± 0.048	0.126 ± 0.139
Wave 1 Phase (degrees)	154.8 ± 33.0	207.1 ± 32.2	107.7 ± 24.2
Wave 2 Phase (degrees)	52.4 ± 7.6	37.1 ± 8.2	117.0 ± 12.4
Wave 3 Phase (degrees)	108.3 ± 11.5	117.3 ± 6.7	114.8 ± 10.8
Wave 4 Phase (degrees)	3.4 ± 10.2	85.4 ± 6.4	88.9 ± 11.4

Table 2.3: Model fit parameters for measurements made at 130 km between 50–70°S during Phase 2. Uncertainties are 1σ .

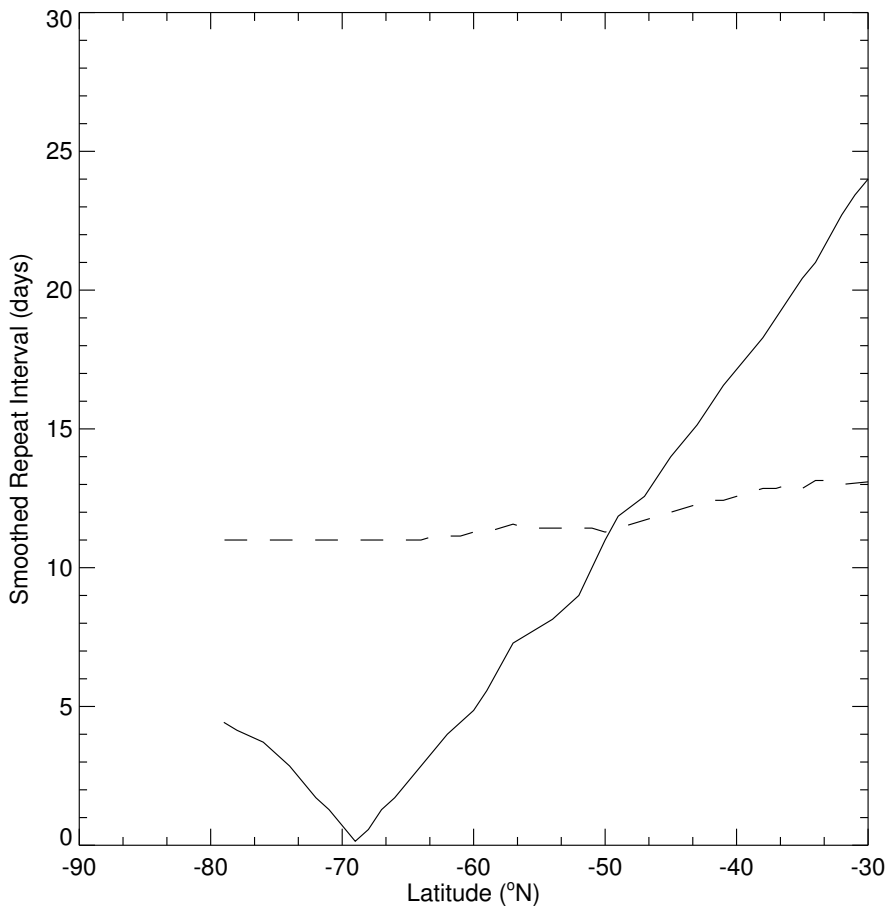


Figure 2.16: Interval between outbound dayside measurements at 130 km altitude and a given latitude and inbound nightside measurements at the same latitude and altitude (solid line) from Phase 2. The minimum near 70°S occurs when periapsis is at its furthest south. At more northern latitudes, outbound dayside measurements precede inbound nightside measurements. At more southern latitudes, inbound nightside measurements precede outbound dayside measurements. Also plotted is the interval between outbound dayside measurements at 130 km altitude and a given latitude and inbound dayside measurements at the same latitude and altitude (dashed line) from Phase 2. Inbound dayside measurements always precede outbound dayside measurements. South of 50°S, the interval between day-night repeat measurements at a given latitude and 130 km altitude is less than that between day-day repeat measurements at that latitude and altitude.

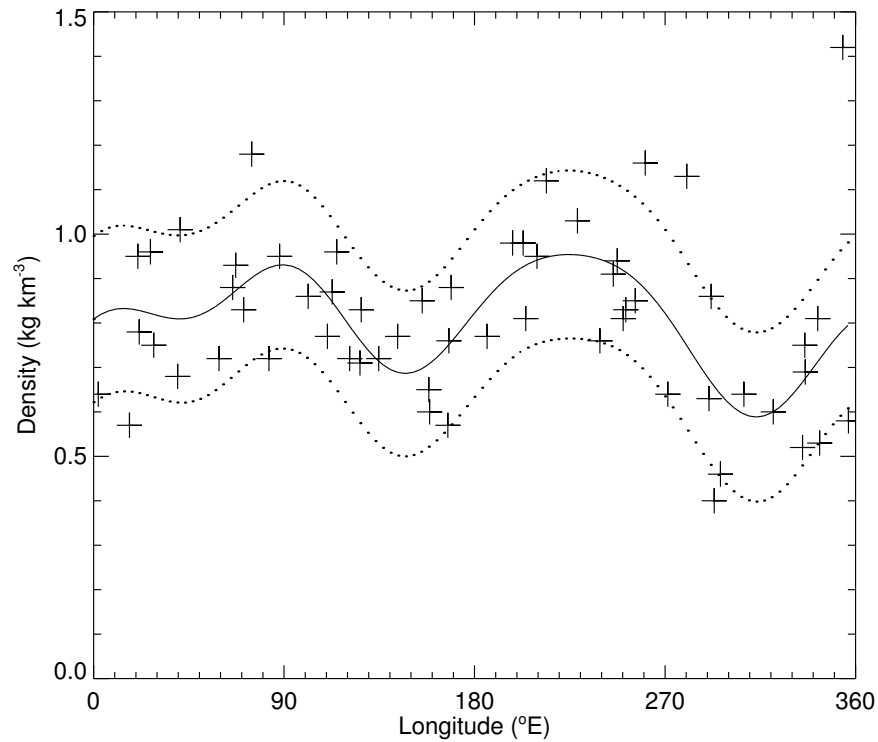


Figure 2.17: All inbound dayside density measurements at 130 km altitude between 50°S and 70°S from Phase 2, crosses, wave-4 harmonic model fit to the data, solid line, and 1σ uncertainties about the fit, dotted lines. The data were collected over about a week, all at an LST of 15 hrs. Measurement uncertainties (not shown) are much smaller than the range in multiple measurements at any longitude. The zonal structure is less pronounced than in Figure 2.5 or others from the tropics, but is still significant above a zonal mean.

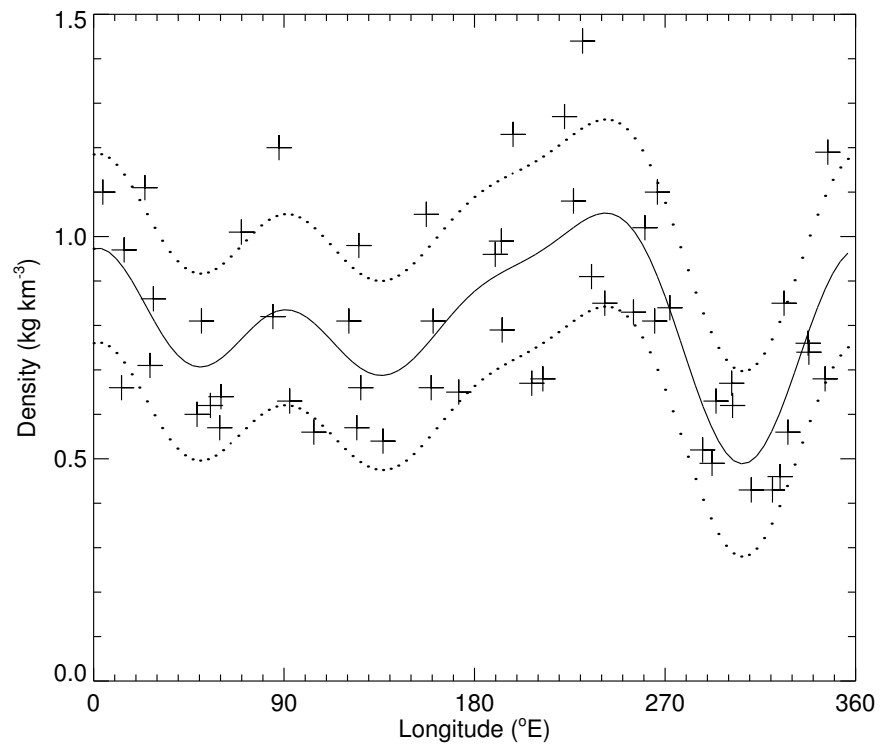


Figure 2.18: As Figure 2.17, but using outbound dayside density measurements. The data used here were collected about 11 days after those in Figure 2.17, but the weak zonal structure is still broadly the same.

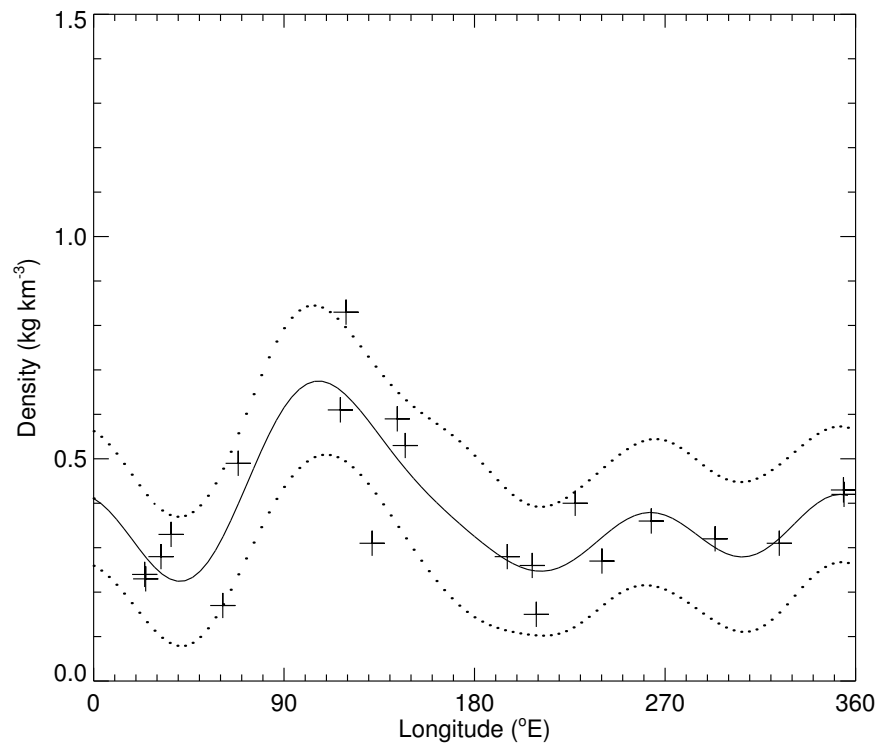


Figure 2.19: As Figure 2.17, but using inbound nightside density measurements. The LST is 02 hrs. Densities have decreased from day to night, and the zonal structure is very different.

approximately 90 degrees, and the phase of the wave-3 harmonic does not change. The wave-4 harmonic is not statistically significant in the nightside wavefit. These phase changes have implications for the nature of the atmospheric phenomenon that I observe as zonal structure and is discussed further in Section 2.6.1.

Bougher et al. (2001) found evidence for a zero phase shift in a wave-3 zonal density harmonic at 64–67°N between 04 and 16 hours LST in their comparisons of electron and neutral density, but did not present a detailed harmonic breakdown.

In summary, the stability of zonal structure is similar in the polar regions and in the tropics and the phases of some harmonics in the zonal structure in the polar regions change with half a sol change in LST.

2.6 Modelling of the Zonal Structure

2.6.1 Constraints on Tidal Modes Responsible for Zonal Structure

The zonal structures observed in the martian upper atmosphere can be studied using tidal theory. “Atmospheric tides are global-scale oscillations in temperature, wind, density, and pressure at periods which are subharmonics of a solar or lunar day” (Forbes, 1995). The dominant forcing in the martian atmosphere is solar heating. My aim in this section of the chapter is to use only the accelerometer data and classical tidal theory to initially identify which σ, s tidal modes are causing the zonal structure in the upper atmosphere. Previous observations and theory that relate to this are discussed in Section 2.6.2 when I re-examine the preliminary conclusions of this section.

Tidal variations in density at fixed altitude, latitude and season with dependence on longitude and LST can be represented as (Chapman and Lindzen, 1970; Forbes and Hagan, 2000; Wilson, 2000a)

$$\rho(\lambda, t_{LST}; z, \theta, L_S) = \quad (2.1)$$

$$\sum_{\sigma,s} \rho_{\sigma,s}(z, \theta, L_S) \cos(\sigma\Omega(t_{LST} - \lambda/2\pi) + s\lambda - \phi_{\sigma,s}(z, \theta, L_S))$$

where ρ is density, λ is east longitude, t_{LST} is local solar time in sols, z is altitude, θ is latitude, L_S is heliocentric longitude or season, σ is the temporal harmonic ($\sigma = 0, 1, 2, \dots$), s is the zonal wavenumber ($s = \dots, -2, -1, 0, 1, 2, \dots$), $\Omega = 2\pi \text{ sol}^{-1}$, and $\phi_{\sigma,s}$ is the phase.

Westward propagating tides have $s > 0$, eastward propagating tides have $s < 0$, and zonally-symmetric tides have $s = 0$. Migrating tides, which have $s = \sigma$, have zonal phase speeds equal to that of the Sun as seen by a fixed observer (Forbes and Hagan, 2000). Non-migrating tides have $s \neq \sigma$. Only migrating tides are excited in a zonally-symmetric atmosphere with zonally-symmetric boundary conditions. If asymmetries are present in the atmospheric boundary conditions, such as albedo, thermal inertia, or topography, then their interactions with the migrating tides generate non-migrating tides (Forbes et al., 1995; Forbes and Hagan, 2000). Zonal inhomogeneities distributed throughout the lower atmosphere, such as dust loading, can also generate non-migrating tides. The non-migrating tides excited by asymmetries of the form $\cos(m\lambda - \phi_m)$, where m is the zonal wavenumber of the asymmetry, are (Forbes and Hagan, 2000)

$$\rho(\lambda, t_{LST}; z, \theta, L_S) = \sum_{\sigma,m} \rho_{\sigma,m}(z, \theta, L_S) \cos(\sigma\Omega t_{LST} \pm m\lambda - (\phi_{\sigma}(z, \theta, L_S) \pm \phi_m)) \quad (2.2)$$

Migrating tides, which are not excited by any asymmetry and have $m = 0$, have no variation with longitude at fixed t_{LST} . The variation with longitude of a non-migrating tide is the same as that of the zonal asymmetry that generated it, but is independent of the temporal harmonic and zonal wavenumber of the migrating tide that generated it.

Solar heating is well described by a combination of diurnal ($\sigma = 1$) and semidiurnal ($\sigma = 2$) harmonics. When the migrating diurnal and semidiurnal tides interact with an $m = 1$ asymmetry, such as topography, they are modulated to

form the $s = 0$ and $s = 2$ diurnal tides and the $s = 1$ and $s = 3$ semidiurnal tides respectively (Forbes and Hagan, 2000). All four of these non-migrating tidal modes appear as zonal variations with wavenumber 1 as seen from the fixed LST reference frame of MGS. Each of the zonal harmonics identified in the accelerometer dataset at fixed LST is influenced by a near-surface asymmetry with the same zonal wavenumber and could be attributable to four possible tidal modes. When I observe a harmonic in the accelerometer dataset, which of the four possible tidal modes is responsible?

I first use classical tidal theory to discuss the behaviour with altitude and latitude of a specific σ, s tidal mode, then reject tidal modes that are not efficiently excited by solar heating, and finally reject those that cannot propagate to the upper atmosphere.

In the classical tidal theory of a highly idealized atmosphere, each σ, s tidal mode can be decomposed into a complete, orthogonal set of functions, called Hough modes (Chapman and Lindzen, 1970). Hough modes are eigenfunctions of the Laplace tidal equation and are labelled with an index n . Conventionally, n may be positive or negative, but not zero, and its absolute value must be greater than or equal to that of s . The meridional structure of each σ, s, n Hough mode is separable from its vertical structure. Note that I refer to a disturbance with a given temporal and zonal structure as a σ, s tidal mode and to one with a given temporal, zonal, meridional, and vertical structure as a specific σ, s, n Hough mode.

Roughly speaking, the meridional structure of a specific σ, s, n Hough mode determines whether it is efficiently excited by solar heating and its vertical structure determines whether it is able to propagate to the upper atmosphere. If none of the σ, s, n Hough modes that make up a given σ, s tidal mode can be efficiently excited by solar heating *and* propagate to the upper atmosphere, then that σ, s tidal mode cannot influence the accelerometer measurements of the zonal structure.

I discuss the meridional structure of Hough modes and their excitation by

solar heating, then discuss the vertical structure of Hough modes and their vertical propagation.

Hough modes are either symmetric or asymmetric about the equator. Those that are symmetric about the equator are either peaked at the equator or poleward of the tropics. For given values of σ and s , the larger the absolute value of n , the more nodes (latitudes at which the value of the Hough mode is zero) the Hough mode has. For a σ, s, n Hough mode to contribute strongly to the zonal structure in the upper atmosphere, it must be efficiently excited by solar heating. Like solar heating, it must be symmetric about the equator, be peaked at the equator rather than poleward of the tropics, and have no nodes too close to the equator. A σ, s, n Hough mode which does not satisfy these excitation criteria is not be efficiently excited by solar heating. Figure 2.20 shows 8 Hough modes with $\sigma = 1, s = -1$. They are all possible causes of the observed wave-2 zonal structure in the upper atmosphere. n ranges from 1 to 4 and from -1 to -4. Only one of the modes, $n = 1$, comes close to satisfying the above excitation criteria. It is the first (*i. e.* lowest absolute value of n) symmetric mode for this σ, s combination. For each of the 16 σ, s tidal modes that could cause wave-1 to wave-4 harmonics in the accelerometer dataset, only the first symmetric σ, s, n Hough mode satisfied the excitation criteria. The first symmetric, diurnal, and eastward propagating Hough mode for a given zonal wavenumber $-s$ is called a diurnal Kelvin wave and labelled as DK s . The $\sigma = 1, s = -1, n = 1$ mode that satisfies the excitation criteria above is DK1.

In the idealized case of classical tidal theory, a Hough mode propagates vertically as either an evanescent or a travelling wave (Chapman and Lindzen, 1970). In reality, damping in the martian atmosphere is quite strong for even the travelling waves (Zurek et al., 1992; Forbes et al., 2001). Figure 2.21 shows the vertical wavelengths of the 16 σ, s, n Hough modes that satisfied the above excitation criteria. An altitude of 130 km, representative of the accelerometer dataset, corresponds to about 15 scale heights above the martian surface. All the evanescent Hough modes in Figure 2.21 should propagate to this altitude with minimal damping, since their

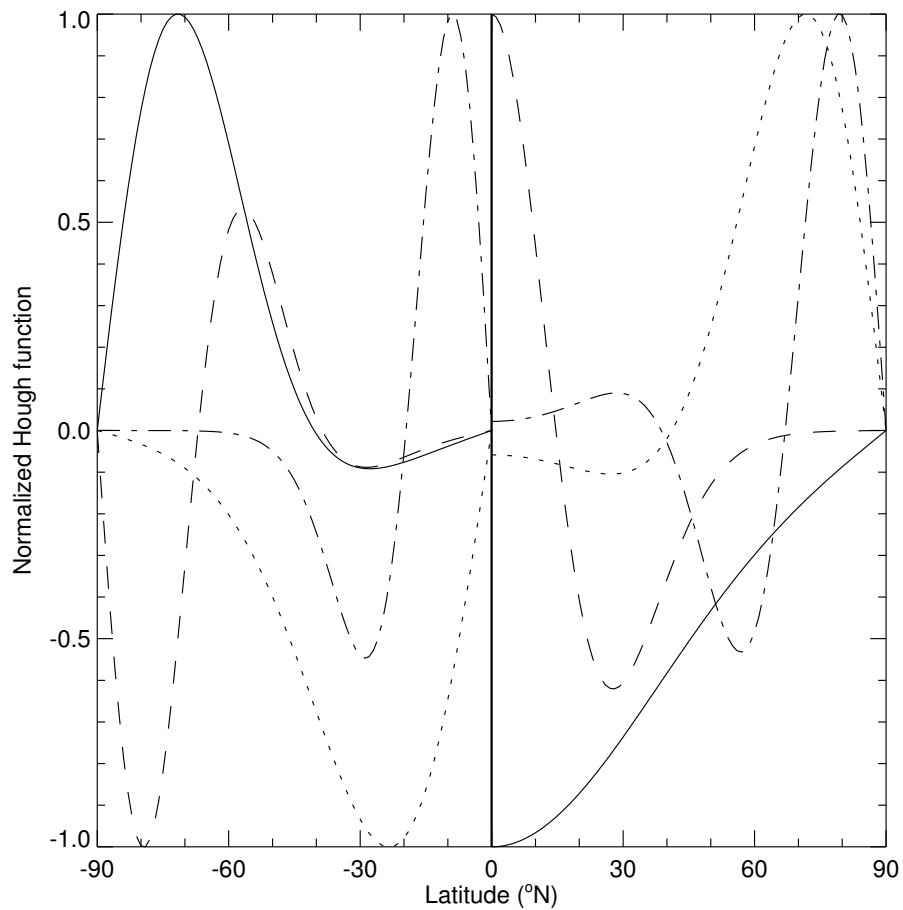


Figure 2.20: Meridional structure of the eight lowest order Hough modes with $\sigma = 1, s = -1$. Asymmetric functions are shown in the southern hemisphere only, symmetric functions are shown in the northern hemisphere only. Asymmetric functions are $n = -1$ (solid line), $n = 2$ (dotted line), $n = -3$ (dashed line), $n = 4$ (dot-dash line). Symmetric functions are $n = 1$ (solid line), $n = -2$ (dotted line), $n = 3$ (dashed line), $n = -4$ (dot-dash line).

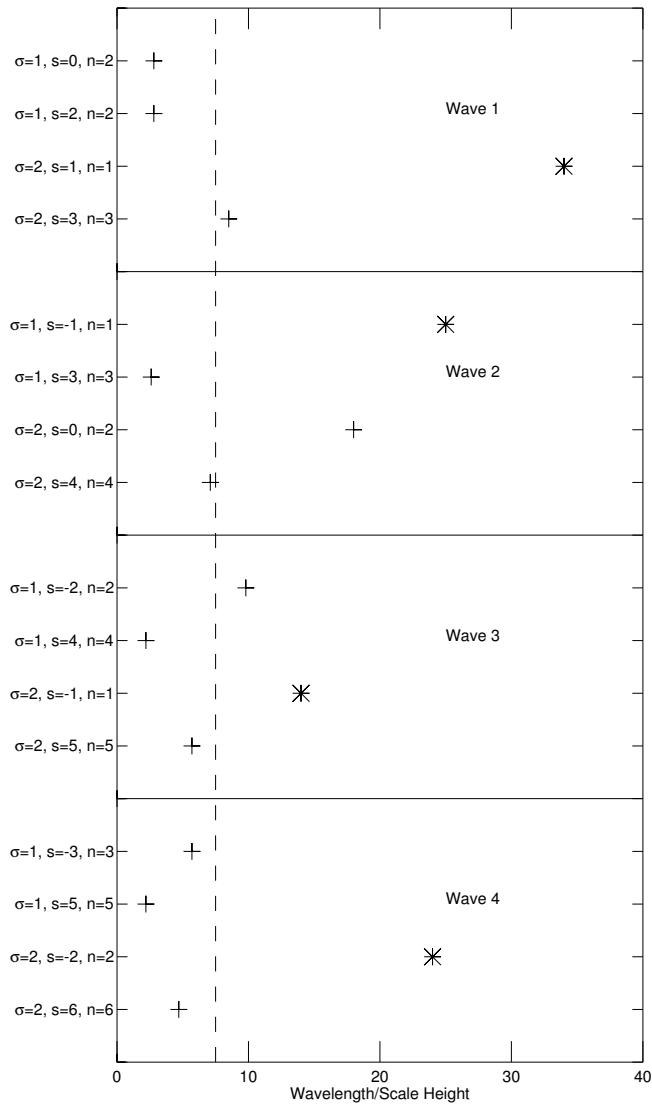


Figure 2.21: Vertical wavelengths of the 16 σ, s, n Hough modes that satisfy the excitation criteria. Travelling waves are marked with a cross and evanescent waves are marked with an asterisk. The dashed line represents the propagation criterion — Hough modes with vertical wavelengths greater than 7.5 scale heights can propagate to the upper atmosphere.

smallest vertical wavelength is 14 scale heights. Some of the travelling Hough modes have undergone 6 or more cycles before reaching this altitude, and they are damped to very low amplitudes in the upper atmosphere. Others have undergone less than a complete cycle before reaching this altitude, and they have not been damped to very low amplitudes. I assert that, of the Hough modes in Figure 2.21, the travelling Hough modes with vertical wavelengths greater than 7.5 scale heights and all the evanescent Hough modes can propagate to the upper atmosphere. Travelling Hough modes with shorter vertical wavelengths are damped to insignificance. This propagation criterion corresponds to travelling waves undergoing no more than two complete cycles before reaching 130 km altitude. This propagation criterion suggests that only the σ, s, n Hough modes listed in Table 2.4 are plausible causes of the zonal structure. In cases where more than one Hough mode could be causing a given zonal density harmonic, both could be operating simultaneously. The relatively rapid decrease in normalized amplitude of the wave-1 harmonic with altitude, discussed in Section 2.5.3, suggests its Hough mode has a shorter vertical wavelength than those causing the other zonal harmonics. This favours the $\sigma = 2, s = 3, n = 3$ Hough mode over the $\sigma = 2, s = 1, n = 1$ Hough mode in Table 2.4.

I do not consider the effects of winds on these Hough modes. Vertical propagation up from the lower atmosphere is affected by the zonal mean winds because these winds Doppler-shift the frequency of the Hough mode. A low frequency, or high period, means a longer time spent propagating through the dissipative regions and more dissipation. Dissipation increases when the tide propagates in the same direction as the zonal mean wind (Forbes et al., 2001). The accelerometer data are measured above eastward zonal winds in the northern hemisphere at the beginning of Phase 2 of aerobraking, then above westward zonal winds around the equator, and finally above eastward winds in the southern hemisphere at the end of Phase 2 of aerobraking (Leovy, 1982; Haberle et al., 1993; Forbes et al., 2001). The broad boundaries of these regions are marked by latitudes where there are eastward zonal wind at one altitude and westward zonal winds at another. This complicated situation is best suited to analysis by detailed modelling work, which is not the aim

Hough Mode	Zonal wavenumber at fixed LST	Wavelength in Scale Heights
$\sigma = 2, s = 1, n = 1$	1	34 (Evanescent)
$\sigma = 2, s = 3, n = 3$	1	8.5
$\sigma = 1, s = -1, n = 1$ (DK1)	2	25 (Evanescent)
$\sigma = 2, s = 0, n = 2$	2	18
$\sigma = 1, s = -2, n = 2$ (DK2)	3	9.8
$\sigma = 2, s = -1, n = 1$	3	14 (Evanescent)
$\sigma = 2, s = -2, n = 2$	4	24 (Evanescent)

Table 2.4: Hough modes satisfying the excitation and propagation criteria.

of this chapter, so I merely state that the different Hough modes are damped to different degrees by the zonal winds, that this damping changes with latitude and season, and that this omission affects my results to some extent.

Observations at widely spaced LSTs can be used to reject some of the possible Hough modes in Table 2.4. Diurnal and semidiurnal Hough modes, if contributing to the zonal structure, cause different changes in the phase of harmonics in the zonal structure over intervals of half a sol.

Recall from Section 2.5.5 that the phase of the wave-1 zonal density harmonic changed by 90 degrees over an interval of half a sol. A diurnal Hough mode would cause the wave-1 phase to shift by 180 degrees over this time and a semidiurnal Hough mode would cause no phase change at all. The phase of the wave-2 zonal density harmonic changed by 90 degrees over an interval of half a sol. A diurnal Hough mode would cause the wave-2 phase to shift by 90 degrees over this time and a semidiurnal Hough mode would cause no phase change at all. The phase of the wave-3 zonal density harmonic did not change over an interval of half a sol. A diurnal Hough mode would cause the wave-3 phase to shift by 60 degrees over this time and a semidiurnal Hough mode would cause no phase change at all. The wave-4 zonal density harmonic is not statistically significant in the nightside wavefit. These observations rule out some of the possible modes listed in Table 2.4.

The results of Section 2.5.5 (Table 2.3) lead me to conclude that the wave-1 zonal density harmonic is not associated with one of the two possible Hough modes in Table 2.4, the wave-2 zonal density harmonic is attributable to the $\sigma = 1, s = -1, n = 1$ Hough mode (DK1), the wave-3 zonal density harmonic to the $\sigma = 2, s = -1, n = 1$ Hough mode, and the wave-4 zonal density harmonic, where present, to the $\sigma = 2, s = -2, n = 2$ Hough mode. The wave-1 zonal density harmonic shows a phase change of about 90° , midway between the 0° change of a semidiurnal harmonic and the 180° change of a diurnal harmonic, so it cannot be explained by this simplified model. These preliminary conclusions are independent of any previous modelling or observational work, have neglected the effects of winds,

and are re-examined at the end of Section 2.6.2.

The studies of Hough modes in Section 2.6.1 were performed using computer programs kindly provided by Jeff Forbes.

2.6.2 Other Tidal Observations and Theory

In this section I discuss previous modelling and observational work on tides in the martian atmosphere that is relevant to Section 2.6.1 and then re-examine that Section's preliminary conclusions in light of the additional information.

Bougher et al. (2001) identified the $\sigma = 2, s = -1$ tidal mode as the most likely cause of the wave-3 harmonic they observed in both neutral density data and electron density data at 64–67°N latitude and $L_S = 70^\circ$.

Joshi et al. (2000) used the results of Hollingsworth and Barnes (1996) to reject the hypothesis of Keating et al. (1998) that stationary waves were responsible for the zonal structure observed during Phase 1 of aerobraking. They also suggested that the observed zonal structure could be due to diurnally varying tidal modes. Simulations at 80 km altitude gave reasonable agreement with the observed phasing of the peaks.

Forbes and Hagan (2000) investigated the $\sigma = 1, s = -1, n = 1$ Hough mode (DK1). For simulated seasons applicable to Phase 1 of aerobraking, they found that DK1 could generate wave-2 zonal structure in upper atmospheric density. These simulations predicted an increase in normalized wave-2 amplitude with increasing altitude up to 200 km at $L_S = 270^\circ$, unlike the decrease observed between 130 km and 150 km at $L_S = 30\text{--}90^\circ$ in Section 2.5.3, and essentially no phase change with increasing altitude. In later simulations applicable to the observations in Section 2.5.3, Forbes et al. (2001) predicted that the amplitude in temperature of DK1 should be constant with altitude between 120 km and 200 km. Since density at a given altitude is sensitive to the vertically integrated temperature below it, this

implies that the normalized wave-2 amplitude in the density should increase from 120 km to 200 km.

Wilson has performed a series of tidal simulations (Wilson and Hamilton, 1996; Wilson, 2000a; Wilson, 2002). Wilson and Hamilton (1996) found that the $\sigma = 1, s = -1, n = 1$ Hough mode (DK1) had twice its usual amplitude during $L_S = 60\text{--}150^\circ$, a period which includes the end of Phase 2 of aerobraking. This may contribute to the noticeable increase in the normalized wave-2 amplitude south of 15°N latitude in Figure 2.12 which is coincident with the arrival of $L_S = 60^\circ$, though simulations also show increasing amplitude to the south at fixed season (Wilson, 2000a). In a comparison of TES temperatures with GCM results using a vertically averaged temperature with a broad weighting centred on 25 km altitude, Wilson (2000a) found that stationary waves, but not tides, are too confined in latitude to cause planet-wide zonal structure, that diurnal tides made larger contributions than semi-diurnal tides, and that each diurnal period, eastward propagating tidal mode had a deep vertical and broad meridional structure consistent with being dominated by the first symmetric Hough mode.

In simulations at 120 km altitude, Wilson (2002) found that the wave-2 zonal structure in the upper atmosphere was predominantly due to the $\sigma = 1, s = -1, n = 1$ Hough mode (DK1), the wave-3 zonal structure was a combination of the $\sigma = 1, s = -2, n = 2$ Hough mode (DK2) and the $\sigma = 2, s = -1$ tidal mode, and that these two wavenumbers dominate. He found the wave-3 zonal structure dominated by the diurnal mode in the tropics and by the semidiurnal mode in the extra-tropics, though he cautioned that those results were sensitive to the (uncertain) details of damping in the model. The wave-3 zonal structure has been observed to be dominated by semidiurnal tidal modes in high latitude observations by Bougher et al. (2001) and my Section 2.5.5. The simulated semidiurnal mode has little phase shift with changing altitude, the diurnal mode has more. Wilson did not address the wave-1 and wave-4 components of zonal structure. The $\sigma = 1, s = -1, n = 1$ Hough mode (DK1) provides a consistent description of the Viking

surface pressure data, TES temperatures at 25 km, and the wave-2 zonal density structure at 130 km, and has also been observed in IRIS data from Mariner 9 (Conrath, 1976; Wilson, 2002).

Banfield et al. (2000) analysed tidal signatures in TES retrievals of lower atmospheric temperatures up to an altitude of ~ 40 km and south of 30°S latitude at $L_S = 180\text{--}390^\circ$ from Phase 1 of aerobraking and the Science Phasing Orbits. They examined the eight σ, s tidal modes with a σ, s, n Hough mode shown in Figure 2.21 that could cause wave-1 or wave-2 zonal structure and found that the $\sigma = 1, s = -1$ tidal mode was largest, followed by the $\sigma = 1, s = 0$ tidal mode. The first of these two tidal modes is probably dominated by the $\sigma = 1, s = -1, n = 1$ Hough mode (DK1) discussed above. The second of these two tidal mode, which causes zonal wave-1 structure, was identified in simulations of temperatures centred on 25 km as the dominant mode in the zonal wave-1 structure by Wilson (2000a). All of the tidal amplitudes of Banfield et al. (2000) suggested increases northward of 30°S . Smith et al. (2001) presented TES data from the later mapping mission, but did not repeat the detailed analysis of Banfield et al. (2000) of the tidal modes. However, a mix of tidal modes is present in their data. Since I have found wave-3 to be a much greater contributor to the zonal structure in the upper atmosphere than wave-1, it would be interesting to repeat the work of Banfield et al. (2000) including wave-3 modes.

Banfield et al. (2003) have also analysed tidal signatures in TES retrievals from post-aerobraking data. Their Figure 11 is probably dominated by the $\sigma = 1, s = -1$ tidal mode and the $\sigma = 1, s = -1, n = 1$ Hough mode (DK1). It shows a relatively weak amplitude during the season corresponding to Phase 2 aerobraking. Like my Figure 2.14, it shows highest amplitudes at the equator and higher amplitudes in the southern hemisphere than in the northern hemisphere. The longitude of the maximum is $\sim 40^\circ\text{E}$ in their lower atmosphere data and $\sim 80^\circ\text{E}$ in my upper atmosphere data, suggesting phase changes with height. Their Figure 12 is probably dominated by the $\sigma = 1, s = -2$ tidal mode and the $\sigma = 1, s = -2, n = 2$

Hough mode (DK2). This is restricted to the tropics in their observations and cannot be responsible for the strong wave-3 harmonic which I observe in the extra-tropics (my Figure 2.15). In Banfield et al. (2003), the maximum amplitude of the $\sigma = 2, s = -1$ tidal mode is no more than half that of DK2. However, since it is not restricted to the tropics, it could be the strongest contributor to the wave-3 zonal harmonic in the upper atmosphere, which would be consistent with my observations of a semidiurnal tidal mode for this harmonic in the southern polar regions.

Unambiguous identification of a particular Hough mode in the martian atmosphere requires many observations. The zonal wavenumber and period of the disturbance must be measured using observations at varied longitudes and LSTs. The meridional profile of the disturbance must be measured using observations at varied latitudes. The vertical profile of the disturbance must be measured using observations at varied altitudes. Observations of the background state of the atmosphere must be used in conjunction with modelling work beyond the classical tidal theory to predict the behaviour of candidate Hough modes as they are generated at the surface and propagate upwards through the spatially and temporally varying lower atmosphere. I am not able to satisfy all these requirements in this chapter. My identifications of certain Hough modes in this chapter are based primarily upon the observed density variations with longitude at fixed LST at many latitudes, the observed density variations with longitude near the South Pole at two LSTs half a sol apart, and classical tidal theory. These restrictions should be understood before the conclusions of this chapter are accepted by the reader. I discuss ways to test my conclusions in Section 2.9.

In summary, my conclusion that the wave-2 zonal structure is attributable to the $\sigma = 1, s = -1, n = 1$ Hough mode (DK1) is consistent with much observational and theoretical work. My conclusion that the wave-3 zonal structure is attributable to the $\sigma = 2, s = -1, n = 1$ Hough mode is consistent with theoretical work and observations at high latitudes, but theoretical work suggests that the $\sigma = 1, s = -2, n = 2$ Hough mode (DK2), which I rejected based on the observed

phase change at high latitudes, may be important at low to mid-latitudes. Observational and theoretical work in the lower atmosphere predicts that the $\sigma = 1, s = 0$ tidal mode dominates the zonal wave-1 structure, but I rejected it as a major influence in the upper atmosphere due to its short vertical wavelength. There has been little work relevant to the wave-4 zonal structure. I make one modification to my preliminary conclusions from Section 2.6.1. Previously rejected, the $\sigma = 1, s = -2, n = 2$ Hough mode (DK2) may make a significant contribution to the wave-3 zonal structure in the tropics.

2.6.3 Effects of the Surface on Zonal Structure

The zonal structure in the upper atmosphere must be caused by a zonal asymmetry in the lower boundary conditions of the atmosphere interacting with solar heating to excite a non-migrating tide. In this section I investigate which zonal asymmetry might have the strongest influence on the zonal structure.

Dust loading is variable on relatively short timescales, so it is unlikely to be responsible for the long-lasting, stable zonal structure. Information on the spatial distribution of dust is available from archived TES results, but recent publications have focused on the dust distribution during dust storms and not during the relatively calm period of Phase 2 of aerobraking (Smith et al., 2000; Smith et al., 2001).

Continuing from Section 2.6.1, it seems reasonable that the meridional profile of the zonal asymmetry that, in conjunction with solar heating, can excite a given Hough mode must overlap significantly with the meridional profile of solar heating (peaked in the tropics, equatorially symmetric, and without any minima close to the equator) for that Hough mode to be efficiently excited. Using Mars Consortium data kindly supplied to me by Jim Murphy and MOLA topography, I performed harmonic decompositions of topography, thermal inertia, and albedo as a function of longitude at different latitudes (Smith et al., 2001b). As shown

in Figure 2.22, the wave-1 component of topography is low near the equator and highest in the extra-tropics. The wave-2 component of topography has high amplitudes throughout the tropics, is greatest at the equator, and decreases into the extra-tropics. Except for a narrow region of low amplitude at 30°S, it is reasonably symmetric about the equator. The wave-3 component has high amplitude at the equator, is quite constant throughout the tropics, and decreases rapidly poleward of 60°. The wave-4 component of topography is low near the equator and highest in the extra-tropics. All amplitudes are below 0.6 km in smooth terrain poleward of 60°. The wave-2 and wave-3 components of topography satisfy the overlap criteria, but none of the components of albedo or thermal inertia do. As discussed in Section 2.6.1, both these components of topography can generate Hough modes with the ability to propagate into the upper atmosphere and appear as wave-2 and wave-3 zonal structure. This is consistent with the observation in Section 2.5.4 that these harmonics are the strongest. Figure 2.23 shows a contour map of martian topography so that the harmonic breakdown in Figure 2.22 can be related to actual topographic features.

It has already been shown that topography, the range of which exceeds an atmospheric scale height, is the main cause of the $\sigma = 1, s = -1, n = 1$ Hough mode (DK1) (Wilson and Hamilton, 1996; Wilson, 2002). This justification for the dominance of wave-2 and wave-3 harmonics in the zonal structure is intended to offer some physical insight as a complement to the rigorous results of more complete models. It could be tested by repeating the work of Wilson and Hamilton (1996) on the $\sigma = 1, s = -1, n = 1$ Hough mode (DK1) on the other Hough modes that are possible contributors to the zonal structure.

2.7 Mars Odyssey and Mars Reconnaissance Orbiter

Aerobraking for Mars Odyssey began in late October, 2001, and was successfully concluded in mid-January, 2002. Approximately 330 orbits of data are currently

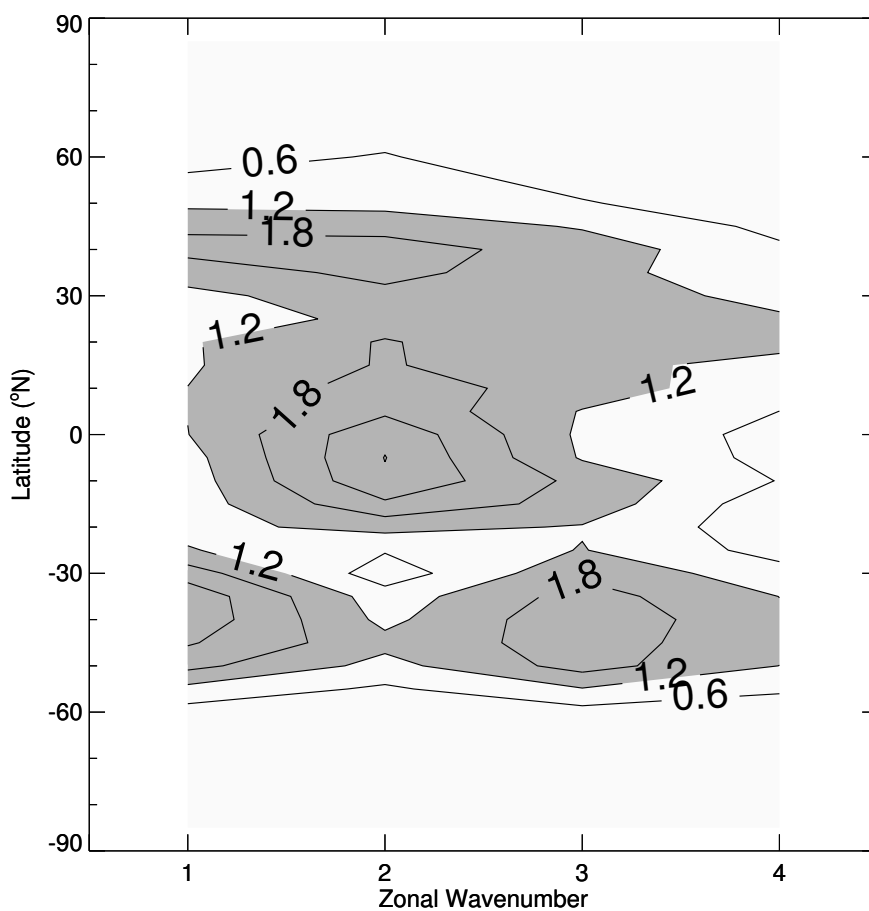


Figure 2.22: Amplitudes, in km, of the various zonal harmonics in martian topography as a function of latitude. Contour intervals are 0.6 km and values greater than 1.2 km are shaded.

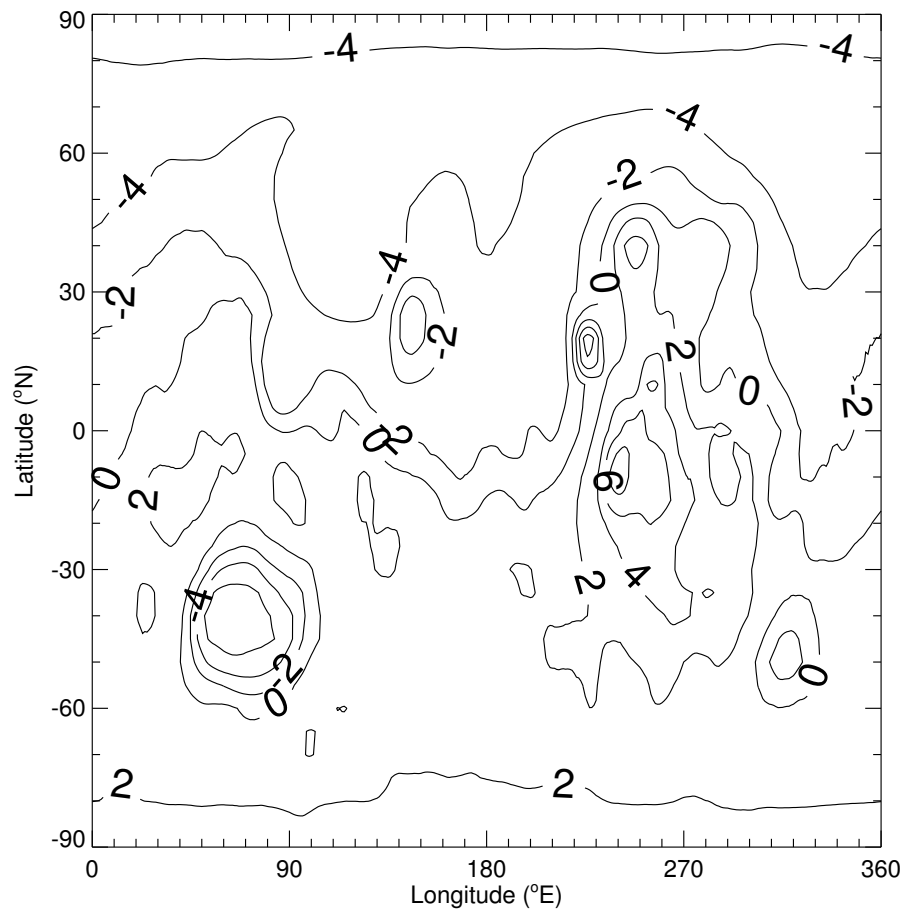


Figure 2.23: Low-resolution contour map of martian topography from MOLA. Contour intervals are 2 km.

being processed and analysed by Keating and colleagues. Results will be published in due course. At the beginning of aerobraking, periapsis occurred at $L_S = 260^\circ$, latitude = 70°N , LST = 18 hours, then precessed northward through midnight LST and across the pole, and continued southward until the end of aerobraking at $L_S = 310^\circ$, latitude = 20°N , LST = 03 hours. Odyssey's aerobraking occurred at a different time in the 11-year solar cycle from that of MGS, and shortly after one of the largest global dust storms ever recorded.

The next anticipated aerobraking dataset is that of the Mars Reconnaissance Orbiter (MRO), scheduled for launch in 2005. The accelerometer instrument on this spacecraft has been upgraded in status from an engineering instrument to a facility science instrument and its high sensitivity promises useful data at altitudes near the exobase during both the aerobraking and the main phases of the mission. The predictions in this chapter for sol-to-sol variability are useful to JPL in their ongoing preparation of MRO's nominal aerobraking plan.

2.8 Future Work

In this section, I discuss opportunities to further develop my work on tides and zonal structure in the martian upper atmosphere. They include searches for temporal effects, study of density scale heights at the same fixed altitudes as this density work, analysis of the individual density profiles and derivation of pressure, temperature, and wind results, examination of Phase 1 data, incorporation of data from other MGS instruments, extension to Mars Odyssey data, and comparisons to useful models.

Upper atmospheric densities are not perfectly described by the fitted zonal structure. Do deviations from the fitted zonal structure have any temporal structure that would suggest the effects of long period waves, such as may be caused by the 28 day solar rotation period, or short term phenomena, such as solar flares? Is high sol-to-sol variability correlated with known periods of high solar activity?

The MGS inbound and outbound data can be carefully compared to identify how stable the zonal structure is on weekly timescales. For example, is the amplitude of the wave-2 harmonic at a given latitude always smaller on inbound than outbound? Is it always smaller relative to the wave-3 harmonic on inbound rather than outbound? These detailed questions have not been addressed in this chapter.

The PDS dataset used throughout this chapter gives density scale heights at fixed altitudes and the altitudes of the 1.26 nbar pressure level for each aerobraking pass, in addition to densities (Keating et al., 2001b). These could be examined for zonal structure or other interesting behaviours.

The individual density profiles from each aerobraking pass contain much more information than the handful of densities extracted at several altitude levels (Keating et al., 2001a). As Chapters 3 and 4 discuss, I am in the early stages of using the assumptions of hydrostatic equilibrium and a uniform zonal wind to derive corresponding pressure and temperature profiles and a zonal wind estimate for each density profile. There have been no previous measurements of winds in the martian upper atmosphere. These new pressure and temperature profiles can be examined for differences between their zonal structure and that of the density data. The accelerometer temperature profiles can be examined for migrating tidal signatures, as have previously been seen in temperature profiles from landers, or gravity waves (Magalhães et al., 1999; Seiff and Kirk, 1977a). The density profiles contain occasional sudden changes in density/acceleration that are still unexplained (Tolson et al., 1999). Densities at any fixed altitude can be extracted from the density profiles and used to study the zonal structure at altitudes as low as about 105 km. Combined with a careful study of the 160 km data, paying due attention to the uncertainties, this increased altitude range may reveal phase shifts in the zonal structure with changing altitude.

The Phase 1 data cover latitudes similar to those at the start of Phase 2 at a different season. They could be studied to examine seasonal changes in the zonal

structure. They also include the upper atmosphere's response to the rise and fall of a regional dust storm, so changes in the upper atmosphere could be compared to changes in winds and vertical temperature structure in the lower atmosphere. The sol-to-sol variability can also be studied at this different season, because Phase 1 contains the 1:1 and 2:1 resonances.

Data from the Mars Horizon Sensor Assembly at several different LSTs will help identify the tidal modes present in the atmosphere (Martin and Murphy, 2001; Murphy et al., 2001). Since Bougher et al. (2001) have used Radio Science observations to show that zonal structure exists in electron densities that appears to mimic that in the neutral densities, other electron density observations from this and possibly other missions can be examined for zonal structure. This permits analysis of changes in the zonal structure with season and LST, for example.

The Mars Odyssey data, when publicly released, will complement the MGS data by covering different latitudes, LSTs, and season. All my analysis techniques, applied here to MGS data, can be readily applied to Odyssey data.

Current surface-bounded GCMs barely reach the lowest aerobraking altitudes (Angelats i Coll et al., 2001; Wilson, 2002). When they are able to span the full altitude range of aerobraking data, or when joint lower atmosphere-upper atmosphere models are coupled closely enough to allow tidal propagation, comparing the accelerometer data with model simulations will be a fruitful avenue for many research paths (Bougher et al., 1999).

In summary, there are many other investigations that can increase our understanding of tides and zonal structure in the martian upper atmosphere in the near future.

2.9 Conclusions

Sol-to-sol variability, or weather, in the martian upper atmosphere is not well modelled by current climate models. As martian climate models develop into weather models with the goal of understanding and interpreting the results of current and anticipated long-term, global-scale, atmospheric monitoring from orbiting instruments with high spatial and temporal resolutions, this variability with short spatial and temporal scales at high altitudes will provide a challenging test of their abilities. This variability is also significant for the design of future aerobraking missions.

For the seasons and latitudes discussed here, the sol-to-sol variability at fixed longitude, altitude, latitude, LST, and season is smaller than the longitudinal variability at fixed altitude, latitude, LST, and season. This repeatable variation with longitude, or zonal structure, can cause densities to change by a factor of two or more over less than 90° of longitude. The zonal structure must be due to thermal tides generated at or near the planet's surface. It is remarkable that surface effects are so significant at altitudes of 150 km.

I have used the changes in the zonal structure with altitude, latitude, and LST, together with a simple application of classical tidal theory, to identify the tidal modes that have the strongest contributions to the zonal structure. The week-to-week stability of the zonal structure and its similar behaviour at all latitudes require a planetary-scale, not localized, phenomenon. The $\sigma = 1, s = -1, n = 1$ (wave-2, DK1) and $\sigma = 2, s = -1, n = 1$ (wave-3) Hough modes have been identified as major contributors to the zonal structure and this is supported by previous theoretical work. The $\sigma = 1, s = -2, n = 2$ (wave-3, DK2) Hough mode is predicted to be present. The wave-4 component of the zonal structure is attributed to the $\sigma = 2, s = -2, n = 2$ Hough mode and the cause of the weak wave-1 component is uncertain. I have presented a simple justification, based on the meridional profiles of solar heating and of various harmonic components of topography, thermal inertia, and albedo, for why the wave-2 and wave-3 components dominate the zonal structure

and suggested that both are controlled by topography.

I believe that my conclusions are robust, although, as discussed in Section 2.6.2, these Hough modes have been identified indirectly. The main ways in which they might be tested are (a) observations of the zonal wavenumbers and periods of any zonal structure in the middle atmosphere which would test my conclusion that certain Hough modes are propagating through the middle atmosphere, (b) upper atmospheric observations at more varied longitudes and LSTs, which, by identifying the zonal wavenumbers and periods of the zonal structure, would test my identification of certain Hough modes in the upper atmosphere, and (c) detailed modelling work, which would test my simplified ideas about vertical propagation of Hough modes. For consistency, these new observations would be most useful if they occurred at the same L_S as the MGS accelerometer observations.

At the surface of the Earth, atmospheric tides are often small-scale fluctuations masked by the effects of weather and only detectable in long duration records. At higher altitudes, they are more prominent. On Mars, whose atmosphere has a greater diurnal variation in solar heating per unit mass than Earth's, tidal effects are greater. They are a major feature in the long-term pressure measurements at the two Viking landing sites and were predicted by the very first martian climate model (Leovy and Mintz, 1969; Zurek et al., 1992). Tides have long been recognized as a basic feature of the dynamics of the martian lower atmosphere; this work, and others, demonstrates that they are important in the upper atmosphere as well. As such, upper atmosphere models which do not have dynamic connections to lower atmosphere models will be unable to reproduce observations or make accurate predictions.

The strength of a tidal mode in the martian upper atmosphere depends on the winds and temperatures in the lower atmosphere. If surface-to-thermosphere models can reliably reproduce the upper atmosphere observations, then only those lower atmosphere conditions which correspond to the observed behaviour in the upper atmosphere are permissible. This offers a way to constrain the behaviour of

the lower atmosphere using only observations from the upper atmosphere.

Accelerometers are the only scientific instruments that will fly again and again into Mars orbit during the next decade. As such, they offer a unique way to study the behaviour of the difficult-to-study upper atmosphere over inter-annual periods and the 11-year solar cycle. Their observations are difficult to compare to most current martian climate models because of their high altitude, and this partially explains why so few recent publications have discussed accelerometer data, but they still have value. Accelerometer datasets will be invaluable in the future when, inevitably, models reach such altitudes, and every opportunity should be taken now to collect and preserve such datasets.

CHAPTER 3

DEVELOPMENT OF A NOVEL “BALANCED ARCH” TECHNIQUE FOR MEASURING WINDS

3.1 Introduction

The general circulation of any atmosphere is defined by the nature of the atmospheric composition, pressure, temperature, and winds as functions of altitude, latitude, longitude, time of day, and season (Zurek et al., 1992). Winds are important because they transport energy, momentum, condensable species, and radiatively important aerosols within an atmosphere (Holton, 1992). Most observations of planetary atmospheres have been made by the remote sensing of electromagnetic radiation. Atmospheric composition, pressure, and temperature all have a direct effect on the transfer of radiation, and can be inferred from such observations (Chamberlain and Hunten, 1987). Winds have only an indirect effect on radiative transfer, so are less easily measured by such techniques. On all the planets, predictions of wind speed and direction as a function of altitude, latitude, longitude, time of day, and season are constrained by far fewer measurements than the complementary predictions for other meteorological fields.

In this Chapter I develop a novel technique for measuring winds and apply it on Mars. On Mars, lower atmospheric winds have previously been constrained by several techniques:

- (1) Cloud tracking on images from ground-based telescopes, Earth-orbiting telescopes, and Mars-orbiting spacecraft have provided direct measurements of

winds, but these do not have systematic latitudinal, longitudinal, and seasonal coverage, do not strongly constrain the relevant altitude, and are restricted to daytime only (Slipher, 1962; Mischna et al., 1998; Kahn, 1983).

(2) Observations of surface streaks and other aeolian geomorphological features have provided direct measurements of average wind direction, but these do not have systematic latitudinal and longitudinal coverage, do not extend above the planetary boundary layer, do not have any temporal resolution, and reveal little about the wind speed (Thomas, 1981; Greeley et al., 2000).

(3) Surface meteorology instruments, including the Viking seismometers, have provided a record of wind speed and direction with very high temporal resolution over periods from a few months to a few Mars years, but they only exist at three locations on the planet and do not extend above a couple of metres high (Nakamura and Anderson, 1979; Zurek et al., 1992; Murphy et al., 2002).

(4) Vertical profiles of horizontal wind speed and direction were obtained during the descent of the two Viking Landers to the martian surface by modelling the effects of winds on the trajectory of the spacecraft. The profiles extend from several tens of kilometres altitude to the surface. However, these measurements only exist at two latitudes, longitudes, times of day, and seasons and are very challenging to extract from the data (Euler et al., 1979).

(5) Much better spatial coverage comes from an indirect technique which applies the gradient wind approximation to vertical profiles of pressure as a function of temperature derived from infra-red spectrometers (IRIS, IRTM, TES, and THEMIS) in Mars orbit (Zurek et al., 1992; Smith et al., 2001). These have poor spatial resolution and are restricted in their latitudinal/longitudinal/time of day coverage by their orbit. For example, TES data only cover two times of day from the sun-synchronous orbit of the Mars Global Surveyor (MGS) spacecraft.

Middle and upper atmospheric winds on Mars are less well constrained:

(1) Observations of stellar occultations, such as the 1976 Epsilon Gem occultation, reveal the oblateness of the martian atmosphere at about the 70 km altitude level (Elliot et al., 1977; French and Elliot, 1979). Similar oblateness measurements from the occultation of 28 Sag by Titan in 1989 were used to constrain wind speeds, but this analysis has not been done for the Epsilon Gem/Mars occultation (Hubbard et al., 1993).

(2) Ground-based spectroscopy with high spectral resolution can measure winds by their Doppler effect on the frequency of emitted radiation (Lellouch et al., 1991). Several groups have tried to make such measurements in the past decade, but only one peer-reviewed paper has been published (Gurwell et al., 1993; Schmülling et al., 1999; Moreno et al., 2001). This bottleneck is due to the difficulty of processing such measurements. Winds measured with this technique are line-of-sight only, are restricted to the Earth-facing hemisphere, and have poor spatial resolution.

Theoretical models which predict winds in the upper atmosphere of Mars are constrained by UV airglow measurements, radio occultations of the ionosphere, and data from the Viking entry accelerometers, retarding potential analyzers, and mass spectrometers as discussed in Bougher and Dickinson (1988) and Barth et al. (1992). The underdeveloped state of our understanding of the physics and chemistry of the martian upper atmosphere was highlighted by the recent Decadal Survey recommendation for a Mars Upper Atmosphere Observer spacecraft (Belton, 2002).

In situ observations relevant to the dynamics of the martian upper atmosphere have recently been made by the Accelerometer Experiment (ACC) on the MGS spacecraft (Keating et al., 1998; Keating et al., 2001a; Keating et al., 2001b). Once in orbit around Mars, MGS's periapsis was lowered into the upper regions of the atmosphere. The subsequent atmospheric drag from this *aerobraking* modified the spacecraft trajectory more cheaply than the use of chemical propellant alone could. The ACC measured the aerodynamic accelerations on the spacecraft during an aerobraking pass. This information was used by the mission operations team in

the hours after the aerobraking pass to plan modifications to the spacecraft’s trajectory by changing the altitude of the next periapsis by small expenditures of chemical propellant at apoapsis, to achieve the desired drag without exceeding heating rate thresholds, and to guide it safely to the desired mapping orbit. The accelerometer readings have been processed to generate two “profiles” of atmospheric density, one for the inbound “leg” and one for the outbound “leg”, from each “aerobraking pass” (Keating et al., 1998; Cancro et al., 1998; Tolson et al., 1999; Tolson et al., 2000; Keating et al., 2001a; Keating et al., 2001b). An “aerobraking pass” refers to a single traverse through the atmosphere from ingress to egress, a “leg” refers to the inbound (pre-periapsis) or outbound (post-periapsis) portion of an aerobraking pass, and a “profile” refers to data from one leg of an aerobraking pass. Unlike planetary entry probes or landers such as Pathfinder, the flight path of MGS through the atmosphere on each aerobraking pass is not near-vertical. The atmospheric flight path extends down from a maximum altitude of approximately 160 km to periapsis and then back out again, typically spanning several tens of degrees of latitude with only small changes in longitude or local solar time (LST). The maximum altitude is set by the need for the signal of the aerodynamic acceleration to exceed the instrument’s noise level. The duration of each aerobraking pass was on the order of a few minutes, short compared to any dynamical timescale for changes in atmospheric properties. In an attempt to keep terminology consistent between one-legged lander entry data and two-legged aerobraking data, I use a “profile” of some type of data to mean a single-valued function of altitude.

Aerobraking took place in two Phases, 1 and 2, separated by a hiatus containing the Science Phasing Orbits (Albee et al., 1998; Albee et al., 2001). Phase 1 included orbits 1 – 201 from mid-September, 1997, to late March, 1998, and Phase 2 included orbits 574 – 1283 from mid-September, 1998, to early February, 1999. At the beginning of Phase 1, $L_s = 180^\circ$, periapsis occurred at 30°N and 18 hrs LST, then moved northwards and earlier in the day to reach 60°N and 11 hrs LST at the end of Phase 1, $L_s = 300$. One hour of LST equals $1/24$ of a martian solar day (sol), not 3600 seconds of elapsed time. At the beginning of Phase 2, during the

next martian year at $L_s = 30^\circ$, periapsis occurred at 60°N and 17 hrs LST, then moved southwards and earlier in the day to cross 80°S at 15 hrs LST. Periapsis then crossed over the south pole, moving through nighttime LSTs, and reached 60°S and 02 hrs LST by the end of Phase 2, $L_s = 90^\circ$. When periapsis was near the south pole, each aerobraking pass's profile of atmospheric density spanned a large range of LST and longitude. This is summarized in Figure 2.1. L_s , heliocentric longitude or season, is 0° at the northern spring equinox, 90° at the northern summer solstice, 180° at the northern autumn equinox, and 270° at the northern winter solstice.

Data from the ACC is archived in the Planetary Data System (PDS) (Keating et al., 2001a). This dataset contains 1600 upper atmospheric density profiles from 800 aerobraking passes. The only previous three atmospheric density profiles are those of the Pathfinder and two Viking landers (Magalhães et al., 1999; Seiff and Kirk, 1977a). Collocated pressure profiles were derived from these three near-vertical density profiles using the assumption that a pressure gradient and gravity are the only forces acting on the atmosphere. This is a slightly more restrictive assumption than the assumption of hydrostatic equilibrium. Hydrostatic equilibrium requires that a pressure gradient be the only force acting in a vertical direction, but permits additional forces, such as those due to atmospheric motions, acting in other directions. An equation of state, appropriate for the independently known atmospheric composition, such as the ideal gas law was used to derive collocated temperature profiles from these density and pressure profiles. The temperature and pressure data are generally more scientifically useful than the density data and I have investigated whether temperature and pressure profiles can be derived from the MGS ACC density profiles. The PDS archive includes the altitude of a constant pressure level, 1.26 nbar, for both the inbound and outbound legs of each aerobraking pass, so it might be thought that some useful information on how pressure profiles can be derived would be present within the archive (Keating et al., 2001a). However, the archive does not include any description of how this pressure was calculated.

Using techniques derived from these established assumptions for each leg of each aerobraking pass, I derived two pressure profiles, inbound and outbound, for each aerobraking pass from the density profiles. Since the two simultaneous pressure profiles both terminate at the same periapsis position, they should be consistent. If the two estimates of periapsis pressure are inconsistent, then the pressure profiles cannot both be correct and I must examine the assumptions and the data for errors. If the two estimates of periapsis pressure are consistent, then the pressure profiles may or may not be correct. I found typical discrepancies of 50% between the two estimates of periapsis pressure on a given aerobraking pass, significantly greater than the uncertainty in the discrepancies. Figure 3.1 shows pressure profiles derived in this way for orbit P679. It has a discrepancy of about 30% between the two estimates of periapsis pressure with an uncertainty in this discrepancy of about 1%.

A matching pair of legs, inbound and outbound, that comprise a single aerobraking pass are required to reveal this problem with the pressure profiles. A single leg, as is obtained for all entry probes, is insufficient. As I shall later show, the problem originates in the non-vertical flight paths of each aerobraking pass. It has less of an effect on profiles from typical entry probes with near-vertical flight paths.

I attribute these discrepancies to the presence of horizontal pressure gradients, which are often associated with winds. These discrepancies are the motivation for the aim of this chapter, which is to study theoretically the effects of winds and horizontal pressure gradients on density profiles from aerobraking or similar measurements.

3.2 Conservation of Momentum in an Atmosphere

$$\frac{\partial \underline{v}}{\partial t} + (\underline{v} \cdot \underline{\nabla}) \underline{v} + 2\underline{\Omega} \times \underline{v} + \nu_{ni} (\underline{v} - \underline{V}_i) + \frac{1}{\rho} \underline{\nabla} \times (\eta \underline{\nabla} \times \underline{v}) = \frac{-1}{\rho} \underline{\nabla} p + \underline{g}_{eff} \quad (3.1)$$

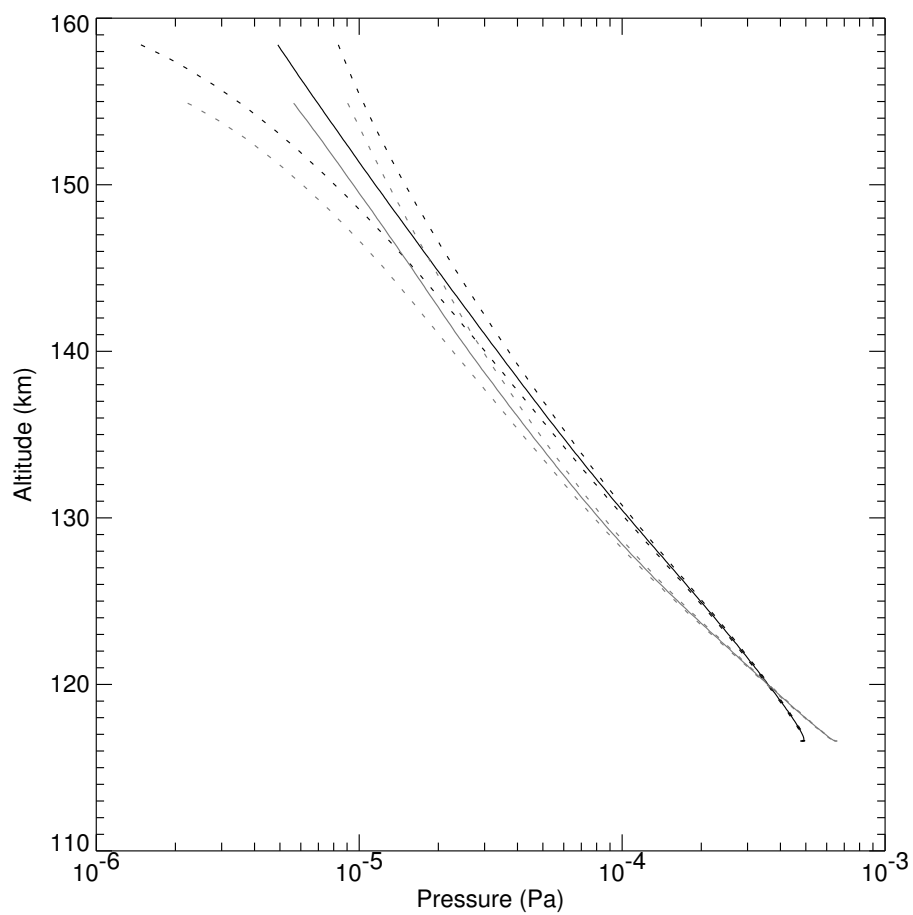


Figure 3.1: Pressure profiles derived for orbit P679 using established assumptions. The inbound profile is the solid black line, the outbound profile is the solid grey line. 1σ uncertainties for both are shown as dotted lines.

Equation 3.1, where \underline{v} is the neutral wind velocity, t is universal time, $\underline{\Omega}$ is the planetary sidereal rotation rate, ν_{ni} is the neutral-ion collision frequency, \underline{V}_i is the ion velocity, ρ is atmospheric density, η is the molecular dynamic viscosity, p is atmospheric pressure, and \underline{g}_{eff} is the sum of gravitational and centrifugal accelerations, conserves momentum in an atmosphere in a planet-fixed rotating reference frame. This equation is discussed in *e. g.* Holton (1992) or Chamberlain and Hunten (1987).

The first term on the left hand side of Equation 3.1 is the acceleration term, the second is the advective term, the third is the Coriolis term, the fourth is the ion-drag term, and the fifth is the viscous term. The first term on the right hand side of Equation 3.1 is the pressure gradient term and the second is the gravitational term. In a static ($\underline{v} = \underline{0}$, $\underline{V}_i = \underline{0}$) atmosphere, the left hand side of Equation 3.1 is zero and pressure gradient forces are exactly balanced by the effective (including centrifugal) force of gravity.

$$\underline{g}_{eff} = \underline{g}_{grav} - \underline{\Omega} \times (\underline{\Omega} \times \underline{r}) \quad (3.2)$$

Equation 3.2 defines \underline{g}_{eff} . The true gravitational acceleration, dependent only on the mass distribution within the planet, is \underline{g}_{grav} , the centrifugal acceleration is $-\underline{\Omega} \times (\underline{\Omega} \times \underline{r})$, and \underline{r} is the position vector measured from the centre of mass of the planet. For a spherically symmetric planet, \underline{g}_{grav} is directed radially. For a real planet, the spherical symmetry may be broken by terms of higher degree and order. The largest contributor to \underline{g}_{eff} is always the spherically symmetric term, $-GM/r^2$ where G is the gravitational constant, M is the mass of the planet and $r = |\underline{r}|$

3.2.1 Simplest Approximation to Equation 3.1

The radial component of the acceleration due to \underline{g}_{eff} is always much greater than the two perpendicular components; if it were not, then the planet's atmosphere

would rapidly escape into space. Maxwellian molecular speeds in a planetary atmosphere are simply too small for the velocity-dependent terms on the left hand side of Equation 3.1 to balance this large acceleration, so the radial pressure gradient term must balance it. This reasoning leads to the following approximation to Equation 3.1:

$$0 = \frac{-1}{\rho} \frac{\partial p}{\partial r} + \frac{-GM}{r^2} \quad (3.3)$$

$$0 = \frac{-1}{\rho} \frac{\partial p}{\partial \theta} \quad (3.4)$$

$$0 = \frac{-1}{\rho} \frac{\partial p}{\partial \phi} \quad (3.5)$$

where θ is colatitude and ϕ is east longitude. This spherical polar coordinate system is centred on the planet's centre of mass. Using the known GM , a boundary condition, and a radial profile of density as a function of altitude, Equation 3.3 can be integrated to obtain a collocated profile of pressure. The boundary condition, which is usually applied at the top of the atmosphere, is usually the assumption of an isothermal atmosphere. The pressure at the top of the atmosphere can then be related to the observable density scale height via $p = \rho g H$. Errors in the derived pressure at this high altitude have a negligible effect on the pressure profile at lower altitudes since pressure has an exponential dependence on altitude. From the independently known atmospheric composition as a function of altitude, an equation of state can be derived and used with the pressure and density profiles to yield a collocated profile of atmospheric temperature.

Slightly more sophisticated versions of this established technique have been successfully applied to near-vertical entry profiles from many spacecraft, as discussed

in Magalhães et al. (1999). However, as discussed in Section 3.1, it fails when applied to the MGS ACC density profiles. A new formulation must be found, one that allows for the non-vertical flight path of the spacecraft and uses the new constraint of two simultaneous profiles. Similar issues were addressed by Seiff et al. (1979) in their analysis of the simultaneous entries of the Pioneer Venus probes. To identify which terms in Equation 3.1 are most important in this situation I perform a scale analysis.

3.2.2 Scale Analysis on Equation 3.1

I work in a spherical polar coordinate frame, so my latitudes and longitudes are planetocentric, rather than planetographic or some other system. I do not use altitude referenced to an equipotential surface, which is the vertical coordinate in the PDS ACC data archive, because of a desire to be rigorous and correct in my vector algebra (Keating et al., 2001a). The change in unit vectors with position would be very complicated to express analytically if a reference surface without a simple form in a Cartesian coordinate system (such as a fourth degree and order equipotential surface) was used. Many atmospheric science applications use pressure as a vertical coordinate, because this can simplify the study of certain phenomena (Holton, 1992). However, this is only true when pressure is well-known. Since the ACC data here are known as a function of position, unlike, *e. g.*, remotely-sensed TES vertical profiles of temperature which are known as functions of pressure, I use a more appropriate “position-centric” coordinate system. Doing so introduces curvature terms as discussed in Appendix C.

The three components of Equation 3.1 become:

$$\begin{aligned} \frac{\partial v_r}{\partial t} + (\underline{v} \cdot \underline{\nabla}) v_r + 2(-\Omega v_\phi \sin \theta) - \frac{v_\theta^2 + v_\phi^2}{r} = \\ \frac{-1}{\rho} \frac{\partial p}{\partial r} + g_{eff,r} - \nu_{ni} (v_r - V_{i,r}) \end{aligned} \quad (3.6)$$

$$\begin{aligned} \frac{\partial v_\theta}{\partial t} + (\underline{v} \cdot \underline{\nabla}) v_\theta + 2(-\Omega v_\phi \cos \theta) + \frac{v_\theta v_r}{r} - \frac{v_\phi^2}{r \tan \theta} = \\ \frac{-1}{\rho r} \frac{\partial p}{\partial \theta} + g_{eff,\theta} + \frac{\eta}{\rho} \frac{\partial^2 v_\theta}{\partial r^2} - \nu_{ni} (v_\theta - V_{i,\theta}) \end{aligned} \quad (3.7)$$

$$\begin{aligned} \frac{\partial v_\phi}{\partial t} + (\underline{v} \cdot \underline{\nabla}) v_\phi + 2\Omega(\cos \theta v_\theta + \sin \theta v_r) + \frac{v_\phi v_r}{r} + \frac{v_\phi v_\theta}{r \tan \theta} = \\ \frac{-1}{\rho r \sin \theta} \frac{\partial p}{\partial \phi} + g_{eff,\phi} + \frac{\eta}{\rho} \frac{\partial^2 v_\phi}{\partial r^2} - \nu_{ni} (v_\phi - V_{i,\phi}) \end{aligned} \quad (3.8)$$

where

$$(\underline{v} \cdot \underline{\nabla}) = v_r \frac{\partial}{\partial r} + \frac{v_\theta}{r} \frac{\partial}{\partial \theta} + \frac{v_\phi}{r \sin \theta} \frac{\partial}{\partial \phi} \quad (3.9)$$

The viscosity term is not included in its full complexity. Only the dominant component, as detailed in Appendix D, is included in Equations 3.7 and 3.8. The dominant viscous component in Equation 3.6 is not included, because the work of Section 3.2.1 and later in this Section show that Equation 3.6 is completely dominated by the balance between gravity and the pressure gradients. The g_{eff} terms are known *a priori*, but estimates must be made for the other terms. I do not estimate the pressure gradient terms: instead, I treat them as unknowns.

$$g_{eff,r} = -\frac{GM}{r^2} - \frac{3GM}{r^2} \left(\frac{r_{ref}}{r}\right)^2 \sqrt{5} \left(\frac{3}{2} \cos^2 \theta - \frac{1}{2}\right) \bar{C}_{20} + r\Omega^2 \sin^2 \theta \quad (3.10)$$

$$g_{eff,\theta} = -\frac{3GM}{r^2} \left(\frac{r_{ref}}{r}\right)^2 \sqrt{5} \sin \theta \cos \theta \bar{C}_{20} + r\Omega^2 \sin \theta \cos \theta \quad (3.11)$$

$$g_{eff,\phi} = 0 \quad (3.12)$$

Equations 3.10 – 3.12 contain an expansion of the gravitational field to second degree and order. r_{ref} is a reference distance and \bar{C}_{20} is the first normalized zonal harmonic coefficient. First degree and order coefficients are zero when the centre of mass is at the origin of the coordinate system. r_{ref} is often, but is not required to be, the mean equatorial radius of the planet. \bar{C}_{20} has meaning only in association with this reference radius. The factor of $\sqrt{5}$ comes from the normalization convention which is discussed in Section 4.1. I work up to second degree and order so that my results do not become dependent on perfect spherical symmetry in the gravitational field, but do not go to higher order because those terms are negligible.

Typical time and length scales for changes in the neutral wind velocity are:

$$\frac{\partial}{\partial t} \sim \frac{\Omega}{2\pi} \quad (3.13)$$

$$\frac{\partial}{\partial r} \sim \frac{1}{H} \quad (3.14)$$

$$\frac{1}{r} \frac{\partial}{\partial \theta} \sim \frac{1}{r_{ref}} \quad (3.15)$$

$$\frac{1}{r} \frac{\partial}{\partial \phi} \sim \frac{1}{r_{ref}} \quad (3.16)$$

where H is an atmospheric scale height. Strictly, the horizontal length scale should be the radial distance to the region of interest. This might be significantly larger than than r_{ref} , which is most probably the planet's equatorial radius. In the cases to be discussed here, either the radial distance to the region of interest is

close to r_{ref} or \bar{C}_{20} is negligible and I can use the radial distance to the region of interest as r_{ref} . These are discussed at the appropriate times. I replace each term in Equations 3.6 – 3.8 with its likely magnitude (Equations 3.17–3.19), see which terms are dominant and which are negligible, then find reasonable approximations to these Equations using only the dominant terms.

$$\begin{aligned} & \frac{v_r \Omega}{2\pi} + \frac{v_r v_r}{H} + \frac{v_\theta v_r}{r_{ref}} + \frac{v_\phi v_r}{r_{ref} \sin \theta} + \\ & 2\Omega v_\phi \sin \theta + \frac{v_\theta^2}{r_{ref}} + \frac{v_\phi^2}{r_{ref}} + \nu_{ni} (v_r - V_{i,r}) = \\ & \frac{1}{\rho} \frac{\partial p}{\partial r} + \frac{GM}{r_{ref}^2} + \frac{3GM}{r_{ref}^2} \sqrt{5} \left(\frac{3}{2} \cos^2 \theta - \frac{1}{2} \right) \bar{C}_{20} + r_{ref} \Omega^2 \sin^2 \theta \end{aligned} \quad (3.17)$$

$$\begin{aligned} & \frac{v_\theta \Omega}{2\pi} + \frac{v_r v_\theta}{H} + \frac{v_\theta v_\theta}{r_{ref}} + \frac{v_\phi v_\theta}{r_{ref} \sin \theta} + \\ & 2\Omega v_\phi \cos \theta + \frac{v_\theta v_r}{r_{ref}} + \frac{v_\phi^2}{r_{ref} \tan \theta} + \nu_{ni} (v_\theta - V_{i,\theta}) = \\ & \frac{1}{\rho r} \frac{\partial p}{\partial \theta} + \frac{3GM}{r_{ref}^2} \sqrt{5} \sin \theta \cos \theta \bar{C}_{20} + r_{ref} \Omega^2 \sin \theta \cos \theta + \frac{\eta v_\theta}{\rho H^2} \end{aligned} \quad (3.18)$$

$$\begin{aligned} & \frac{v_\phi \Omega}{2\pi} + \frac{v_r v_\phi}{H} + \frac{v_\theta v_\phi}{r_{ref}} + \frac{v_\phi v_\phi}{r_{ref} \sin \theta} + \\ & 2\Omega v_\theta \cos \theta + 2\Omega v_r \sin \theta + \frac{v_\phi v_r}{r_{ref}} + \frac{v_\phi v_\theta}{r_{ref} \tan \theta} + \nu_{ni} (v_\phi - V_{i,\phi}) = \\ & \frac{1}{\rho r \sin \theta} \frac{\partial p}{\partial \phi} + \frac{\eta v_\phi}{\rho H^2} \end{aligned} \quad (3.19)$$

The ion-drag term only operates if the magnetic field is strong enough to control the motion of the ions (Rees, 1989). If the ion gyrofrequency, f_{gyro} , is greater than the ion-neutral collision frequency, ν_{in} , then the motions of the ions are controlled by the magnetic field, else they are not. The ratio of the ion-neutral collision frequency (frequency of collisions of neutrals with a given ionic particle)

to the neutral-ion collision frequency (frequency of collisions of ions with a given neutral particle) equals the ratio of the neutral number density to the ion number density, so the ion-neutral collision frequency is greater than the neutral-ion collision frequency.

$$f_{gyro} = \frac{1}{2\pi} \frac{q_{ion} B}{m_{ion}} \quad (3.20)$$

$$\nu_{in} = n_{neutral} A_{neutral} \sqrt{\frac{3kT_{ion}}{m_{ion}}} \quad (3.21)$$

$$\frac{f_{gyro}}{\nu_{in}} = \frac{q_{ion}}{2\pi} \frac{1}{\sqrt{3k}} \frac{B}{n_{neutral} A_{neutral}} \frac{1}{\sqrt{m_{ion} T_{ion}}} \quad (3.22)$$

where q_{ion} is the magnitude of the ionic charge, typically the same as an electron, B is the magnetic field strength, m_{ion} is the ion mass, $n_{neutral}$ is the number density of neutral particles, $A_{neutral}$ is the cross-sectional area of a neutral particle, k is Boltzmann's constant, and T_{ion} is the temperature of the ions. If this ratio is greater than unity, then \underline{V}_i differs from the neutral wind velocity \underline{v} and the ion-drag term is non-zero. \underline{V}_i can be estimated by assuming that the ions remain fixed on field-lines and rotate with the planet.

I perform this scale analysis for Venus, Mars, and Titan. At Venus, the Orbiter Neutral Mass Spectrometer (ONMS) of the Pioneer Venus Orbiter (PVO) measured density profiles that, like the MGS ACC, descend into and rise out of the atmosphere (Niemann et al., 1980). The compositional information from this instrument has been analysed in detail, but its dynamical implications have been less well-studied (Kasprzak et al., 1993). Relevant Mars observations come from the aerobraking of MGS, Mars Odyssey (2001 – 2002), MRO (planned for 2005 – 2006) and, depending on its operational usage, the Nozomi mass spectrometer which

arrives at Mars in 2003 (Lammer et al., 2000). At Titan, Cassini’s Ion Neutral Mass Spectrometer (INMS) will measure density profiles analogously to PVO at Venus (Kasprzak et al., 1996). It is likely that similar data exist for Earth.

Now I must estimate the magnitude of each of these terms using values appropriate for the planet and dataset in question. I consider each advective term in the equations separately, unlike *e. g.* page 39 of Holton (1992). I do this in order to consider vertical, zonal, and meridional terms separately for maximum understanding of the force balances. Relevant parameters are listed in Table 3.1.

3.3 Mars Scale Analysis

Order of magnitude estimates of the parameters in Equations 3.17 – 3.19 for ACC data from MGS aerobraking are given in Table 3.1.

In this case, the radial distance to aerobraking altitudes of 100 km is not significantly different from r_{ref} for the gravitational field. I can use the gravitational field’s r_{ref} as the lengthscale for some of the dynamical terms, as discussed in Section 3.2.2.

The ratio of f_{gyro} to ν_{in} is ~ 0.1 , so the ion-drag term has no effect. I later show that even if this ratio is of order unity, then the ion-drag term is still negligible.

3.3.1 r component

The first row of Table 3.2 shows the magnitude of each term from Equation 3.17. The dominant term is the 3.73 m s^{-2} gravitational term. The known contributions to the gravitational effects from \bar{C}_{20} and the centrifugal term are much smaller. The largest dynamical term on the left hand side of Equation 3.17 is the $1/\sin \theta$ part of the advective term at polar latitudes. Only when $\theta < 4.5^\circ \times 10^{-3}$ does this term

Parameter	Venus (day, CO ₂)	Venus (night, O)	Mars	Titan
GM (m ³ s ⁻²)	3.2E14 [1]	3.2E14 [1]	4.3E13 [1]	9.0E12 [1]
\bar{C}_{20} (dimless)	-2.0E-6 [2]	-2.0E-6 [2]	-8.8E-4 [1]	?
Ω (rad s ⁻¹)	1.2E-8 [1]	1.2E-8 [1]	7E-5 [1]	4.6E-6 [12]
r_{ref} (m)	6.2E6 [1,3]	6.2E6 [1,3]	3.4E6 [1]	3.5E6 [11]
H (m)	5E3 [3]	5E3 [3]	1E4 [8]	8E4 [12]
v_r (m s ⁻¹)	1 [4]	1 [4]	1 [7]	1 [13]
v_θ (m s ⁻¹)	5 [5]	5 [5]	30 [7]	20 [13]
v_ϕ (m s ⁻¹)	100 [5]	100 [5]	100 [7]	100 [13]
η (kg m ⁻¹ s ⁻¹)	1.0E-5 [6]	1.1E-5 [6]	1.0E-5 [6]	1.3E-5 [12]
ρ (kg m ⁻³)	5E-10 [3]	2E-11 [3]	1E-9 [8]	8.5E-11 [12]
q_{ion} (C)	1.6E-19	1.6E-19	1.6E-19	1.6E-19
B (T)	<3E-10 [1]	<3E-10 [1]	1E-6 [9]	<1.6E-9 [10]
$n_{neutral}$ (m ⁻³)	8E15 [3]	5E14 [3]	1E16 [8]	1.9E15 [12]
$A_{neutral}$ (m ²)	1E-18	1E-18	1E-18	1E-18
m_{ion} (kg)	7.3E-26 [3]	2.7E-26 [3]	7.3E-26 [1]	4.5E-26 [1]
T_{ion} (K)	280 [3]	110 [3]	200 [7,8]	200 [12]

Table 3.1: Relevant Parameters. References are: [1] Lodders and Fegley (1998); [2] National Space Science Data Center (2003); [3] Niemann et al. (1980); [4] Kerzhanovich and Marov (1983); [5] Schubert (1983); [6] Lide (1994); [7] Bougher et al. (1990); [8] Keating et al. (2001a); [9] Purucker et al. (2000); [10] Neubauer et al. (1984); [11] Yelle (pers. comm., 2002); [12] Rishbeth et al. (2000); [13] Müller-Wodarg et al. (2000)

approach 10% of the dominant 3.73 m s^{-2} gravitational term. So at all latitudes Equation 3.6 is well-approximated by:

$$0 = \frac{-1}{\rho} \frac{\partial p}{\partial r} + \frac{-GM}{r^2} \quad (3.23)$$

3.3.2 θ component

The first row of Table 3.3 shows the magnitude of each term from Equation 3.18.

The two $\sin \theta \cos \theta$ terms contributing to $g_{eff,\theta}$ are known *a priori*. The latitude-independent viscous term is not. The dominant term on the left hand side of Equation 3.18 depends on latitude as shown in Table 3.4. The competing terms are the largest latitude-independent part of the advective term, the $1/\sin \theta$ part of the advective term, the $\cos \theta$ Coriolis term, and the $1/\tan \theta$ part of the curvature term. The competing terms are symmetric about the equator.

The Coriolis term, $2\Omega v_\phi \cos \theta$, is dominant, but only by factors of a few, between $\theta = 30^\circ$ and $\theta = 60^\circ$, corresponding to latitudes between 30° and 60° in either hemisphere. The poleward limit is set by the curvature term, $v_\phi^2/r_{ref} \tan \theta$. The viscous term is not many times smaller than the Coriolis term, but I feel that I have underestimated the vertical lengthscale for changes in wind velocity by equating it to the scale height. There is no compelling reason for many reversals in the wind speed over the many scale heights-extent of the upper atmosphere. This reasoning suggests that neither the viscous nor largest latitude-independent part of the advective term are as large as I have outlined above. At mid-latitudes Equation 3.7 is well-approximated by:

$$-2\Omega v_\phi \cos \theta = \frac{-1}{r\rho} \frac{\partial p}{\partial \theta} + g_{eff,\theta} \quad (3.24)$$

(A) Object	$\frac{v_r \Omega}{2\pi}$	$\frac{v_r v_r}{H}$	$\frac{v_\theta v_r}{r_{ref}}$	$\frac{v_\phi v_r}{r_{ref} \sin \theta}$
Mars	1.1×10^{-5}	10^{-4}	8.85×10^{-6}	$\frac{2.95 \times 10^{-5}}{\sin \theta}$
Venus	1.2×10^{-9}	2.0×10^{-4}	8.1×10^{-7}	$\frac{1.6 \times 10^{-5}}{\sin \theta}$
Titan	7.3×10^{-7}	1.3×10^{-5}	5.7×10^{-6}	$\frac{2.9 \times 10^{-5}}{\sin \theta}$

(B) Object	$ 2\Omega v_\phi \sin \theta $	$\frac{v_\theta^2}{r_{ref}}$	$\frac{v_\phi^2}{r_{ref}}$
Mars	$0.014 \sin \theta$	2.6×10^{-4}	2.9×10^{-3}
Venus	$2.4 \times 10^{-6} \sin \theta$	4.0×10^{-6}	1.6×10^{-3}
Titan	$9.2 \times 10^{-4} \sin \theta$	1.1×10^{-4}	2.9×10^{-3}

(C) Object	$\frac{1}{m.s^{-2}} \left(\frac{-1}{\rho} \frac{\partial p}{\partial r} \right)$	$\frac{GM}{r_{ref}^2}$
Mars	$\frac{1}{m.s^{-2}} \left(\frac{-1}{\rho} \frac{\partial p}{\partial r} \right)$	3.73
Venus	$\frac{1}{m.s^{-2}} \left(\frac{-1}{\rho} \frac{\partial p}{\partial r} \right)$	8.3
Titan	$\frac{1}{m.s^{-2}} \left(\frac{-1}{\rho} \frac{\partial p}{\partial r} \right)$	6.6×10^{-1}

(D) Object	$\frac{3GM}{r_{ref}^2} \sqrt{5} \left(\frac{3}{2} \cos^2 \theta - \frac{1}{2} \right) \bar{C}_{20}$	$ r_{ref} \Omega^2 \sin^2 \theta $
Mars	$0.015 \left(\frac{3}{2} \cos^2 \theta - \frac{1}{2} \right)$	$0.017 \sin^2 \theta$
Venus	$7.4 \times 10^{-5} \left(\frac{3}{2} \cos^2 \theta - \frac{1}{2} \right)$	$8.9 \times 10^{-10} \sin^2 \theta$
Titan	$3.0 \bar{C}_{20} \left(\frac{3}{2} \cos^2 \theta - \frac{1}{2} \right)$	$7.4 \times 10^{-5} \sin^2 \theta$

Table 3.2: Scale Analysis of Equation 3.6. Units are $m s^{-2}$. Each term in (A) and (B) corresponds to a term on the left-hand side of Equation 3.17, (C) and (D) to the right-hand side.

(A) Object	$\frac{v_\theta \Omega}{2\pi}$	$\frac{v_r v_\theta}{H}$	$\frac{v_\theta v_\theta}{r_{ref}}$	$\frac{v_\phi v_\theta}{r_{ref} \sin \theta}$
Mars	3.3×10^{-4}	3×10^{-3}	2.7×10^{-4}	$\frac{8.85 \times 10^{-4}}{\sin \theta}$
Venus	9.5×10^{-9}	1.0×10^{-5}	4.0×10^{-6}	$\frac{8.1 \times 10^{-5}}{\sin \theta}$
Titan	1.5×10^{-5}	2.5×10^{-4}	1.1×10^{-4}	$\frac{5.7 \times 10^{-4}}{\sin \theta}$

(B) Object	$ 2\Omega v_\phi \cos \theta $	$\frac{v_\theta v_r}{r_{ref}}$	$\frac{v_\phi^2}{r_{ref} \tan \theta}$
Mars	$0.014 \cos \theta$	8.8×10^{-6}	$\frac{2.9 \times 10^{-3}}{\tan \theta}$
Venus	$2.4 \times 10^{-6} \cos \theta$	8.1×10^{-7}	$\frac{1.6 \times 10^{-3}}{\tan \theta}$
Titan	$9.2 \times 10^{-4} \cos \theta$	5.7×10^{-6}	$\frac{2.9 \times 10^{-3}}{\tan \theta}$

(C) Object	$\frac{1}{m s^{-2}} \frac{-1}{\rho r} \frac{\partial p}{\partial \theta}$	$\frac{3GM}{r_{ref}^2} \sqrt{5} \sin \theta \cos \theta \bar{C}_{20}$
Mars	$\frac{1}{m s^{-2}} \frac{-1}{\rho r} \frac{\partial p}{\partial \theta}$	$0.0225 \sin \theta \cos \theta$
Venus	$\frac{1}{m s^{-2}} \frac{-1}{\rho r} \frac{\partial p}{\partial \theta}$	$1.1 \times 10^{-4} \sin \theta \cos \theta$
Titan	$\frac{1}{m s^{-2}} \frac{-1}{\rho r} \frac{\partial p}{\partial \theta}$	$4.4 \bar{C}_{20} \sin \theta \cos \theta$

(D) Object	$ r_{ref} \Omega^2 \sin \theta \cos \theta $	$\frac{\eta v_\theta}{\rho H^2}$
Mars	$0.017 \sin \theta \cos \theta$	3×10^{-3}
Venus	$8.9 \times 10^{-10} \sin \theta \cos \theta$	4.0×10^{-3} (day) or 1.1×10^{-1} (night)
Titan	$7.4 \times 10^{-5} \sin \theta \cos \theta$	4.8×10^{-4}

Table 3.3: Scale Analysis of Equation 3.7. Units are $m s^{-2}$. Each term in (A) and (B) corresponds to a term on the left-hand side of Equation 3.18, (C) and (D) to the right-hand side.

θ (degrees)	$\frac{v_r v_\theta}{r_{ref}}$	$\frac{v_\phi v_\theta}{r_{ref} \sin \theta}$	$ 2\Omega v_\phi \cos \theta $	$\frac{v_\phi^2}{r_{ref} \tan \theta}$
10	3.6E-3	5.1E-3	0.014	0.017
20	3.6E-3	2.6E-3	0.013	8.1E-3
30	3.6E-3	1.8E-3	0.012	5.1E-3
40	3.6E-3	1.4E-3	0.011	3.5E-3
50	3.6E-3	1.2E-3	9.0E-3	2.5E-3
60	3.6E-3	1.0E-3	7.0E-3	1.7E-3
70	3.6E-3	9.4E-4	4.8E-3	1.1E-3
80	3.6E-3	9.0E-4	2.4E-3	5.2E-4

Table 3.4: Dominant Terms in Equation 3.18 for Mars case. Units are m s^{-2} .

If geostrophic balance held in the upper atmosphere, this equation would be the same. If I desired to push back the poleward limit, I could also include the $v_\phi^2/r \tan \theta$ curvature term in Equation 3.24 and have a quadratic in v_ϕ for the left hand side.

Returning to the ion-drag term, I decided to estimate the magnitude of the ion-drag term in Equation 3.18 as if the gyrofrequency criterion were satisfied. I set ν_{in} equal to f_{gyro} , then calculated ν_{ni} from the ratio of ion and neutral number densities. The peak ion number density is about 10^{11} m^{-3} at an altitude of 140 km in the example shown in Bougher et al. (2001). This corresponds to a neutral mass density of about $10^{-9} \text{ kg m}^{-3}$ or number density for CO_2 of 10^{16} m^{-3} in the MGS ACC PDS data. With these numbers, the ion-drag term is still two orders of magnitude smaller than the Coriolis term.

3.3.3 ϕ component

The first row of Table 3.5 shows the magnitude of each term from Equation 3.19.

The largest latitude-independent term on the left hand side of Equation 3.19 is the $0.01 \text{ m s}^{-2} v_r \partial v_\phi / \partial r$ part of the advective term. At polar latitudes the $1/\sin \theta$ part of the advective term is comparable to this. The viscous term is also comparable at all latitudes. The latitude-independent term is dominant for latitudes equatorward of 73° , and at equatorial and mid-latitudes Equation 3.8 is well-approximated by:

$$v_r \frac{\partial v_\phi}{\partial r} = \frac{-1}{r \rho \sin \theta} \frac{\partial p}{\partial \phi} + \frac{\eta}{\rho} \frac{\partial^2 v_\phi}{\partial r^2} \quad (3.25)$$

If my earlier comments about the correct vertical lengthscale being greater than a scale height are correct, then several other terms should probably be included. However, since I am about to neglect this whole equation, I do not investigate that.

(A) Object	$\frac{v_\phi \Omega}{2\pi}$	$\frac{v_r v_\phi}{H}$	$\frac{v_\theta v_\phi}{r_{ref}}$	$\frac{v_\phi v_\phi}{r_{ref} \sin \theta}$
Mars	1.1×10^{-3}	0.01	8.85×10^{-4}	$\frac{2.95 \times 10^{-3}}{\sin \theta}$
Venus	1.9×10^{-7}	2.0×10^{-2}	8.1×10^{-5}	$\frac{1.6 \times 10^{-5}}{\sin \theta}$
Titan	7.3×10^{-5}	1.3×10^{-3}	5.7×10^{-4}	$\frac{2.9 \times 10^{-3}}{\sin \theta}$

(B) Object	$ 2\Omega v_\theta \cos \theta $	$ 2\Omega v_r \sin \theta $	$\frac{v_\phi v_r}{r_{ref}}$	$\frac{v_\phi v_\theta}{r_{ref} \tan \theta}$
Mars	$4.2 \times 10^{-3} \cos \theta$	$1.4 \times 10^{-4} \sin \theta$	2.9×10^{-5}	$\frac{8.8 \times 10^{-4}}{\tan \theta}$
Venus	$1.2 \times 10^{-7} \cos \theta$	$2.4 \times 10^{-8} \sin \theta$	1.6×10^{-5}	$\frac{8.1 \times 10^{-5}}{\tan \theta}$
Titan	$1.8 \times 10^{-4} \cos \theta$	$9.2 \times 10^{-6} \sin \theta$	2.9×10^{-5}	$\frac{5.7 \times 10^{-4}}{\tan \theta}$

(C) Object	$\frac{-1}{\rho r \sin \theta} \frac{\partial p}{\partial \phi}$	$\frac{\eta v_\phi}{\rho H^2}$
Mars	$\frac{-1}{\rho r \sin \theta} \frac{\partial p}{\partial \phi}$	1×10^{-2}
Venus	$\frac{-1}{\rho r \sin \theta} \frac{\partial p}{\partial \phi}$	8.0×10^{-2} (day) or 2.2×10^0 (night)
Titan	$\frac{-1}{\rho r \sin \theta} \frac{\partial p}{\partial \phi}$	2.4×10^{-3}

Table 3.5: Scale Analysis of Equation 3.8. Units are m s^{-2} . Each term in (A) and (B) corresponds to a term on the left-hand side of Equation 3.19, (C) to the right-hand side.

3.3.4 Approximate Equations

Between $\theta = 30^\circ$ and $\theta = 60^\circ$ Equations 3.6 – 3.8 can be approximated by:

$$0 = \frac{-1}{\rho} \frac{\partial p}{\partial r} + \frac{-GM}{r^2} \quad (3.26)$$

$$-2\Omega v_\phi \cos \theta = \frac{-1}{r\rho} \frac{\partial p}{\partial \theta} + g_{eff,\theta} \quad (3.27)$$

$$v_r \frac{\partial v_\phi}{\partial r} = \frac{-1}{r\rho \sin \theta} \frac{\partial p}{\partial \phi} \quad (3.28)$$

The dynamical terms on the left hand sides of Equations 3.27 and 3.28 have about the same magnitude — 0.01 m s^{-2} . Since MGS collected data from a sunsynchronous, near-polar orbit, changes in latitude during a pass are much greater than changes in longitude — at least in the mid-latitudes considered here. On orbit P750 for example, MGS travelled 30° in latitude and 4° in longitude. Even allowing for the effects of the $\sin \theta$ in the denominator of Equation 3.28, changes in pressure along an aerobraking pass are dominated first by changes in vertical position over changes in horizontal position, then by changes in latitude over changes in longitude. Effects of changes in longitude and Equation 3.28 itself can be neglected when deriving pressure profiles from MGS ACC density profiles. The Coriolis term in Equation 3.6 also has a magnitude of 0.01 m s^{-2} . However, since its contribution to the pressure depends on the radial distance travelled, it has a much smaller effect on the total pressure than the Coriolis term in Equation 3.27 and can be neglected from Equation 3.26.

The general conservation of momentum equations are Equations 3.6 – 3.8. The simplest approximation to them are Equations 3.3 – 3.5. The simplest approximation to them that is useful for analysing MGS ACC data is:

$$0 = \frac{-1}{\rho} \frac{\partial p}{\partial r} + \frac{-GM}{r^2} \quad (3.29)$$

$$-2\Omega v_\phi \cos \theta = \frac{-1}{r\rho} \frac{\partial p}{\partial \theta} + g_{eff,\theta} \quad (3.30)$$

The θ component of these equations is in geostrophic balance. The atmosphere itself is not in geostrophic balance, because Equation 3.28 is not dominated by the Coriolis force. I call this situation “quasi-geostrophic” balance. The only unknown quantity affecting the horizontal pressure gradient is the zonal wind, v_ϕ . So, in principle, the horizontal pressure gradients that caused the inbound and outbound estimates of periapsis pressure to differ can be used to solve for v_ϕ . This solution then gives self-consistent pressure and temperature profiles. I later outline a method for doing this in Section 3.7.

3.4 Venus Scale Analysis

Pioneer Venus Orbiter collected many neutral mass spectrometer measurements on passes through the upper atmosphere of Venus. These can be considered as density profiles. As Table 3.1 shows, there are significant differences between the dayside and the nightside of Venus’s upper atmosphere. The dayside atmosphere is dominated by CO₂ and has a significantly higher density than the colder nightside O atmosphere (Niemann et al., 1980).

In this case, the radial distance to periapsis altitudes of 150 km is not significantly different from r_{ref} for the gravitational field. I use the radial distance to periapsis altitude as r_{ref} , as discussed in Section 3.2.2.

The ratio of f_{gyro} to ν_{in} is $\sim 3 \times 10^{-5}$ for the Venus dayside and $\sim 1 \times 10^{-3}$ for the nightside, so the ion-drag term has no effect in either case.

3.4.1 r component

For both the dayside and nightside parameters, the second row of Table 3.2 shows the magnitude of each term from Equation 3.17. The dominant term is the 8.3 m s^{-2} gravitational term. The known contributions to the gravitational effects from \bar{C}_{20} and the centrifugal term are much smaller. The largest latitude-independent term on the left hand side is negligible and the largest latitude-dependent term only approaches 10% of 8.3 m s^{-2} gravitational term when $\theta < 1.1^\circ \times 10^{-3}$. So at all latitudes Equation 3.6 is well-approximated by:

$$0 = \frac{-1}{\rho} \frac{\partial p}{\partial r} + \frac{-GM}{r^2} \quad (3.31)$$

3.4.2 θ component

The second row of Table 3.3 shows the magnitude of each term from Equation 3.18. This does vary between day and night. The dominant unknown terms are the $1/\tan \theta$ curvature term and the viscous term at effectively all latitudes. Equation 3.7 is well-approximated by:

$$-\frac{v_\phi^2}{r \tan \theta} = \frac{-1}{\rho r} \frac{\partial p}{\partial \theta} + \frac{\eta}{\rho} \frac{\partial^2 v_\theta}{\partial r^2} \quad (3.32)$$

3.4.3 ϕ component

The second row of Table 3.5 shows the magnitude of each term from Equation 3.19. The dominant unknown term is the viscous term at effectively all latitudes. Equation 3.8 is well-approximated by:

$$0 = \frac{-1}{\rho r \sin \theta} \frac{\partial p}{\partial \phi} + \frac{\eta}{\rho} \frac{\partial^2 v_\phi}{\partial r^2} \quad (3.33)$$

3.4.4 Approximate Equations

For both dayside and nightside, Equations 3.6 – 3.8 can be approximated by:

$$0 = \frac{-1}{\rho} \frac{\partial p}{\partial r} + \frac{-GM}{r^2} \quad (3.34)$$

$$-\frac{v_\phi^2}{r \tan \theta} = \frac{-1}{\rho r} \frac{\partial p}{\partial \theta} + \frac{\eta}{\rho} \frac{\partial^2 v_\theta}{\partial r^2} \quad (3.35)$$

$$0 = \frac{-1}{\rho r \sin \theta} \frac{\partial p}{\partial \phi} + \frac{\eta}{\rho} \frac{\partial^2 v_\phi}{\partial r^2} \quad (3.36)$$

The θ and ϕ components of the conservation of momentum equations are dominated by the effects of viscosity in terms of analysing either the nightside or dayside PVO data. Observed horizontal pressure gradients could, in principle, be related to the second derivative of horizontal wind speed, but this is not a particularly interesting measurement.

Since it is easier to relate horizontal pressure gradients to winds in the Mars and Titan cases than in the Venus case, I do not investigate the Venus case any further.

3.5 Titan Scale Analysis

Cassini will pass through the upper atmosphere of Titan on numerous occasions during its mission. Using a neutral mass spectrometer like PVO, it will also measure density profiles.

In this case, the radial distance to periapsis altitudes of 1000 km is significantly different from the planetary radius. Since \bar{C}_{20} is not known, I use the

radial distance to periapsis altitude as r_{ref} in Equations 3.6 – 3.8, as discussed in Section 3.2.2

The ratio of f_{gyro} to ν_{in} is $\sim 1 \times 10^{-3}$ for Titan, so the ion-drag term has no effect.

3.5.1 r component

The third row of Table 3.2 shows the magnitude of each term from Equation 3.17. The dominant term is the 0.66 m s^{-2} gravitational term as long as \bar{C}_{20} is not unfeasibly large. The largest latitude-independent term on the left hand side is negligible and the largest latitude-dependent term only approaches 10% of 0.66 m s^{-2} gravitational term when $\theta < 2.5^\circ \times 10^{-5}$. So at all latitudes Equation 3.6 is well-approximated by:

$$0 = \frac{-1}{\rho} \frac{\partial p}{\partial r} + \frac{-GM}{r^2} \quad (3.37)$$

3.5.2 θ component

The third row of Table 3.3 shows the magnitude of each term from Equation 3.18. \bar{C}_{20} will be measured by Cassini at the same time as the density profiles, so the dominant unknown term is the $1/\tan \theta$ curvature term for all latitudes more than 20 degrees away from the equator. Equation 3.7 is well-approximated by:

$$\frac{v_\phi^2}{r \tan \theta} = \frac{1}{\rho r} \frac{\partial p}{\partial \theta} \quad (3.38)$$

3.5.3 ϕ component

The third row of Table 3.5 shows the magnitude of each term from Equation 3.19. The dominant unknown terms are two parts of the advective term and the viscous term. Equation 3.8 is well-approximated by:

$$v_r \frac{\partial v_\phi}{\partial r} + \frac{v_\phi}{r \sin \theta} \frac{\partial v_\phi}{\partial \theta} = \frac{-1}{\rho r \sin \theta} \frac{\partial p}{\partial \phi} + \frac{\eta}{\rho} \frac{\partial^2 v_\phi}{\partial r^2} \quad (3.39)$$

3.5.4 Approximate Equations

Equation 3.39 is quite intractable. However, some of Cassini's orbits will be sufficiently close to polar that the change in pressure due to changes in longitude will be negligible. In those cases, Equations 3.6 – 3.8 can be approximated by:

$$0 = \frac{-1}{\rho} \frac{\partial p}{\partial r} + \frac{-GM}{r^2} \quad (3.40)$$

$$\frac{v_\phi^2}{r \tan \theta} = \frac{1}{\rho r} \frac{\partial p}{\partial \theta} \quad (3.41)$$

Since Equation 3.41 is similar in form to the case of cyclostrophic balance, I call this situation “quasi-cyclostrophic” balance.

3.6 Summary of Simplified Equations

For each of these three cases, the approximation to the ϕ -component of Equation 3.1 (Equation 3.8) contains spatial derivatives of the wind velocity. It is much easier to deal with equations which contain the undifferentiated wind speed, so I only consider

near-polar orbits for which the change in pressure along a leg due to changes in longitude are negligible compared to those due to changes in latitude.

For the quasi-geostrophic case of Mars, my approximate equations are:

$$\frac{1}{\rho} \frac{\partial p}{\partial r} = -\frac{GM}{r^2} \quad (3.42)$$

$$2\Omega v_\phi \cos \theta = \frac{1}{\rho r} \frac{\partial p}{\partial \theta} - g_{eff,\theta} \quad (3.43)$$

For the quasi-cyclostrophic case of Titan, my approximate equations are:

$$\frac{1}{\rho} \frac{\partial p}{\partial r} = -\frac{GM}{r^2} \quad (3.44)$$

$$\frac{v_\phi^2}{r \tan \theta} = \frac{1}{\rho r} \frac{\partial p}{\partial \theta} - g_{eff,\theta} \quad (3.45)$$

The importance of latitudinal changes in pressure can be gauged by comparing the inbound and outbound estimates for periapsis pressure where these estimates assume that pressure gradients and gravity are the only forces acting. If they are identical, then latitudinal changes in pressure are negligible. If they are very different, then latitudinal changes in pressure are significant. I define E as the ratio of the difference of these two periapsis pressure estimates to their mean. $E = 0$ corresponds to the case of negligible latitudinal effects, $E \neq 0$ corresponds to the case of significant latitudinal effects. Appendix E outlines a method for estimating E , with some rather sweeping assumptions to deal with the effects of changing latitude on the trigonometric terms. The results are that $E \sim 0.2$ for the MGS ACC case at Mars and $E \sim 0.05$ for the Cassini INMS case at Titan. The martian estimate is

similar to my measurement of $E \sim 0.5$ in Section 3.1. Detecting this effect on Titan in the near-polar orbits of the Cassini data might be possible, because the INMS instrument has high performance characteristics, but the ever-changing geometry of the flybys will be a major complication.

3.7 “Balanced Arch” Technique for Estimating Wind Speed

In the quasi-geostrophic balance case, the zonal wind speed can be estimated as follows. The conservation of momentum equations between $\theta = 30^\circ$ and $\theta = 60^\circ$ are approximated as:

$$\frac{\partial p}{\partial r} = \rho g_{eff,r} \quad (3.46)$$

$$\frac{\partial p}{\partial \theta} = \rho r g_{eff,\theta} + 2\rho r \Omega v_\phi \cos \theta \quad (3.47)$$

Unknowns are v_ϕ and p as functions of r and θ . A zeroth order estimate of periapsis pressure from the inbound density profile, neglecting winds, is:

$$\int_{entry}^{peri} \rho g_{eff,r} dr + \int_{entry}^{peri} \rho r g_{eff,\theta} d\theta \quad (3.48)$$

Where the integration path is along the flight path. If v_ϕ is known, this estimate can be improved so that it gives the correct periapsis pressure by adding it to an offset term:

$$\int_{entry}^{peri} 2\Omega \rho r v_\phi \cos \theta d\theta \quad (3.49)$$

Similar expressions exist for the outbound leg, with exit replacing entry.

If I assume that v_ϕ is uniform, then it can be moved outside the integration and the offset term becomes:

$$v_\phi \int_{\text{entry}}^{\text{peri}} 2\Omega\rho r \cos\theta d\theta \quad (3.50)$$

Periapsis pressure is therefore given by both the following:

$$\int_{\text{entry}}^{\text{peri}} \rho g_{eff,r} dr + \int_{\text{entry}}^{\text{peri}} \rho r g_{eff,\theta} d\theta + v_\phi \int_{\text{entry}}^{\text{peri}} 2\Omega\rho r \cos\theta d\theta \quad (3.51)$$

$$\int_{\text{exit}}^{\text{peri}} \rho g_{eff,r} dr + \int_{\text{exit}}^{\text{peri}} \rho r g_{eff,\theta} d\theta + v_\phi \int_{\text{exit}}^{\text{peri}} 2\Omega\rho r \cos\theta d\theta \quad (3.52)$$

Equating these two expressions and rearranging them to solve for v_ϕ gives:

$$v_\phi = \frac{\left(\int_{\text{entry}}^{\text{peri}} \rho g_{eff,r} dr + \int_{\text{entry}}^{\text{peri}} \rho r g_{eff,\theta} d\theta\right) - \left(\int_{\text{exit}}^{\text{peri}} \rho g_{eff,r} dr + \int_{\text{exit}}^{\text{peri}} \rho r g_{eff,\theta} d\theta\right)}{\int_{\text{exit}}^{\text{peri}} 2\Omega\rho r \cos\theta d\theta - \int_{\text{entry}}^{\text{peri}} 2\Omega\rho r \cos\theta d\theta} \quad (3.53)$$

Which can be solved for v_ϕ using the density profiles and Ω . This solution for v_ϕ represents a characteristic zonal wind speed in the region spanned by the aerobraking pass. It is affected by all the neglected terms omitted from Equations 3.29 – 3.30. I call this result the “derived zonal wind speed” to emphasize that it is averaged over an unrealistically large spatial extent.

This technique, as currently implemented, satisfies an integrated version of Equation 3.30 and gives a single estimate of v_ϕ for the entire pass. By comparing latitudinal pressure gradients at every altitude on the pass and using the unintegrated Equation 3.30, a vertical profile of zonal wind speed can be derived. I leave this for future work.

With this zonal wind estimate, pressure profiles which are consistent at periapsis can be derived by substituting the value for v_ϕ into Equations 3.29 – 3.30 and then integrating in both r and θ with the usual boundary condition at the top of the atmosphere.

Uncertainties on the zonal wind estimate are calculated from the formal uncertainties in the various terms in Equation 3.53. To perform the integrations, I used a simple first order routine, stated below in Equation 3.54. Errors are propagated formally through the summation. The simple integration routine enables simple error calculations.

$$\int_{x_{start}}^{x_{stop}} y(x) dx = \sum_{i=0}^{i=n-1} y(x_i) (x_{i+1} - x_i) \quad (3.54)$$

ACC density measurements are evenly distributed in time, not r or θ , so not all dr are the same. Uncertainties in the pressure profile are also calculated by formally propagating errors through a first order summation for the integrations in Equation 3.51. These formal uncertainties do not consider any effects of the terms neglected in arriving at Equations 3.29 – 3.30. Monte Carlo simulations could be used to estimate the effects of these neglected terms on the uncertainty in the derived wind speed.

The analogous procedure for the case of cyclostrophic balance is as follows:

$$v_\phi^2 = \frac{\left(\int_{entry}^{peri} \rho g_{eff,r} dr + \int_{entry}^{peri} \rho r g_{eff,\theta} d\theta \right) - \left(\int_{exit}^{peri} \rho g_{eff,r} dr + \int_{exit}^{peri} \rho r g_{eff,\theta} d\theta \right)}{\int_{exit}^{peri} \frac{\rho r}{\tan \theta} d\theta - \int_{entry}^{peri} \frac{\rho r}{\tan \theta} d\theta} \quad (3.55)$$

Unlike the quasi-geostrophic case, the direction of the zonal wind is not known from this solution, only its magnitude. The direction must be inferred from other information.

I call this technique for measuring wind speeds using two simultaneous

density profiles the “Balanced Arch” technique to emphasize (a) the need to balance one leg of the aerobraking pass against the other and (b) the arched, non-vertical shape of each leg of the aerobraking pass.

3.8 Validation of “Balanced Arch” Technique

This proposed technique should be tested before results from it are accepted. The best validation would be to have measurements of winds, densities, and pressures in the martian upper atmosphere with excellent spatial coverage and resolution, apply this technique to the densities corresponding to an aerobraking pass, and test whether the derived wind bears any resemblance to the actual measured winds. Unfortunately, such a dataset does not exist. I tried a two-stage approach for validation instead. The first stage was to test this technique on a very simple model of an atmosphere which satisfies perfectly most of the assumptions made in deriving Equations 3.29 – 3.30 perfectly. The second stage was to test this technique on a general circulation model of an atmosphere which does not neglect these terms.

3.8.1 Test on a Simple Atmosphere

To test this technique I created an idealized atmosphere that satisfies Equation 3.1. It is isothermal (150K), has $v_r = 0$, $v_\theta = 0$, and $v_\phi = \text{constant}$ everywhere, includes rotation at martian angular speeds, has a martian GM , a uniform radius equal to r_{ref} , and spherically symmetric g_{grav} equal to GM/r_{ref}^2 . Ω , GM , and r_{ref} are as tabulated in Table 3.1. Periapsis latitude is 45°N and periapsis altitude is 120 km. The aerobraking profile passes through the top of the atmosphere at 30°N and 150 km and its altitude has a quadratic dependence on latitude, as discussed in Appendix E.

The initial condition for the integration equates the pressure at the top of the atmosphere to $\rho g H$, where H is the density scale height. It is calculated from

an exponential best-fit ($\ln \rho = \ln \rho_0 - r/H$) to the first ten kilometres in altitude of the density profile. The r range of ten kilometres is chosen as a reasonable *a priori* estimate for the scale height, which is actually 7.6 km. As usual, this estimate for the top of the atmosphere scale height assumes an isothermal atmosphere (which happens to be correct in this idealized model) *and* ignores the effects of latitudinal changes on the pressure. Equation E.17 shows how a later solution for v_ϕ could be used to account for latitudinal effects, which could be significant on rapidly-rotating planet or one with very fast zonal wind speeds, but I do not worry about this in the current work. Errors in this boundary condition become negligible in the pressure profile at lower altitudes.

Extracting a density profile from this model atmosphere, and then applying the Balanced Arch technique of Equation 3.53 yields the correct, *i. e.* the one specified in the simulation, result for the zonal wind speed. Changing the uniform zonal wind speed, the uniform temperature, periapsis latitude, latitudinal width of the pass, periapsis altitude, or the altitude of the top of the atmosphere do not affect the technique, it still gives the correct result for the applied uniform zonal wind field. The latitudinal limits on the technique are due to neglected terms becoming important. In this idealized kind of simulation the neglected terms are equal to zero, so the limits do not occur.

Next, I set the zonal wind speed equal to 100 m s^{-1} at periapsis and 0 m s^{-1} at the top of the atmosphere. Zonal wind speed was constant and uniform in the atmosphere, except across an artificial discontinuity placed at a fixed altitude. Increasing the boundary altitude between periapsis and the top of the atmosphere led to a high derived zonal wind speed, and decreasing it led to a low derived zonal wind speed. For each set of periapsis altitude and latitude, top of the atmosphere altitude, and temperature, I varied the boundary altitude to find that which gave a measured zonal wind speed of 50 m s^{-1} , *i. e.* the mean of the two extreme values. The boundary altitude always remained within 2 or 3 km of periapsis, so I conclude that this technique derives zonal wind speeds that are heavily weighted to periapsis

altitude.

This is probably due to the weighting by $1/\rho$ in Equation 3.30. The greatest contribution to changes in p , which is what is needed to fix the periapsis pressure mismatch and constrain v_ϕ , occurs when density is the highest, which is at periapsis. Altitudes where the change in latitude is greatest per unit change in altitude are also favoured. With a parabolic aerobraking pass, this again causes periapsis to have the largest effect on the derived zonal wind speed.

I then set the zonal wind speed equal to 100 m s^{-1} at periapsis and 0 m s^{-1} at the furthest latitudes. Zonal wind speed was constant in the atmosphere, except across two artificial discontinuities placed at fixed latitudes. Zonal wind speed was symmetric about periapsis latitude. Moving the boundaries close to the periapsis latitude led to a low derived zonal wind speed, moving them away from the periapsis latitude led to a high derived zonal wind speed. The boundary latitude was always about 25% of the way from periapsis to the furthest latitudes. For MGS's aerobraking passes this means that the boundary latitude intersects the parabolic profile within 2 to 3 km above periapsis.

Derived zonal wind speeds are weighted towards wind speeds at the periapsis latitude and are heavily weighted to those at the periapsis altitude.

3.8.2 MTGCM Testing

Section 3.8.1 shows that zonal wind speeds can be measured using this technique in an atmosphere that satisfies perfectly the assumptions leading to Equations 3.29 – 3.30. However, in a real atmosphere the neglected terms do not vanish and I tried to validate this technique on a more realistic atmospheric model. Since the effects of zonal winds on pressure profiles are predicted to be greatest on Mars, and since the data analysis sections of this dissertation (Chapter 4) concentrate exclusively on martian data, I wished to use a more detailed model of the martian atmosphere.

General Circulation Models include much of the physics that is neglected by imposing quasi-geostrophic balance and are more realistic depictions of the mean state of an atmosphere. I note that they are climate, not weather, models, and so actual observations contain additional noise and small-scale disturbances that cannot be included in the GCM. I planned to extract density profiles from GCM simulations representative of those from MGS aerobraking, apply this technique to measure the zonal wind speed, and compare the derived zonal wind speed to the actual zonal wind speed in the simulation. However, when I began working with the data from simulations, I found problems with the conservation of momentum. The simulations did not appear to be satisfying what I thought were the correct conservation equations, Equations 3.6 – 3.8. After some experimentation I discovered a problem with the simulations. They do not exactly conserve the horizontal components of momentum. The size of the error is comparable to the Coriolis term that I expect to retain as the only dynamical term. The reason for this problem is a simple one; the simulations, which require large quantities of supercomputing time, were not instructed to run for long enough to reach a perfect steady state. They were instructed to consider steady state reached when they were actually somewhat away from a perfect steady state. Additional simulations are in progress which will more closely approach a perfect steady state and thus have reduced errors in the momentum equations. These results are not yet available, but will be discussed in later work.

CHAPTER 4

APPLICATION OF “BALANCED ARCH” TECHNIQUE TO MGS ACCELEROMETER DATA

4.1 Introduction

I have used this technique to derive wind speeds from most of the MGS aerobraking profiles. Profiles with periapses poleward of 60° latitude or equatorward of 30° latitude were not used, as discussed in Section 3.3. As discussed by Tolson et al. (1999), there are some orbits in the ACC dataset that show unusual behaviour such as apparently constant density over significant changes in altitude. Strange phenomena of this nature may mean that the density data in this spot are bogus. If they are not bogus, then some of the assumptions that went into developing this technique are probably be invalid for that orbit, which makes the derived zonal wind speed very unrepresentative of the actual wind speeds in the atmosphere. These profiles have not been studied in great detail by anyone yet, so they probably contain lots of interesting behaviour that should cause individual orbits to be rejected. I discuss results from groups of orbits, averaging them together, so I hope that individual strange orbits do not bias the averaged results. Much work remains to be done to catalogue and understand all the small-scale phenomena in the ACC dataset.

The MGS ACC dataset is not published in the spherical polar coordinate system that I am working in. The MGS ACC PDS dataset uses altitude above a reference surface, aerocentric latitude, and aerocentric longitude as its three spatial coordinates (Keating et al., 2001a). The `altds.cat` file states that the “altitude is

above the IAU reference ellipsoid, with $a=3393.4$ km and $f=0.0052083$ and including corrections for (4,4) gravitational potential” (Keating et al., 2001a). This means that the reference surface is not actually an IAU reference ellipsoid. It is instead a fourth degree and order equipotential surface. Unfortunately, the archive does not state the coefficients that define the equipotential surface.

Such an equipotential surface is defined by a reference radius, a rotation rate, and many coefficients. Here I outline how a published set of coefficients can be related to the formula defining the surface. The total potential is the sum of gravitational and rotational potentials.

$$U = \frac{GM}{r} \left(1 + \sum_{l=2}^{l=\infty} \sum_{m=0}^{m=l} \left(\frac{r_{ref}}{r} \right)^l \bar{P}_{lm}(\cos \theta) \left(\bar{C}_{lm} \cos m\phi + \bar{S}_{lm} \sin m\phi \right) + \frac{r^3 \Omega^2 \sin^2 \theta}{2GM} \right) \quad (4.1)$$

Where \bar{P}_{lm} is the normalized associated Legendre polynomial of l th degree and m th order, \bar{C}_{lm} is the normalized tesseral harmonic coefficient of l th degree and m th order, and \bar{S}_{lm} is the normalized sectorial harmonic coefficient of l th degree and m th order. The equipotential surface $r_{ep}(\theta, \phi)$ has $U = U_{ep}$. For this equipotential surface I chose $U_{ep} = GM/r_{ref}$ and use $r_{ep} = r_{ref} + \delta r$:

$$\frac{GM}{r_{ref}} = \frac{GM}{r_{ref} + \delta r} \left(1 + \sum_{l=2}^{l=\infty} \sum_{m=0}^{m=l} \left(\frac{r_{ref}}{r_{ep}} \right)^l \bar{P}_{lm}(\cos \theta) \left(\bar{C}_{lm} \cos m\phi + \bar{S}_{lm} \sin m\phi \right) + \frac{r_{ep}^3 \Omega^2 \sin^2 \theta}{2GM} \right) \quad (4.2)$$

Since $\delta r \ll r_{ref}$:

$$\frac{\delta r}{r_{ref}} = \sum_{l=2}^{l=\infty} \sum_{m=0}^{m=l} \bar{P}_{lm}(\cos \theta) (\bar{C}_{lm} \cos m\phi + \bar{S}_{lm} \sin m\phi) + \frac{r_{ref}^3 \Omega^2 \sin^2 \theta}{2GM} \quad (4.3)$$

The normalization convention is important.

$$\bar{P}_{lm}(x) = N_{lm} P_{lm}(x) \quad (4.4)$$

Where N_{lm} is given by:

$$N_{lm} = \left((2 - \delta_{lm}) (2l + 1) \frac{(l - m)!}{(l + m)!} \right)^{1/2} \quad (4.5)$$

And $P_{lm}(x)$ is given by:

$$P_{lm}(x) = (1 - x^2)^{m/2} \frac{d^m}{dx^m} P_l(x) \quad (4.6)$$

Where $P_l(x)$ is the Legendre polynomial of l th degree and is given by:

$$P_l(x) = \frac{1}{2^l l!} \frac{d^l}{dx^l} (x^2 - 1)^l \quad (4.7)$$

This definition of $P_l(x)$ has the property that $P_l(1) = 1$. This normalization of the associated Legendre polynomials is consistent with that of Kaula (1966) and many subsequent publications. The harmonic coefficients used in the MGS ACC PDS dataset were provided to me by Bob Tolson (personal communication, 2002). The reference radius in this case was 3382.4 km. These harmonic coefficients are consistent with those in Lemoine et al. (2001) which used a reference radius of 3397 km.

To transform PDS altitudes, z , into radial distances, r , I used $r = r_{ep}(\theta, \phi) + z$. Aerocentric latitudes, l_c , were transformed into aerographic latitudes, l_g , as follows:

$$\tan(l_c) = (1 - f)^2 \tan(l_g) \quad (4.8)$$

Colatitudes, θ , are simply $90^\circ - l_c$. Aerocentric longitudes and aerographic longitudes, ϕ are identical.

The break between inbound and outbound legs where the pressure profiles are required to match is somewhat arbitrary. In deriving zonal wind speeds, I set this break at the minimum radial distance along the profile. This is not necessarily the same as the minimum altitude above the spatially varying equipotential surface nor as the minimum value of either of the two altitude scales in the PDS archive. The PDS archive has different altitude scales for 7s and 40s density averages.

In the discussions that follow, periapsis altitudes quoted for individual aerobraking passes are those taken from the PDS constant altitude dataset (Keating et al., 2001b). Where I have used periapsis altitude to select subsets of data, I also used this source for the periapsis altitude. I tend to group data by periapsis altitude, not by radial distance, because atmospheric conditions at the same altitude above the equipotential surface should be more similar than those at the same radial distance. This is because changes in gravitational potential have a greater effect on a parcel of atmosphere than mere changes in radial distance.

Formal uncertainties in zonal wind speed, as discussed in Section 3.7, are about 6 m s^{-1} for a typical aerobraking pass. These uncertainties are significantly smaller than the range in any subset of the derived zonal wind speeds from orbits which might be expected (similar latitude, longitude, altitude, *etc.*) to have the same winds. This range represents the effects of weather and the neglected terms. Accordingly, I treat the mean of a subset of derived zonal wind speeds as the

background zonal wind speed. Since the range in the data subset is much greater than any formal uncertainty on an individual zonal wind speed from one aerobraking pass, I use the unweighted mean:

$$\langle v \rangle = \frac{1}{N} \sum_{i=1}^{i=N} v_i \quad (4.9)$$

The standard deviation of the distribution of zonal wind speeds is:

$$\sqrt{\frac{1}{N-1} \sum_{i=1}^{i=N} (v_i - \langle v \rangle)^2} \quad (4.10)$$

The standard deviation of the mean of the zonal wind speeds is (Bevington, 1969):

$$\frac{1}{\sqrt{N}} \sqrt{\frac{1}{N-1} \sum_{i=1}^{i=N} (v_i - \langle v \rangle)^2} \quad (4.11)$$

I use the standard deviation of the mean to test whether two subsets of data are different. If the mean plus its standard deviation in one data subset overlaps with the mean minus its standard deviation in another data subset, then I consider the two data subsets to be indistinguishable. If they do not overlap, then I consider them to be different.

4.2 Hemispheric Averages

Due to the complicated changes in MGS's orbit, data from Phase 2 of aerobraking and dayside LSTs are best for grouping aerobraking passes with similar parameters and the chance of building up reasonable statistics on the background zonal wind

speed. I first split the derived wind speeds into the two hemispheres, northern (NH) and southern (SH).

The NH orbits have L_s of 30° to 50° , periapsis latitudes of 60° to 30°N , and LSTs of 16.7 to 15.6 hrs. Most periapsis altitudes are between 111 and 118 km, with nine higher periapses at the start of this phase of aerobraking. Longitudinal coverage is good. With 149 orbits, the mean zonal wind speed is -74 m s^{-1} with an uncertainty of 5 m s^{-1} . Note that negative wind speeds are westward, or easterly, and blow from east to west.

The SH orbits have L_s of 75° to 85° , periapsis latitudes of 30° to 60°S , and LSTs of 14.7 to 14.8 hrs. All periapsis altitudes are between 104 and 114 km, and longitudinal coverage is good. With 100 orbits, the mean zonal wind speed is 34 m s^{-1} with an uncertainty of 7 m s^{-1} . Positive wind speeds are eastward, or westerly, and blow from west to east.

The derived zonal wind speeds in the NH are almost all negative and the standard deviation of their distribution is 62 m s^{-1} . The derived zonal wind speeds in the SH are mostly positive, but there are numerous negative results, and the standard deviation of their distribution is 71 m s^{-1} .

To learn how these derived zonal wind speeds vary with latitude, altitude, and longitude in each hemisphere, I examined subsets of the data where two of those parameters could be restricted and the other allowed to vary in a controlled way. Since the ACC data collection was motivated by the desire for the spacecraft to reach its mapping orbit, and not by any desire to maximize the scientific return of this engineering instrument, I was not always able to study these trends well.

4.3 Northern Hemisphere

4.3.1 NH — Effects of Longitude

I only consider orbits from the dayside of Phase 2 aerobraking with periapsis latitudes between 30° and 45°N and periapsis altitudes between 113 and 114 km. I shall show later in Section 4.3.2 that there is no significant variation in derived zonal wind speed with latitude in this range.

Results are shown in Table 4.1. With 60° wide longitude bins, only the $60\text{--}120^\circ\text{E}$ (-145 m s^{-1}) and $180\text{--}240^\circ\text{E}$ (-75 m s^{-1}) results can be statistically distinguished from each other, and not by very much. This is not strong evidence for variations with longitude, especially in comparison to the later latitude and altitude results for the NH (Sections 4.3.2 and 4.3.3). If I expand the longitude bins to 90° wide, then there are six or more measurements in each bin and all the results are statistically indistinguishable from each other. I conclude that there is no evidence for longitudinal variation in zonal wind speed in the NH.

4.3.2 NH — Effect of Latitude

I only consider orbits from the dayside of Phase 2 aerobraking with periapsis altitudes between 113 and 114 km. As Section 4.3.1 has shown that there is no significant effect of periapsis longitude on derived zonal wind speed in the dayside Phase 2 data, I do not impose any constraints on periapsis longitude. Results are shown in Table 4.2. Using 5° wide latitude bins, I see that the derived zonal wind speed becomes less negative (slower but still westward) as periapsis latitude increases to the north. This can be seen more clearly if the data are split into just two latitude bins with the boundary at 43°N .

Lon. Range (°E)	Mean v_ϕ (m s ⁻¹)	σ of Dist. (m s ⁻¹)	σ of Mean (m s ⁻¹)	N
0–60	-74	86	43	4
60–120	-145	76	44	3
120–180	-87	39	15	7
180–240	-75	41	18	5
240–300	-67	65	46	2
300–360	-90	93	31	9
0–90	-84	71	29	6
90–180	-104	61	22	8
180–270	-72	43	16	7
270–360	-90	93	31	9

Table 4.1: NH — Effects of Longitude

Lat. Range (°N)	Mean v_ϕ (m s ⁻¹)	σ of Dist. (m s ⁻¹)	σ of Mean (m s ⁻¹)	N
30–35	-78	66	20	11
35–40	-106	69	23	9
40–45	-85	75	24	10
45–50	-43	45	18	6
30–43	-95	70	14	26
43–50	-43	39	12	10

Table 4.2: NH — Effects of Latitude

4.3.3 NH — Effect of Altitude

I only consider orbits from the dayside of Phase 2 aerobraking with periapsis latitudes between 30° and 50°N . As Section 4.3.1 has shown that there is no significant effect of periapsis longitude on derived zonal wind speed in the dayside Phase 2 data, I do not impose any constraints on periapsis longitude. Results are shown in Table 4.3. Zonal wind speed becomes more negative (the winds are faster and more westward) as altitude increases. This can be seen more clearly if the middle altitude sections are combined. The surprisingly large change in derived zonal wind speed over 5 km is discussed in Section 4.5.

4.3.4 NH — Summary

The mean zonal wind speed from the dayside of Phase 2 aerobraking is -74 m s^{-1} with an uncertainty of 5 m s^{-1} . No variation in zonal wind speed with longitude was observed, zonal wind speed became more negative as altitude increased, and zonal wind speed became less negative as latitude increased northward.

4.4 Southern Hemisphere

4.4.1 SH — Effect of Longitude

The significant change in periapsis altitude with change in periapsis latitude during this part of aerobraking prevents me from repeating the approach of Section 4.3.1 here. Instead, I study a smaller subset of data which is more suited to studying the effects of longitude, but which does not have as many orbits per longitude bin as Section 4.3.1. The orbital period of MGS decreased on each orbit due to the effects of atmospheric drag. At the start of aerobraking it was over 30 hours long, at the end of aerobraking it was less than two hours long. Whenever the orbital period was a submultiple of Mars's 24.6 hour rotational period, periapsis longitude was repeated

Alt. Range (km)	Mean v_ϕ (m s ⁻¹)	σ of Dist. (m s ⁻¹)	σ of Mean (m s ⁻¹)	N
111–112	-40	52	14	13
112–113	-73	62	13	24
113–114	-81	67	11	36
114–115	-72	68	16	18
115–116	-96	56	17	11
111–112	-40	52	14	13
112–115	-76	65	7	78
115–116	-96	56	17	11

Table 4.3: NH — Effects of Altitude

at intervals of one martian day. Changes in periapsis latitude and altitude were usually small over this interval, so orbits during this short-lived “resonance period” provide several derived zonal wind speeds at very restricted latitudes, altitudes, and longitudes.

The 8:1 resonance spans orbits 1030–1057 and periapsis latitudes of 41–49°S. Results are shown in Table 4.4. Longitude is correlated with periapsis altitude due to the orbital dynamics and shape of Mars, so there are two slightly different sets of data here — high and low. “High” orbits have periapsis altitudes of 109–110 km, and “low” orbits have periapsis altitudes of 108–109 km. The number of measurements in each longitude bin is equal to the number of periapsis altitudes in the last column of Table 4.4. I have discarded a few orbits from this resonance to make sure that each longitude bin has a range in periapsis altitude of no more than 1.2 km. Comparing derived zonal wind speeds from the 20°E and 335°E longitude bins or 245°E and 290°E longitude bins makes it clear that significant longitudinal variations exist in the SH zonal winds.

4.4.2 SH — Effect of Latitude

I only consider orbits from the dayside of Phase 2 aerobraking with periapsis latitudes between 30° and 50°S and periapsis altitudes between 108 and 110 km. If I do not impose any constraints on periapsis longitude, then there are no statistically significant changes in zonal wind speed with latitude. If I try to restrict periapsis longitude in some way and compare derived zonal wind speeds from one latitude/longitude/altitude bin to another with the same altitude and longitude, but different latitude, then it is difficult to find enough orbits to generate meaningful statistics. This is because periapsis altitude and periapsis latitude change together during this part of aerobraking. As periapsis latitude precessed towards the south pole and the atmosphere became colder and less dense, periapsis altitude was decreased by the mission operations team to maintain the same periapsis

Lon. (°E)	Mean v_ϕ (m s ⁻¹)	σ of Dist. (m s ⁻¹)	σ of Mean (m s ⁻¹)	Peri. Alts. (km)
20	-55	63	36	110.0, 109.5, 108.8 (high)
65	18	72	42	108.8, 108.3, 107.6 (low)
110	62	50	29	109.2, 108.6, 108.2 (low)
155	86	37	21	110.0, 109.4, 108.8 (high)
200	-49	35	25	110.5, 109.4 (high)
245	70	41	24	109.0, 108.5, 107.9 (low)
290	7	36	21	108.8, 108.3, 108.0 (low)
335	122	38	22	110.2, 109.7, 109.2 (high)

Table 4.4: SH — Effects of Longitude

density.

Results are shown in Table 4.5. Extreme variations with longitude are seen at 30–35°S. Two longitude bins show derived zonal wind speeds becoming more positive, with statistical significance, as latitude moves southward, and one (0–120°E) shows more negative zonal wind speed as latitude moves southward, though without statistical significance. These data hint at generally more positive zonal wind speed as periapsis latitude moves southward, but it is not able to test this hypothesis well.

4.4.3 SH — Effects of Latitude and Altitude

I only consider orbits from the dayside of Phase 2 aerobraking with periapsis latitudes between 35° and 60°S. Periapsis altitude (which ranges between 104 and 114 km) is not used to discard any orbits. Periapsis latitudes between 30° and 35°S are not considered because they do not follow the trend of periapses moving poleward and downward simultaneously. I split the remaining data into two parts by either which side of 108 km or which side of 50°S it falls on. The two splitting techniques give exactly the same results. Four longitude bins, each 90° wide, are considered. Results are shown in Table 4.6.

I show in the table the mean derived zonal wind speed \pm the standard deviation of the mean for the relevant subsets of data. Values are rounded to the nearest 10 m s⁻¹ in this table only to highlight the major trends. On each side of the split, the four longitude bins have similar means and standard deviations for altitude and latitude. Longitudinal differences cannot be caused by differences in the latitudinal or vertical distribution that was sampled by each longitudinal bin. All the longitude bins contain more than 10 data points. Derived zonal wind speeds become more positive as periapsis altitude decreases/latitude moves southward for two of the four longitude bins, but in the remaining two it stays constant. There are longitudinal differences both in the value of the derived zonal wind speed at any

Lat. Range (°S)	Mean v_ϕ (m s ⁻¹)	σ of Dist. (m s ⁻¹)	σ of Mean (m s ⁻¹)	N
30–35 (0–360°E)	20	110	33	11
40–50 (0–360°E)	47	66	13	24
30–35 (0–120°E)	99	112	56	4
30–35 (120–240°E)	-68	115	67	3
30–35 (240–360°E)	7	51	26	4
40–50 (0–120°E)	25	72	23	10
40–50 (120–240°E)	63	56	25	5
40–50 (240–360°E)	62	64	21	9

Table 4.5: SH — Effects of Latitude

Lon. Range (°E)	High and North	Low and South
0–90	0 ± 20	0 ± 20
90–180	20 ± 20	40 ± 20
180–270	0 ± 20	60 ± 20
270–360	60 ± 20	60 ± 20

Table 4.6: SH — Effects of Latitude and Altitude

given latitude and in how this value changes with latitude/altitude. This reinforces the results of Section 4.4.1 that longitude is an important factor in the SH zonal wind speeds.

This result was unexpected. Why is there such longitudinal variability in the southern, but not the northern, hemisphere? Are the longitudinal variations in derived zonal wind speed related to longitudinal variations in density?

4.4.4 SH — Summary

The mean zonal wind speed is 34 m s^{-1} with an uncertainty of 7 m s^{-1} . Extensive variation in zonal wind speed with longitude was observed. Zonal wind speeds became more positive as altitude decreased/latitude moved southward for some longitude bins, but stayed constant in others. Altitude and latitude are coupled in the data, which makes it difficult to separate their effects.

4.5 Discussion of Results

It is unfortunate that I have not been able to validate this technique on an actual dataset. With one exception, all the zonal wind speeds that I have derived above seem physically plausible. The exception is in Section 4.3.3 where the zonal wind speed doubles over a change in altitude of 5 km, less than a scale height. If this is not an accurate representation of the atmosphere, what is it? Measurements made between 111 and 112 km in this Section have very different results than those in any other 1 km wide altitude range in Table 4.3. Measurements in this altitude range are predominantly collected towards the north of the $30 - 50^\circ\text{N}$ latitude band. As was shown in Section 4.3.2, the northern third of this latitude band has quite different derived zonal wind speeds from the southern two-thirds. Section 4.3.3 may have misattributed changes due to latitude to altitude. While I have tried to mitigate that problem by careful selection of subsets of data, it is not possible to eliminate it.

Two subsets of data never have exactly the same population of latitude, longitude, and time (meaning date/time of measurement, which might be important if the weather is windy for a few days and then quiet for the next few days) to permit study of the effects of altitude without any interference from other effects.

I believe that the hemispherically averaged wind speeds are robust. They include over 100 data points in each hemisphere, which should be sufficient to smooth out variations due to longitude and altitude. Sections 4.4.1 and 4.4.3 have used two different approaches to discover that longitudinal variations are important in the southern hemisphere. My work on variations in zonal wind speed with latitude within a hemisphere, with altitude over a range less than a scale height, and with longitude in the northern hemisphere has not convinced me that any of these suggested trends are free from all interference.

4.6 Comparison to Simulations

No observations exist that can be compared to my results for the zonal wind speed in the martian upper atmosphere. Instead, I compare my results to simulations from a General Circulation Model (MTGCM) (Bougher et al., 1999).

Results from MTGCM simulations relevant for the northern hemisphere work are shown in Figure 4.1 and for the southern hemisphere work in Figure 4.2. My derived zonal wind speed of -74 m s^{-1} for the northern hemisphere between 30 and 60°N and 111 to 118 km is very different from the MTGCM value of $20 - 40 \text{ m s}^{-1}$. My derived zonal wind speed of 34 m s^{-1} for the southern hemisphere between 30 and 60°S and 104 to 114 km is also somewhat different from the MTGCM value of $60 - 100 \text{ m s}^{-1}$, but the discrepancy is less.

In both Section 4.3.2 and Figure 4.1 the zonal wind speed becomes more positive as latitude increases northward. The simulated zonal wind speed in Figure 4.1 barely changes with altitude at all. This is not consistent with the $111 - 112$

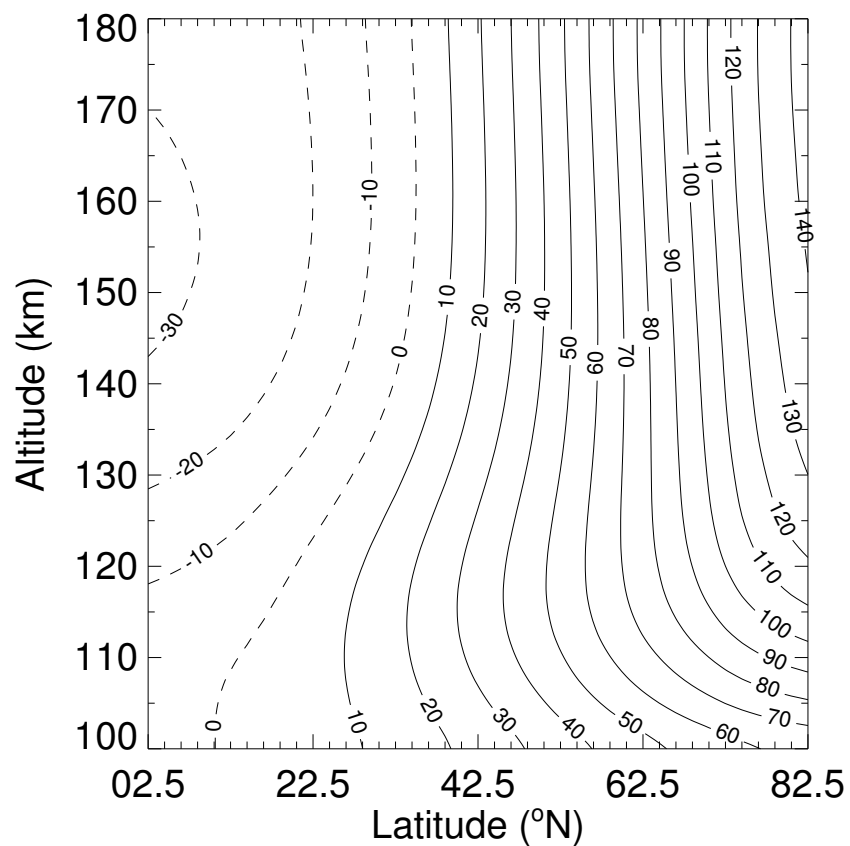


Figure 4.1: Zonal wind speed (m s^{-1}) from an MTGCM simulation relevant for $L_s = 30^{\circ}$, LST = 16 hrs. Solid contours are positive (eastward) zonal winds, dashed contours are negative (westward).

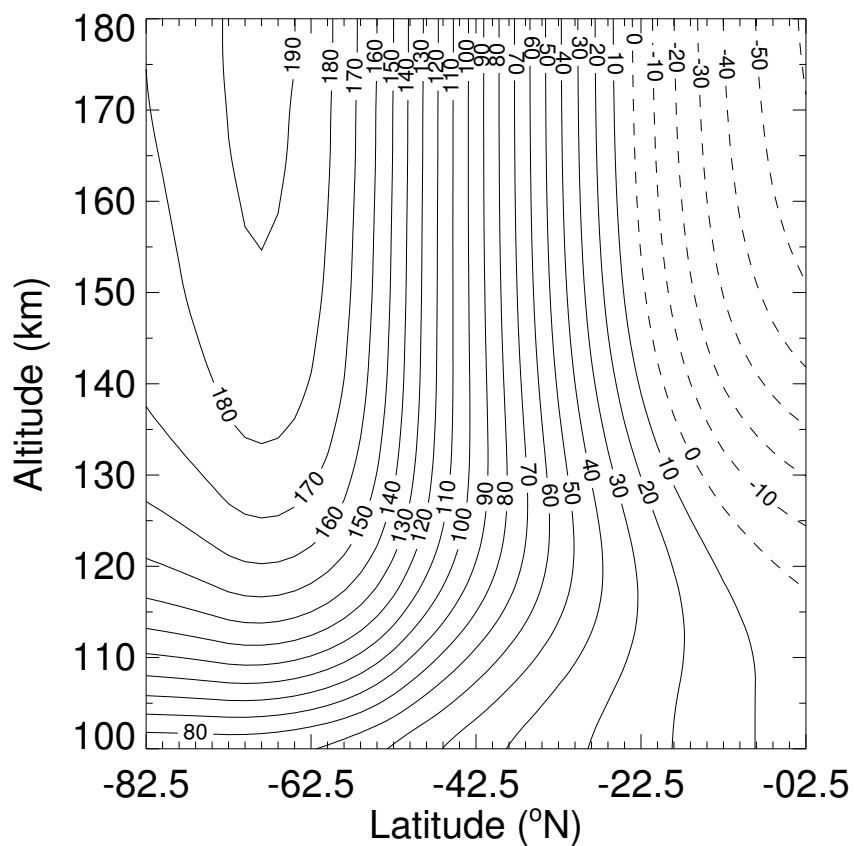


Figure 4.2: Zonal wind speed (m s^{-1}) from an MTGCM simulation relevant for $L_s = 90^{\circ}$, LST = 15 hrs. Solid contours are positive (eastward) zonal winds, dashed contours are negative (westward).

km data discussed in Section 4.3.3, but is consistent with the other altitude bins. As discussed in Section 4.5 the 111 – 112 km data may not be representative of the effects of altitude after all.

In Section 4.4.2 the data hint at the zonal wind speed becoming more positive as latitude trends southward. This is consistent with Figure 4.2. Averaged over all longitudes, Section 4.4.3 does not show any great difference between wind speeds above 108 km and north of 50°S and wind speeds below 108 km and south of 50°S. This is consistent with Figure 4.2 in which the wind speed contours slope in the correct direction to give no great change in wind speed between these two conditions.

The MTGCM simulations shown here are not capable of studying the effects of longitude since they are zonally averaged. Of the three results that I am most comfortable with from this work, one (SH longitude) cannot be compared to the MTGCM simulations, one (NH average) differs from the simulations by 100 m s⁻¹, and the other (SH average) differs from the simulations by 30 m s⁻¹. Since the wind speeds predicted in the simulations have never been compared to direct observations, it is difficult to know which is most likely to be correct. MTGCM simulations with detailed coupling to a lower atmosphere model are in progress and preliminary results show that winds are significantly affected by zonal averaging and that results are very sensitive to the atmospheric dust distribution.

4.7 Future Work

The “Balanced Arch” technique originated in my desire to derive pressure and temperature profiles from the MGS ACC data using the same techniques that have been applied to density profiles from landers and entry probes. I have shown that winds complicate this significantly. There are many assumptions that have been made to derive this technique, more than I would like. This technique needs to be applied to GCM simulations to see how robust it is. I would also like to apply it

to some real data, which include weather and other transient phenomena which are not present in the GCM. A suitable dataset from Mars is not likely to arrive in the near future. Maybe terrestrial measurements at low geomagnetic activity levels are suitable for this testing.

However, since there are so few measurements of winds in atmospheres other than Earth, uncertain results are still scientifically useful. Even something as simple as knowing which way the wind blows in the martian upper atmosphere would be valuable. I have not presented any pressure or temperature profiles here. It may be that this technique does a reasonable job of obtaining the averaged pressure profile, but erases all small-scale structure. Or the opposite might be true. Either would be useful. There is much to study in derived pressure and temperature profiles, whatever technique is used to acquire them.

The Pathfinder entry profile is closer to vertical than an MGS aerobraking pass, but it still covers 1000 km of horizontal distance during a 200 km vertical descent. It would be interesting to use the results of this work to see how much uncertainty winds introduce into these, and the Viking, results. The Galileo entry profile may also be affected by this, but its measurements of winds with the Doppler Wind Experiment might provide a way to correct any errors.

If, after further study, I find that the “Balanced Arch” technique does work well in obtaining zonal wind speeds and pressure and temperature profiles, it will be easy to extend it to derive a vertical profile of zonal wind speed between the two legs of a single aerobraking pass. In this work I have concentrated on demonstrating the simplest possible implementation of my ideas as I think it is better to validate the concept before pushing it to its formal limits.

CHAPTER 5

ANALYSIS OF ENTRY ACCELEROMETER DATA

5.1 Abstract

Accelerometers are regularly flown on atmosphere-entering spacecraft. Using their measurements, the spacecraft's trajectory and the vertical structure of density, pressure, and temperature in the atmosphere through which it descends can be calculated. I review the general procedures for trajectory and atmospheric structure reconstruction and outline them here in detail. I discuss which physical properties are important in atmospheric entry instead of working exclusively with the dimensionless numbers of fluid dynamics. Integrations of the equations of motion governing the spacecraft trajectory are carried out in a novel and general formulation. This does not require an axisymmetric gravitational field or many of the other assumptions that are present in the literature. I discuss four techniques — *head-on*, *drag-only*, *acceleration ratios*, and *gyroscopes* — for constraining spacecraft attitude, which is the critical issue in the reconstructions. The *head-on* technique uses an approximate magnitude and direction for the aerodynamic acceleration, whereas the *drag-only* technique uses the correct magnitude and an approximate direction. The *acceleration ratios* technique uses the correct magnitude and an indirect way of finding the correct direction, and the *gyroscopes* technique uses the correct magnitude and a direct way of finding the correct direction. The *head-on* and *drag-only* techniques are easy to implement and require little additional information. The *acceleration ratios* technique requires extensive and expensive aerodynamic modelling and the *gyroscopes* technique requires additional onboard instrumentation. The effects of errors are briefly addressed. My implementations of these trajectory

reconstruction procedures have been verified on the Mars Pathfinder dataset. I find inconsistencies within the published work of the Pathfinder science team, and even in the PDS archive itself, relating to the entry state of the spacecraft. My atmospheric structure reconstruction, which uses only a simple aerodynamic database, is consistent with the PDS archive to about 4%. Surprisingly accurate profiles of atmospheric temperatures can be derived without needing any information about the spacecraft aerodynamics. Using no aerodynamic information whatsoever about Pathfinder, my profile of atmospheric temperature is still consistent with the PDS archive to about 8%. As a service to the community, I have placed simplified versions of my trajectory and atmospheric structure computer programmes online for public use.

5.2 Introduction

5.2.1 Uses of Accelerometers in Spaceflight

An accelerometer instrument measures the linear, as opposed to angular, accelerations experienced by a test mass. When rigidly mounted inside a spacecraft and flown into space, an accelerometer instrument measures aerodynamic forces and additional contributions from any spacecraft thruster activity or angular motion of the test mass about the spacecraft's centre of mass (Tolson et al., 1999). The gravitational force acting on the spacecraft's centre of mass cannot be detected by measurements made in a frame fixed with respect to the spacecraft, since the spacecraft, accelerometer instrument, and test mass are all free-falling at the same rate. In practice, three dimensional acceleration measurements are synthesized from three orthogonal one dimensional acceleration measurements, each measured by a different instrument with inevitably slightly different properties. Instrument biases, sampling rates, digitization errors, and so on also affect the accelerometer measurement.

When a spacecraft passes through the atmosphere of a planetary body, it experiences aerodynamic forces in addition to gravity. These forces affect the spacecraft's trajectory. The gravitational acceleration is usually known as a function solely of position from a pre-existing gravity model for the planetary body. In the absence of an atmosphere, the spacecraft trajectory can be calculated accurately from that alone. However, the presence of an atmosphere and consequent aerodynamic forces cause the spacecraft's trajectory to differ from the gravity-only case. Additional measurements are needed to define accurately the spacecraft's trajectory. Onboard accelerometer measurements of the aerodynamic acceleration of the spacecraft can be combined with the gravity model to give the total acceleration experienced by the spacecraft. The equations of motion can then be integrated to reveal the spacecraft's modified trajectory.

If the spacecraft is merely passing, or aerobraking, through a planetary atmosphere, then the accelerometer measurements can be analysed later, upon transmission to Earth, for the trajectory analysis and to reveal properties of the atmosphere (Tolson et al., 1999). If the spacecraft is actively reacting to the forces acting on it to reach a desired orbit, such as some aerocapture scenarios, then the accelerometer data must be used in real-time onboard the spacecraft (Wercinski and Lyne, 1994). If the spacecraft is a planetary lander or entry probe approaching the surface or interior of the planetary body and needs to prepare for landing or deploy sensors intended for lower atmosphere use only, then the accelerometer data can also be used in real-time onboard the spacecraft (Tu et al., 2000). The accelerometer data are not absolutely necessary for this; if there is sufficient confidence in a model of the planetary atmosphere, a timer-based approach can be used instead. However, this is rarely used due to the increased risk.

An atmosphere-entering spacecraft must carry an accelerometer for its trajectory to be known and, for landers and entry probes, to control its entry, descent, and possible landing, although radar altimetry and other techniques can also control parts of the entry. These are the operational uses of accelerometer data. Scientific

uses are also important.

5.2.2 Fluid Dynamics and Atmospheric Entry

The forces and torques acting on a rigid body, such as a spacecraft, traversing a fluid region, such as an atmosphere, are, in principle, completely constrained given the size, shape, and mass of the rigid body, its orientation, the far-field speed of the fluid with respect to the rigid body, the composition of the fluid, and the thermodynamic state of the fluid (Landau and Lifshitz, 1959; Landau and Lifshitz, 1969a; Landau and Lifshitz, 1969b). Specifying the thermodynamic state of a fluid requires two intensive thermodynamic variables, such as density and pressure. As an inverse problem, knowledge of the forces and torques acting on a rigid body, physical characteristics of the rigid body, flow velocity, and fluid composition is just one relationship short of completely constraining the thermodynamic state of the fluid.

When a spacecraft is much smaller than the volume of the atmosphere, its passage has no effect on atmospheric bulk properties. The atmosphere continues to obey the same laws of conservation of mass, momentum, and energy that it did prior to the arrival of the spacecraft. Conservation of momentum in a gravitational field provides a relationship between the fluid density and pressure (Landau and Lifshitz, 1959). This additional relationship supplies the needed final constraint.

Measurements of the aerodynamic forces and torques acting on a spacecraft can uniquely define both the atmospheric density and pressure along the spacecraft trajectory. Using an appropriate equation of state reveals the corresponding atmospheric temperature. Linear and angular acceleration measurements can be converted into forces and torques using the known spacecraft mass and moments of inertia.

Practical application, with the appropriate equations, of this abstract physical reasoning follows later. For now it is enough that I demonstrate that a unique

solution exists. Accelerometer data can define profiles of atmospheric density, pressure, and temperature along the spacecraft trajectory, *provided* the aerodynamic properties of the spacecraft are known sufficiently well. These profiles are of great utility to atmospheric scientists.

5.2.3 Flight Heritage

Accelerometers have successfully flown on the following entry probes/landers: PAET (Planetary Atmosphere Experiments Test vehicle), Mars 6, both Viking landers, the 4 Pioneer Venus probes, Veneras 8–14, the Space Shuttle, the Galileo probe, and Mars Pathfinder (Seiff et al., 1973; Kerzhanovich, 1977; Seiff and Kirk, 1977a; Seiff et al., 1980; Avduevskii et al., 1983; Avduevskii et al., 1983; Blanchard et al., 1989; Seiff et al., 1998; Magalhães et al., 1999). Accelerometers have successfully been used in the aerobraking of Atmosphere Explorer-C and its successors on Earth, Mars Global Surveyor, and Mars Odyssey (Marcos et al., 1977; Keating et al., 1998). Atmospheric drag at Venus was studied without using accelerometers on both Pioneer Venus Orbiter and Magellan (Strangeway, 1993; Croom and Tolson, 1994). Failed planetary missions involving accelerometers include Mars 7, Mars 96, Mars Polar Lander, Deep Space 2, and Mars Climate Orbiter. Upcoming missions involving accelerometers include Beagle 2 and NASA’s Mars Exploration Rovers for the 2003 Mars launch opportunity, and Huygens, currently on its way to Titan (Lebreton et al., 1994; Sims et al., 1999; Squyres, 2001).

5.3 Equations of Motion

5.3.1 Previous Work

The aim of the trajectory integration is to reconstruct the spacecraft’s position and velocity as a function of time. Although it is easy to understand the concept of trajectory integration as “sum measured aerodynamic accelerations and known

gravitational accelerations, then integrate forward from known initial position and velocity” it is more challenging to actually perform the integrations. The primary complications are that aerodynamic accelerations are measured in the frame of the spacecraft, but the equations of motion are simplest in an inertial frame and the final trajectory is most usefully expressed in a rotating frame fixed to the surface of the planetary body.

Many of the publications in this field provide specific equations for the trajectory reconstruction as applied to their work. Of these, most neglect planetary rotation or include only the radial component of the gravitational field (Seiff, 1963; Peterson, 1965b; Peterson, 1965a; Sommer and Yee, 1969; Seiff et al., 1973). Both of these assumptions are sometimes valid, but I wish to describe a general technique for performing the trajectory integrations. Individual cases can then be examined for terms which can be neglected. The trajectory reconstruction work for the Viking landers includes only the radial component of the gravitational field (Seiff and Kirk, 1977a), whereas the trajectory reconstruction work for the Pioneer Venus probes does not provide specific equations (Seiff et al., 1980). Galileo probe trajectory reconstruction introduced the concept of changing frames between each integration step to remove the Coriolis and centrifugal forces (Seiff et al., 1998). The trajectory reconstruction integration for Pathfinder was performed in a planet-centred spherical coordinate system rotating with the planet (Magalhães et al., 1999).

5.3.2 Alternative Formulation

I have elected not to perform the trajectory integration in the rotating, planet-fixed frame. Instead, I perform the integrations in an inertial frame. To express the trajectory in a rotating, planet-fixed frame, I followed the work of the Galileo trajectory reconstruction and used different intermediate frames at each timestep (Seiff et al., 1998). These intermediate frames are instantaneously coincident with a rotating, planet-fixed frame at the relevant point in time. Since the integrations of

the equations of motion are being performed in an inertial frame, there is no need for the Coriolis or centrifugal forces. Vector positions, velocities, and accelerations can be transformed between frames with standard techniques. These frame transformations do not require the Coriolis or centrifugal forces either. This formulation does not encourage an analytical solution, but this is not a great loss since any realistic trajectory integration will be performed numerically. Thus I introduce two sets of reference frames, *inertial* and *momentary*, in both *Cartesian* and *spherical* polar coordinate systems. The subscripts *inert* and *mom* are used to label these.

5.3.3 Inertial Cartesian and Spherical Frames

A righthanded Cartesian coordinate system is defined with an origin at the centre of mass of a planet and z-axis aligned with the planetary rotation axis, with the positive x-axis to pass through the rotating planet's zero east longitude line at time $t = 0$. The y-axis completes a righthanded set. This is the *inertial Cartesian frame*. One can then construct the usual spherical polar coordinate system about this set. This is the *inertial spherical frame*. Most introductory mechanics or applied mathematics textbooks, such as Arfken and Weber (1995), have diagrams of these frames and their coordinates.

5.3.4 Momentary Cartesian and Spherical Frames

The position vector is \underline{r} . I use the magnitude of \underline{r} , r_{mom} , a colatitude referenced to the surface of the planet, θ_{mom} , and an east longitude referenced to the surface of the planet, ϕ_{mom} , as a spherical coordinate frame. At any time t , it is non-rotating and transformations between it and the *inertial Cartesian frame* do not need to consider fictitious Coriolis and centrifugal forces. An instant later, as the planet has rotated slightly, this frame is removed and redefined so that colatitudes and east longitudes once again match up with surface features. It is not a rotating frame, it only exists for an instant, and so only instantaneous transformations between it

and other frames can be made. No integration with time can be done in this frame because it does not exist for the duration of a timestep. This is the *momentary spherical frame*.

One can then use the *momentary spherical frame* to construct a Cartesian coordinate system with the usual conventions. This also only exists for an instant and no integration with time can be done in this frame. This is the *momentary Cartesian frame*.

5.3.5 Transformations between Frames

There are many different conventions for defining latitude and east longitude on the surface of a planet. Geographic, geodetic, and geocentric are some of the more well-known ones that are applied to the Earth (Lang, 1999). I shall assume that all latitudes and east longitudes referenced to the surface of the planet are in a planetocentric system. I use the east-positive planetocentric system for mathematical convenience, as was used for Galileo, Mars Global Surveyor, and Pathfinder. Care must be taken when comparing data to older planetary data products which may use a west-positive planetographic system.

Consider an arbitrary vector \underline{B} :

$$\underline{B} = B_x \hat{x} + B_y \hat{y} + B_z \hat{z} = B_r \hat{r} + B_\theta \hat{\theta} + B_\phi \hat{\phi} \quad (5.1)$$

Unit vectors are indicated by carets and subscripts indicate the direction of vector components. Expressions for the unit vectors of one frame in terms of the other frame's unit vectors are needed to transform between *spherical* and *Cartesian* frames. These are given in, for example, Chapter 2 of Arfken and Weber (1995). These apply to transformations between the two *momentary* frames and transformations between the two *inertial* frames. Finally, I need a transformation for \underline{B} between the *momentary* and *inertial* frames.

The *momentary Cartesian* and *inertial Cartesian* frames are related as follows:

$$\hat{x}_{inert} = \hat{x}_{mom} \cos(\omega t) - \hat{y}_{mom} \sin(\omega t) \quad (5.2)$$

$$\hat{y}_{inert} = \hat{x}_{mom} \sin(\omega t) + \hat{y}_{mom} \cos(\omega t) \quad (5.3)$$

$$\hat{z}_{inert} = \hat{z}_{mom} \quad (5.4)$$

Where ω is the planetary rotation rate. It is now possible to transform any vector quantity, such as a position, velocity, or acceleration, between all four frames. I have assumed that the centre of mass of the planet is at rest in some inertial frame. Its motion around the Sun and other motions, such as the motion of the solar system, are neglected. The resultant error is small and can easily be quantified.

5.3.6 Solution Procedure for the Gravity-only Case

In an *inertial* frame, the equations of motion of the centre of mass of a rigid body, the spacecraft, are:

$$\dot{\underline{r}} = \underline{v} \quad (5.5)$$

$$\dot{\underline{v}} = \underline{a} \quad (5.6)$$

Where \underline{v} is velocity and \underline{a} is acceleration. If the only force acting on the centre of mass of the rigid body is gravity due to the nearby planet, then:

$$\underline{a} = \underline{g}(\underline{r}) = \underline{\nabla}U(\underline{r}) \quad (5.7)$$

Where $\underline{g}(\underline{r})$ is the gravitational acceleration and $U(\underline{r})$ is the gravitational potential. $\underline{g}(\underline{r})$ does not include any centrifugal component since I am working in an inertial frame. Here I expand $U(\underline{r})$ only to second degree and order (Smith et al., 1993). C_{20} is the tesseral normalized spherical harmonic coefficient of degree 2 and order 0. $P_{20}(x)$ is the normalized associated Legendre function of degree 2 and order 0. It is proportional to $3x^2 - 1$. There are many conventions for spherical harmonic expansions. I use that of Lemoine et al. (2001) which follows Kaula (1966) in that $P_{20}(1) = \sqrt{5}$. The normalization convention for C_{20} must be consistent with that for $P_{20}(x)$.

$$U(\underline{r}) = \frac{GM}{r_{mom}} \left(1 + \left(\frac{r_{ref}}{r_{mom}} \right)^2 P_{20}(\cos \theta_{mom}) C_{20} \right) \quad (5.8)$$

Where GM is the product of the gravitational constant and the mass of the planet and r_{ref} is a reference radius. Substituting in for P_{20} , Equation 5.8 becomes:

$$\begin{aligned} \underline{g}(\underline{r}) = & \frac{-GM}{r_{mom}^2} \left(1 + \frac{3}{2} \sqrt{5} \left(\frac{r_{ref}}{r_{mom}} \right)^2 (3 \cos^2 \theta_{mom} - 1) C_{20} \right) \hat{r}_{mom} \\ & - \frac{GM}{r_{mom}^2} \left(\frac{r_{ref}}{r_{mom}} \right)^2 \frac{1}{2} \sqrt{5} (6 \cos \theta_{mom} \sin \theta_{mom}) C_{20} \hat{\theta}_{mom} \end{aligned} \quad (5.9)$$

Given the coefficients of the gravitational field and an initial position and velocity, the trajectory integration is straight-forward. I describe it below to illustrate the techniques that are used in the more complicated cases that follow.

Schematically, this trajectory reconstruction procedure can be expressed as:

Begin with $t, x_{inert}, y_{inert}, z_{inert}, v_{x,inert}, v_{y,inert}, v_{z,inert}$.

Start loop.

$$x_{inert}, y_{inert}, z_{inert} \rightarrow r_{mom}, \theta_{mom}, \phi_{mom} \quad (5.10)$$

$$r_{mom}, \theta_{mom}, \phi_{mom} \rightarrow g_{r,mom}, g_{\theta,mom}, g_{\phi,mom} \quad (5.11)$$

$$g_{r,mom}, g_{\theta,mom}, g_{\phi,mom} \rightarrow g_{x,inert}, g_{y,inert}, g_{z,inert} \quad (5.12)$$

$$dx_{inert} = v_{x,inert}dt, dy_{inert} = v_{y,inert}dt, dz_{inert} = v_{z,inert}dt \quad (5.13)$$

$$dv_{x,inert} = g_{x,inert}dt, dv_{y,inert} = g_{y,inert}dt, dv_{z,inert} = g_{z,inert}dt \quad (5.14)$$

Is $|r_{inert}| < \text{Planetary Radius}$?

Either stop or loop again.

The gravitational field is axisymmetric when truncated at second degree and order. In this case, gravitational accelerations in either of the inertial frames are functions of position only and can be found without needing to use the *momentary spherical* frame. If the gravitational field is not axisymmetric, then the gravitational effects of mass concentrations rotate with the planet and gravitational accelerations in either of the inertial frames are functions of position and time. This technique, which is designed to be as general as possible, permits the use of non-axisymmetric gravitational fields. If only axisymmetric fields are to be considered, then the technique could be simplified.

To include aerodynamic accelerations, this procedure is adapted to incorporate the transformation of aerodynamic acceleration from the frame of original measurements, which is fixed with respect to the spacecraft, to the *inertial Cartesian* frame.

5.3.7 The Spacecraft Frame

Suppose that the accelerometer, which is rigidly mounted within the spacecraft, measures the linear accelerations of the spacecraft's centre of mass in three orthogonal directions. I define a fifth and final frame consisting of right-handed Cartesian axes along these three orthogonal directions. This is the *spacecraft frame*. I label it with the subscript *sct*.

The axis most nearly parallel to the flow velocity during atmospheric entry is conventionally chosen as the z_{sct} axis. For axisymmetric spacecraft, such as those with blunted cone shapes, this axis is also usually the axis of symmetry.

The orientation of the *spacecraft* frame, or spacecraft attitude, with respect to any of the other frames I have discussed so far is not fixed or necessarily known. The transformation of acceleration measurements between this frame and any of the other frames is the main complication to be addressed in Section 5.4. First I assume that an as-yet-undefined *attitude tracking function* exists that transforms the measured acceleration components $a_{aero,x,sct}$, $a_{aero,y,sct}$, $a_{aero,z,sct}$ into the *inertial Cartesian* frame, $a_{aero,x,inert}$, $a_{aero,y,inert}$, $a_{aero,z,inert}$, where I use the subscript *aero* to indicate effects due to aerodynamics. I then outline the solution procedure using this function. Finally I discuss different ways of generating this *attitude tracking function* explicitly.

5.4 The Effects of an Atmosphere on Trajectory Reconstructions

5.4.1 Addition of Aerodynamics to the Solution Procedure

The trajectory reconstruction procedure from Section 5.3.6 is modified to include an additional calculation (Equation 5.19) which transforms the linear accelerations of the spacecraft's centre of mass due to aerodynamic forces from the *spacecraft* frame to the *inertial Cartesian* frame, using the *attitude tracking function*, and to include these accelerations in the integration step.

Schematically, this trajectory reconstruction procedure can be expressed as:

Begin with $t, x_{inert}, y_{inert}, z_{inert}, v_{x,inert}, v_{y,inert}, v_{z,inert}$.

Start loop.

$$x_{inert}, y_{inert}, z_{inert} \rightarrow r_{mom}, \theta_{mom}, \phi_{mom} \quad (5.15)$$

$$r_{mom}, \theta_{mom}, \phi_{mom} \rightarrow g_{r,mom}, g_{\theta,mom}, g_{\phi,mom} \quad (5.16)$$

$$g_{r,mom}, g_{\theta,mom}, g_{\phi,mom} \rightarrow g_{x,inert}, g_{y,inert}, g_{z,inert} \quad (5.17)$$

$$dx_{inert} = v_{x,inert}dt, dy_{inert} = v_{y,inert}dt, dz_{inert} = v_{z,inert}dt \quad (5.18)$$

$$a_{aero,x,sct}, a_{aero,y,sct}, a_{aero,z,sct} \rightarrow a_{aero,x,inert}, a_{aero,y,inert}, a_{aero,z,inert} \quad (5.19)$$

$$\begin{aligned}
dv_{x,inert} &= (g_{x,inert} + a_{aero,x,inert}) dt \\
dv_{y,inert} &= (g_{y,inert} + a_{aero,y,inert}) dt \\
dv_{z,inert} &= (g_{z,inert} + a_{aero,z,inert}) dt
\end{aligned} \tag{5.20}$$

Is $|r_{inert}| < \text{Planetary Radius}$?

Either stop or loop again.

The key to implementing the above approach successfully is constraining the attitude of the spacecraft. I discuss four options that can be used — head-on, drag-only, acceleration ratios, and gyroscopes. One of these four will be applicable to the vast majority of cases, but other options may exist.

5.4.2 The *Head-on* Option for Constraining Spacecraft Attitude

This option assumes that the spacecraft aerodynamics and attitude during atmospheric entry are such that all aerodynamic forces acting on the spacecraft's centre of mass are directed along one of the axes, which I call the major axis, of the *spacecraft frame* **and also** parallel to the flow velocity. The magnitude of the aerodynamic acceleration is assumed to be that of the acceleration along the major axis. Acceleration measurements along the other two minor axes are ignored, regardless of their importance. The direction of the aerodynamic acceleration is assumed to be parallel to the known flow velocity. This is considered reasonable since spacecraft with a blunted cone shape are usually approximately axisymmetric, with the axis of symmetry being roughly parallel to both the flow velocity and the major *spacecraft frame* axis, conventionally the z-axis. Galileo used this option (Seiff et al., 1998). In neglecting acceleration measurements from the two other minor axes I assume that they contain nothing but noise, which is a source of error. Since the spacecraft is unlikely to align itself precisely along the flow velocity at all times, the direction in which the acceleration is assumed to act is not precisely correct and this is another

source of error. The flow velocity is the relative velocity of the fluid with respect to the spacecraft in an inertial frame and I use the subscript *rel* to label this. The atmosphere is assumed to rotate with the same angular velocity, ω , as the planet. I label the velocity of the atmosphere with the subscript *wind*.

The *attitude tracking* step of the trajectory reconstruction for the *Head-On* option can be expressed schematically as:

$$\underline{v_{wind,inert}} = \omega \hat{z}_{inert} \times \underline{r} \quad (5.21)$$

$$\underline{v_{rel,inert}} = \underline{v_{inert}} - \underline{v_{wind,inert}} \quad (5.22)$$

$$|\underline{v_{rel}}| = \left(v_{rel,x,inert}^2 + v_{rel,y,inert}^2 + v_{rel,z,inert}^2 \right)^{1/2} \quad (5.23)$$

$$|a_{aero}| = \left(a_{aero,z,sct}^2 \right)^{1/2} \quad (5.24)$$

$$\underline{a_{aero,inert}} = -1 \times \frac{|a_{aero}|}{|\underline{v_{rel}}|} \underline{v_{rel,inert}} \quad (5.25)$$

5.4.3 The *Drag-only* Option for Constraining Spacecraft Attitude

This option assumes that the spacecraft aerodynamics and attitude during atmospheric entry are such that all aerodynamic forces acting on the spacecraft's centre of mass are directed parallel to the flow velocity. The square root of the sum of the

squares of the three orthogonal acceleration measurements in the *spacecraft frame* is the magnitude of the total aerodynamic acceleration. The direction of this acceleration is assumed to be parallel to the known direction of the flow velocity. This is very similar to the *head-on* option. The difference is that the *head-on* option uses only the major axis acceleration measurement in the *spacecraft frame*, whereas this *drag-only* option uses all three orthogonal acceleration measurements. This option assumes that there are no aerodynamic forces, called lift forces or side forces, acting orthogonal to the flow velocity. Aerodynamic drag forces always act parallel to the flow velocity. If the two minor axis acceleration measurements are predominantly due to noise and rotational effects, then it is not useful to use them to reconstruct the spacecraft's trajectory and the *head-on* option is better than the *drag-only* option. If, on the other hand, the spacecraft is usually several degrees away from being head-on to the flow, then these two minor axis acceleration measurements are sensitive to those components of the aerodynamic acceleration along the flow vector that are not parallel to the major axis of the spacecraft frame. In this case, the *drag-only* option is better than the *head-on* option because it includes these accelerations in the trajectory reconstruction. The *drag-only* option works well if the spacecraft aerodynamics are designed to minimize aerodynamic forces perpendicular to the flow velocity. One example of a class of objects which works well with this option is a sphere. Aeroplanes, which use their wings to generate lift, would be very badly modelled with this approach.

The *attitude tracking* step of the trajectory reconstruction for the *Drag-Only* option can be expressed schematically as:

$$\underline{v_{wind,inert}} = \omega \hat{z}_{inert} \times \underline{r} \quad (5.26)$$

$$\underline{v_{rel,inert}} = \underline{v_{inert}} - \underline{v_{wind,inert}} \quad (5.27)$$

$$\left| \underline{v}_{rel} \right| = \left(v_{rel,x,inert}^2 + v_{rel,y,inert}^2 + v_{rel,z,inert}^2 \right)^{1/2} \quad (5.28)$$

$$\left| \underline{a}_{aero} \right| = \left(a_{aero,x,sct}^2 + a_{aero,y,sct}^2 + a_{aero,z,sct}^2 \right)^{1/2} \quad (5.29)$$

$$\underline{a}_{aero,inert} = -1 \times \frac{\left| \underline{a}_{aero} \right|}{\left| \underline{v}_{rel} \right|} \underline{v}_{rel,inert} \quad (5.30)$$

5.4.4 The *Acceleration Ratios* Option for Constraining Spacecraft Attitude

If the aerodynamic properties of the spacecraft are well-constrained and not a singular case, then the ratio of linear accelerations along any pair of *spacecraft frame* axes uniquely defines one of the two angles necessary to define the spacecraft attitude with respect to the flow velocity (Peterson, 1965b). Forming a second ratio of linear accelerations along a different pair of *spacecraft frame* axes uniquely defines the second and final angle. PAET used this option (Seiff et al., 1973). As in the *drag-only* option, the square root of the sum of the squares of the three orthogonal acceleration measurements in the *spacecraft frame* is the magnitude of the total aerodynamic acceleration. Unlike the *drag-only* option, the direction of the aerodynamic acceleration is known since the spacecraft attitude is known, rather than it being assumed to be parallel to the flow velocity.

The *acceleration ratios* option offers an unexpectedly elegant way to constrain spacecraft attitude indirectly (Peterson, 1965b). For a known fluid composition and thermodynamic state, an axisymmetric spacecraft of known mass, size, and shape, and a known fluid speed with respect to the spacecraft, only the angle between the spacecraft symmetry axis and the flow direction is needed to constrain completely the forces acting parallel to and perpendicular to the symmetry axis

of the spacecraft. The thermodynamic state is defined by pressure and temperature or any other pair of intensive thermodynamic variables. Numerical modelling and wind-tunnel experiments can generate an expression for the parallel force as a function of this angle and a similar expression for the perpendicular force. The ratio of these two forces, equal to the measurable ratio of accelerations, can also be expressed as a function of this angle. If this function is single-valued, then it can be inverted into an expression for spacecraft attitude angle as a function of acceleration ratio. The ratio of linear accelerations measured in the spacecraft frame can uniquely define the attitude of the spacecraft. Extension to asymmetric spacecraft is simple, involving the $a_{aero,x,sct}/a_{aero,z,sct}$ and $a_{aero,y,sct}/a_{aero,z,sct}$ acceleration ratios constraining the two angles necessary to define spacecraft attitude relative to the velocity vector of the fluid. Note that only two angles, rather than the traditional three Euler angles, are required to completely define the orientation of a rigid body since a third piece of directional information is supplied by the velocity vector of the fluid. Once the two angles are known, they and the direction of $\underline{v_{rel,inert}}$ are sufficient information to completely define the orientation of the *spacecraft frame* relative to the *inertial Cartesian* frame. The aerodynamic accelerations can then be transformed from the *spacecraft frame* to the *inertial Cartesian* frame. The details of the transformation depend on the definition of the two angles and may be worked out using a text on the motions of a rigid body and relevant coordinate transformations, such as Goldstein (1980).

The requirement for the acceleration ratios to be “well-behaved” functions of spacecraft attitude is usually satisfied. However, the *acceleration ratios* option requires knowledge of the atmospheric density, pressure, and temperature as the trajectory reconstruction is being carried out, whereas the other options separate the trajectory and atmospheric structure reconstruction processes completely. This option also requires a comprehensive knowledge of the spacecraft aerodynamics as a function of atmospheric pressure and temperature and spacecraft attitude. The other options do not require this information until the atmospheric structure reconstruction.

In some cases, the x, y, and z-axis accelerations and the spacecraft aerodynamics might not all be known accurately enough to provide very useful constraints on spacecraft attitude. A simpler option, such as the *head-on* or *drag-only* options, might be all that is justified.

The aerodynamic database needed for the *acceleration ratios* option must contain the values of the $a_{aero,x,sct}/a_{aero,z,sct}$ and $a_{aero,y,sct}/a_{aero,z,sct}$ acceleration ratios for all possible values of fluid composition, pressure, temperature, speed with respect to the spacecraft, and the two angles, α, β , necessary to define spacecraft attitude. α and β must be clearly defined relative to the orientation of the velocity vector in the spacecraft frame and Peterson (1965b) offers one convention.

Since the aerodynamic properties of the spacecraft vary with atmospheric pressure, p , and temperature, T , assumed profiles of atmospheric pressure and temperature must be used in the trajectory reconstruction. After the trajectory reconstruction is completed profiles of atmospheric pressure and temperature are derived using the reconstructed trajectory. If these profiles derived using the results of the trajectory reconstruction are not the same as the assumed profiles that went into the trajectory reconstruction, then the process is inconsistent. The trajectory reconstruction should be repeated using these derived profiles in place of the assumed profiles and then the atmospheric structure reconstruction should be repeated using the updated trajectory. This process should be iterated until the assumed profiles used in the trajectory reconstruction match the profiles derived from the subsequent atmospheric structure reconstruction. Only a small number of iterations is usually needed (Magalhães et al., 1999).

The *attitude tracking* step of the trajectory reconstruction for the *Acceleration Ratios* option can be expressed schematically as:

$$\underline{v_{wind,inert}} = \omega_{\hat{z}_{inert}} \times \underline{r} \quad (5.31)$$

$$\underline{v_{rel,inert}} = \underline{v_{inert}} - \underline{v_{wind,inert}} \quad (5.32)$$

$$composition, p, T, |\underline{v_{rel}}| \rightarrow \frac{a_{aero,x,sct}}{a_{aero,z,sct}}(\alpha, \beta), \frac{a_{aero,y,sct}}{a_{aero,z,sct}}(\alpha, \beta) \quad (5.33)$$

$$\begin{aligned} & \frac{a_{aero,x,sct}}{a_{aero,z,sct}}(\alpha, \beta), \frac{a_{aero,y,sct}}{a_{aero,z,sct}}(\alpha, \beta) \rightarrow \\ & \alpha \left(\frac{a_{aero,x,sct}}{a_{aero,z,sct}}, \frac{a_{aero,y,sct}}{a_{aero,z,sct}} \right), \beta \left(\frac{a_{aero,x,sct}}{a_{aero,z,sct}}, \frac{a_{aero,y,sct}}{a_{aero,z,sct}} \right) \end{aligned} \quad (5.34)$$

$$\alpha, \beta, \underline{v_{rel,inert}}, \underline{a_{aero,sct}} \rightarrow \underline{a_{aero,inert}} \quad (5.35)$$

5.4.5 The *Gyroscopes* Option for Constraining Spacecraft Attitude

Gyroscopes measure the angular acceleration of the *spacecraft frame* about its centre of mass. These additional measurements are incorporated into the equations of motion for a rigid body, which then yield spacecraft position, velocity, attitude, and angular velocity all along the trajectory. An initial angular position and velocity, possibly provided by star tracking, are required as initial conditions. Viking used this option (Seiff and Kirk, 1977a). As in the *acceleration ratios* option, the square root of the sum of the squares of the three orthogonal acceleration measurements in the *spacecraft frame* is the magnitude of the total aerodynamic acceleration. Unlike the *acceleration ratios* option, spacecraft attitude, which gives the direction of the aerodynamic acceleration in a useful frame, is tracked directly, rather than being inferred from measured acceleration ratios and an aerodynamic database. The *gyroscopes* option is, in principle, the best of the four. However, the additional

instruments required by this option need money, mass, and volume that might not be available. For spacecraft that satisfy any of the first three options, gyroscopes are a redundant luxury for trajectory and atmospheric structure reconstruction. However, operational requirements to monitor the engineering performance of the spacecraft might justify that redundancy.

This is more complicated than simply inserting a subroutine into the pre-existing algorithm, so I outline the entire algorithm. The relationship between the *spacecraft frame* and the *inertial Cartesian* frame can be described using Euler angles. These three angles provide sufficient information to transform acceleration measurements made in the *spacecraft frame* into the *inertial Cartesian* frame. There are many arbitrary conventions concerning Euler angles. Here I use the xyz-convention from page 608 of Goldstein (1980) in which Goldstein's unprimed coordinate system is the *inertial Cartesian* frame and Goldstein's primed coordinate system is the *spacecraft frame*. This choice allows rates of change of the Euler angles to be expressed in terms of the Euler angles and angular velocities in the *spacecraft frame*, which simplifies my integrations. In actual calculations quaternions may be preferred because Euler angles can be indeterminate for certain attitudes — just as the east longitude of the north pole is indeterminate. I present Euler angles here because the formulation is relatively simple.

The Euler matrix in the xyz-convention, \underline{EM} , is constructed from the Euler angles as described in Goldstein (1980) and enables the conversion of vectors between the *inertial Cartesian* (unprimed) frame and the *spacecraft* (primed) frame.

$$\underline{B}' = \underline{EM} \underline{B} \quad (5.36)$$

Where \underline{B} is an arbitrary vector. I expand the initial condition to include the three Euler angles, ϕ_{Euler} , ψ_{Euler} , θ_{Euler} and the angular velocity of the spacecraft, Ω , about its axes at the appropriate time. For example, the angular velocity might be a predetermined spin. The Euler angles change with time due to the rotation

of the spacecraft about its axes. Rearrangement of Goldstein's equations B-14xyz gives:

$$\dot{\phi}_{Euler} = \frac{\Omega_{y,sct} \sin \psi_{Euler} + \Omega_{z,sct} \cos \psi_{Euler}}{\cos \theta_{Euler}} \quad (5.37)$$

$$\dot{\psi}_{Euler} = \Omega_{x,sct} + \tan \theta_{Euler} \times (\Omega_{y,sct} \sin \psi_{Euler} + \Omega_{z,sct} \cos \psi_{Euler}) \quad (5.38)$$

$$\dot{\theta}_{Euler} = \Omega_{y,sct} \cos \psi_{Euler} - \Omega_{z,sct} \sin \psi_{Euler} \quad (5.39)$$

$\dot{\Omega}_{x,sct}, \dot{\Omega}_{y,sct}, \dot{\Omega}_{z,sct}$ are the components of the angular acceleration of the spacecraft about the three *spacecraft frame* axes. They are directly measured by the gyroscopes.

The trajectory reconstruction for the *Gyroscopes* option can be expressed schematically as:

Begin with $t, x_{inert}, y_{inert}, z_{inert}, v_{x,inert}, v_{y,inert}, v_{z,inert}, \phi_{Euler}, \psi_{Euler}, \theta_{Euler}, \dot{\Omega}_{x,sct}, \dot{\Omega}_{y,sct}, \dot{\Omega}_{z,sct}$

Start loop.

$$x_{inert}, y_{inert}, z_{inert} \rightarrow r_{mom}, \theta_{mom}, \phi_{mom} \quad (5.40)$$

$$r_{mom}, \theta_{mom}, \phi_{mom} \rightarrow g_{r,mom}, g_{\theta,mom}, g_{\phi,mom} \quad (5.41)$$

$$g_{r,mom}, g_{\theta,mom}, g_{\phi,mom} \rightarrow g_{x,inert}, g_{y,inert}, g_{z,inert} \quad (5.42)$$

$$\phi_{Euler}, \psi_{Euler}, \theta_{Euler} \rightarrow \underline{\underline{EM}} \quad (5.43)$$

$$\underline{\underline{a_{aero,inert}}} = \underline{\underline{EM}} \underline{\underline{a_{sct,inert}}} \quad (5.44)$$

$$dx_{inert} = v_{x,inert} dt, \quad dy_{inert} = v_{y,inert} dt, \quad dz_{inert} = v_{z,inert} dt \quad (5.45)$$

$$dv_{x,inert} = (g_{x,inert} + a_{aero,x,inert}) dt \quad (5.46)$$

$$dv_{y,inert} = (g_{y,inert} + a_{aero,y,inert}) dt$$

$$dv_{z,inert} = (g_{z,inert} + a_{aero,z,inert}) dt$$

$$d\phi_{Euler} = \left(\frac{\Omega_{y,sct} \sin \psi_{Euler} + \Omega_{z,sct} \cos \psi_{Euler}}{\cos \theta_{Euler}} \right) dt \quad (5.47)$$

$$d\psi_{Euler} = (\Omega_{x,sct} + \tan \theta_{Euler} \times (\Omega_{y,sct} \sin \psi_{Euler} + \Omega_{z,sct} \cos \psi_{Euler})) dt \quad (5.48)$$

$$d\theta_{Euler} = (\Omega_{y,sct} \cos \psi_{Euler} - \Omega_{z,sct} \sin \psi_{Euler}) dt \quad (5.49)$$

$$d\Omega_{x,sct} = \dot{\Omega}_{x,sct} dt, \quad d\Omega_{y,sct} = \dot{\Omega}_{y,sct} dt, \quad d\Omega_{z,sct} = \dot{\Omega}_{z,sct} dt \quad (5.50)$$

Is $|r_{inert}| < \text{Planetary Radius}$?

Either stop or loop again.

5.4.6 Summary of Techniques Used to Constrain Spacecraft Attitude

The *head-on*, *drag-only*, and *acceleration ratios* options require knowledge of the flow velocity. The simplest assumption is that the atmosphere of the planet is rotating with the same angular velocity as the interior of the planet. Atmospheric bulk motions, winds, can modify this flow pattern. If precise knowledge of the flow velocity is important, then direct wind measurements or predictions from climate models can be used to define it.

In practice, accelerometers are rarely mounted at the spacecraft's exact centre of mass. In addition to aerodynamic accelerations, these poorly-positioned accelerometers also measure terms due to the angular motions of the spacecraft about its centre of mass. If these are periodic, they can be isolated within the measured accelerations and removed. The justification for this additional data processing is strongest if the period can be related to known properties of the spacecraft, such as its moments of inertia. Unless there is a justification for the periodic acceleration, it is not known whether or not it is appropriate to remove it. It might be signal, not noise. Spencer et al. (1999) identified a signal related to the 2-rpm roll rate of Pathfinder in its accelerometer measurements. If the x- and y-axis aerodynamic accelerations are small, due to the majority of the aerodynamic accelerations being aligned with the z-axis, and the x- and y-axis accelerometers are located far enough from the centre of mass to have their measurements significantly affected by these rotational terms, then it may be best to neglect the x- and y-axis measurements and just use the z-axis measurements in the *head-on* option.

In summary, the *head-on and drag-only* options are simple to implement and do not require any additional datasets such as aerodynamic databases or in-flight gyroscopic measurements, but use idealized, approximate aerodynamics that introduce uncertainties. The *acceleration ratios* option can indirectly reconstruct spacecraft attitude without any additional flight hardware, but requires an accurate aerodynamic database and may accumulate uncertainties during the indirect

reconstruction process. The *gyroscopes* option can directly reconstruct spacecraft attitude but requires additional flight hardware. Unless the spacecraft has a significant amount of lift, the simple *head-on* or *drag-only* options often give just as useful results for the trajectory and atmospheric structure reconstruction as the more complicated and expensive *acceleration ratios* or *gyroscopes* options.

5.4.7 Parachute Considerations

Many planetary entry spacecraft deploy parachutes. These would be torn apart if deployed early in the entry when the spacecraft is typically travelling at hypersonic speeds. Deployed at slower, near-sonic speeds, they decrease the terminal velocity of descent and allow the spacecraft to make more scientific measurements during descent. They also allow landings without impractically large retrorockets. The aerodynamic properties of disk-gap-band parachutes, a common type for planetary spacecraft, are much more complicated than those of the aeroshells which typically encase spacecraft during entry (Bendura et al., 1974; Braun et al., 1999). This makes the *acceleration ratios* option impractical after parachute deployment. Apart from that, the main effect of parachute deployment on the trajectory reconstruction is to introduce some oscillatory motions into the spacecraft, and hence into the measured accelerations as well, as it swings around on the end of its parachute (Magalhães et al., 1999). Trajectory reconstructions using the *head-on* or *drag-only* options are correct in an average sense, but the actual trajectory deviates from this reconstruction due to the swinging of the spacecraft. Trajectory reconstructions using the *gyroscopes* option should remain accurate. In practice, the sampling rate is often reduced after parachute deployment to reduce data volume and care must obviously be taken that this does not degrade the reconstruction.

5.4.8 Error Considerations

Several sources of error, including winds and rotational effects on accelerometers positioned away from the centre of mass, have been mentioned thus far. There are many others, including uncertainties in the spacecraft's entry state, in the planet's gravitational field, in the end-to-end gain and offset of the accelerometers and their temperature dependences, in the alignment and position of the accelerometers, and also noise, numerical accuracy of reconstruction software, and the digitization of the accelerometer signal (Peterson, 1965a). The effects of these errors and uncertainties on the accuracy of the trajectory reconstruction can be estimated as follows (Peterson, 1965a):

The spacing in time of points along the reconstructed trajectory is controlled by the accelerometer sampling rate. For example, 10 Hz sampling gives a spacing of 0.1 s.

The vertical resolution of the data points is the ratio of the vertical speed and the accelerometer sampling rate. For example, a vertical speed at entry of 1 km s⁻¹ and a sampling rate of 10 Hz corresponds to a vertical resolution of 100 m.

The uncertainty in the absolute altitude of each data point is affected by:

- Acceleration uncertainty and error, Δa , due to instrument resolution, noise, changes in gain and offset since calibration, any systematic offset, corrections for off-centre instrument position, *etc.*, integrates to an uncertainty in altitude of $0.5 t^2 \times \Delta a$. For example, Δa of 10^{-4} m s⁻² and t of 1000 s gives an uncertainty of 50 m.
- Uncertainty in the gravitational field, Δg , at a known position integrates to an uncertainty in altitude of $0.5 t^2 \times \Delta g$. For example, Δg of 10^{-4} m s⁻² and t of 1000 s gives an uncertainty of 50 m.
- Uncertainty in vertical entry velocity, Δv , integrates to an uncertainty in

altitude of $t \times \Delta v$. For example, Δv of 0.1 m s^{-1} and t of 1000 s gives an uncertainty of 100 m .

- Uncertainty in the entry state altitude, which was about 2 km for Pathfinder (Magalhães et al., 1999). If the planet's topography is well-known, then the landed altitude may be known to better than this from the landed latitude and east longitude, although this requires integrating backwards in time through the parachute region of descent. Uncertainties in landed latitude and east longitude may still be large, but selection of a relatively flat target for landing ensures a relatively small uncertainty in altitude. This landed position can be used in preference to the entry position as a boundary condition on the integration for the trajectory reconstruction. For example, 100 m may be the uncertainty in altitude for a landing on flat terrain with much larger uncertainties in horizontal position.
- Uncertainty in gravitational acceleration due to uncertainty in position. Uncertainty in gravity equals uncertainty in altitude $\times 2g/r$. This is in addition to any uncertainties in the gravitational field at any known position. This should be included with the earlier Δg term.

The uncertainties in the absolute latitude and east longitude of each data point is affected by:

- Acceleration uncertainty and error, Δa , due to instrument resolution, noise, changes in gain and offset since calibration, any systematic offset, corrections for off-centre instrument position, *etc.*, integrates to an uncertainty in latitude and east longitude of $0.5 t^2 \times \Delta a$. For example, Δa of 10^{-4} m s^{-2} and t of 1000 s gives an uncertainty of 50 m .
- Uncertainty in horizontal entry velocity, Δv , yields an uncertainty in altitude of $t \times \Delta v$. For example, Δv of 0.1 m s^{-1} and t of 1000 s gives an uncertainty of 100 m .

- Uncertainty in the entry state latitude and east longitude, which was about 2 km for Pathfinder (Magalhães et al., 1999).

Since the errors in position due to acceleration uncertainties and errors accumulate as the square of time since entry, it is imperative that the accelerometers be well-calibrated. Whilst the error due to noise is important on short timescales, but averages to zero on long timescales, any offset or gain error is cumulative through the integration process.

Whichever option is used for constraining spacecraft attitude, the transformation of measured accelerations from the *spacecraft frame* to the *inertial Cartesian* frame introduces additional uncertainties. The uncertainties introduced by the *head-on* and *drag-only* options should be estimated by, *e. g.*, altering the prescribed direction of the acceleration vector by some amount and performing another trajectory reconstruction with this altered dataset. Maximum likely changes in direction have to be estimated from the aerodynamic modelling work that was used to justify the use of these simple options. Comparison to the nominal trajectory reconstruction provides an estimate of the uncertainties that could accumulate under these options. The uncertainties introduced by the *acceleration ratios* option should be found by formally propagating the uncertainties in the measured accelerations and in the aerodynamic database through the various steps in the frame transformation procedure. The uncertainties introduced by the *gyroscopes* option should be calculated by propagating the additional instrumental and entry state uncertainties through the frame transformation procedure. The *head-on*, *drag-only*, and *acceleration ratios* options should compare likely atmospheric winds beyond those included in the trajectory reconstruction to the spacecraft velocity and propagate this uncertainty in the velocity of the spacecraft relative to the atmosphere through the various steps in the frame transformation procedure.

Generally mission goals, such as accuracy of reconstructed position and velocity, are set before flight and a detailed uncertainty analysis can evaluate if the

proposed instrument specifications can achieve those goals. Since space missions involve redundancy further constraints on the trajectory reconstruction, which reduce the errors, can be provided by additional information such as:

- The Doppler shift of telemetry during descent places crude constraints on the descent speed. The transmitted frequency of the telemetry is not usually known well enough to provide very accurate constraints.
- Any radar altimetry during descent, which is nominally a trigger for events during entry, descent, and landing, constrains the altitude and descent speed if the underlying topography is “well-behaved” or known.
- The Doppler shift of transmissions after landing enables the landing site position to be located to very high precision and accuracy. This is most helpful if the spacecraft does not roll/bounce too far between its initial impact and coming to rest.
- The measured acceleration due to gravity at the landing site places crude constraints on the accuracy of the accelerometers. Uncertainties in the gravitational field at the landing site mean that this does not provide very accurate constraints. The landed orientation of the spacecraft will be known from images of its surroundings, so any tilt can be corrected for.

5.5 Trajectory Reconstruction applied to Mars Pathfinder

5.5.1 Programming Details

I have written computer programmes in Research Systems’s IDL programming language which perform trajectory reconstructions as discussed in the previous section. The *head-on*, *drag-only*, and *gyroscopes* options have been implemented. At the time I developed these programmes I did not have access to a realistic aerodynamic database for a planetary entry spacecraft, so I have not yet implemented

the *acceleration ratios* option. I have recently been made aware of the publication of a significant portion of the Pathfinder aerodynamic database in Moss et al. (1998) and Gnoffo et al. (1996). I hope to use this database to implement the *acceleration ratios* option in my programmes in the future. The integrations are performed using IDL's fourth order Runge-Kutta procedure when accuracy is most important. I have tested it on the publicly available Mars Pathfinder dataset, PDS volume MPAM_0001 (Golombek et al., 1997; Golombek, 1999). All the information necessary to reconstruct Pathfinder's trajectory is present in this volume.

Since Pathfinder was not equipped with gyroscopes my trajectory reconstruction is restricted to using the *head-on* or *drag-only* options for determining spacecraft attitude. Since work by the Pathfinder accelerometer engineering and science teams using a good aerodynamic database and the *acceleration ratios* option showed that Pathfinder's symmetry axis is very close to the direction of aerodynamic decelerations experienced during its atmospheric entry, I was able to use the *head-on* option in my trajectory reconstruction (Spencer et al., 1999; Magalhães et al., 1999).

5.5.2 Assembly and Preparation of Pathfinder's Accelerometer Data

Pathfinder's entry state, as stated in the PDS file /document/edlddrds.htm, is a radial distance from the centre of mass of Mars, r , of 3597.2 ± 1.7 km, an areocentric latitude, θ , of $23^\circ \pm 0.04^\circ\text{N}$, an east longitude, ϕ , of $343.67^\circ \pm 0.01^\circ\text{E}$, an entry speed, v_{entry} , of 7444.7 ± 0.7 m s⁻¹, a flight path angle below the horizontal, γ , of $16.85^\circ \pm 0.02^\circ$, and a flight path azimuth measured clockwise from north, ψ , of $255.41^\circ \pm 0.02^\circ$. All these are quoted in a Mars-fixed, *i. e.*, rotating, coordinate system at July 4th, 1997, 1651:12.28 UTC. I label this entry state as the PDS entry state.

The spacecraft position in this frame is identical to position in the *momentary spherical* frame at this instant, so it can easily be transformed into the *inertial*

Cartesian frame for the first step in the trajectory integration using the results of Section 5.3.5. The spacecraft velocity can be transformed from this frame into the *inertial spherical* frame as follows:

$$v_{r,mom} = -v_{entry} \sin \gamma \quad (5.51)$$

$$v_{\theta,mom} = -v_{entry} \cos \gamma \cos \psi \quad (5.52)$$

$$v_{\phi,mom} = v_{entry} \cos \gamma \sin \psi + \omega r \sin \theta \quad (5.53)$$

An alternative entry state has been published by the Pathfinder engineers (Spencer et al., 1999). In theory, a trajectory reconstruction using one entry state should pass through the other entry state. This entry state, which I label as the engineering entry state, is a radial distance from the centre of mass of Mars, r , of 3522 km, an areocentric latitude, θ , of 22.6303°N, an east longitude, ϕ , of 337.9976°E, an entry speed, v_{entry} , of 7264.2 m s⁻¹, a flight path angle below the horizontal, γ , of 14.0614°, and a flight path azimuth measured clockwise from north, ψ , of 253.1481°. The relevant time is July 4th, 1997, 1651:50.482 UTC. Uncertainties were not published. The position is once again quoted in the Mars-fixed, *i. e.*, rotating, coordinate system, but the velocity is not. The velocity is given in an inertial, *i. e.*, non-rotating, coordinate system. The spacecraft velocity can be transformed from this frame into the *inertial spherical* frame as follows:

$$v_{r,mom} = -v_{entry} \sin \gamma \quad (5.54)$$

$$v_{\theta,mom} = -v_{entry} \cos \gamma \cos \psi \quad (5.55)$$

$$v_{\phi, mom} = v_{entry} \cos \gamma \sin \psi \quad (5.56)$$

Note that Equations 5.54 – 5.56 are identical to Equations 5.51 – 5.53 with $\omega = 0$. The PDS entry state corresponds to an altitude of about 210 km above the final landing site, the engineering entry state, about 38 seconds later, corresponds to an altitude of about 130 km. I shall initially use the PDS entry state.

There are many files of accelerometer data archived in the PDS volume in the /edl_erdr directory. As discussed in the file /document/edler_ds.htm, the best is the file /edl_erdr/r_sacc_s.tab because of its high (32 Hz) sampling rate. The data need to be multiplied by a reference value for the Earth’s gravity, $9.795433 \text{ m s}^{-2}$, which is given in the file /edl_erdr/r_sacc_s.lbl.

One x-axis data point is 0.0, a clear outlier from the neighboring data points. One z-axis data point is also 0.0 and an outlier. These are mentioned in Magalhães et al. (1999) but not in the file /document/edler_ds.htm. I replaced these with an interpolation from neighboring data points. There are also about ten data points in the y-axis data that are zero. However, these are consistent with neighboring data points and have not been modified.

The accelerometers have several different gain states. The gain state of each accelerometer changed several times during atmospheric entry. When an accelerometer changes gain state, there is a brief acceleration pulse that is an artifact of the electronic time constant of the sensor (Magalhães et al., 1999). From calibration studies, as discussed in the file /document/edl_ddrds.htm, it was found that 1 second’s worth of data are corrupted immediately after a change in gain state. Gain state changes can be located by examining the listing of the gain states of each accelerometer as a function of time in the file /edl_erdr/r_sacc_s.lbl. The corrupted 1 second intervals of data were replaced with an interpolation from neighboring data points.

The accelerometers continued to record data for a short time after impact when the spacecraft was bouncing and rolling around on the surface. The head-on option for constraining spacecraft attitude is clearly useless after impact, so all data recorded after landing are discarded from the data files. The moment of impact is easily identified in the accelerometer data as the first of a series of 10 g spikes in the accelerometer data, each about half a second in duration.

The first acceleration measurements are made at 1 Hz, not 32 Hz. For computational simplicity, I interpolated the earliest measurements to the same sampling rate as the rest of the dataset.

Acceleration measurements in the data file begin earlier than the PDS entry state. Those that precede the initial position and velocity that provide the boundary conditions for the trajectory integration are discarded, although of course they could be back integrated to recover the trajectory prior to the entry state. The files `/edl_erdr/r_sacc.s.lbl` and `/edl_erdr/r_sacc.s.tab` provide the times of each data point.

The planetary sidereal day of 24.6229 hours is necessary for all the frame transformations (Lodders and Fegley, 1998). The planet's gravitational field is specified by GM , r_{ref} , and C_{20} as discussed in Section 5.3.6. These values are updated regularly in light of improved data, but significant changes are confined to the higher order terms. The original reconstructions of the Mars Pathfinder trajectory and atmospheric structure occurred before the MGS revolution in martian geodesy and used values from the model GMM-1 (Smith et al., 1993).

The relevant values are $GM = 4.282828 \times 10^{13} \text{ m}^3 \text{ s}^{-2}$, $r_{ref} = 3394.2 \text{ km}$, $C_{20} = -8.75977 \times 10^{-4}$. This value for C_{20} corresponds to a normalization convention for P_{20} of $P_{20}(1) = \sqrt{5}$ (Kaula, 1966).

Since my aim is to reproduce the archived Pathfinder results, I did not use the latest values for these parameters. Higher order terms are neglected since they are not large enough to significantly affect the trajectory reconstruction.

This is all the information necessary to reconstruct the trajectory of Mars Pathfinder. For convenience, I also tracked the altitude of the reconstructed trajectory above the landing site by subtracting the planetary radius of the final landing site, 3389.715 km, from the reconstructed radial distances. This is given in the file `/document/edlldrds.htm` to six significant figures and in Magalhães et al. (1999). All references to “altitude” imply radial distance with this value subtracted — never distance from an equipotential or any other reference surface.

To verify my trajectory reconstruction, I compared it to that archived with the PDS in files `/edl_ddr/edl_ddr.lbl` and `/edl_ddr/edl_ddr.tab`. This archived trajectory begins at an altitude of about 140 km, significantly below the PDS entry state at 210 km altitude. It ends at parachute deployment, at about 10 km altitude.

5.5.3 Entry State Problems

Using the PDS entry state at 210 km, my reconstructed trajectory systematically differs from the PDS’s by about a degree in both latitude and east longitude, as shown in Figures 5.1 and 5.2.

My latitudes as a function of time are about a degree south of the PDS’s. My east longitudes as a function of time are about a degree east of the PDS’s. These are many times greater than the hundredths of degree-scale uncertainties in latitude and east longitude in the PDS entry state. A significant problem exists in either my work or the PDS archive. The trajectory archived with the PDS only extends up to 140 km altitude, yet Figure 2 of Magalhães et al. (1999) shows the trajectory up to 210 km altitude. Below 140 km altitude, the PDS trajectory and Figure 2 of Magalhães et al. (1999) appear identical under visual inspection. Magalhães et al. (1999) quote the PDS entry state exactly as the initial conditions used for their paper. However their Figure 2 shows a latitude of between 23.8 and 24.0°N and an east longitude of between 342.5 and 343.0°E at 210 km altitude — while the entry state gives a latitude of $23^\circ \pm 0.04^\circ\text{N}$ and an east longitude of $343.67^\circ \pm$

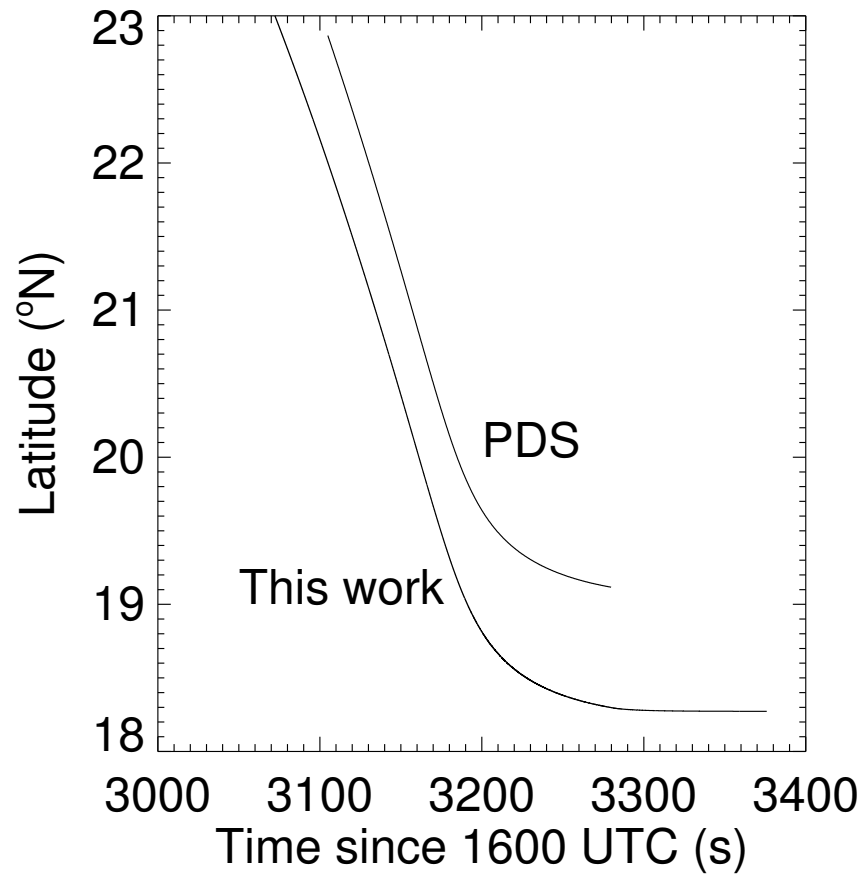


Figure 5.1: Reconstructed latitude as a function of time from the PDS archive and the results of this chapter using the PDS entry state. The PDS trajectory extends from 140 km to 10 km altitude. The trajectory derived in this chapter extends from 210 km to 0 km altitude.

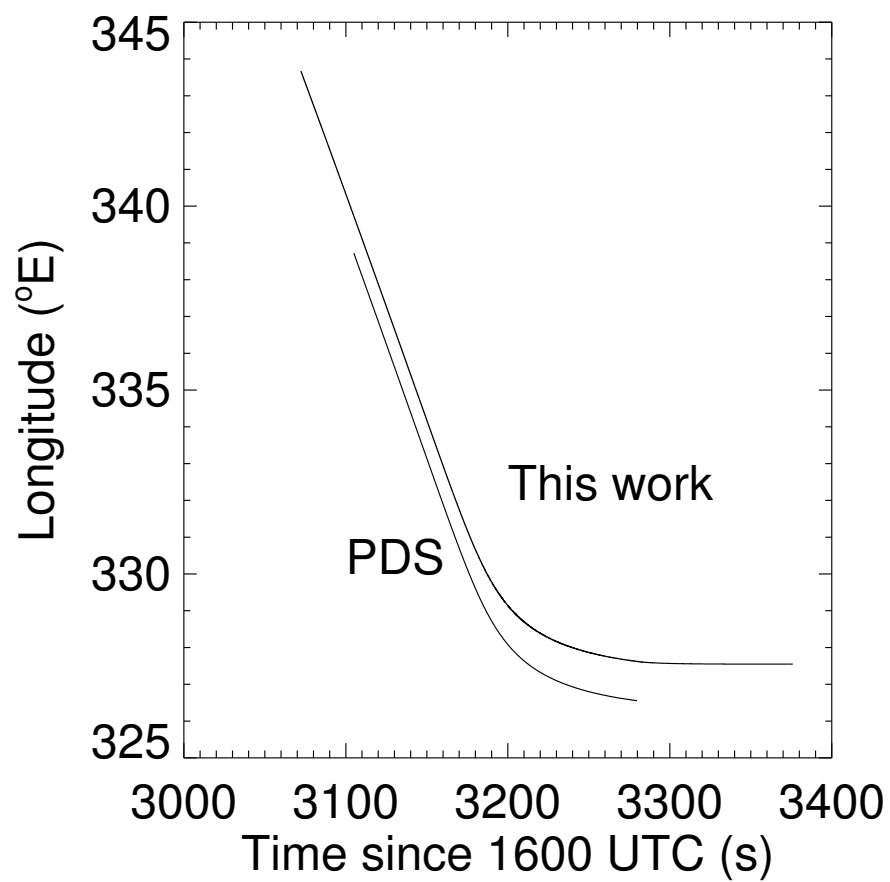


Figure 5.2: As Figure 5.1, but east longitude.

0.01°E. This appears to me to be an inconsistency within Magalhães et al. (1999), regardless of any of my trajectory reconstruction work. This offset is of the same size and in the same direction as the offset between my reconstructed trajectory and the PDS values.

If I instead use the engineering entry state at 130 km altitude from Spencer et al. (1999), the systematic offset between my reconstructed trajectory and the PDS trajectory reduces to a few hundredths of a degree in both latitude and east longitude, as shown in Figures 5.3 and 5.4, which is comparable with the likely uncertainties in latitude and east longitude in the engineering entry state. I assume that the uncertainties in the engineering entry state are comparable to the uncertainties in the PDS entry state since both are derived from the same tracking data.

I have taken the engineering entry state and integrated its trajectory backwards in time under the influence of gravity only. Under visual inspection, it appears identical to Figure 2 of Magalhães et al. (1999) and hence does not pass through the position quoted as the PDS entry state. At the time of the engineering entry state, the position of the engineering entry state differs from that of the PDS trajectory by only $\sim 0.1^\circ$ in latitude and east longitude.

A reviewer points out that the engineering entry speed is slower than the PDS entry speed, despite being at a lower altitude. Before significant atmospheric deceleration occurs, the spacecraft should speed up as it approaches Mars due to the attraction of martian gravity. This is another inconsistency between the engineering and PDS entry states.

I conclude that there is an error in Magalhães et al. (1999), most likely in the entry state. This error is probably present in the PDS archive as well. Considering these inconsistencies, I elected to use the engineering entry state in my trajectory integrations. Since the engineering entry state occurs at a later time than the PDS entry state I again discard any accelerometer measurements that preceeded

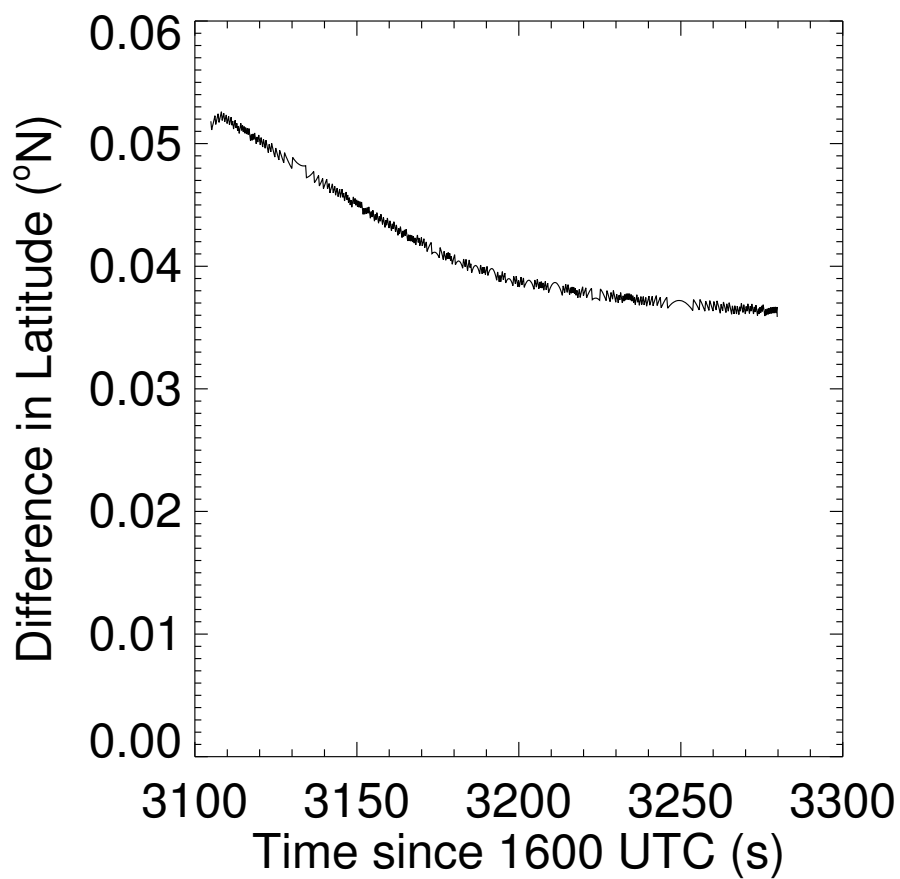


Figure 5.3: Derived Pathfinder latitude subtracted from the PDS reconstructed latitude using the engineering entry state as a basis.

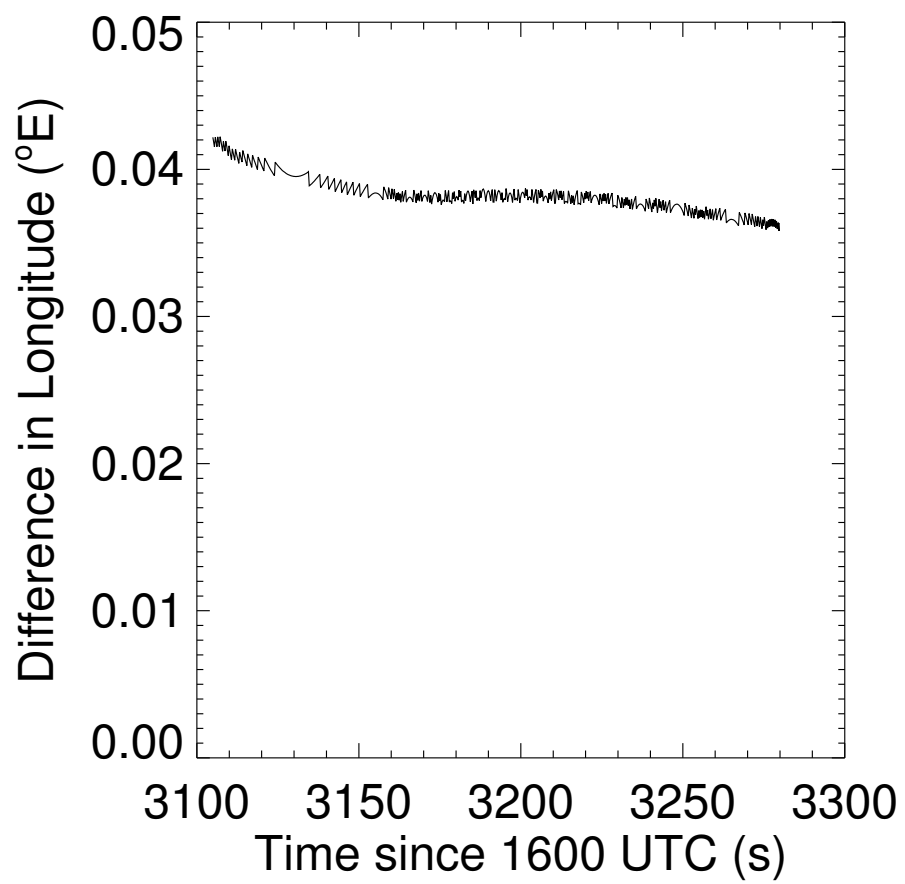


Figure 5.4: As Figure 5.3, but east longitude.

it.

5.5.4 Results

Using the engineering entry state, the trajectory reconstruction results shown in Figures 5.3 – 5.5 are of good quality.

Differences in latitude and east longitude between my values and the PDS data are on the order of a few hundredths of a degree. Differences in altitude are less than the uncertainty quoted for the PDS entry state and are on the order of a percent. I attribute the systematic offset in latitude and east longitude to the fact that the PDS trajectory is shifted to reproduce the landed position (Magalhães et al., 1999). I do not have a convincing explanation for the diminishing offset in altitude.

Continuing the trajectory through the parachute phase, my position at the time of landing is 502.7 m altitude below the reference radius of 3389.715 km, 19.054 degrees north latitude, and 326.445 degrees east longitude. The PDS landed position is at the reference radius of 3389.715 km, 19.09 degrees north latitude, and 326.48 degrees east longitude

Note that these results have been achieved without using any sophisticated aerodynamics.

5.6 Atmospheric Structure Reconstruction

5.6.1 Fluid Dynamics During an Atmospheric Entry

The forces and torques acting on a rigid body moving through a fluid are, in principle, completely constrained given the size, shape, and mass of the rigid body, the flow velocity of the fluid with respect to the rigid body, the composition of the fluid,

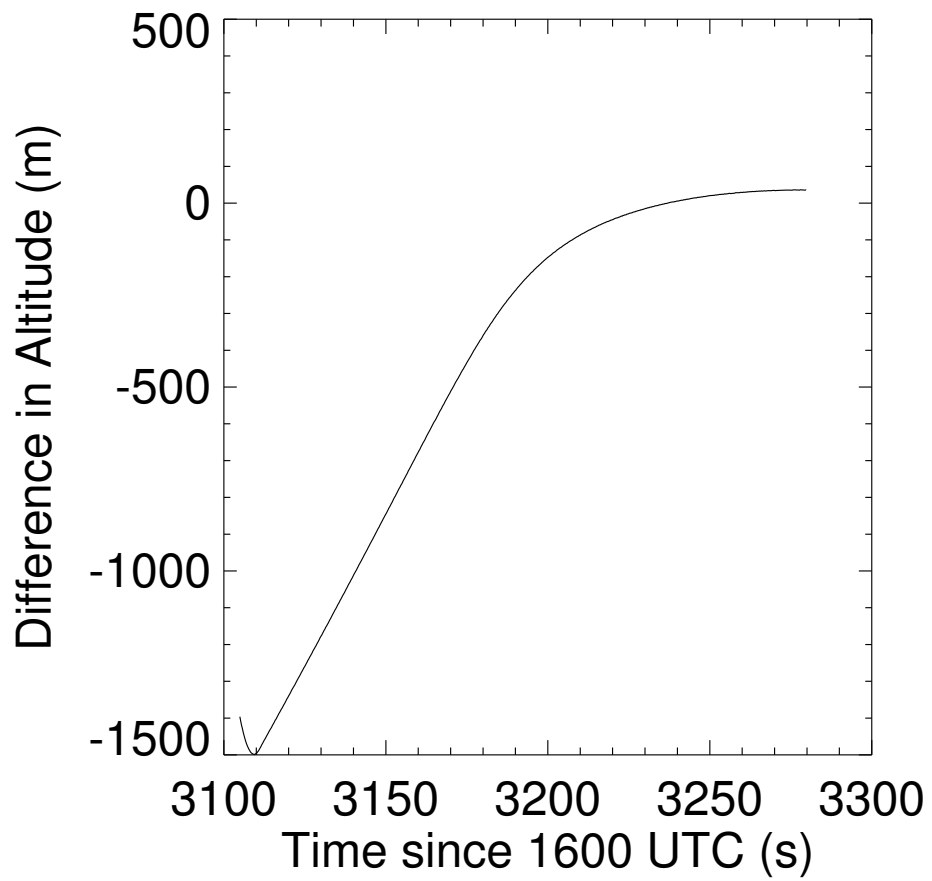


Figure 5.5: As Figure 5.3, but altitude.

and the thermodynamic state of the fluid. Specifying the thermodynamic state of a fluid requires two intensive thermodynamic variables, such as density and pressure.

For any given direction which may be related either to the *spacecraft* frame or to the direction of the fluid velocity, the aerodynamic force, F_{aero} , acting on the spacecraft can be expressed as follows:

$$F_{aero} = \frac{-\rho C A V^2}{2} = ma \quad (5.57)$$

Where ρ is the fluid density, A is a characteristic spacecraft area, V is the speed of the spacecraft relative to the fluid, m is the mass of the spacecraft, and a is the acceleration of the spacecraft.

This is simply the result of a dimensional analysis of the problem, with the factor of two used by convention. All of the dependences on the body's shape, orientation, fluid composition, fluid temperature, and so on are hidden away in the dimensionless force coefficient C . If the chosen direction is parallel to the spacecraft's velocity with respect to the atmosphere, C is the drag coefficient and is often labelled with a subscript D. If the chosen direction is in the plane defined by the spacecraft's velocity with respect to the atmosphere and the direction of gravity and is also perpendicular to the spacecraft's velocity with respect to the atmosphere, C is the lift coefficient and is often labelled with a subscript L. If the chosen direction is perpendicular to the drag and lift forces, C is the side force coefficient and is often labelled with a subscript Y. If the spacecraft is axisymmetric and the chosen direction is parallel to this axis, C is the axial force coefficient and is often labelled with a subscript A. If the chosen direction is perpendicular to this axis, C is the normal force coefficient and is often labelled with a subscript N. To emphasize that this force balance can be applied to any chosen direction, I retain the general force coefficient C rather than working with the common special cases of either the drag coefficient C_D or normal force coefficient C_N .

Changes in the spacecraft's speed and the atmosphere's physical properties during an atmospheric entry affect the spacecraft's aerodynamics. Here I outline the different aerodynamic regimes important for an atmosphere-entering spacecraft. I focus on the most important physical phenomena rather than on the exact numerical values of the force coefficients. I do not discuss changes in a given force coefficient with changes in spacecraft attitude. Vinh et al. (1980) discuss this issue. I focus on the drag coefficient since this is usually the most useful of the force coefficients.

The Navier-Stokes equation for the conservation of linear momentum in a continuum fluid can be written as:

$$\rho \left[\frac{\partial \underline{v}}{\partial t} + (\underline{v} \cdot \underline{\nabla}) \underline{v} \right] = -\underline{\nabla} p - \underline{\nabla} \times (\eta \underline{\nabla} \times \underline{v}) \quad (5.58)$$

Where η is the dynamic viscosity of the fluid. Working in the rest frame of a spacecraft in a planetary atmosphere, the spacecraft can be considered as an immersed object around which the continuum fluid must flow. This equation must be satisfied throughout the fluid and boundary conditions apply at the spacecraft-fluid interface.

By expressing each quantity in this equation (say x) in terms of the product of a characteristic value for that quantity (x_0) and a dimensionless number (x'), the equation can be rearranged to yield:

$$\rho' \left[\frac{\partial \underline{v}'}{\partial t'} + (\underline{v}' \cdot \underline{\nabla}') \underline{v}' \right] = - \left(\frac{p_0}{\rho_0 v_0^2} \right) \underline{\nabla}' p' - \left(\frac{\eta_0}{\rho_0 L_0 v_0} \right) \underline{\nabla}' \times (\eta' \underline{\nabla}' \times \underline{v}') \quad (5.59)$$

The spatial derivative, $\underline{\nabla}$, is expressed as $\underline{\nabla}'/L_0$. The first ratio of characteristic values in parentheses is related to the Mach number, Ma , which is defined as the ratio of the characteristic speed to the sound speed. For an ideal gas, the sound speed is given by $(\gamma_{fluid} p/\rho)^{1/2}$ where γ_{fluid} is the ratio of specific heats of the fluid

Landau and Lifshitz (1959). Hence this first ratio is $1/\gamma_{fluid} Ma^2$. Note that it contains a dependence on the composition of the fluid through γ_{fluid} . The second ratio of characteristic values in parentheses is defined as the inverse of the Reynolds number, Re . Physically different situations have identical dimensionless solutions for this equation if they have the same Re , Ma , and dimensionless boundary conditions (Bertin and Smith, 1979). This means that the aerodynamic behaviour of a large spacecraft under a specified atmospheric composition, density, and temperature can be studied experimentally with small-scale models immersed in a fluid of different density or temperature. This is significantly easier than building a wind tunnel large enough to contain a full-size spacecraft, capable of generating many different flow speeds, and able to be filled with a range of gases, such as CO_2 for Mars, N_2 for Titan, and H_2 for Jupiter, with various densities.

I first consider small Ma for which the fluid is incompressible. For small Re where viscous forces dominate over inertial forces, Stokes drag causes values of the drag coefficient far exceeding unity and inversely proportional to Re (Faber, 1995). As Re increases, the drag coefficient decreases towards values near unity. The increase in Re confines the effects of viscosity to a thin layer, the boundary layer, near the surface of the body. Flow is at first laminar within the boundary layer (Bertin and Smith, 1979). The bulk of the fluid behaves as if it were inviscid. As Re increases further, the flow within the boundary layer becomes turbulent, which decreases the drag, and the boundary layer separates from the surface, which increases the drag (Faber, 1995). Which of these two transitions occurs first and which dominates depends on the specific situation under consideration. For a vanishingly small viscosity, or large Re , there is still appreciable resistance to flow. For the idealized case of a perfectly inviscid fluid and infinite Re , there should be no forces on the spacecraft at all. Flow at low Re is laminar, flow at high Re is turbulent and this fact is not dependent on Ma (Owczarek, 1964).

This picture is modified as Ma increases and the fluid becomes more compressible, which means that work can be done upon it. Variations in temperature

within the fluid become large enough that heat transfer is important and the conservation of energy must be considered in constructing equations to describe the flow (Owczarek, 1964). This extra conservation law, which is considered simultaneously with the conservation of momentum, alters the behaviour of the flow and the force coefficients. Flows in which Ma is everywhere less than one are called subsonic. A transonic flow contains regions where Ma is less than one and where Ma is more than one. Theoretical models of transonic flow are challenging because they must include both subsonic and supersonic flow. Flows in which Ma is everywhere greater than 1 are called supersonic. Hypersonic flows are supersonic flows in which the fluid cannot be treated as an ideal gas, either because it becomes dissociated, is no longer in thermodynamic equilibrium, or for some other reason. A working definition of hypersonic flow is $Ma > 5$.

A thermal boundary layer develops in compressible flows, similar to the viscous boundary layer, within which the effects of compressibility and heat transfer are confined (Owczarek, 1964). This affects the flow of the fluid and the force coefficients. Shock waves develop in regions of the fluid where the flow is supersonic. Thermodynamic and flow properties can be discontinuous across a shock. Interactions between the boundary layer and shock waves also alter the drag. These become more important as Ma increases and the shock waves approach closer to the spacecraft's surface and the boundary layer. At hypersonic speeds the effects of viscosity and compressibility are important throughout the shocked region of the flow, rather than being confined to boundary layers (Owczarek, 1964). At hypersonic speeds it is a reasonable approximation to consider the force coefficients independent of Ma and Re (Vinh et al., 1980).

The continuum fluid model only applies if molecular collisions within the fluid are much more frequent than collisions between molecules and the spacecraft. Equivalently, if gradients in thermodynamic properties are shorter than the mean free path of molecules within the fluid then the continuum model does not apply (Bird, 1994). The Knudsen number, Kn , defined as the ratio of the mean free path

of molecules within the fluid to the characteristic length, is useful here. Using the kinetic theory of gases, $Ma/Re \sim Kn/\gamma_{fluid}^{1/2}$ (Owczarek, 1964). If Kn is less than 0.01, then continuum flow applies. In this limit the fluid adjacent to the spacecraft surface is at rest with respect to it. As molecular collisions become less frequent, the fluid adjacent to the spacecraft surface can acquire some tangential velocity with respect to it. This intermediate regime, $0.01 < Kn < 1$, is the transitional flow regime. Finally, as the effects of molecule-molecule collisions become insignificant compared to those of spacecraft-molecule collisions, the free-molecular flow regime with $Kn > 1$ is entered. In this regime molecules hitting the spacecraft reflect somewhere between specularly and diffusely with an energy that is somewhere between their energy upon hitting the surface and the thermal energy of the spacecraft's surface temperature (Bird, 1994). Chemical reactions are also possible between the spacecraft and impinging molecules.

The stated boundaries of the various flow regimes for Ma and Kn are not absolute. A single value for Ma or Kn may be appropriate for most of the flow, but there are always be some regions of the flow where local values of these dimensionless numbers differ significantly from the mean value. The shape of the spacecraft has an effect on precisely where these boundaries are.

The composition of the fluid is important in most flow regimes because it affects the partition of energy between kinetic and internal (*e. g.* vibrational) modes and how the disturbed fluid returns to thermodynamic equilibrium (Bird, 1994). This, in turn, affects the transfer of momentum and energy between the spacecraft and the fluid. There is also the possibility of chemical reactions in the disturbed fluid which change its physical properties. The chemical and physical state of the spacecraft can also be a factor. Chemical reactions between the spacecraft and the fluid can affect the drag. Ablation or thermal expansion of the spacecraft can also affect the drag. As an extreme example, consider a chocolate spacecraft. This will rapidly melt upon entry. Real spacecraft are not made of chocolate, but none of them have the idealized physical properties of a perfectly rigid, inert body.

Continuum flow can be studied experimentally, such as in wind-tunnel experiments (Intrieri et al., 1977), or in numerical models such as HALIS or LAURA (Gnoffo et al., 1996). Rarefied flow is much harder to study experimentally (Blanchard et al., 1997). It can be modelled numerically with direct simulation Monte Carlo (DSMC) methods (Bird, 1994). Comparison to Viking flight data and ground-based validation experiments shows that the DSMC methods are accurate (Blanchard et al., 1997).

Pathfinder, which is a typical planetary lander or entry probe, experienced free-molecular flow upon first entering the martian atmosphere. This was followed by transitional flow, hypersonic continuum flow, and transonic continuum flow before its parachute was released for subsonic continuum flow (Magalhães et al., 1999). The drag coefficient was constant and about 2 in free-molecular flow. It decreased during the transitional flow regime, but remained relatively stable during the hypersonic continuum flow regime. It then changed more rapidly in the transonic continuum flow regime. The opening of the parachute changed the aerodynamic properties of the spacecraft immensely. The drag coefficient will behave similarly for other typical atmospheric entries. I do not generalize further about the behaviour of the drag coefficient during an atmospheric entry because it is so dependent on the shape of the spacecraft. Discussions relevant to specific spacecraft can be found in the literature.

5.6.2 Generalized Density Reconstruction

With the exception of the *acceleration ratios* option discussed earlier in Section 5.4.4, this takes place separately from the trajectory reconstruction. It uses the results of the trajectory reconstruction.

Putting the *measured* aerodynamic accelerations aside initially, the results of the trajectory reconstruction, spacecraft mass, size, and shape, and an assumed

profile of atmospheric density and pressure are sufficient information for the aerodynamic database to predict the aerodynamic forces and torques at each point along the reconstructed trajectory. The specific results that are used from the trajectory reconstruction are spacecraft attitude with respect to the fluid velocity and the fluid speed.

For the chosen direction, Equation 5.57 can then be trivially rearranged to give:

$$C_{estimated} = \frac{-2F_{aero,predicted}}{\rho_{assumed}AV^2} \quad (5.60)$$

which can then be solved to find $C_{estimated}$ at each point along the trajectory. C is a slowly varying function of the density and pressure of the atmosphere, so an *estimate* of C with an *assumed* density and pressure should be reasonably accurate for the *actual* state of the atmosphere. Reintroducing the measured aerodynamic accelerations, and treating C as known and ρ as unknown, can provide an *estimate* of atmospheric density at each point along the profile.

$$\rho_{estimated} = \frac{-2ma}{C_{estimated}AV^2} \quad (5.61)$$

If this *estimate* agrees with the *assumed* value (which was needed to find $C_{estimated}$), then this density value is the *actual* atmospheric density. The *estimated* value is typically closer to the *actual* value than the initially *assumed* value is, so the *assumed* profile is replaced by the *estimated* profile and the whole process can be repeated iteratively until *assumed* (input) and *estimated* (output) profiles converge satisfactorily on the *actual* profile. Only a small number of iterations is usually needed (Magalhães et al., 1999). Magalhães et al. (1999) chose a direction parallel to the spacecraft's velocity with respect to the atmosphere, the drag direction, and used a constant value of C in their first iteration. C changes by only tens of percent

for many orders of magnitude change in density and pressure. If C were not such a weak function of density and pressure, then convergence could not be guaranteed.

Similar procedures can be implemented for a total of three linearly independent axes for both force balances and torque balances. This gives six estimates for density at each point along the profile, all of which should be consistent. In practice, uncertainties on the force balance along the axis closest to the flow direction are much lower than on the others so this estimate is used alone.

This process is a pointwise solution procedure applied along the trajectory, and does not integrate densities from one timestep to the next. The term A is a reference area included to make C dimensionless, but it may or may not be the most obvious area one might select as a reference. Both A and m may change along the trajectory due to, for example, heat shield ablation. If this is likely, then additional measurements are needed to constrain these values during the atmospheric entry. Modelling to predict F_{aero} should of course use the appropriate value of A .

5.6.3 Generalized Pressure and Temperature Reconstructions

An inviscid fluid, such as a planetary atmosphere, satisfies Euler's equation (Houghton, 2002):

$$\frac{\nabla p}{\rho} - \underline{g} + (\underline{v} \cdot \nabla) \underline{v} + \frac{\partial \underline{v}}{\partial t} = 0 \quad (5.62)$$

In the radial direction, the latter two terms that are due to atmospheric motions are much smaller than the first two terms, and so the equation of hydrostatic equilibrium applies (Holton, 1992):

$$\frac{dp}{dr} = \rho g_r \quad (5.63)$$

Note that g_r is negative. It is usually also assumed that the horizontal extent of the entry trajectory is small enough that the pressure at a given altitude does not change significantly over that extent. This is again neglecting atmospheric motions. The equation of hydrostatic equilibrium can be integrated to yield a pressure profile — but it needs a constant of integration. This can be ignored and set to zero at high altitude, but the resultant pressure profile is an underestimate. If the actual pressure at the top of the density profile is 1, then the actual pressure n scale heights below is $\exp(n)$. If the estimated pressure at the top of the density profile is mistakenly set to 0, then the estimated pressure n scale heights below is $\exp(n) - 1$. The fractional underestimate in the pressure n scale heights below is therefore $\exp(-n)$. Two scale heights below the top of the density profile this underestimate is 14%, four scale heights below it is reduced to 2%.

A better approach uses the fact that atmospheric density and pressure are both changing exponentially with height, but atmospheric temperature is only changing linearly with height. The ideal gas law is:

$$p = \rho T \frac{k_B}{m_{mol}} \quad (5.64)$$

where T is temperature, k_B is Boltzmann's constant, and m_{mol} is the mean molecular mass. With an ideal gas equation of state and the assumption that both atmospheric mean molecular mass and temperature vary much more slowly with altitude than atmospheric density does, one has:

$$\frac{d\rho}{\rho} = \frac{dp}{p} \quad (5.65)$$

Substituting Equation 5.65 into Equation 5.63 gives:

$$\frac{p}{\rho} \frac{d\rho}{dr} = \rho g_r \quad (5.66)$$

$$p \frac{d(\ln \rho)}{dr} = \rho g_r \quad (5.67)$$

This gives an estimate for the pressure at the top of the density profile, where $r = r_0$, that can be calculated from the density profile alone:

$$p(r_0) = \rho(r_0) g_r(r_0) \times \left(\frac{d}{dr} (\ln \rho) \Big|_{r_0} \right)^{-1} \quad (5.68)$$

This can then be used as the boundary condition when integrating Equation 5.63 to get the pressure profile.

$$p(r) = \rho(r_0) g_r(r_0) \times \left(\frac{d}{dr} (\ln \rho) \Big|_{r_0} \right)^{-1} + \int_{r_0}^r \rho(r) g_r(r) dr \quad (5.69)$$

Finally the derived density and pressure profiles can be substituted into Equation 5.64 to give the temperature profile.

Modelling and the final reconstructed temperature profile can be used to estimate how much uncertainty the isothermal and ideal gas assumptions introduce into the constant of integration. More complicated equations of state can be considered if desired, but planetary atmospheres are sufficiently rarefied when first detected by current accelerometers that an ideal gas equation of state is very accurate.

5.6.4 Error Considerations

The inaccuracies in the trajectory reconstruction affect the aerodynamic modelling and contribute to errors in C . However C is also affected by intrinsic uncertainties in the aerodynamic modelling. These uncertainties in C , in the trajectory reconstruction (V), and in the measured accelerations then contribute to errors in the

estimated value for ρ at each point along the trajectory. Errors in p are introduced by the assumption of a static atmosphere, by uncertainties in ρ and by uncertainties in the gravitational field at the inaccurately known position of each point along the trajectory. Errors in T come from uncertainties in the atmospheric composition, ρ , p , and an assumed equation of state. As discussed in Section 5.7.3, errors in temperature can be significantly less than those in pressure and density.

Direct measurements of atmospheric properties including density, pressure, temperature, and wind velocity can improve the atmospheric structure reconstruction (Seiff and Kirk, 1977a), while mass spectrometer measurements of atmospheric composition can yield an independent profile of atmospheric density (Nier and McElroy, 1977).

5.7 Atmospheric Structure Reconstruction applied to Mars Pathfinder

5.7.1 The Importance of an Aerodynamic Database

Any atmospheric structure reconstruction depends heavily upon its aerodynamic database. Since atmospheric density is inversely proportional to the force coefficient for the chosen direction, relative uncertainties in density are greater than or equal to those in the force coefficients. Aerodynamic databases are typically constructed by a mixture of physical experiments, such as wind tunnel tests, and numerical modelling on supercomputers. Both of these are expensive and time-consuming. As discussed in Section 5.5.1, I did not use the Moss et al. (1998) and Gnoffo et al. (1996) aerodynamic database for Pathfinder. Instead I used Figure 3 of Magalhães et al. (1999) which shows a profile of C_D as a function of altitude as appropriate to their trajectory reconstruction. I scanned and digitized this figure, then used this vertical profile of C_D as my aerodynamic database. If my trajectory reconstruction has a different speed at a given altitude than theirs, then I am forced to use the

value of C_D appropriate to their speed. This is a source of error, but since my trajectory reconstruction is reasonably close to theirs, the major source of error is in the crude scanning and digitization.

5.7.2 Results

As stated in the PDS file `/document/edladdrds.htm`, the spacecraft reference area, A , is 5.526 m² and its mass, m , is 585.3 kg. These, the results of the trajectory reconstruction, and my crude aerodynamic database are all that is needed to derive the profile of atmospheric density. For the constant of integration in the equation of hydrostatic equilibrium, I estimated the density scale height over the uppermost 10 km of the density profile and assigned this value to the altitude in the midpoint of this range. I used a spherically symmetric gravitational field and numerically integrated the equation of hydrostatic equilibrium. Uncertainties due to the crude aerodynamic database dwarf the neglected effects of higher order terms in the gravitational field.

The mean molecular mass assumed in the ideal gas equation of state, m_{mol} , was 43.49 g mol⁻¹ in the lower atmosphere, and decreased with altitude as discussed in Magalhães et al. (1999) and tabulated in PDS file `/document/edladdrds.htm`.

As a function of the independent variable in the reconstruction, time, the density, pressure, and temperature results, shown in Figures 5.6 – 5.8 are consistent to within a few percent. When more usefully plotted against reconstructed altitude in Figures 5.9 – 5.11, the density and pressure results are only consistent to 20% or so. This apparent worsening of my results is due to differences between my profile of reconstructed altitude versus time and that of the PDS. However, the temperature versus reconstructed altitude results are still consistent to about 5%. Sudden jumps in the difference between my results and the PDS results at 85 and 65 km altitude occur at changes in accelerometer gain state. I believe that I and the PDS have used different interpolation techniques to replace the corrupted second of data.

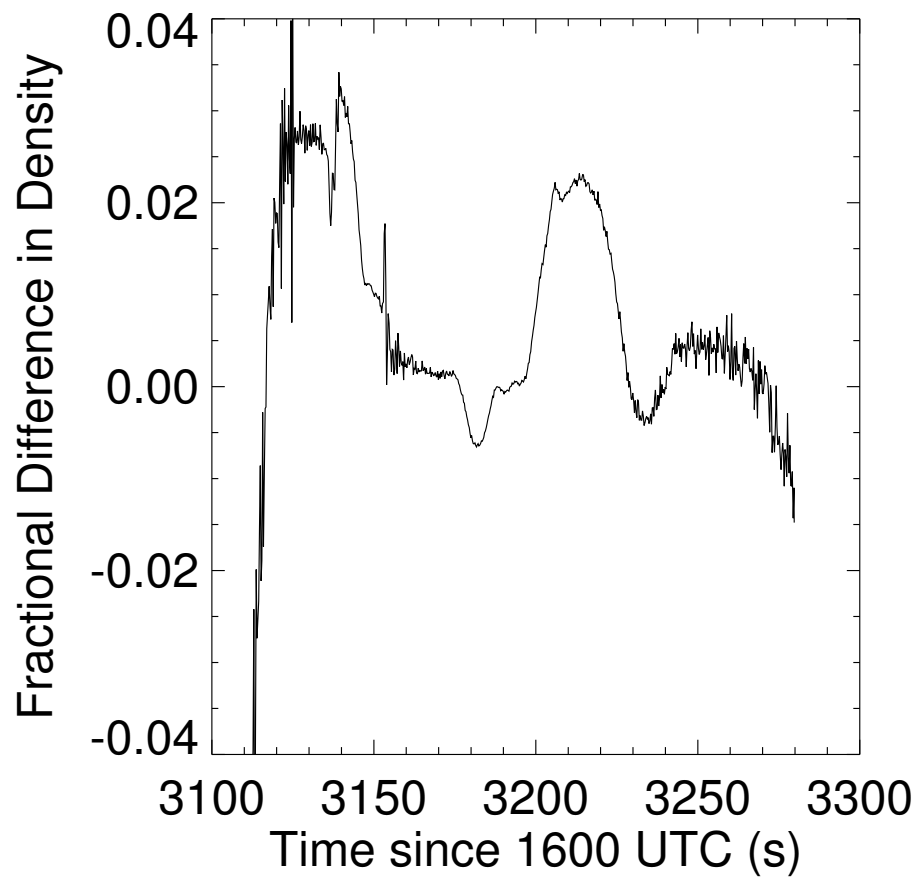


Figure 5.6: The ratio of (PDS reconstructed density minus the results of this chapter using the engineering entry state) to the PDS reconstructed density, plotted against the independent variable time.

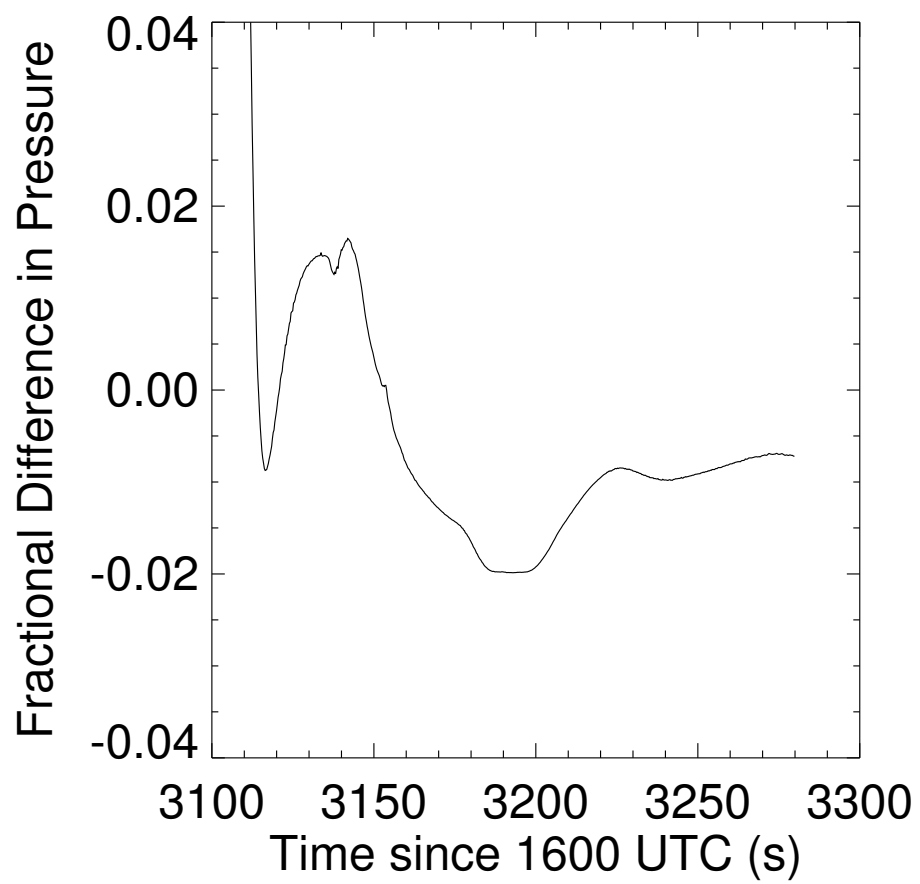


Figure 5.7: As Figure 5.6, but pressure.

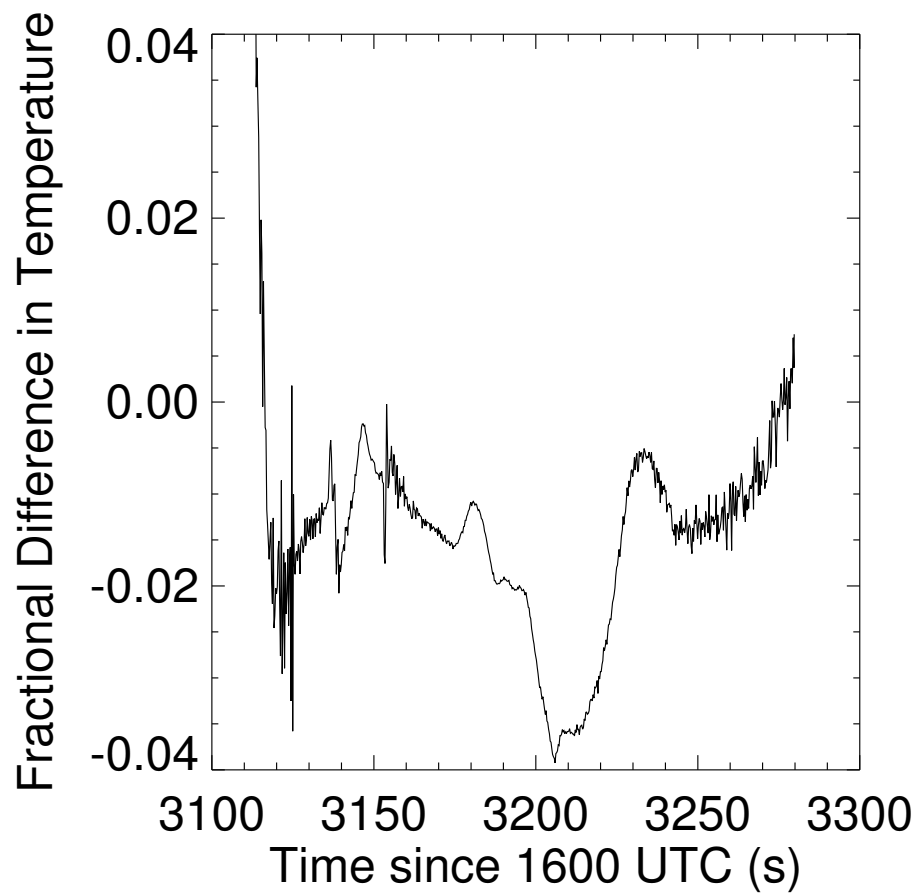


Figure 5.8: As Figure 5.6, but temperature.

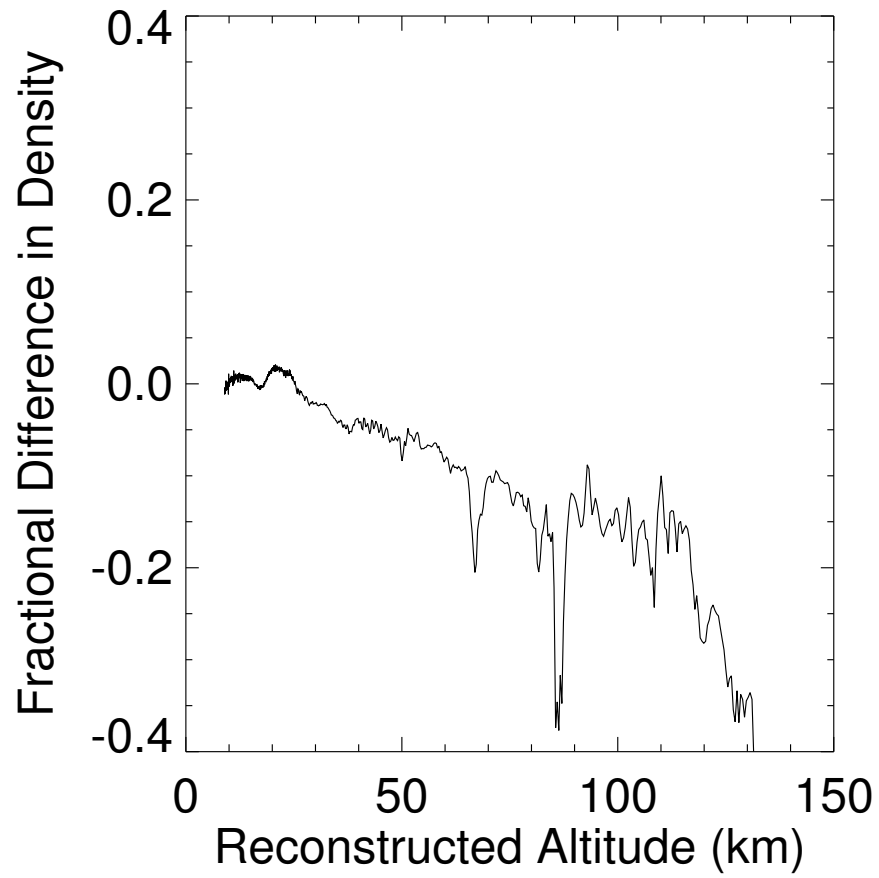


Figure 5.9: The ratio of (PDS reconstructed density minus the results of this chapter using the engineering entry state) to the PDS reconstructed density, plotted against reconstructed altitude.

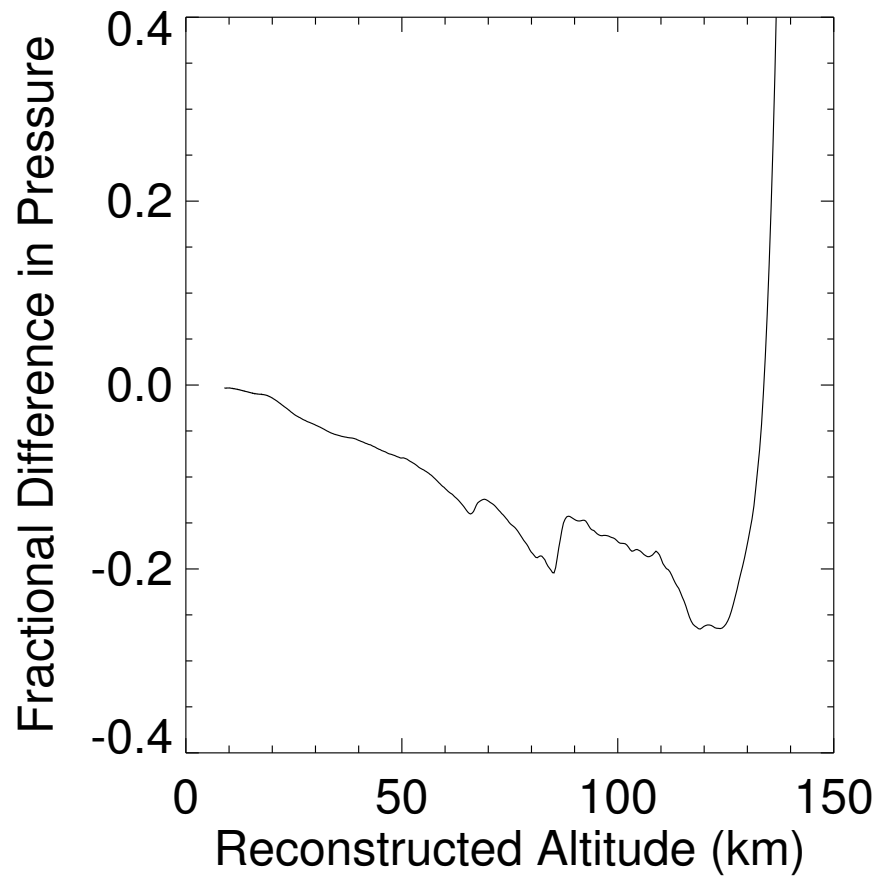


Figure 5.10: As Figure 5.9, but pressure.

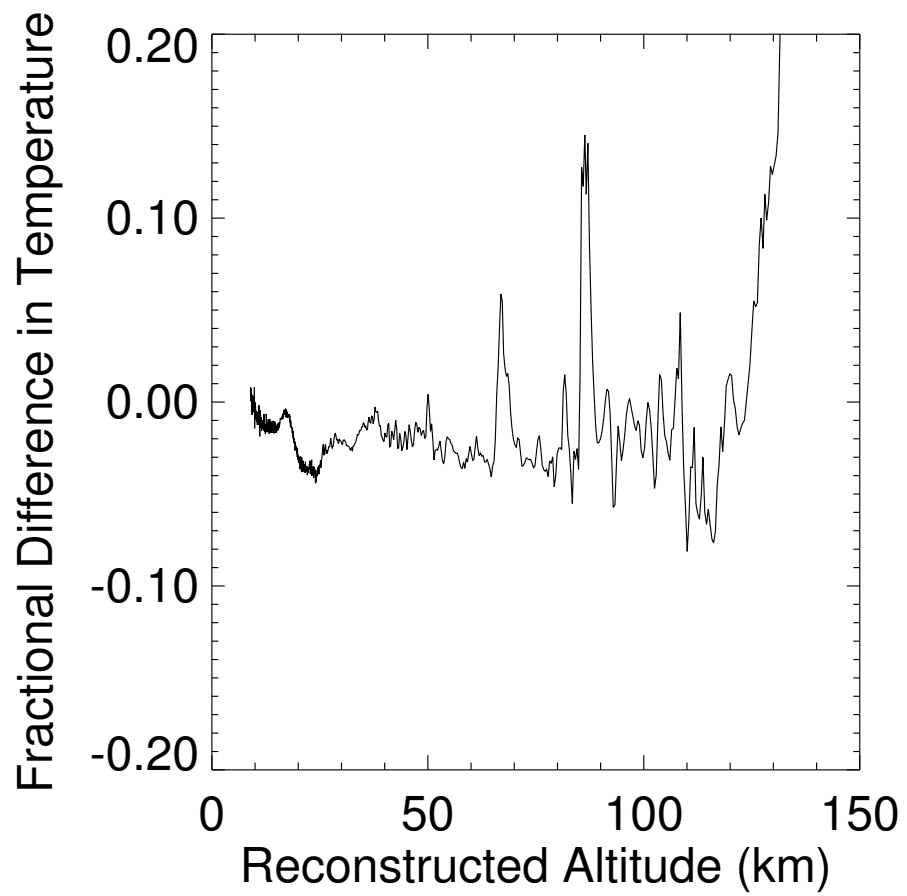


Figure 5.11: As Figure 5.9, but temperature.

5.7.3 $C_D = 2$ Approximation

In sufficiently rarefied atmospheres, *i. e.* at sufficiently high altitudes, the motions of atmospheric molecules are not affected by those of other molecules. In this situation, atmospheric molecules below the spacecraft are dynamically unaware of its impending arrival and are accelerated from near-zero thermal speeds to the kilometre per second-scale entry speed of the spacecraft as they are physically swept up by its passage. The spacecraft sweeps through a volume of atmosphere Av per unit time. It accelerates the mass ρAv of this volume to a speed v . The momentum transferred by the spacecraft to the atmosphere per unit time is therefore ρAv^2 . This is the force exerted parallel to the velocity of the spacecraft with respect to the atmosphere and so, by reference to Equation 5.57, C for this direction should be 2. This is C_D , the drag coefficient. C_D does not change by orders of magnitude during an atmospheric entry, only by tens of percent. This is many times less than the acceleration and velocity, the other terms which change in Equation 5.57 to affect the measurement of atmospheric density.

$C_D = 2$ might be used as a default aerodynamic database in the unfortunate case where no aerodynamic information is available or when a very rapid atmospheric characterization is required. I plot temperature as a function of reconstructed altitude in Figure 5.12 using this approximation. The error increases from about 4% (variable C_D) to about 8% ($C_D = 2$), which is a remarkably accurate result considering how much time-consuming and expensive aerodynamic modelling has been neglected. The fractional error in density, not shown, is equal to the negative fractional difference between the actual and assumed values of C_D . Gravity is nearly constant over the altitude range of atmospheric entry, so pressure is effectively proportional to the integral of density with respect to altitude. Since density is inversely proportional to C_D , and C_D changes slowly with altitude, the ratio of pressure to density is only slightly dependent on C_D . Using the ideal gas equation of state, temperature is proportional to the ratio of pressure to density and also only slightly dependent on C_D . Hence errors in C_D , which may be very important

for the density or pressure results, cause the uncertainty in the temperature results to increase by only a few percentage points.

Two effects are important in understanding why temperature is so weakly dependent on C_D . Neither of them alone is sufficient. First, C_D varies by only tens of percent during atmospheric entry. Second, temperature is proportional to a ratio between an integration of C_D^{-1} over altitude and C_D^{-1} , not directly to C_D .

5.8 Conclusions

I have developed procedures to analyse accelerometer data for trajectory and atmospheric structure reconstruction and outlined them in detail. Different approaches to the problem of tracking spacecraft attitude have been compared and contrasted. My trajectory reconstruction procedures have been verified on the Pathfinder entry. They have uncovered inconsistencies within the previously published work, including the PDS archive. The iterative approach needed to obtain an accurate atmospheric density profile and the pointwise nature of the procedure have been emphasized in my outline of the theory of atmospheric structure reconstruction. My atmospheric structure reconstruction results have been verified on the Pathfinder entry using a very crude aerodynamic database. The results for both the trajectory and atmospheric structure reconstructions are good. A remarkably accurate profile of atmospheric temperature may be obtained without any aerodynamic database whatsoever.

As a service to the community, I have placed simplified versions of my trajectory and atmospheric structure computer programmes online for public use. Interested parties should contact the author, who will be happy to provide them with further details. They are currently online at: <http://www.lpl.arizona.edu/~withers/beagle2/>. Currently the programmes assume a spherically symmetric planet and gravitational field, use only a first order integration technique and model spacecraft aerodynamics with constant C and the *head-on*

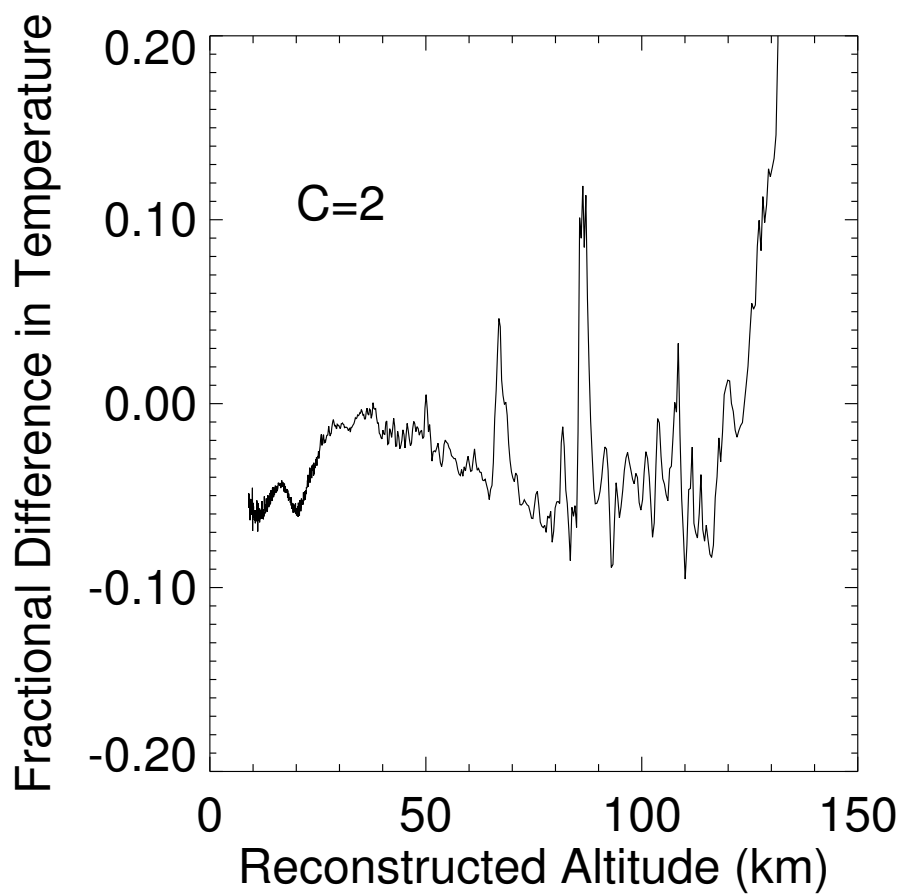


Figure 5.12: The ratio of (PDS reconstructed temperature minus the results of this chapter using the engineering entry state and taking $C_D = 2$) to the PDS reconstructed temperature, plotted against reconstructed altitude.

or *drag-only* options. However it is my intent to further develop them for application to upcoming planetary missions.

5.9 Acknowledgements

Atmospheric structure reconstruction from planetary entry accelerometer data was pioneered by Al Seiff and this chapter owes much to his ideas and achievements (Young and Magalhães, 2001). This work was performed whilst I was a consultant at the Open University working with John Zarnecki, Martin Towner, and Brijen Hathi. It will be published in *Planetary and Space Science* with them as coauthors. John Zarnecki provided supervision and financial support. Martin Towner provided insight into real-world issues with instrumentation and commented on many early drafts of this chapter/publication. There are several short passages in this chapter that are more his words than mine. Brijen Hathi provided helpful discussions on the coordinate frames and aerodynamics. I also acknowledge helpful discussions with Dave Atkinson, Ralph Lorenz, and Bob Tolson.

CHAPTER 6

SCIENTIFIC USES OF CRUDE TELEMETRY DURING ATMOSPHERIC ENTRY

6.1 Abstract

Spacecraft entering an atmosphere often transmit information at a low data rate about their health and activities during this high-risk phase of their mission. If the spacecraft should catastrophically fail during the atmospheric entry, then this telemetry is invaluable for determining what went wrong and preventing future missions from failing in that manner. Sometimes high priority scientific data collected during the entry are also transmitted. In this Section I investigate what scientifically useful information about the atmosphere can be deduced from the basic telemetry signal. My goals are to recover some science from the mission in case of failure and verify, at a crude level, the accuracy of any atmospheric measurements made during the entry if these are later transmitted safely to Earth.

The motivation for this work comes from the failure of Mars Polar Lander, which did not return any telemetry to Earth during its atmospheric entry, and from the upcoming atmospheric entries (with telemetry) of NASA's two Mars Exploration Rovers in early 2004. I was also inspired by the problems of first measuring the surface pressure of Mars and the proposal to send very crude, expendable atmospheric probes to measure density, pressure, and temperature profiles whose results would enable the design of the first landers (Seiff, 1963). This idea was not implemented because early Mariner flybys measured the surface pressure at about the same time that earth-based observations reached a consensus. (Snyder and Moroz,

1992).

I do not analyse any data contained in the telemetry. I use only the Doppler-shifted received telemetry frequency, which depends on the speed of the spacecraft, to determine the spacecraft's trajectory and the atmosphere's properties.

In Section 6.2 I calculate the acceleration, velocity, and position of a spacecraft during atmospheric entry. In Section 6.3 I derive atmospheric properties from the spacecraft's trajectory. In Sections 6.4 –6.7 I apply my results to a hypothetical atmospheric entry to see how useful any of my techniques are in any practical applications.

6.2 Deriving Acceleration, Velocity, and Position

I first consider the dynamics of a spacecraft entering an atmosphere. For simplicity I assume a vertical entry into a non-rotating atmosphere where the only force acting on the spacecraft is aerodynamic drag:

$$\dot{z} = -v \tag{6.1}$$

$$\dot{v} = a = -\frac{\rho C_D v^2 A}{m} \tag{6.2}$$

Where z is altitude, v is speed (positive), a is \dot{v} (negative), ρ is atmospheric density, C_D is the spacecraft's drag coefficient, A is the spacecraft's projected area, and m is the spacecraft's mass. An overdot indicates differentiation with respect to time. I have neglected the effects of gravity for simplicity. They are often smaller than those of drag and can easily be reintroduced into the formalism if desired. Assuming that the spacecraft's attitude is stable, C_D is a known function of the atmospheric composition (assumed known and uniform), v , ρ , and the atmospheric

temperature. Its value is usually close to 2. A and m are assumed to be known and constant during the atmospheric entry. ρ is not known. These equations are discussed in Magalhães et al. (1999).

I assume that, from analysis of the Doppler-shifted received frequency of the telemetry, v is known at equally-spaced points in time and that v changes at most linearly with t between these time points. The time interval is Δ . I label quantities corresponding to the n th time point with a subscript- n . z_0 and v_0 (at the start of the atmospheric entry) are known very accurately from spacecraft tracking during its cruise phase.

I assume that each measurement of v has the same random error, σ_v , except for v_0 which is much better known. The validity of this assumption is discussed later.

Since v changes linearly with t :

$$v(t) = v_n + (v_{n+1} - v_n) \frac{(t - t_n)}{\Delta} \quad (6.3)$$

This is valid between t_n and t_{n+1} . Using Equations 6.1 and 6.3, z_{n+1} can be found in terms of z_n :

$$z_{n+1} = z_n - \int_{t_n}^{t_{n+1}} v(t) dt \quad (6.4)$$

$$z_{n+1} = z_n - \int_{t_n}^{t_{n+1}} v_n + (v_{n+1} - v_n) \frac{(t - t_n)}{\Delta} dt \quad (6.5)$$

$$z_{n+1} = z_n - \int_0^{\Delta} v_n + (v_{n+1} - v_n) \frac{t}{\Delta} dt \quad (6.6)$$

$$z_{n+1} = z_n - v_n \Delta - \frac{(v_{n+1} - v_n) \Delta^2}{2} \quad (6.7)$$

$$z_{n+1} = z_n - \frac{(v_{n+1} + v_n) \Delta}{2} \quad (6.8)$$

Since z_0 is known, all z_n can be found in this way.

I calculate uncertainties for all of the quantities that I derive. I use extensively the following relationship, which is valid for independent, random errors:

$$f = f(x, y, \dots) \quad (6.9)$$

$$(\sigma_f)^2 = \left(\frac{\partial f}{\partial x} \sigma_x \right)^2 + \left(\frac{\partial f}{\partial y} \sigma_y \right)^2 + \dots \quad (6.10)$$

The uncertainty in z_{n+1} is:

$$\sigma_{z_{n+1}}^2 = \sigma_{z_n}^2 + \frac{\Delta^2}{4} (\sigma_{v_{n+1}}^2 + \sigma_{v_n}^2) \quad (6.11)$$

$$\sigma_{z_{n+1}}^2 = \sigma_{z_n}^2 + \frac{\Delta^2 \sigma_v^2}{2} \quad (6.12)$$

Since $z_n - z_{n+1}$ is used later, I also use Equation 6.8 to calculate:

$$\sigma_{z_n - z_{n+1}} = \frac{\Delta \sigma_v}{2} \quad (6.13)$$

Since a is constant between time points, it must change discontinuously at each time point. This makes finding a_{n+1} challenging. I could use the average of the easily calculated a during the preceding and subsequent time intervals, but this would make a_{n+1} dependent on v_{n+2} and earlier v . This does not seem like the most appropriate way of proceeding. Instead, I look at values of a , v , and z halfway between t_n and t_{n+1} . This time is $t_{n+1/2}$. $a_{n+1/2}$, $v_{n+1/2}$, and $z_{n+1/2}$ can all be defined in terms of v_{n+1} and earlier v .

Since a is assumed constant during each Δ time interval:

$$a_{n+1/2} = \frac{v_{n+1} - v_n}{\Delta} \quad (6.14)$$

$$\sigma_{a_{n+1/2}} = \frac{\sigma_v \sqrt{2}}{\Delta} \quad (6.15)$$

And:

$$v_{n+1/2} = \frac{v_n + v_{n+1}}{2} \quad (6.16)$$

$$\sigma_{v_{n+1/2}} = \frac{\sigma_v}{\sqrt{2}} \quad (6.17)$$

$z_{n+1/2}$ is slightly more complicated to find:

$$z_{n+1/2} = z_n - \int_{t_n}^{t_{n+1/2}} v(t) dt \quad (6.18)$$

$$z_{n+1/2} = z_n - \int_{t_n}^{t_{n+1/2}} v_n + (v_{n+1} - v_n) \frac{(t - t_n)}{\Delta} dt \quad (6.19)$$

$$z_{n+1/2} = z_n - \int_0^{\Delta/2} v_n + (v_{n+1} - v_n) \frac{t}{\Delta} dt \quad (6.20)$$

$$z_{n+1/2} = z_n - \frac{v_n \Delta}{2} - \frac{(v_{n+1} - v_n) \Delta^2}{\Delta} \frac{1}{8} \quad (6.21)$$

$$z_{n+1/2} = z_n - \frac{\Delta (3v_n + v_{n+1})}{4} \quad (6.22)$$

$$\sigma_{z_{n+1/2}}^2 = \sigma_{z_n}^2 + \frac{5\Delta^2 \sigma_v^2}{32} \quad (6.23)$$

It is later useful to know $z_{n+3/2} - z_{n+1/2}$, so I first use Equation 6.22 to find $z_{n+3/2}$:

$$z_{n+3/2} = z_{n+1} - \frac{\Delta (3v_{n+1} + v_{n+2})}{4} \quad (6.24)$$

Using Equation 6.8:

$$z_{n+3/2} = z_n - \frac{(v_{n+1} + v_n) \Delta}{2} - \frac{\Delta (3v_{n+1} + v_{n+2})}{4} \quad (6.25)$$

$$z_{n+3/2} = z_n - \frac{3\Delta (4v_{n+1} + 4v_n + 3v_{n+1} + v_{n+2})}{2 \cdot 12} \quad (6.26)$$

$$z_{n+3/2} = z_n - \frac{3\Delta (4v_n + 7v_{n+1} + v_{n+2})}{2 \cdot 12} \quad (6.27)$$

Using Equation 6.22 to compare this to $z_{n+1/2}$:

$$z_{n+1/2} = z_n - \frac{3\Delta}{2} \frac{(3v_n + v_{n+1})}{12} \quad (6.28)$$

I find that:

$$z_{n+3/2} - z_{n+1/2} = \Delta \frac{(v_n + 6v_{n+1} + v_{n+2})}{8} \quad (6.29)$$

$$\sigma_{z_{n+3/2}-z_{n+1/2}}^2 = \frac{\Delta^2}{64} (\sigma_v^2 + 36\sigma_v^2 + \sigma_v^2) \quad (6.30)$$

$$\sigma_{z_{n+3/2}-z_{n+1/2}}^2 = \frac{\Delta^2}{32} (19\sigma_v^2) \quad (6.31)$$

6.3 Deriving Atmospheric Properties

Useful atmospheric properties that can be obtained from these data include vertical profiles of density, pressure, and temperature. There is more than one way to calculate atmospheric properties from measurements of v . Different techniques involve different approximations. An approximate technique may be better than a formally correct technique if the uncertainty on the formally correct estimate of, say, temperature is many times greater than that on the approximate estimate. I shall outline several techniques and then investigate which of them are most useful.

I shall outline one technique for deriving atmospheric density, three techniques for atmospheric pressure, and four for atmospheric temperature. I shall use a variety of superscripts to distinguish pressures and temperatures derived by different techniques. All uncertainty calculations are discussed in Appendix F.

6.3.1 First Technique for Density

Rearranging Equation 6.2, I find that:

$$\rho = \frac{-a}{v^2} \frac{m}{C_D A} \quad (6.32)$$

If C_D is known, then Equation 6.32 can be solved to give the value of ρ at each $t_{n+1/2}$. Since z is also known at these times from Equation 6.22, I have ρ as a function of z .

$$\rho_{n+1/2} = \frac{-a_{n+1/2}}{v_{n+1/2}^2} \frac{m}{C_D A} \quad (6.33)$$

Using Equations 6.14 and 6.16:

$$\rho_{n+1/2} = \frac{v_{n+1} - v_n}{(v_n + v_{n+1})^2} \frac{4m}{\Delta A C_D} \quad (6.34)$$

6.3.2 First Technique for Pressure

In the usual manner, this density profile can be converted into a pressure profile using hydrostatic equilibrium. A temperature profile can then be obtained using an equation of state and the density and pressure profiles. To distinguish the results of this technique from later ones, I label pressures calculated using this technique by p^* .

$$p = \int -\rho g dz \quad (6.35)$$

Where p is pressure and g is the planet's acceleration due to gravity. Rather than using a complicated upper boundary condition, I set p_0 equal to zero. This does not affect results in the lower atmosphere and, as I shall show later, uncertainties in the upper atmosphere are large enough that they prevent any useful estimate of p_0 from the density scale height.

$$p_{n+1}^* = p_n^* + \rho_{n+1/2} g (z_n - z_{n+1}) \quad (6.36)$$

$\rho_{n+1/2}$ can be calculated from Equation 6.34 and $z_n - z_{n+1}$ can be calculated from Equation 6.8.

6.3.3 First Technique for Temperature

To distinguish the results of this technique from later ones, I label temperatures calculated using this technique by T^* . Atmospheric temperature is given by the ideal gas equation of state:

$$T = \frac{pM_{mol}}{\rho k_B} \quad (6.37)$$

Where M_{mol} is the mean molecular mass of the atmosphere (assumed known), and k_B is Boltzmann's constant. Unfortunately, I have calculated above p_n^* and $\rho_{n+1/2}$. A reasonable estimate for ρ_n is the geometric mean of $\rho_{n-1/2}$ and $\rho_{n+1/2}$:

$$\rho_n^2 = \rho_{n-1/2} \rho_{n+1/2} \quad (6.38)$$

$\rho_{n-1/2}$ and $\rho_{n+1/2}$ can be calculated from Equation 6.34. This is correct in the case when v stays constant between $t_{n-1/2}$ and $t_{n+1/2}$ and the atmosphere is isothermal between $z_{n-1/2}$ and $z_{n+1/2}$.

$$T_n^* = \frac{M_{mol} p_n^*}{k_B \rho_n} \quad (6.39)$$

p_n^* can be calculated from Equation 6.36 and ρ_n can be calculated from Equation 6.38.

6.3.4 Second Technique for Temperature

Another technique can also be used. I label temperatures calculated using this technique by $T_n^{\textcircled{a}}$ to distinguish them from those of Section 6.3.3. For an isothermal atmosphere in hydrostatic equilibrium, $\rho(z)$ can be related to atmospheric temperature, T :

$$T = \frac{-M_{mol} g}{k_B} \frac{dz}{d \ln \rho} \quad (6.40)$$

$$T_n^{\textcircled{a}} = \frac{-M_{mol} g}{k_B} \frac{z_{n+1/2} - z_{n-1/2}}{\ln \rho_{n+1/2} - \ln \rho_{n-1/2}} \quad (6.41)$$

$$T_n^{\textcircled{a}} = \frac{-M_{mol} g}{k_B} \frac{z_{n+1/2} - z_{n-1/2}}{\ln \left(\frac{\rho_{n+1/2}}{\rho_{n-1/2}} \right)} \quad (6.42)$$

Using Equation 6.29:

$$T_n^{\textcircled{a}} = \frac{M_{mol} g}{8k_B} \Delta \frac{(v_{n-1} + 6v_n + v_{n+1})}{\ln \left(\frac{\rho_{n+1/2}}{\rho_{n-1/2}} \right)} \quad (6.43)$$

As long as C_D does not change significantly between $t_{n-1/2}$ and $t_{n+1/2}$, the ratio of densities can be calculated without it. Using Equation 6.34:

$$\frac{\rho_{n+1/2}}{\rho_{n-1/2}} = \frac{v_{n+1} - v_n}{(v_n + v_{n+1})^2} \frac{(v_{n-1} + v_n)^2}{v_n - v_{n-1}} \quad (6.44)$$

$$T_n^{\textcircled{a}} = \frac{M_{mol}g}{8k_B} \Delta \frac{(v_{n-1} + 6v_n + v_{n+1})}{\ln \left(\frac{v_{n+1} - v_n}{(v_n + v_{n+1})^2} \frac{(v_{n-1} + v_n)^2}{v_n - v_{n-1}} \right)} \quad (6.45)$$

6.3.5 Second Technique for Pressure

I label pressures calculated in this section as $p^{\textcircled{a}}$. To find the pressure from the density and temperature, I use the ideal gas equation of state and ρ_n from Equation 6.38:

$$p_n^{\textcircled{a}} = \rho_n T_n^{\textcircled{a}} \frac{k_B}{M_{mol}} \quad (6.46)$$

$T_n^{\textcircled{a}}$ can be calculated using Equation 6.45 and ρ_n can be calculated from Equation 6.38.

6.3.6 Third Technique for Temperature

If the acceleration is constant between three, not just two, time points, then Equation 6.45 for $T_n^{\textcircled{a}}$ can be simplified. I label this calculation of T as $T^{\#}$. Using $v_{n-1} = v_n + \delta$ and $v_{n+1} = v_n - \delta$, Equation 6.45 gives:

$$T_n^{\#} = \frac{M_{mol}g}{8k_B} \Delta \frac{8v_n}{\ln \left(\frac{-\delta}{(2v_n - \delta)^2} \frac{(2v_n + \delta)^2}{-\delta} \right)} \quad (6.47)$$

$$T_n^\# = \frac{M_{mol}g}{k_B} \Delta \frac{v_n}{2 \ln \left(\frac{1+\delta/2v_n}{1-\delta/2v_n} \right)} \quad (6.48)$$

$$T_n^\# = \frac{M_{mol}g}{k_B} \Delta \frac{v_n}{2 \ln (1 + \delta/v_n)} \quad (6.49)$$

$$T_n^\# = \frac{M_{mol}g}{k_B} \Delta \frac{v_n^2}{2\delta} \quad (6.50)$$

$$T_n^\# = \frac{M_{mol}g\Delta}{k_B} \frac{v_n^2}{v_{n-1} - v_{n+1}} \quad (6.51)$$

Uncertainties for this derivation of temperature are small, but there are only restricted circumstances in which it can be used.

6.3.7 Third Technique for Pressure

There is yet another approach to finding atmospheric properties. v and z are better known than a , since a involves taking the difference of two large, inaccurate numbers. I label pressures calculated by this technique $p^\#$. Dividing Equation 6.1 by Equation 6.2 gives:

$$\frac{dv}{dz} = \frac{\rho C_D A v}{m} \quad (6.52)$$

$$\int \frac{dv}{v} = \int \frac{\rho g C_D A}{m g} dz \quad (6.53)$$

If I assume that C_D is constant, then by hydrostatic equilibrium:

$$\int \frac{dv}{v} = \frac{-C_D A}{mg} \int dp^\# \quad (6.54)$$

$$\ln \left(\frac{v_n}{v_x} \right) = \frac{-C_D A}{mg} (p_n^\# - p_x) \quad (6.55)$$

$$(p_n^\# - p_x) = \frac{-mg}{C_D A} \ln \left(\frac{v_n}{v_x} \right) \quad (6.56)$$

This formula for p , unlike Equation 6.34 for ρ , does not depend on the difference between two velocities. p_x is unknown, but if I use the top of the atmosphere as a boundary condition, where $v_x = v_0$ is known accurately and p_x is small, then its actual value is irrelevant for values of p lower in the atmosphere.

6.3.8 Fourth Technique for Temperature

I label temperatures calculated by this technique $T^\$$. Similarly to before, assuming an isothermal atmosphere gives:

$$T^\$ = \frac{-M_{mol}g}{k_B} \frac{dz}{d(\ln p^\#)} \quad (6.57)$$

$$T_{n+1/2}^\$ = \frac{M_{mol}g}{k_B} \frac{z_n - z_{n+1}}{\ln p_{n+1}^\# - \ln p_n^\#} \quad (6.58)$$

Using Equation 6.8:

$$T_{n+1/2}^{\$} = \frac{M_{mol}g\Delta}{2k_B} \frac{v_n + v_{n+1}}{\ln\left(\frac{p_{n+1}^{\#}}{p_n^{\#}}\right)} \quad (6.59)$$

$p_n^{\#}$ can be calculated from Equation 6.56.

6.3.9 Summary

The techniques in Sections 6.3.1 – 6.3.6 are closely related to the traditional method of entry accelerometer data analysis practised by Seiff and colleagues. I have not come across the techniques in Sections 6.3.7 – 6.3.8 in the literature of this discipline. Treating C_D as constant is a source of error that I have not considered in the formal uncertainty analysis. Figure 3 of Magalhães et al. (1999) shows how C_D changed during Pathfinder’s descent. However, if there are other large sources of error, this incorrect assumption may be justified. C_D changes by at most 25% over the entire descent of Pathfinder, so densities derived with this assumption are only incorrect by 25% due to this assumption. With changes in density of 8 orders of magnitude, that is not necessarily a major problem. Pressures are in error by a similar amount. The error in density is due to errors in C_D at that instant. However, the errors in pressure are proportional to accumulated errors in C_D over the previous 2 scale heights or so. Densities are directly proportional to C_D , so estimates of the ratio of two densities are not affected by this error as long as C_D does not change greatly between the two points of interest. Estimates of the ratio of two pressures are similarly robust, as are temperatures estimated from the ratio of a pressure and a density measurement.

6.4 Uncertainties in Transmitted Frequency

In the special case in which the line of sight between spacecraft and receiver is parallel to the vertical trajectory of the spacecraft, v is related to the received and

transmitted frequencies as follows:

$$\frac{v}{c} = \frac{f_{trans} - f_{rec}}{f_{trans}} = 1 - \frac{f_{rec}}{f_{trans}} \quad (6.60)$$

$$c - v = c \frac{f_{rec}}{f_{trans}} \quad (6.61)$$

Where c is the speed of light, f_{trans} is the transmitted frequency and f_{rec} is the received frequency. c is known exactly, and f_{rec} is known much more accurately than f_{trans} .

$$\frac{\sigma_{c-v}}{c - v} = \frac{\sigma_{f_{trans}}}{f_{trans}} \quad (6.62)$$

$$\sigma_{c-v} = \sigma_v = (c - v) \frac{\sigma_{f_{trans}}}{f_{trans}} \quad (6.63)$$

$$\sigma_v = c \frac{f_{rec}}{f_{trans}} \frac{\sigma_{f_{trans}}}{f_{trans}} \quad (6.64)$$

Since $v \ll c$ in Equation 6.61:

$$\sigma_v = c \frac{\sigma_{f_{trans}}}{f_{trans}} \quad (6.65)$$

Sam Thurman of JPL has also considered this problem. He sent me some information on the uncertainties in transmitted frequency for Mars Pathfinder (personal communication, 2002). The nominal transmission frequency was about 8.4

GHz. The free-fall drift rate of the oscillator, measured prior to entry, was a few tenths of Hz per second. Extrapolated through the three hundred second atmospheric entry this causes a frequency drift of about 100 Hz. The oscillator frequency is very sensitive to acceleration. Thurman modelled this as a quadratic in g with coefficients of 10 Hz g^{-1} and 5 Hz g^{-2} . In the worst case in which these two terms both cause frequency shifts in the same direction, this effect causes a frequency shift of 600 Hz at maximum acceleration of 10 g. Random noise levels prior to parachute opening were modelled as 3 Hz. This increased to 50 Hz after parachute opening. Parachute opening caused an instantaneous 250 Hz shift in frequency. In this work I am only interested in behaviour prior to parachute opening and find it simplest to model $\sigma_{f_{trans}}$ as random noise. I use $\sigma_{f_{trans}}/f_{trans} = 10^{-7}$. This is slightly larger than Thurman's modelling of the systematic drift which dominates $\sigma_{f_{trans}}$. Assuming that $\sigma_{f_{trans}}$ is random noise allows me to use the equations above. If I assumed a systematic drift, then a more complicated treatment of the errors would be needed.

6.5 Simulated Trajectory and Atmospheric Properties

To see how useful all of this is, I need to use some realistic numbers. I chose those of Mars Pathfinder: $m = 500 \text{ kg}$ and $A = 5 \text{ m}^2$. The martian atmosphere has $M_{mol} = 44 \times 1.67 \times 10^{-27} \text{ kg}$ and $g = 3.7 \text{ m s}^{-2}$. Of course, $k_B = 1.38 \times 10^{-23} \text{ J K}^{-1}$.

I use a vertical atmospheric entry from 120 km altitude to the surface. For simplicity I allow my spacecraft to impact the surface at high speed without braking with parachutes or rockets. I assume a vertical entry speed of 2 km s^{-1} , which is the same as Pathfinder's vertical component of velocity. Pathfinder's actual speed was faster, but on a shallower flight path. I assume that $C_D = 2$ under all conditions. The atmosphere is isothermal at 200 K, with a surface density of $10^{-2} \text{ kg m}^{-3}$ and a scale height of 10 km.

I first calculate v , z , a , ρ , p , and T that are actually experienced during

the simulated descent as functions of t . a is known from Equation 6.2, v from integrating Equation 6.2, and z from integrating Equation 6.1. I use a simple first-order integration routine with a timestep of 1 s. Using shorter timesteps did not change the derived trajectory. T is always 200 K. ρ is found from integrating Equation 6.40 and p is found from Equation 6.37. z , v , a , ρ , and p are plotted as functions of t in Figures 6.1 – 6.5.

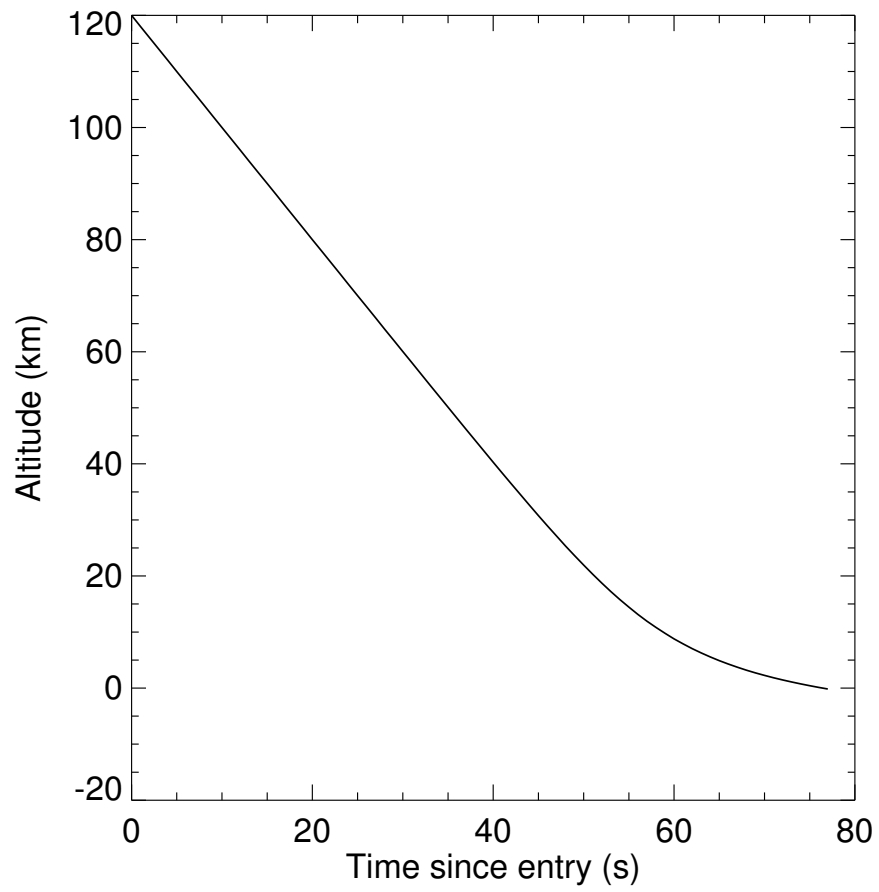


Figure 6.1: Altitude versus time for the simulated atmospheric entry

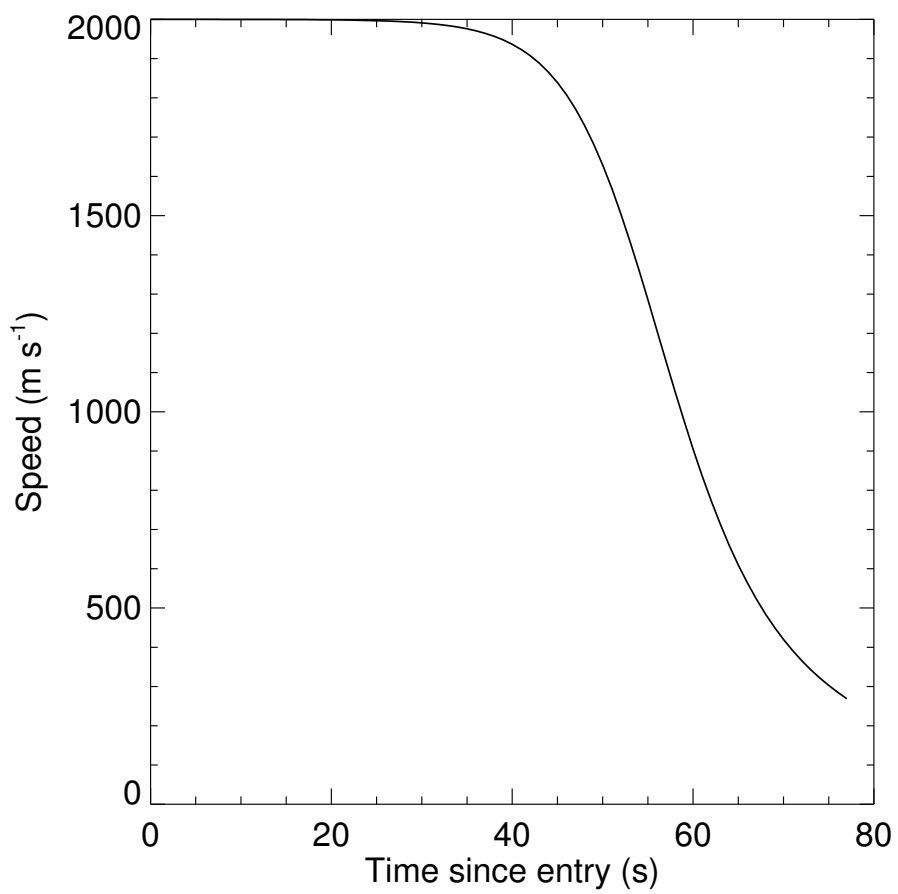


Figure 6.2: Speed versus time for the simulated atmospheric entry

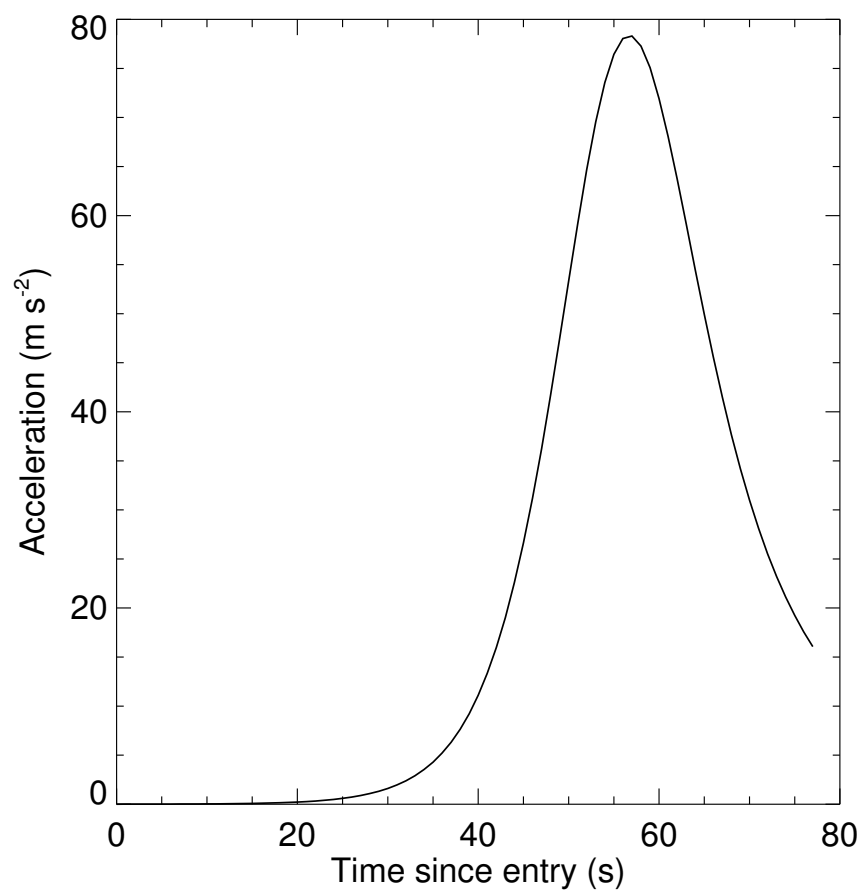


Figure 6.3: Acceleration versus time for the simulated atmospheric entry

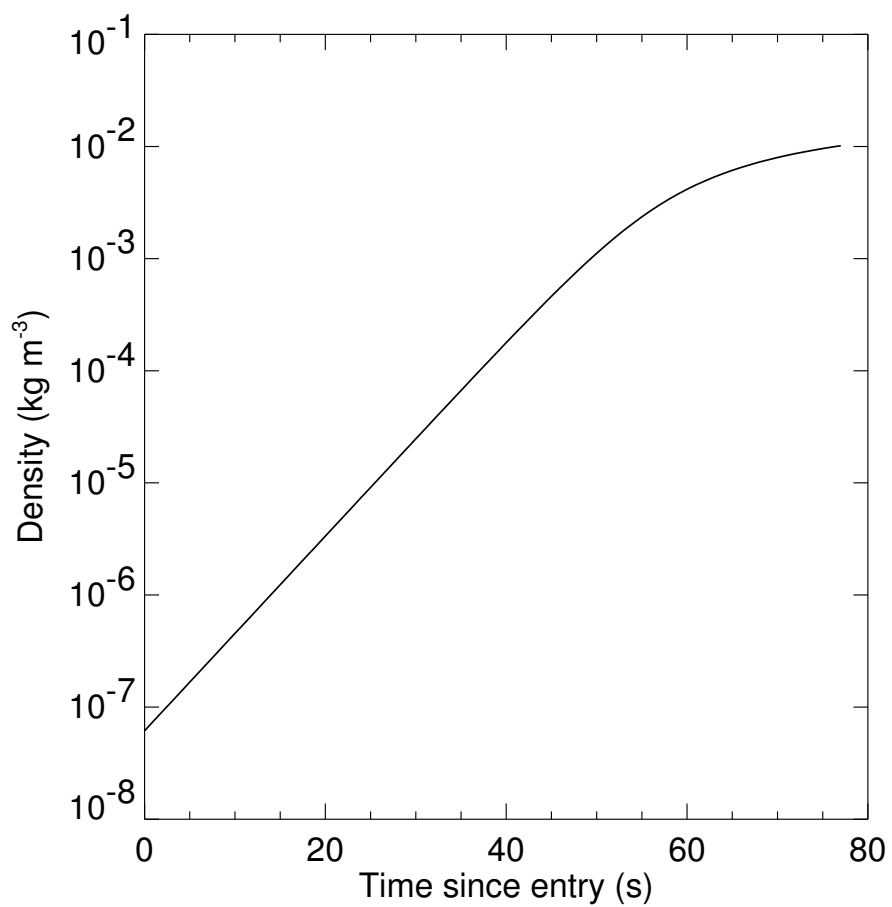


Figure 6.4: Density versus time for the simulated atmospheric entry

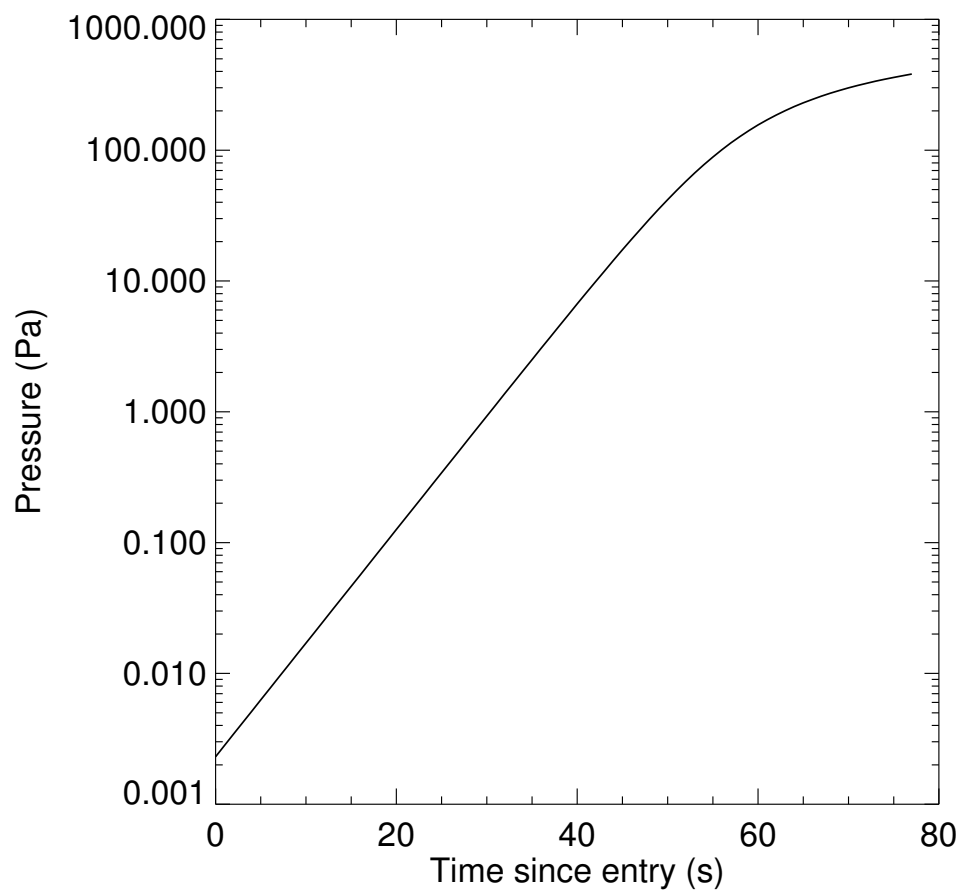


Figure 6.5: Pressure versus time for the simulated atmospheric entry

The total flight time is about 70 – 80 seconds. This is much shorter than Pathfinder’s 300 s descent because of Pathfinder’s shallower flight path. I chose Δ to be 4 s. In reality telemetry is continuous, not intermittent. In that case signals within a certain time interval are averaged to reduce their random noise level. The time interval should be long enough to usefully reduce the noise and short enough that atmospheric properties are not changing too much during it. Since I am representing a systematic drift as a random noise in order to get an idea for what’s going on, I cannot average to reduce the noise level. 4 s at 2 km s⁻¹ corresponds to travelling nearly an atmospheric scale height.

6.6 Derived Trajectory and Atmospheric Properties Using Clean v

First, I calculated $z, v, a, \rho, p,$ and T from my various techniques using the simulated values of v with the specified σ_v of $c/10^7$. With this approach, calculated quantities should be close to their simulated values and the uncertainties should be somewhat realistic. Afterwards I use noisy values of v to calculate all these quantities.

Figures 6.6 – 6.19 show $z_n, z_{n+1/2}, v_n, v_{n+1/2}, a_{n+1/2}, \rho_{n+1/2}, \rho_n, p_n^*, p_n^{\textcircled{Q}}, p_n^{\#}, T_n^*, T_n^{\textcircled{Q}}, T_n^{\#},$ and $T_{n+1/2}^{\textcircled{S}}$ as functions of t . Uncertainties for each quantity are plotted, as are the simulated values experienced during entry.

Both z_n and $z_{n+1/2}$ (Figures 6.6 and 6.7) have uncertainties smaller than the size of the symbols. $v_{n+1/2}$ (Figure 6.9) has uncertainties smaller than the size of the symbols. $a_{n+1/2}$ (Figure 6.10) has large uncertainties. This suggests that quantities derived from $a_{n+1/2}$ are uncertain. $\rho_{n+1/2}$ (Figure 6.11) only has small uncertainties after $t = 40$ s. ρ_n (Figure 6.12) only has small uncertainties between $t = 45$ s and 70 s. p_n^* (Figure 6.13) only has small uncertainties after $t = 40$ s. $p_n^{\textcircled{Q}}$ (Figure 6.14) never has small uncertainties. $p_n^{\#}$ (Figure 6.15) only has small uncertainties after $t = 40$ s. T_n^* (Figure 6.16) only has uncertainties of less than 100 K between $t = 50$ s and 60 s. $T_n^{\textcircled{Q}}$ (Figure 6.17) is similar. $T_n^{\#}$ (Figure 6.18) is interesting. This temperature measurement is only valid when a is constant during two consecutive

time intervals. This corresponds to the peak in Figure 6.10. If this peak can be accurately located in the data, then *one* good temperature measurement with small uncertainties can be made. In this case, it is at about $t = 55$ s. Using simulated (not noisy) v gives a very good measurement of the temperature at this point. I shall later investigate how good the measurement is using noisy v data. $T_{n+1/2}^{\$}$ (Figure 6.19) has uncertainties of less than 100 K after $t = 40$ s.

p_n^* and $p_n^\#$ have smaller uncertainties than p_n° . $T_{n+1/2}^{\$}$ has smaller uncertainties than T_n^* and T_n° . $T_n^\#$ may give one and only one accurate temperature measurement during descent at the time of maximum acceleration.

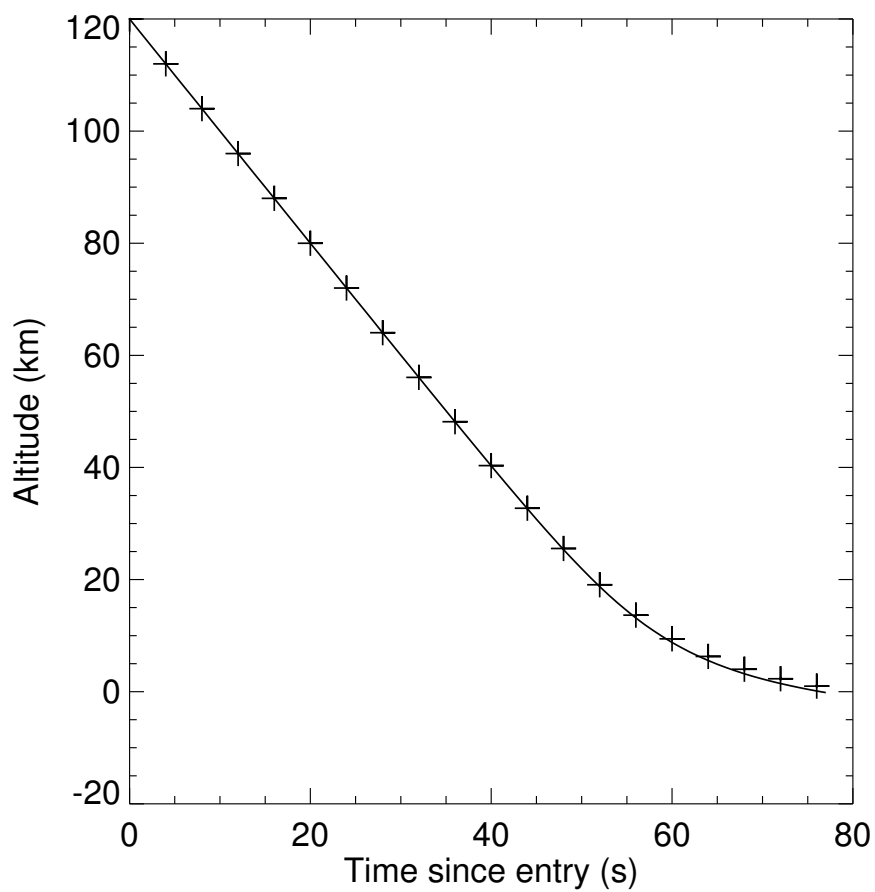


Figure 6.6: z_n (crosses) and σ_{z_n} (vertical lines) versus time calculated using simulated v . Continuous curve is simulated z versus t experienced during the atmospheric entry.

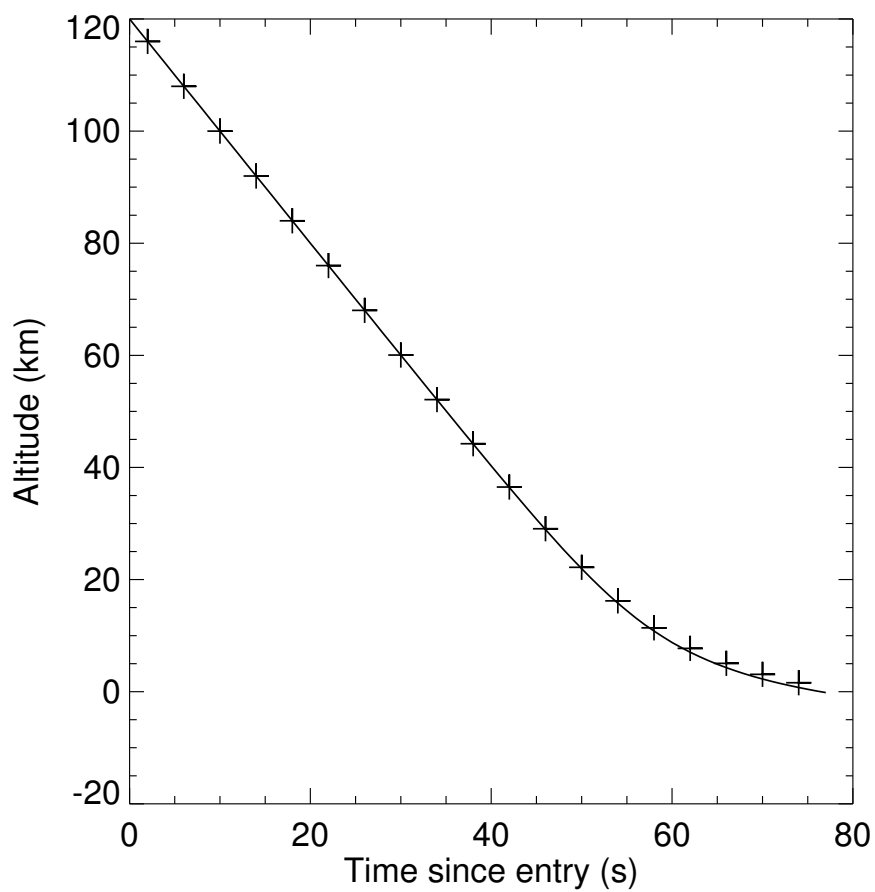


Figure 6.7: $z_{n+1/2}$ (crosses) and $\sigma_{z_{n+1/2}}$ (vertical lines) versus time calculated using simulated v . Continuous curve is simulated z versus t experienced during the atmospheric entry.

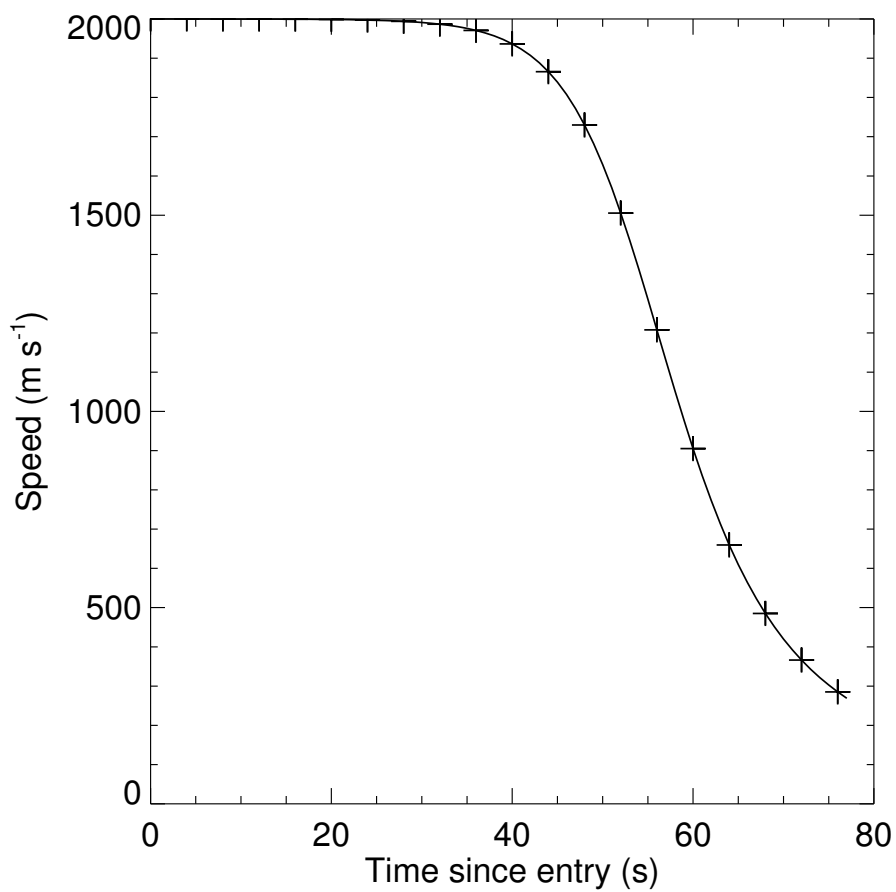


Figure 6.8: v_n (crosses) and σ_{v_n} (vertical lines) versus time calculated using simulated v . Continuous curve is simulated v versus t experienced during the atmospheric entry.

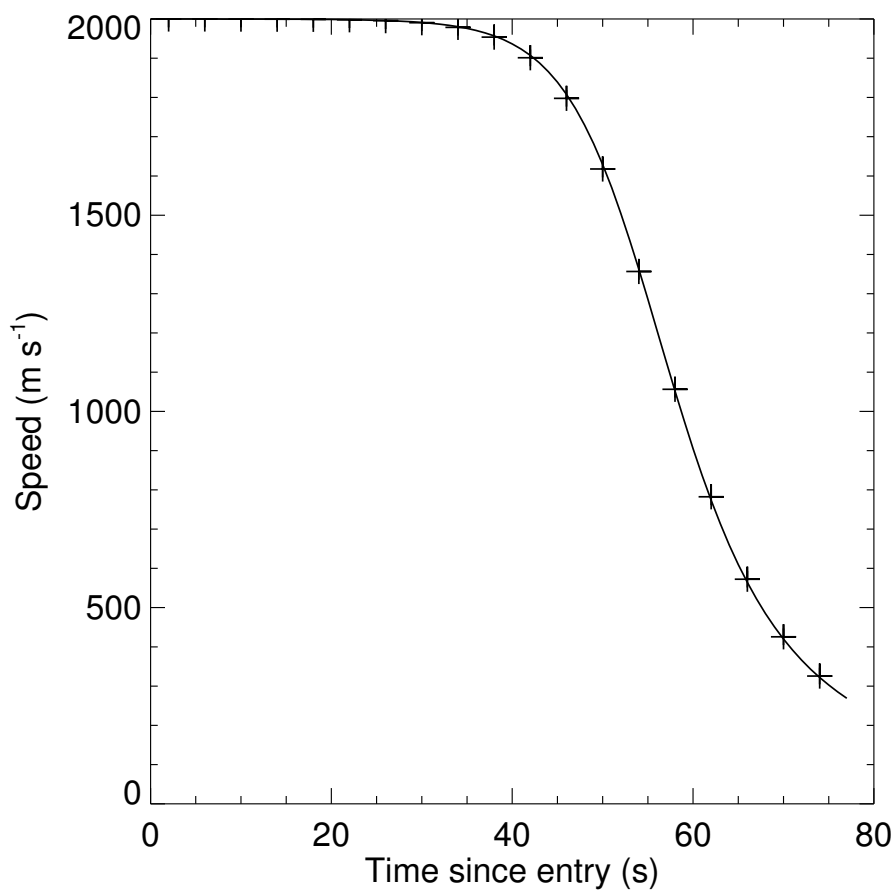


Figure 6.9: $v_{n+1/2}$ (crosses) and $\sigma_{v_{n+1/2}}$ (vertical lines) versus time calculated using simulated v . Continuous curve is simulated v versus t experienced during the atmospheric entry.

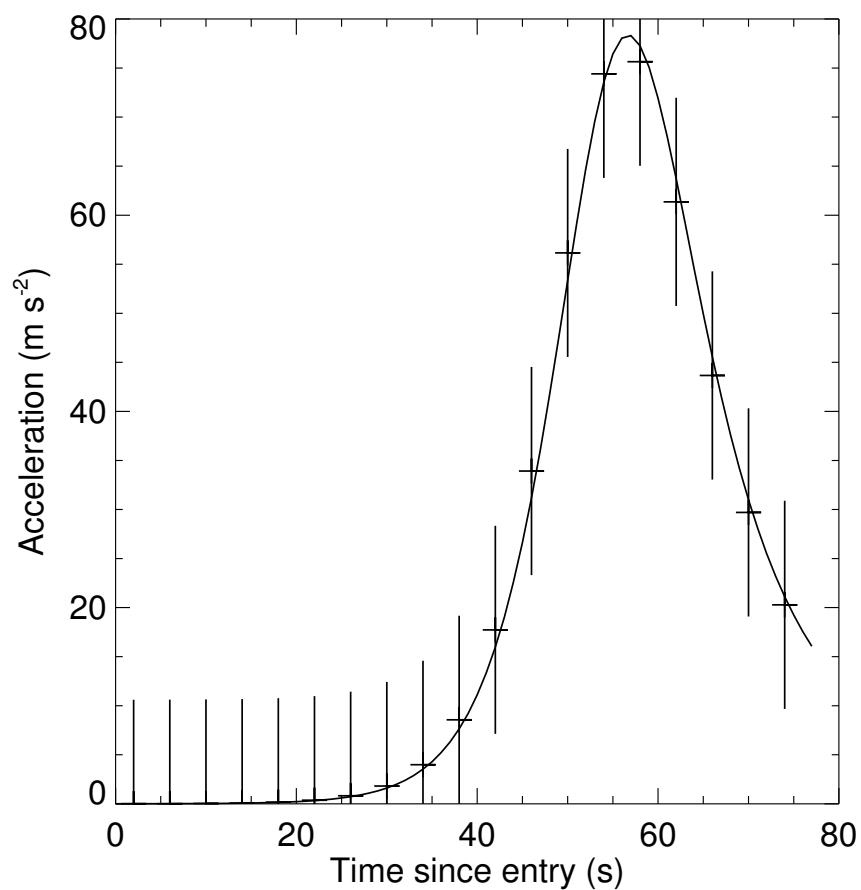


Figure 6.10: $a_{n+1/2}$ (crosses) and $\sigma_{a_{n+1/2}}$ (vertical lines) versus time calculated using simulated v . Continuous curve is simulated a versus t experienced during the atmospheric entry.

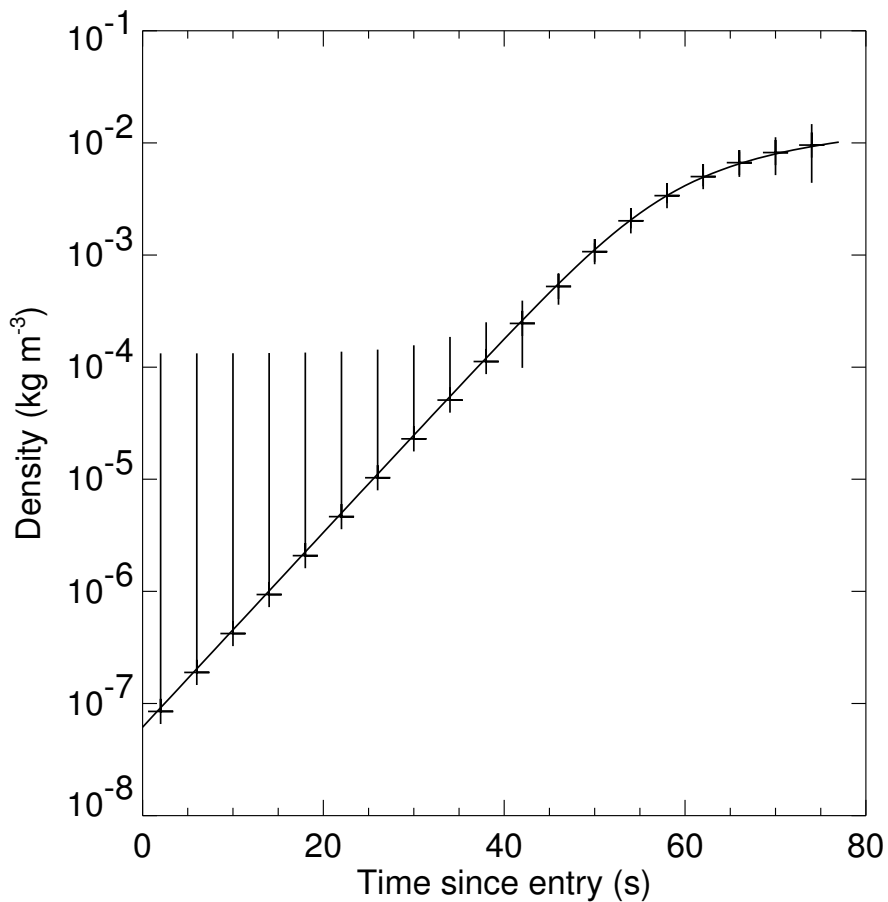


Figure 6.11: $\rho_{n+1/2}$ (crosses) and $\sigma_{\rho_{n+1/2}}$ (vertical lines) versus time calculated using simulated v . If $\rho_{n+1/2} - \sigma_{\rho_{n+1/2}}$ is negative, then only one side of the error bar is plotted. Continuous curve is simulated ρ versus t experienced during the atmospheric entry.

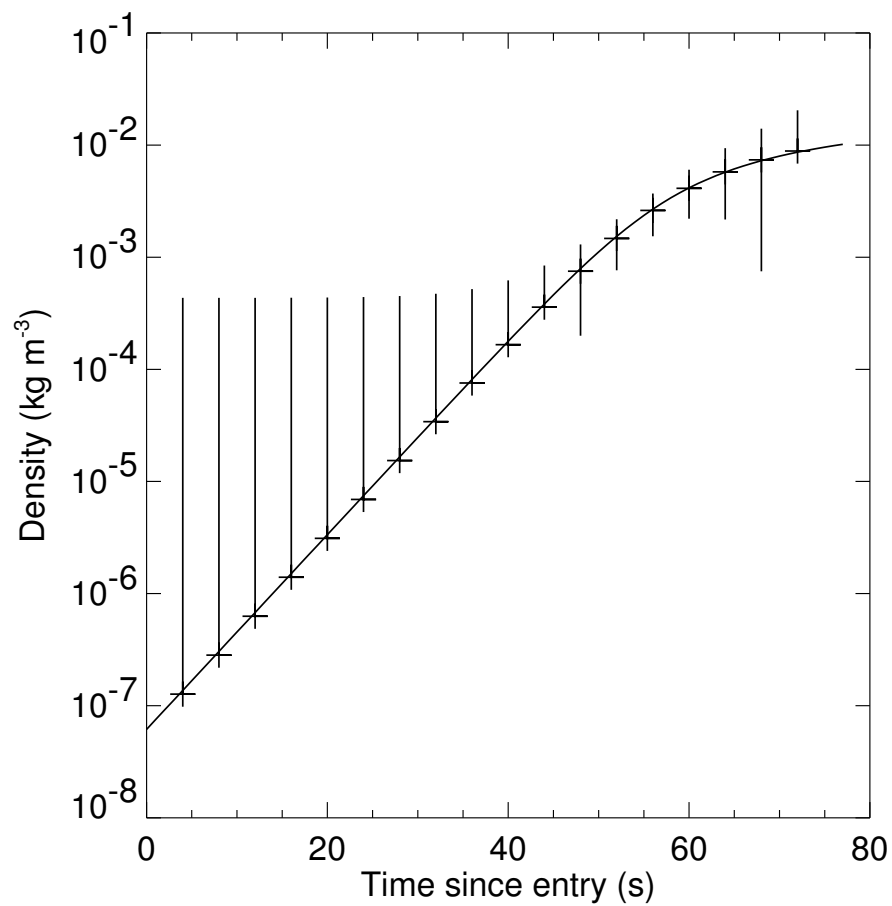


Figure 6.12: ρ_n (crosses) and σ_{ρ_n} (vertical lines) versus time calculated using simulated v . If $\rho_n - \sigma_{\rho_n}$ is negative, then only one side of the error bar is plotted. Continuous curve is simulated ρ versus t experienced during the atmospheric entry.

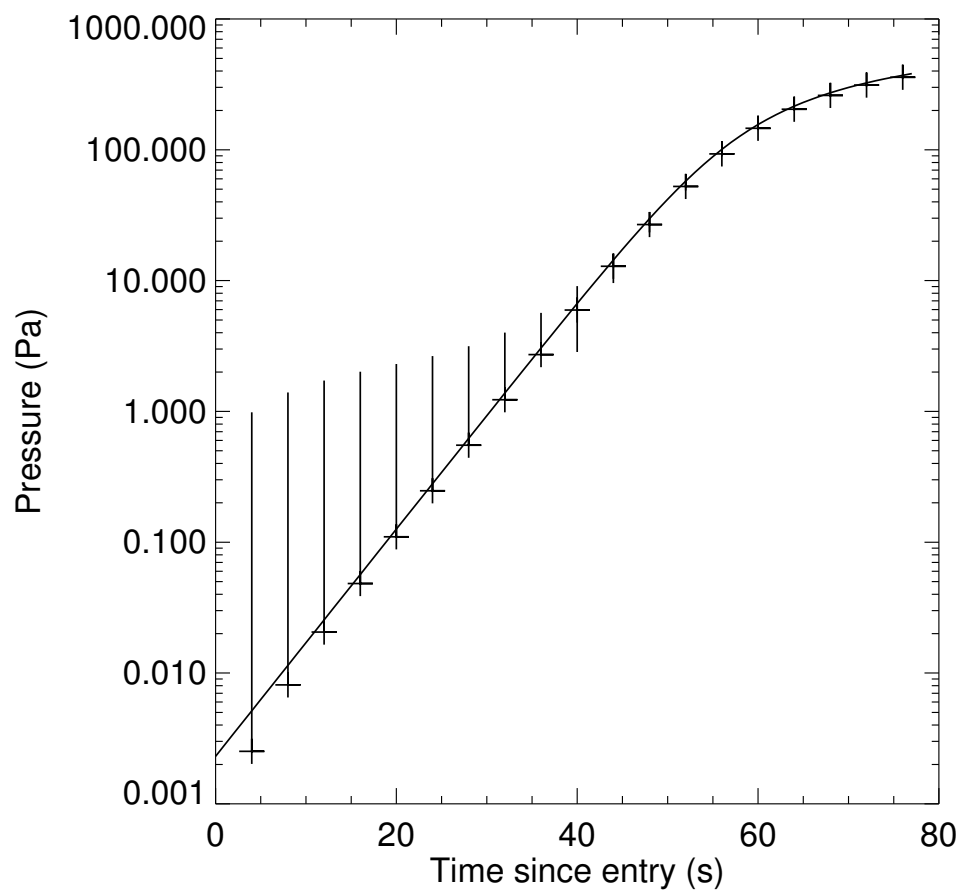


Figure 6.13: p_n^* (crosses) and $\sigma_{p_n^*}$ (vertical lines) versus time calculated using simulated v . If $p_n^* - \sigma_{p_n^*}$ is negative, then only one side of the error bar is plotted. Continuous curve is simulated p versus t experienced during the atmospheric entry.

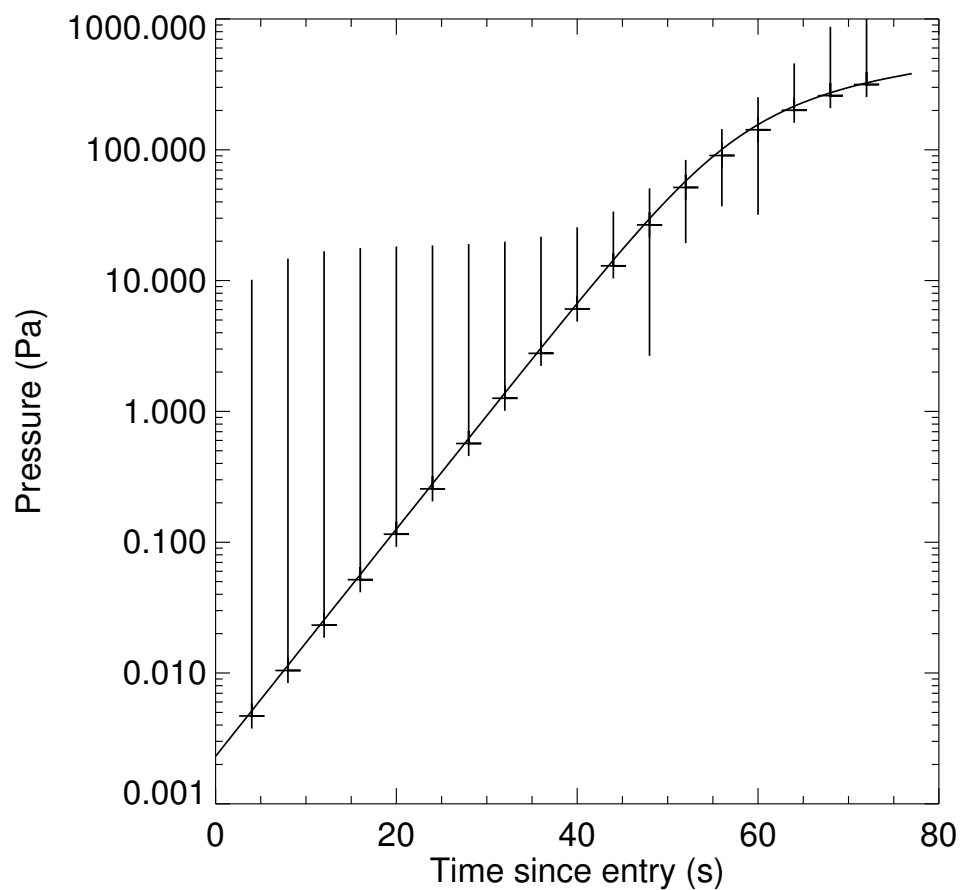


Figure 6.14: $p_n^{\textcircled{a}}$ (crosses) and $\sigma_{p_n^{\textcircled{a}}}$ (vertical lines) versus time calculated using simulated v . If $p_n^{\textcircled{a}} - \sigma_{p_n^{\textcircled{a}}}$ is negative, then only one side of the error bar is plotted. Continuous curve is simulated p versus t experienced during the atmospheric entry.

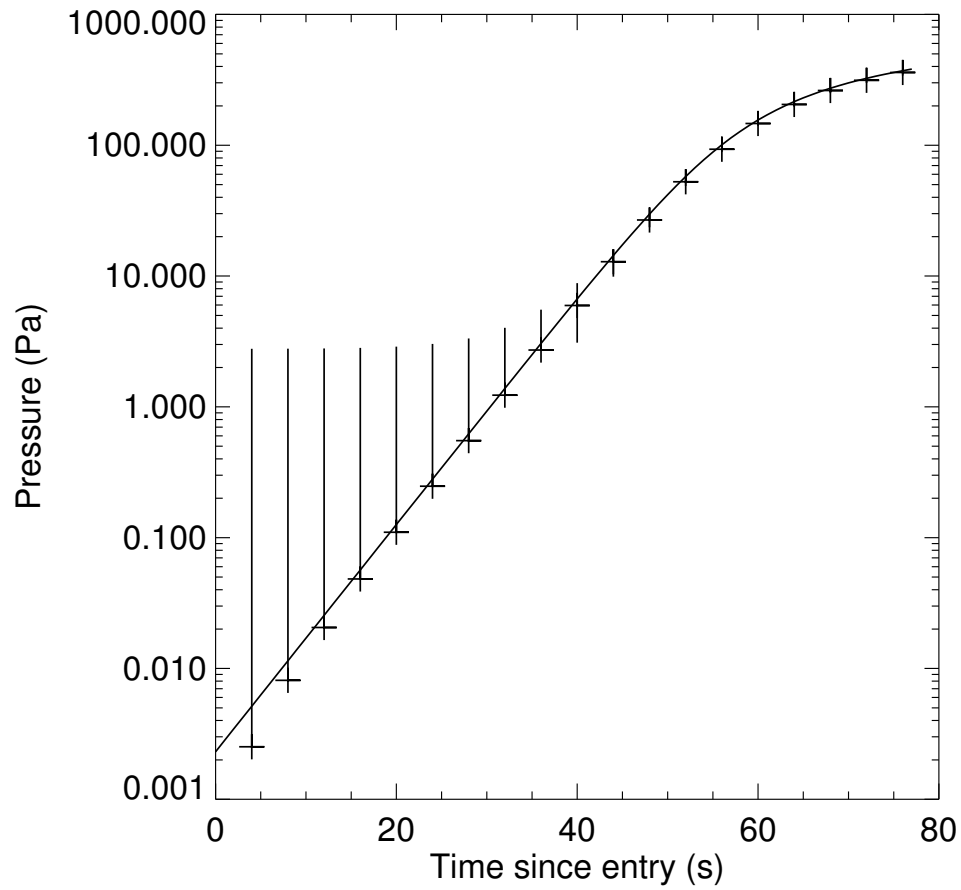


Figure 6.15: $p_n^\#$ (crosses) and $\sigma_{p_n^\#}$ (vertical lines) versus time calculated using simulated v . If $p_n^\# - \sigma_{p_n^\#}$ is negative, then only one side of the error bar is plotted. Continuous curve is simulated p versus t experienced during the atmospheric entry.

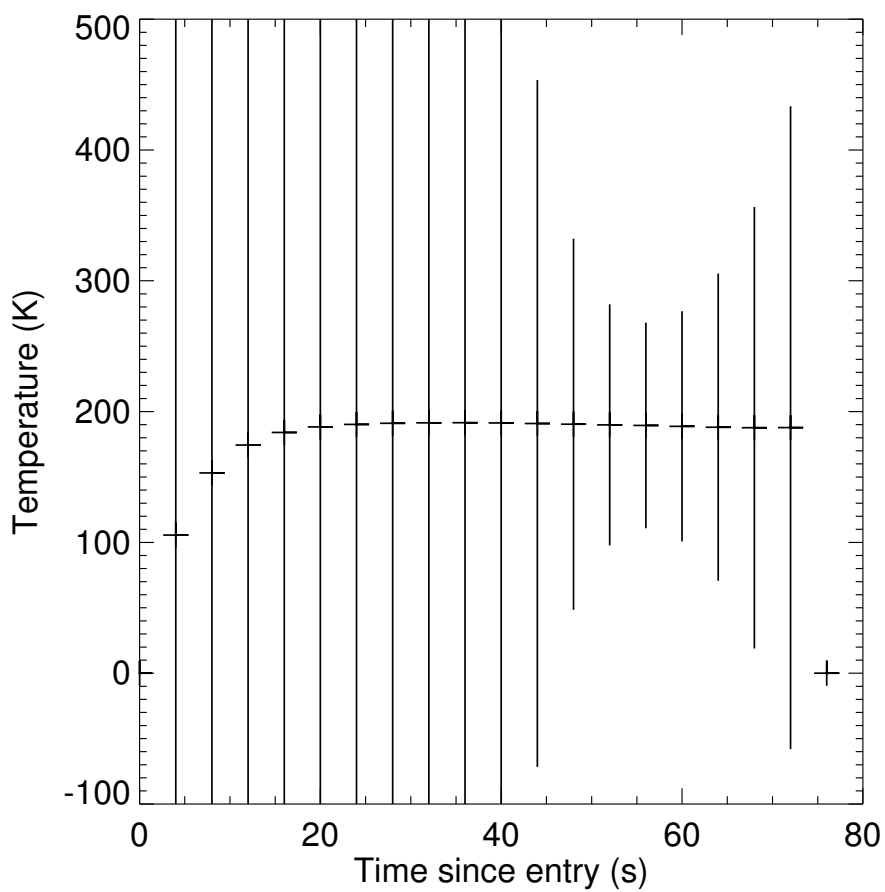


Figure 6.16: T_n^* (crosses) and $\sigma_{T_n^*}$ (vertical lines) versus time calculated using simulated v . Simulated T during the atmospheric entry is 200 K.

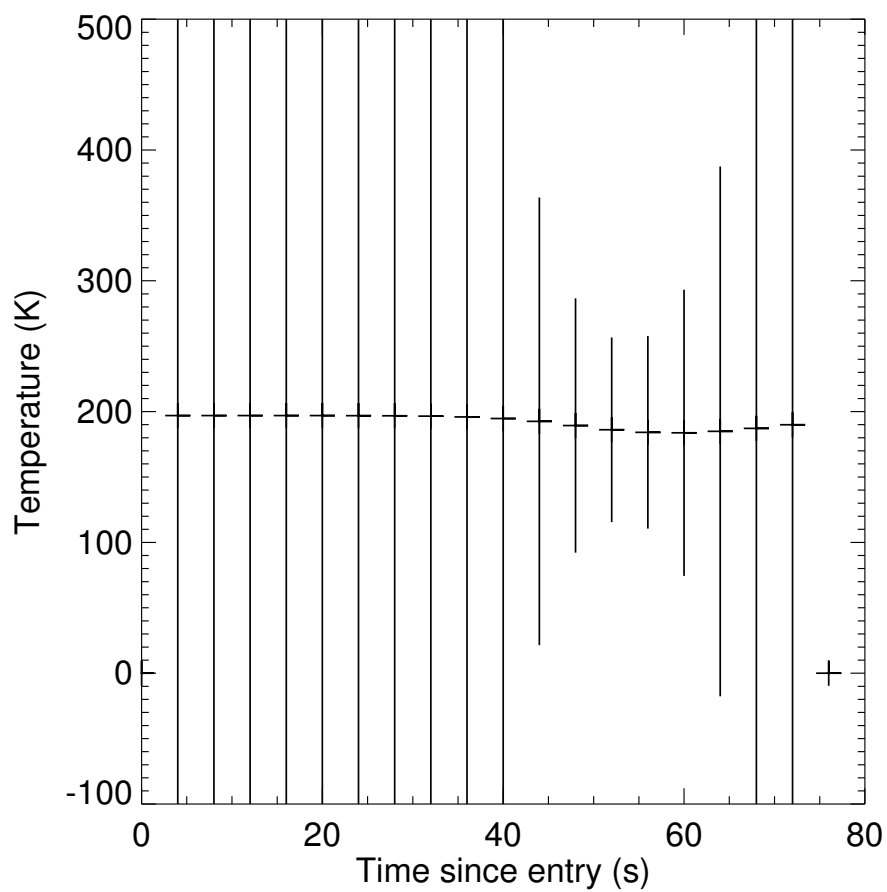


Figure 6.17: $T_n^{\textcircled{a}}$ (crosses) and $\sigma_{T_n^{\textcircled{a}}}$ (vertical lines) versus time calculated using simulated v . Simulated T during the atmospheric entry is 200 K.

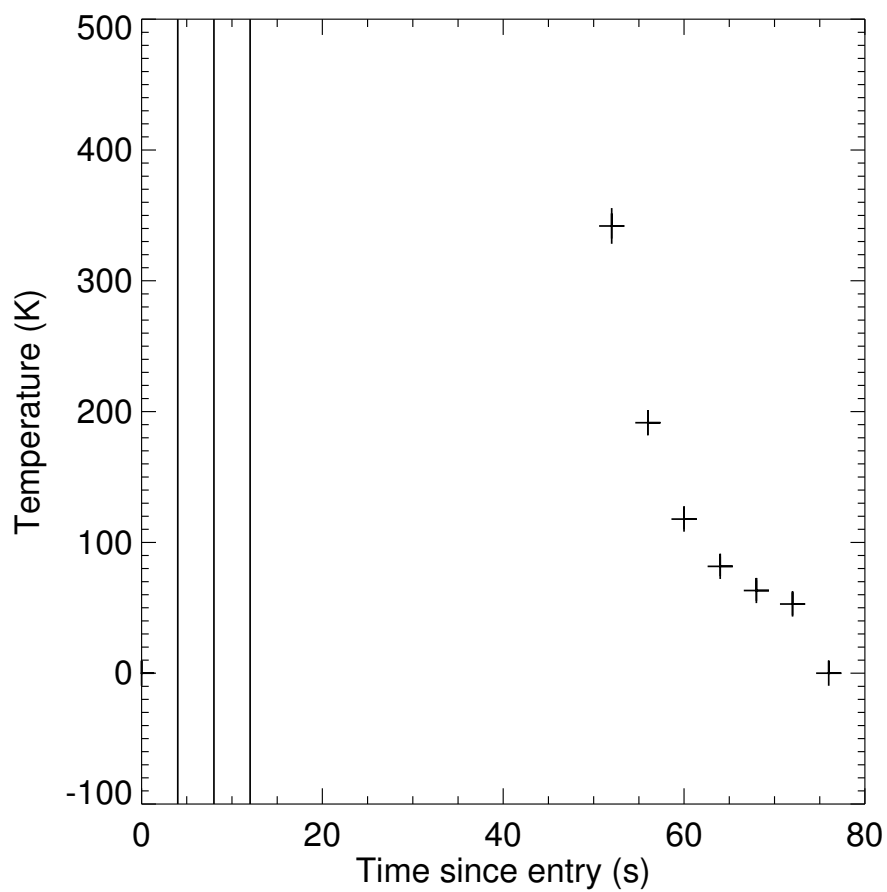


Figure 6.18: $T_n^\#$ (crosses) and $\sigma_{T_n^\#}$ (vertical lines) versus time calculated using simulated v . Simulated T during the atmospheric entry is 200 K.

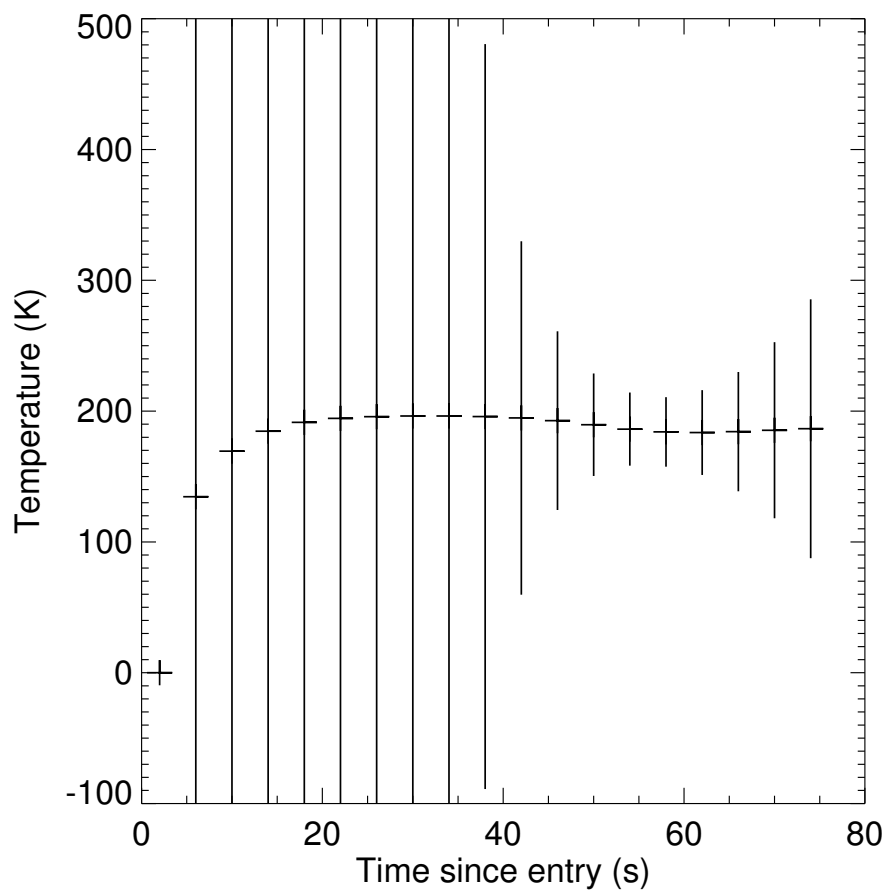


Figure 6.19: $T_{n+1/2}^{\$}$ (crosses) and $\sigma_{T_{n+1/2}^{\$}}$ (vertical lines) versus time calculated using simulated v . Simulated T during the atmospheric entry is 200 K.

6.7 Derived Trajectory and Atmospheric Properties Using Noisy v

Next I added random noise corresponding to σ_v to the v_n derived at each time point from the telemetry. I used the noisy v_n and σ_v to calculate z, v, a, ρ, p , and T from my various techniques. This is the closest analogy to actual practical application of these techniques on real data.

Figures 6.20 – 6.33 show $z_n, z_{n+1/2}, v_n, v_{n+1/2}, a_{n+1/2}, \rho_{n+1/2}, \rho_n, p_n^*, p_n^{\textcircled{a}}, p_n^{\#}, T_n^*, T_n^{\textcircled{a}}, T_n^{\#}$, and $T_{n+1/2}^{\textcircled{s}}$ as functions of t . Uncertainties for each quantity are plotted, as are the simulated values experienced during entry.

Both z_n and $z_{n+1/2}$ (Figures 6.20 and 6.21) are accurately derived and have uncertainties smaller than the size of the symbols. $v_{n+1/2}$ (Figure 6.23) is accurately derived and has small uncertainties. $a_{n+1/2}$ (Figure 6.24) is not very accurately derived and has large uncertainties. However, the peak is quite well identified and this bodes well for the one useful result of $T_n^{\#}$. $\rho_{n+1/2}$ (Figure 6.25) is accurately derived after $t = 45$ s. ρ_n (Figure 6.26) is accurately derived, with larger uncertainties, between $t = 45$ s and 65 s. p_n^* (Figure 6.27) is accurately derived with small uncertainties after $t = 45$ s. $p_n^{\textcircled{a}}$ (Figure 6.28) has such large uncertainties as to be useless. $p_n^{\#}$ (Figure 6.29) is accurately derived with small uncertainties after $t = 45$ s. T_n^* (Figure 6.30) has uncertainties of about 100 K between $t = 45$ s and 65 s. The temperature values in this time range are clearly centred on the correct 200 K result, so averaging them would improve the temperature measurement at the cost of vertical resolution. $T_n^{\textcircled{a}}$ (Figure 6.31) is useless. All values of $T_n^{\#}$ that appear in Figure 6.32 have small uncertainties. However, only the measurement closest to the peak in acceleration is correct. If that peak can be identified well, then $T_n^{\#}$ provides one correct temperature measurement with a small uncertainty. In this example, the peak is clear and the $T_{54s}^{\#}$ measurement of about 200 K is easily selected. By repeating this work for different noisy values of v , I find that the peak in acceleration is almost always clear enough to narrow down the useful $T_n^{\#}$ measurement to at most two possibilities. $T_{n+1/2}^{\textcircled{s}}$ (Figure 6.33) has uncertainties

of less than 100 K between $t = 45$ s and 65 s. The temperature values in this time range are clearly centred on the correct 200 K result, so averaging them would improve the temperature measurement at the cost of vertical resolution.

The spacecraft's position as a function of time can be derived quite well using the techniques presented here. Correct values of atmospheric densities and pressures after 45 s (below 30 km) can be accurately derived with small uncertainties. Atmospheric temperatures can be accurately measured at the point of peak acceleration if that peak can be accurately identified. $T_{n+1/2}^{\$}$ is the most useful of the other techniques for measuring temperature. By reformulating the problem to eliminate poorly-constrained differences in speed, the uncertainties are reduced.

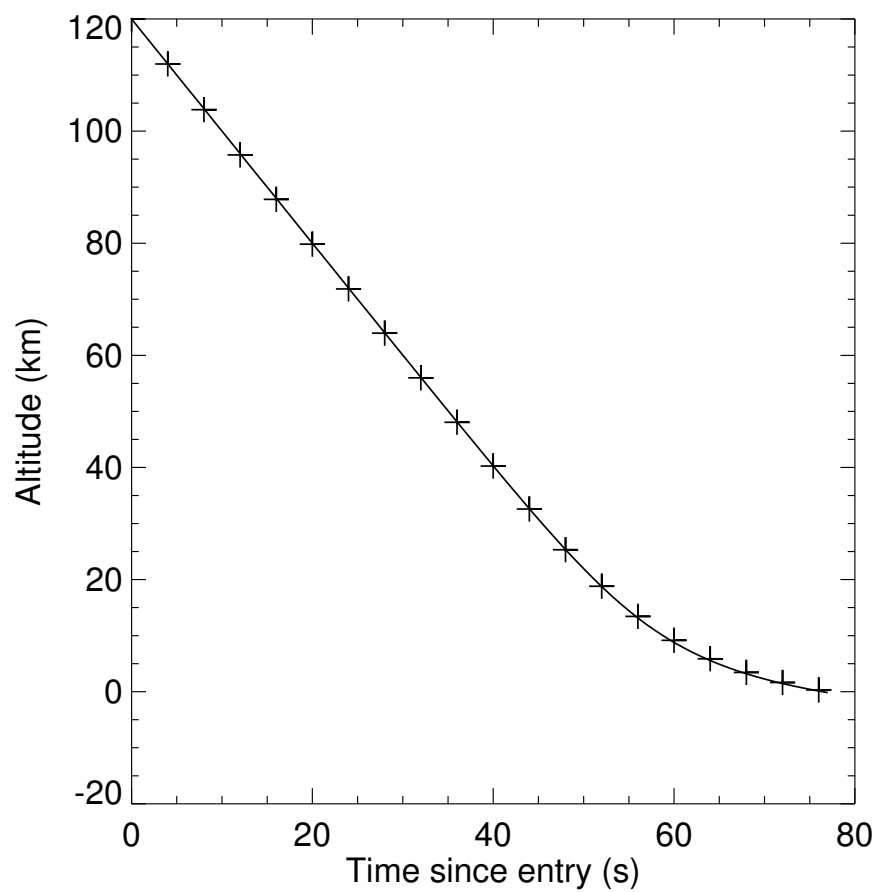


Figure 6.20: z_n (crosses) and σ_{z_n} (vertical lines) versus time calculated using noisy v . Continuous curve is simulated z versus t experienced during the atmospheric entry.

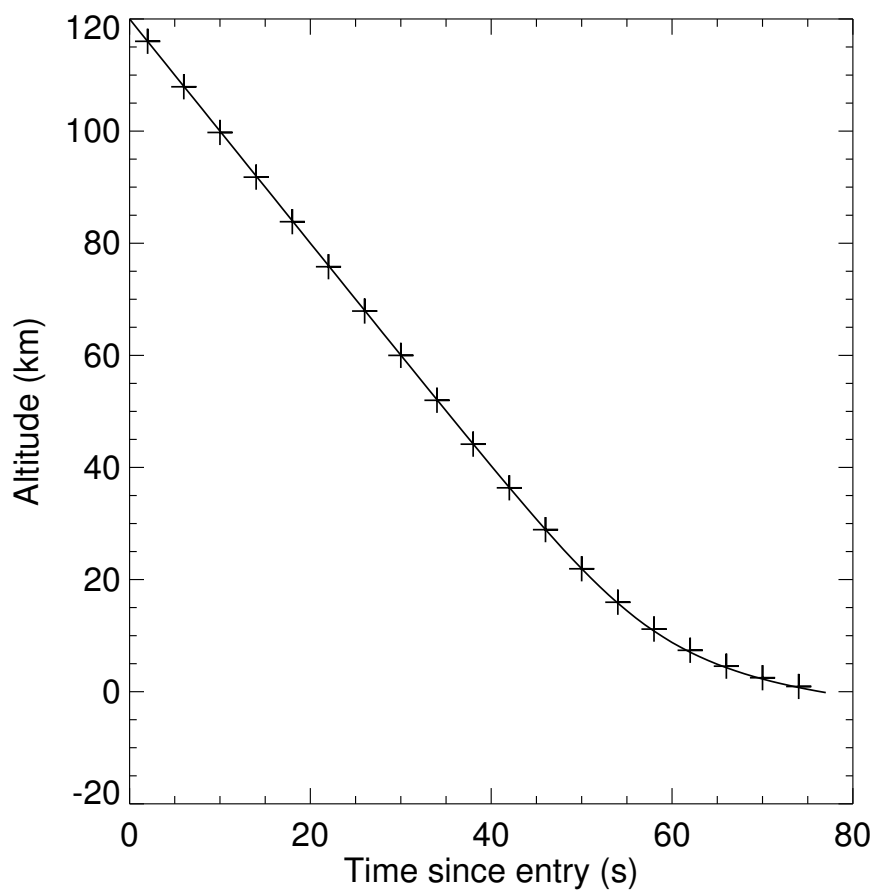


Figure 6.21: $z_{n+1/2}$ (crosses) and $\sigma_{z_{n+1/2}}$ (vertical lines) versus time calculated using noisy v . Continuous curve is simulated z versus t experienced during the atmospheric entry.

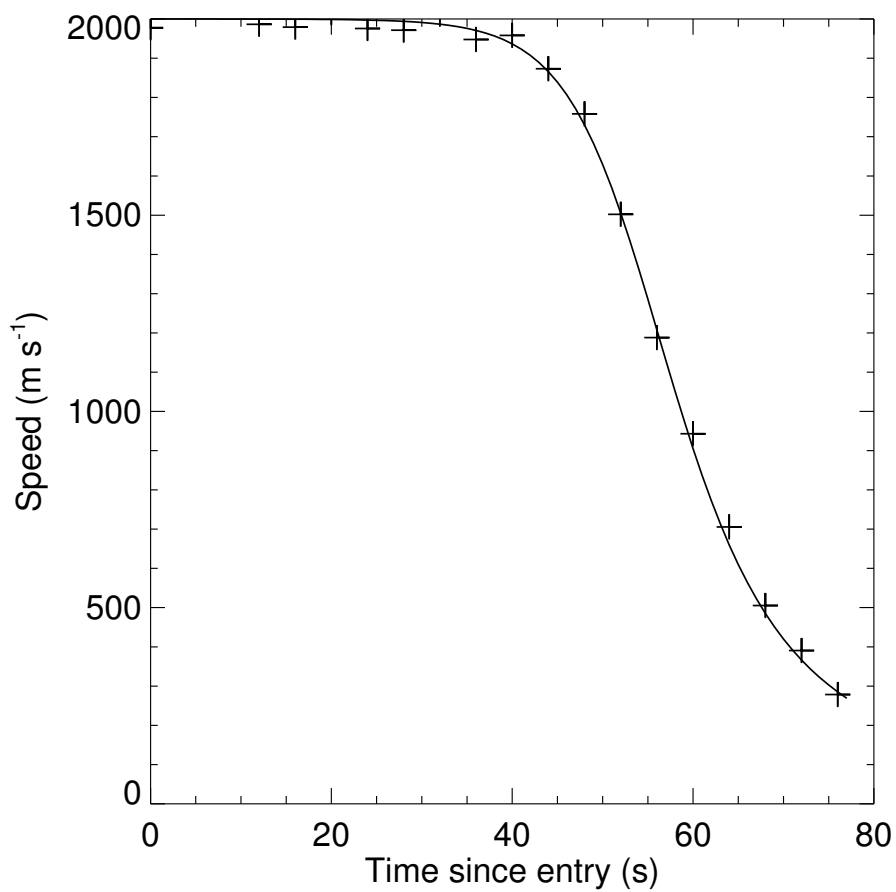


Figure 6.22: v_n (crosses) and σ_{v_n} (vertical lines) versus time calculated using noisy v . Continuous curve is simulated v versus t experienced during the atmospheric entry.

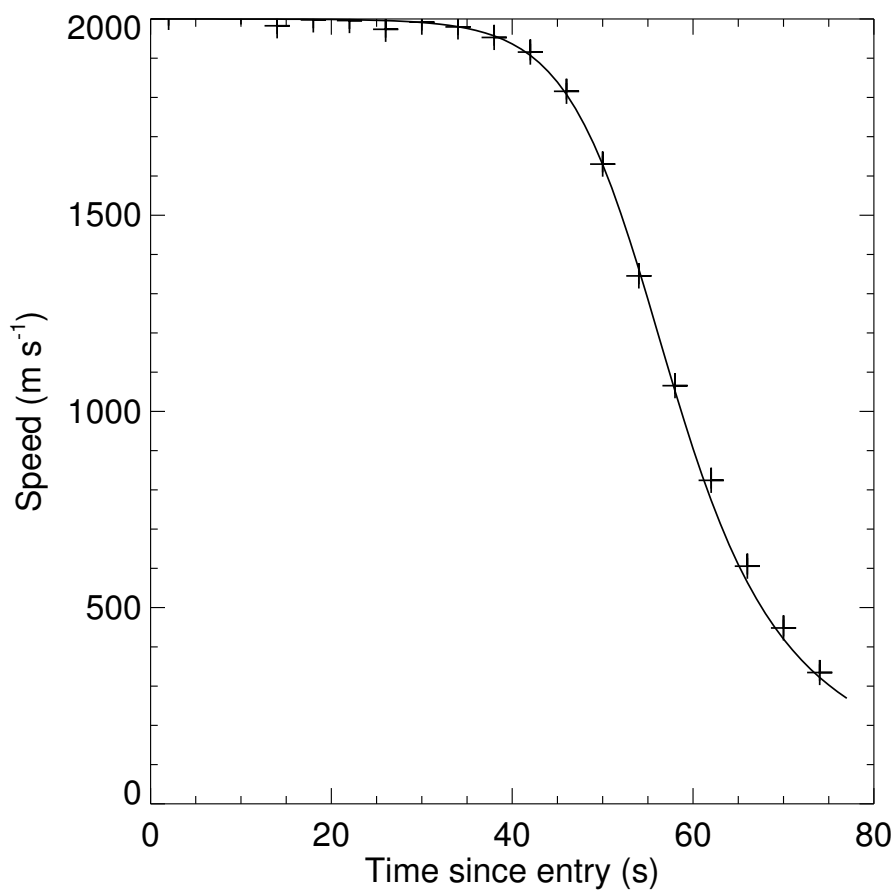


Figure 6.23: $v_{n+1/2}$ (crosses) and $\sigma_{v_{n+1/2}}$ (vertical lines) versus time calculated using noisy v . Continuous curve is simulated v versus t experienced during the atmospheric entry.

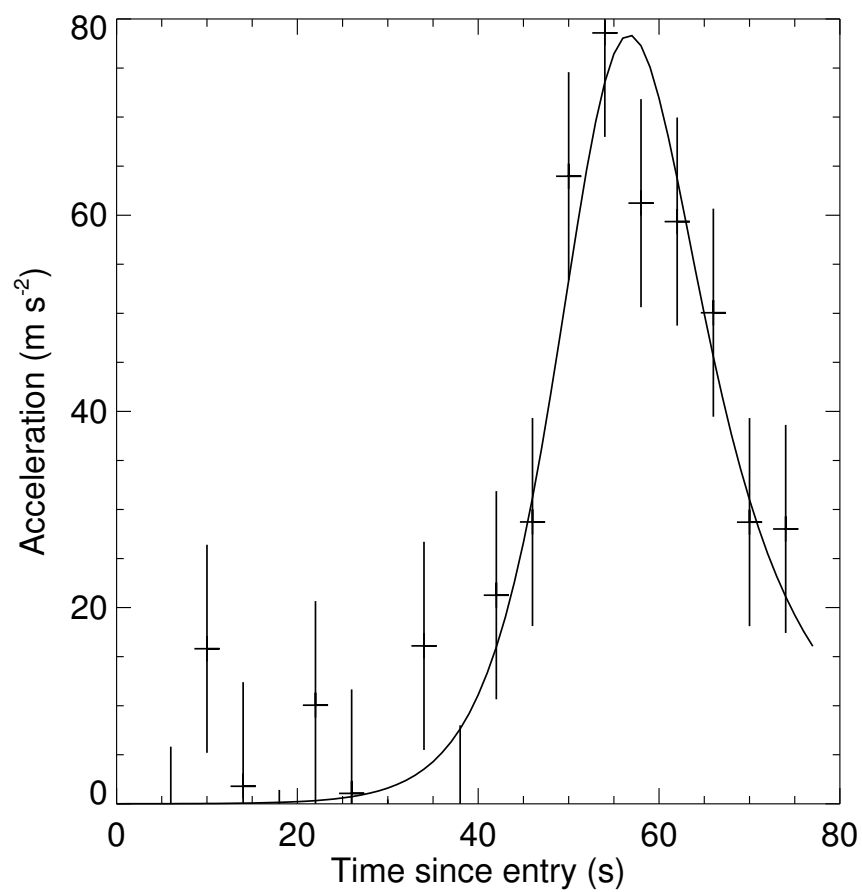


Figure 6.24: $a_{n+1/2}$ (crosses) and $\sigma_{a_{n+1/2}}$ (vertical lines) versus time calculated using noisy v . Continuous curve is simulated a versus t experienced during the atmospheric entry.

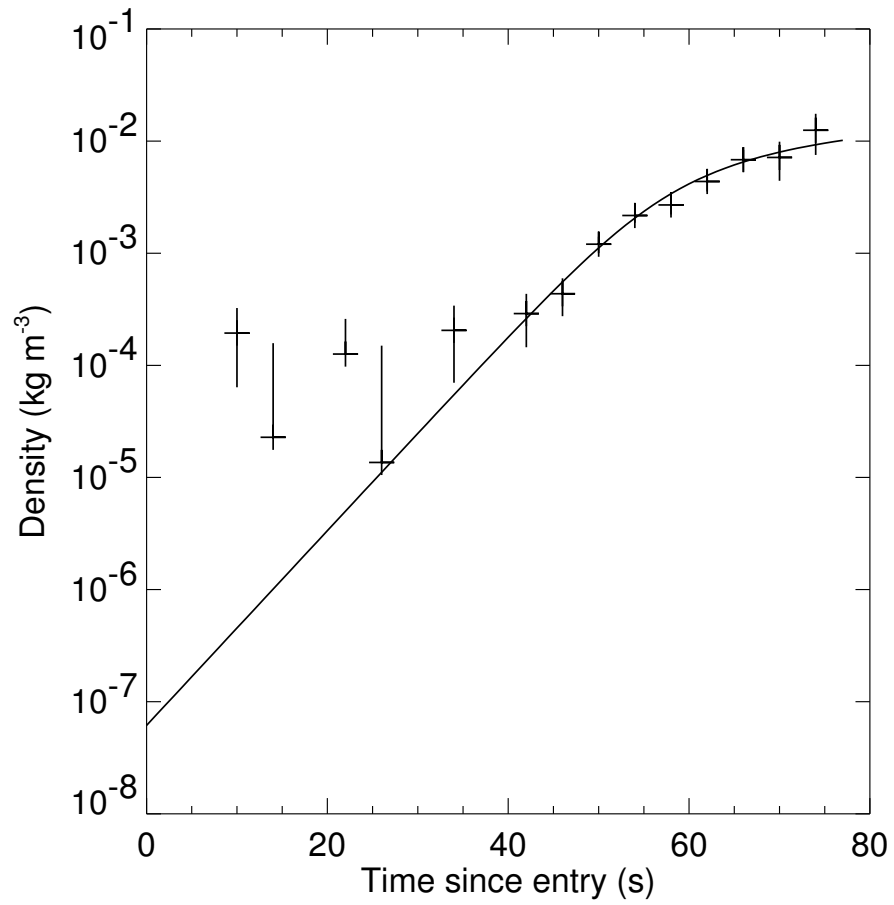


Figure 6.25: $\rho_{n+1/2}$ (crosses) and $\sigma_{\rho_{n+1/2}}$ (vertical lines) versus time calculated using noisy v . If $\rho_{n+1/2} - \sigma_{\rho_{n+1/2}}$ is negative, then only one side of the error bar is plotted. Continuous curve is simulated ρ versus t experienced during the atmospheric entry.

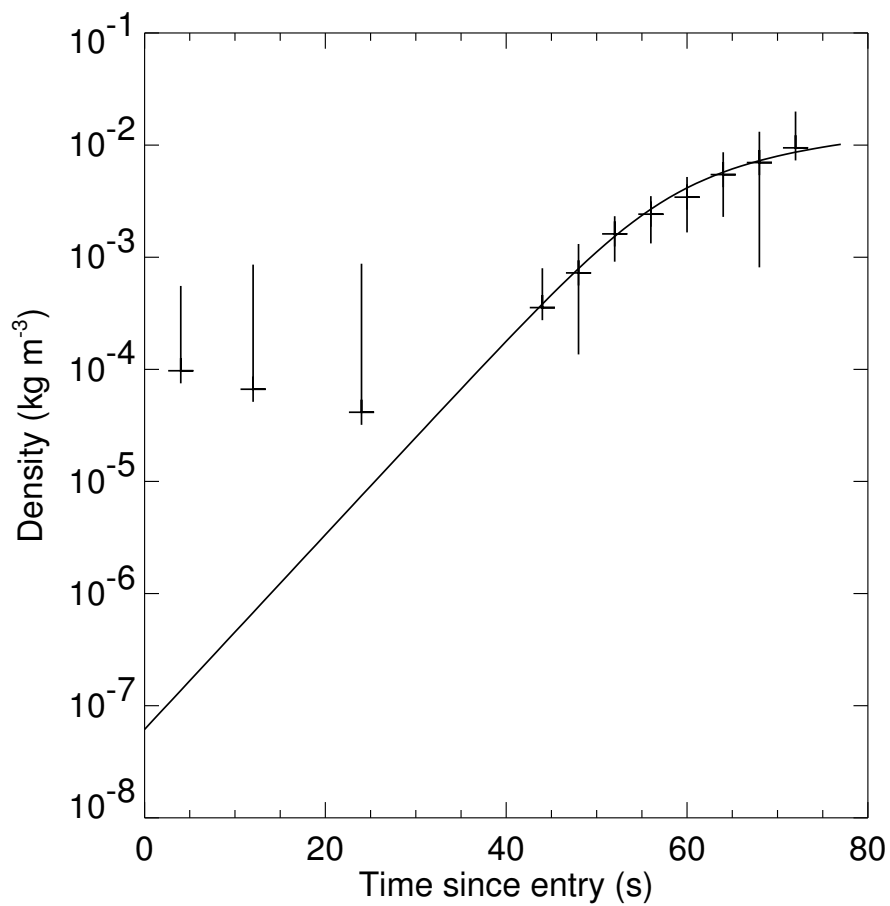


Figure 6.26: ρ_n (crosses) and σ_{ρ_n} (vertical lines) versus time calculated using noisy v . If $\rho_n - \sigma_{\rho_n}$ is negative, then only one side of the error bar is plotted. Continuous curve is simulated ρ versus t experienced during the atmospheric entry.

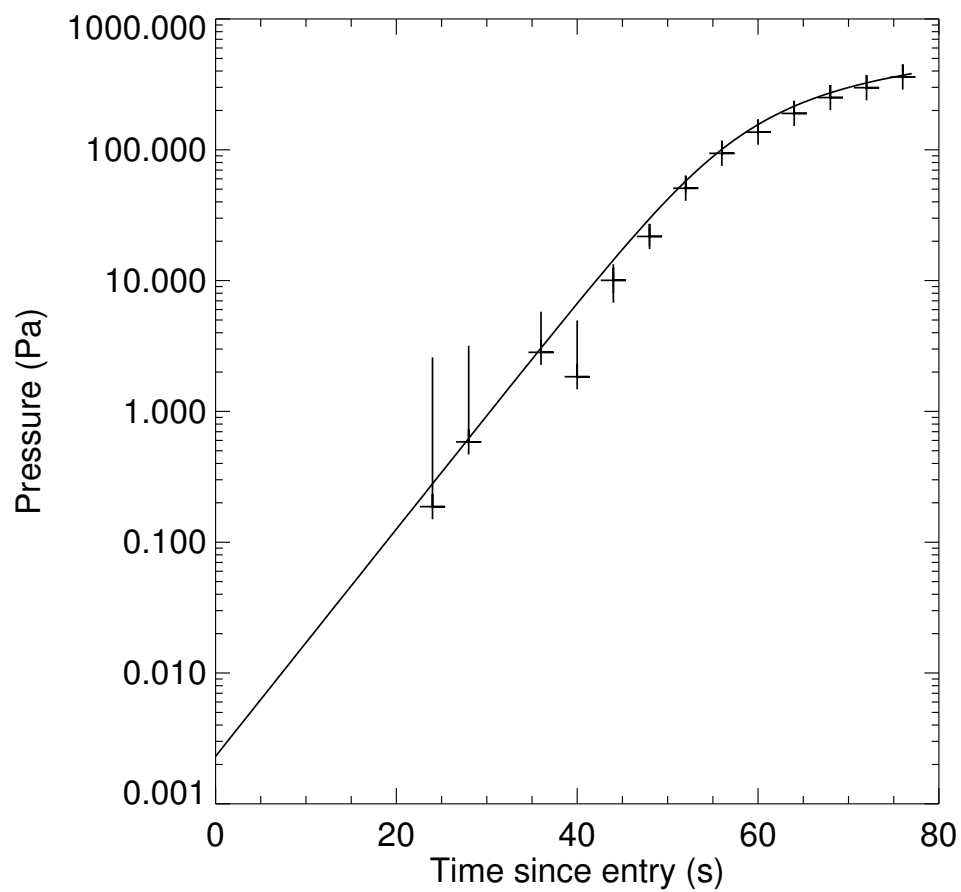


Figure 6.27: p_n^* (crosses) and $\sigma_{p_n^*}$ (vertical lines) versus time calculated using noisy v . If $p_n^* - \sigma_{p_n^*}$ is negative, then only one side of the error bar is plotted. Continuous curve is simulated p versus t experienced during the atmospheric entry.

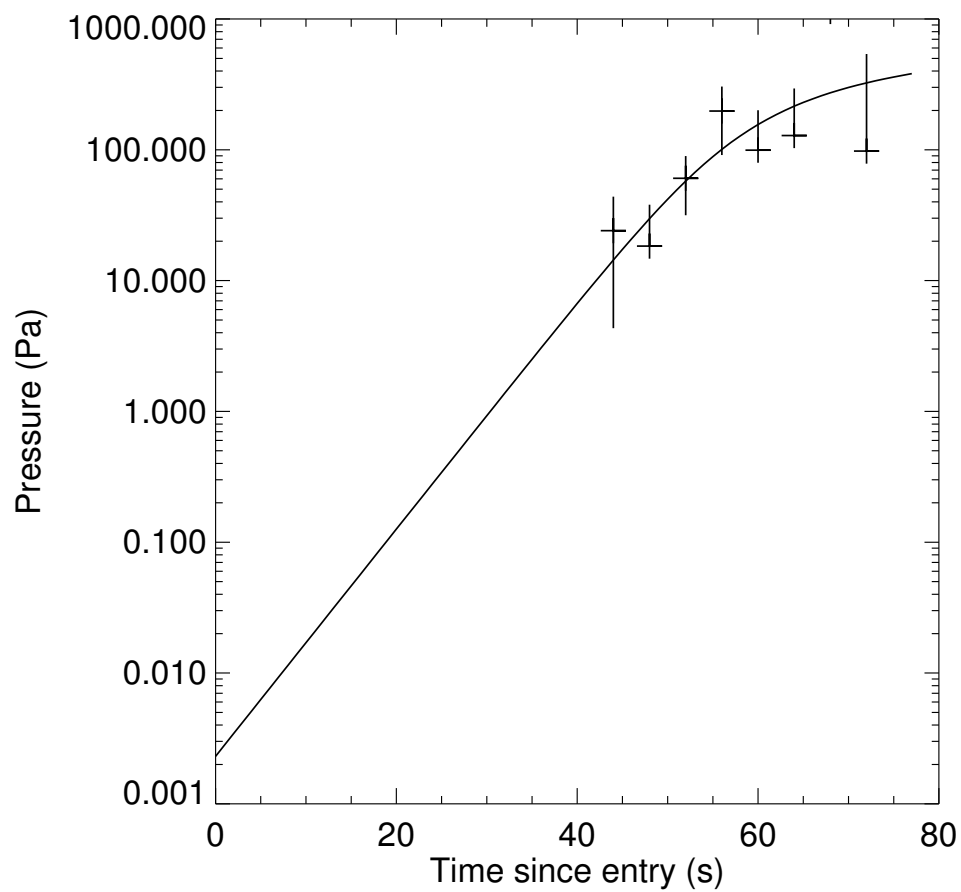


Figure 6.28: $p_n^{\textcircled{a}}$ (crosses) and $\sigma_{p_n^{\textcircled{a}}}$ (vertical lines) versus time calculated using noisy v . If $p_n^{\textcircled{a}} - \sigma_{p_n^{\textcircled{a}}}$ is negative, then only one side of the error bar is plotted. Continuous curve is simulated p versus t experienced during the atmospheric entry.

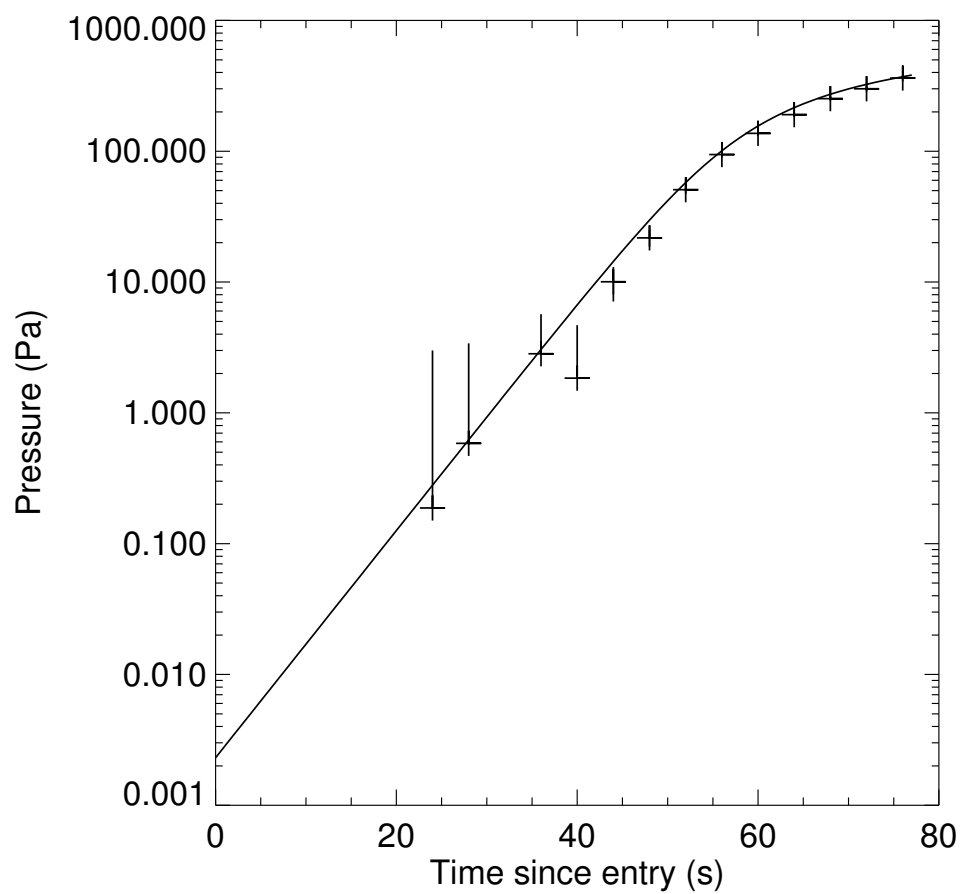


Figure 6.29: $p_n^\#$ (crosses) and $\sigma_{p_n^\#}$ (vertical lines) versus time calculated using noisy v . If $p_n^\# - \sigma_{p_n^\#}$ is negative, then only one side of the error bar is plotted. Continuous curve is simulated p versus t experienced during the atmospheric entry.

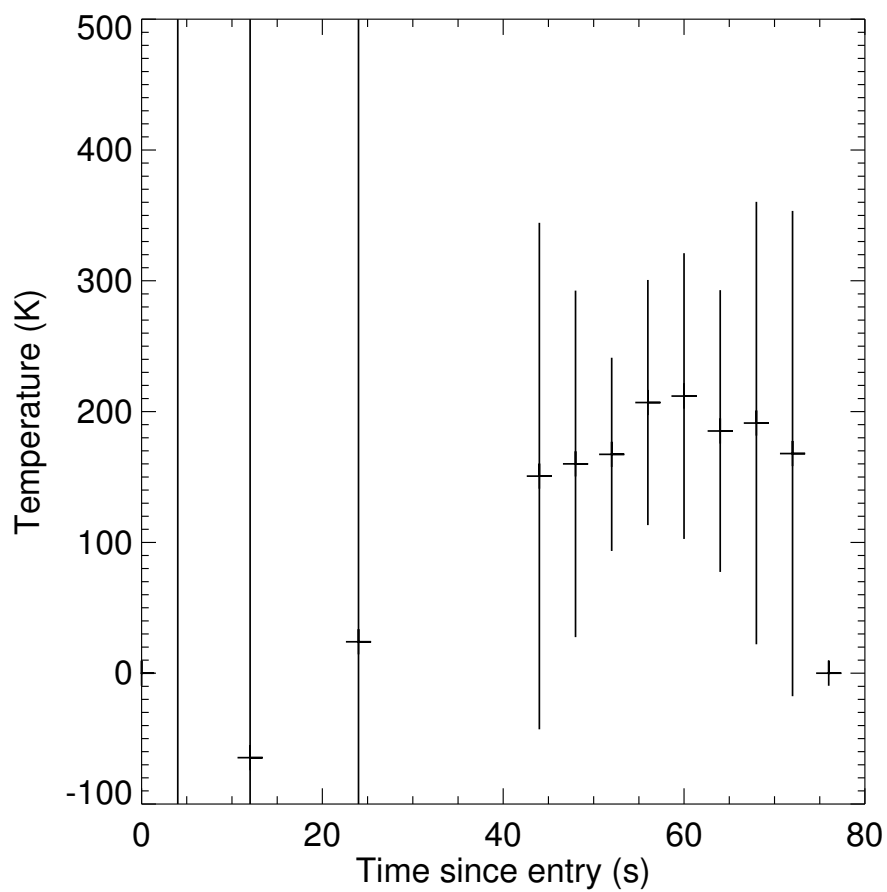


Figure 6.30: T_n^* (crosses) and $\sigma_{T_n^*}$ (vertical lines) versus time calculated using noisy v . Simulated T during the atmospheric entry is 200 K.

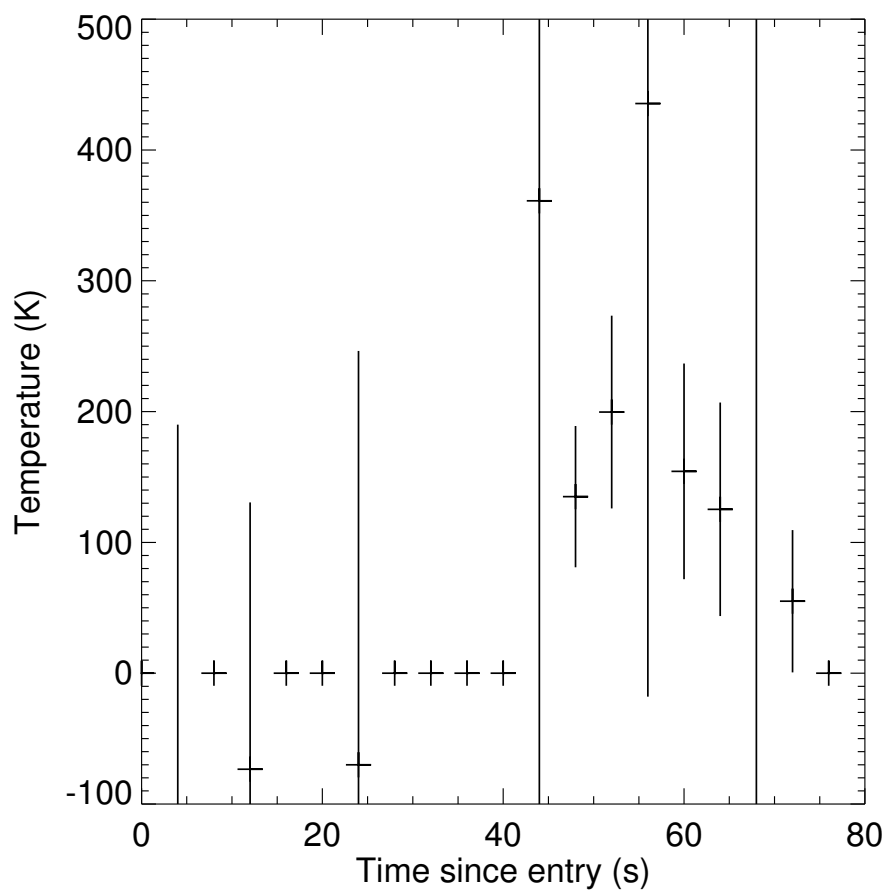


Figure 6.31: $T_n^{\text{ⓐ}}$ (crosses) and $\sigma_{T_n^{\text{ⓐ}}}$ (vertical lines) versus time calculated using noisy v . Simulated T during the atmospheric entry is 200 K.

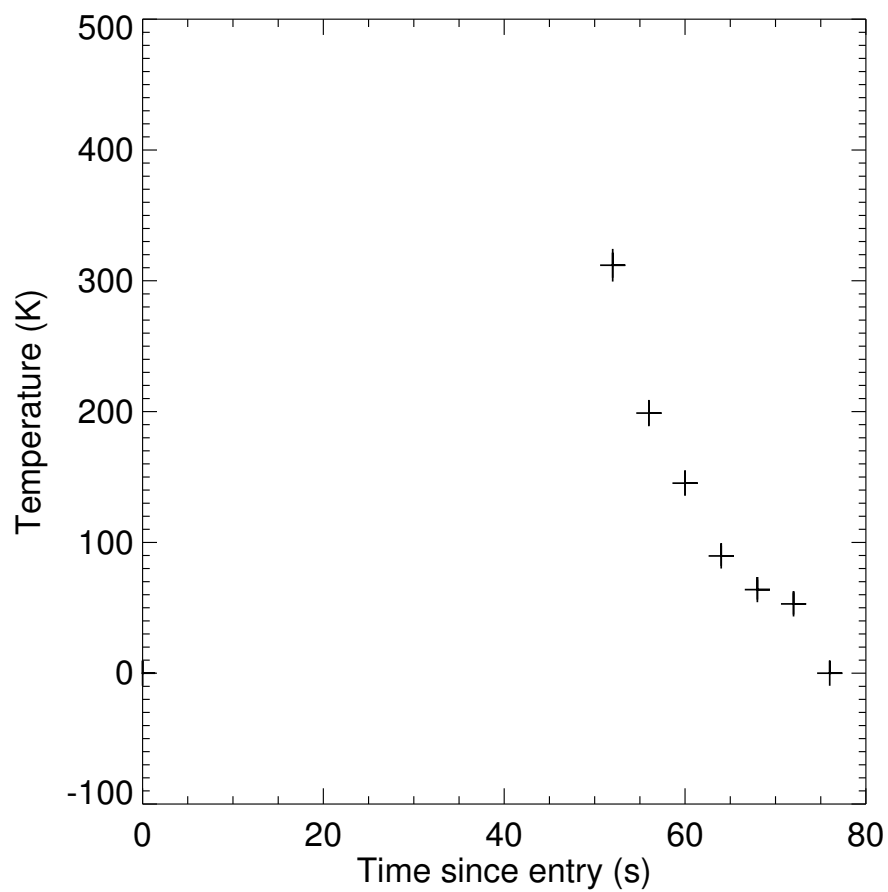


Figure 6.32: $T_n^\#$ (crosses) and $\sigma_{T_n^\#}$ (vertical lines) versus time calculated using noisy v . Simulated T during the atmospheric entry is 200 K.

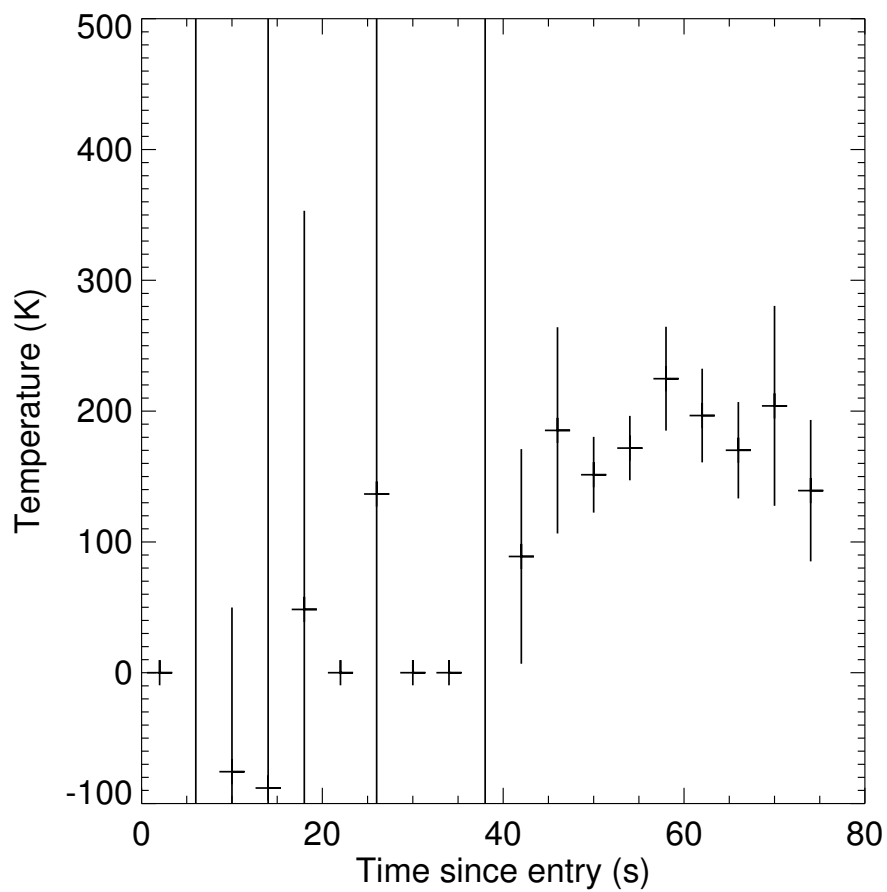


Figure 6.33: $T_{n+1/2}^{\S}$ (crosses) and $\sigma_{T_{n+1/2}^{\S}}$ (vertical lines) versus time calculated using noisy v . Simulated T during the atmospheric entry is 200 K.

6.8 Conclusions

Several different techniques for measuring atmospheric properties during entry from telemetry have been compared. Some, such as p^* , $p^\#$, T^* , $T^\#$, and T^s , appear useful. When trying to measure and analyse small changes in noisy data, it is clear that great care must be taken to select the best approach.

Two assumptions that I have made deserve further discussion. Firstly, I have assumed that the measured v are dominated by random noise when they are actually dominated by systematic errors due to the transmitter being very sensitive to acceleration. Uncertainties in derived quantities are not too greatly affected by this, but the values of the derived quantities are. Small differences in speed, which are interpreted as accelerations, could be dominated by frequency drift. The T^s technique is least affected by this. To quantify whether this renders some of my techniques useless, I would have to see how a prescribed frequency drift affects my calculations of z , a , ρ , p , and T . Secondly, I have often assumed a constant value of C_D . In Chapter 5 I have shown that this assumption is useful. Where I have calculated densities or pressures using this assumption, an extra uncertainty of 25% should be incorporated. Where I have calculated temperatures using this assumption, the extra uncertainty is much smaller ($\sim 10\%$).

My simplified geometry and neglect of gravity on the spacecraft's trajectory are useful for describing the techniques, but are not difficult to incorporate into a real analysis tool. How useful might these techniques be in practice? Clearly this work can be performed much more accurately using onboard accelerometers, but these techniques should give reasonable trajectories. The derived atmospheric properties have such large uncertainties that they are only likely to be useful either if the planet's atmosphere has not been well studied before or if there is public or political interest in poor quality results from an otherwise failed mission. An over-riding problem is the separation of changes in frequency due to drift and due to the Doppler shift. Time intervals may need to be increased such that the change in frequency

due to the change in speed during the extended time interval is comfortably greater than the likely drift in frequency.

CHAPTER 7

COMPARISON OF VIKING LANDER 1 AND MOLA TOPOGRAPHY

7.1 Abstract

Each Viking Lander measured a topographic profile during entry. Comparing to MOLA, I find a vertical offset of 1 – 2 km in the Viking trajectory. Hence Viking atmospheric densities and pressures at a given altitude are 10 – 20% too large.

7.2 Summary

Comparison of the martian topographic profile measured by Viking Lander 1 beneath its atmospheric entry trajectory and high-resolution topographic data generated by the Mars Orbiter Laser Altimeter (MOLA) instrument on the Mars Global Surveyor (MGS) spacecraft reveals a vertical offset of over one km in the Viking profile. The Viking profile, generated from accelerometer and radar altimeter measurements during descent through the martian atmosphere, is a major constraint on derived vertical profiles of atmospheric density, pressure, and temperature. These atmospheric profiles have been at the heart of the Mars Reference Atmosphere for two decades. The error in the topographic profile causes previously published values of atmospheric density and pressure at a given altitude to be too large by a systematic and correctable offset of 10 – 20%.

7.3 Introduction

During its descent through the martian atmosphere, Viking Lander 1 experienced aerodynamic deceleration. Regular measurements of this deceleration were used with an initial entry state and knowledge of the martian gravitational field to reconstruct the spacecraft's trajectory to landing. They were then combined with knowledge of the spacecraft's aerodynamic characteristics to deduce profiles of atmospheric density, pressure, and temperature. Additional data sets, including radar altimeter measurements of altitude above the spatially-varying martian topography, were used to constrain the reconstructed trajectory and atmospheric profiles (Seiff and Kirk, 1977b).

7.4 Altimetry from the Viking Landers

A by-product of this analysis was a profile of planetary radius relative to the landing site as a function of distance from the landing site, where distance is measured beneath the spacecraft trajectory (Seiff, 1993; Seiff and Kirk, 1977c). The Viking 1 profile was published by Seiff (1993) (Figure 13). Using the spacecraft trajectory, archived at the National Space Science Data Center as dataset PSPA-00269, and the landing site coordinates (22.272 ± 0.002 °N, 47.94 ± 0.2 °W, Viking-era areocentric coordinates) I converted distance beneath the trajectory into areocentric latitude and longitude (Mayo et al., 1977). West areocentric longitudes, when subtracted from 360 degrees, give east areocentric longitudes. 0.2 degrees was then subtracted from the Viking-era east longitudes to convert them into MGS-era (1991 IAU) east longitudes used by MOLA (Smith et al., 1998a; Smith et al., 1999). I used these latitudes and longitudes in the MOLA 1/16 degree resolution planetary radius dataset to obtain corresponding MOLA values for planetary radius relative to the landing site as a function of distance from the Viking 1 landing site.

7.5 Comparison with MOLA Altimetry

Figure 7.1 shows the Viking 1 profile, as scanned and manually digitized, and the corresponding MOLA profile (Seiff, 1993). No vertical offset has been applied. Many features in one profile can be seen at the same distance along the other profile. This suggests that the radar altimeter was working well during atmospheric entry. A vertical offset is present between the two profiles. The Viking 1 profile is 2.3 km too high at 640 km distance from the landing site. The spacecraft is at approximately 130 km altitude at this time. This offset decreases, approximately linearly, to 0.8 km at 140 km distance from the landing site. The spacecraft is at approximately 30 km altitude at this time. This offset in the Viking topographic profile must also be present in the altitude scale for the atmospheric profiles. Figure 7.2 shows a shaded relief map of the MOLA 1/16 degree resolution planetary radius dataset. Topographic features along the ground track can be matched to features on the profiles in Figure 7.1. Smoothed contour intervals are also shown on this figure. No region 6 km above the Viking 1 landing site is closer than about 1000 km to the landing site, significantly farther away than the 600 km or so inferred from Seiff's figure. This provides a quick and simple way of discovering the offset in the Viking topographic profile.

The direction of the offset can be calculated in the following manner. When the Viking Lander radar altimeter measures that it is 120 km above the terrain below, the original trajectory reconstruction, primarily from the accelerometer data, locates the spacecraft at 126 km above, and some 600 km horizontally from, the landing site. This puts the underlying terrain at this point along the ground track at 6 km above the landing site, as shown in Figure 7.1. The radar altimeter value of 120 km is correct but, due to uncertainties in the trajectory reconstruction, the trajectory reconstruction value of 126 km is not correct. Since accurate MOLA data show that the underlying terrain is only 4 km above the landing site, the spacecraft is only 124 km above the landing site. This is 2 km below the original trajectory

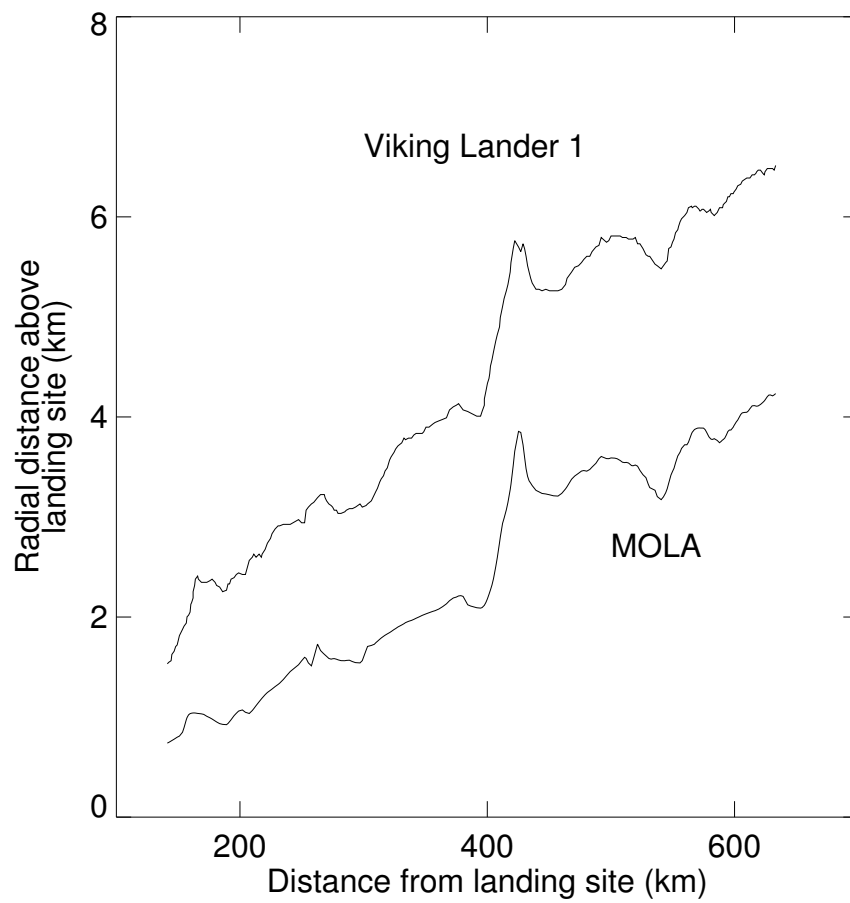


Figure 7.1: Topographic profiles beneath the Viking Lander 1 entry trajectory as derived by Viking Lander 1 and by MOLA.

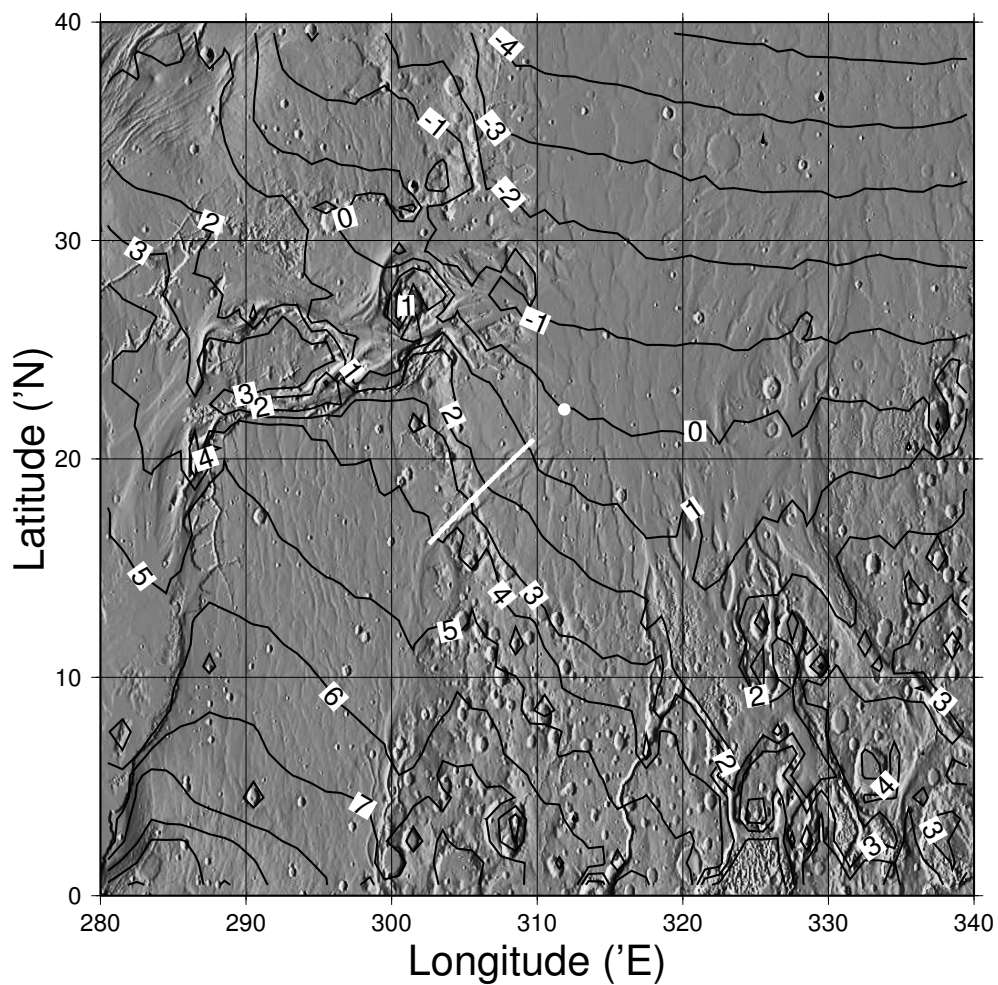


Figure 7.2: Shaded relief map of 1/16 degree resolution MOLA planetary radius data, referenced to the Viking 1 landing site. Smoothed contours are drawn in black at one kilometre intervals. The portion of the ground track shown in Figure 7.1 is marked in white, as is the landing site.

reconstruction. The original density profile has a value of about 10^{-8} kg m⁻³ at 126 km altitude. This density value is actually valid at 124 km altitude, 2 km below where it was originally located. Consequently, the density value reassigned to 126 km altitude is a lower value than it was originally. Altitudes as a function of density are too large and densities as a function of altitude are also too large. The same altitude scale is used for the pressure and temperature profiles, so the same corrections apply.

7.6 Implications for Viking Atmospheric Structure Results

The close correspondence between the small-scale structures in the Viking and MOLA profiles in Figure 7.1 suggests that the errors in latitude and longitude for the trajectory reconstruction are less than a few tenths of a degree, which is very small compared to the lengthscale for changes in atmospheric properties. Constraining these horizontal offsets further using a scanned figure is not really practical. A vertical offset of 1 – 2 km is present in the Viking Lander 1 entry and atmospheric structure reconstruction. Using a scale height of 10 km, this corresponds to previously published densities and pressures at a given altitude being systematically too large by approximately 10 – 20% (Seiff and Kirk, 1977b). Atmospheric temperatures are minimally affected. Since these atmospheric profiles have been at the heart of the Mars Reference Atmosphere for the past two decades, the error is significant (Seiff, 1982). However, it is correctable.

7.7 Correcting the Viking Atmospheric Structure Results

The best possible correction to the Viking Lander 1 trajectory and atmospheric structure reconstruction would be to rederive it from the original accelerometer and radar altimeter data using the newly available MOLA dataset as a constraint. This requires access to, and detailed understanding of the uncertainties in, large amounts

of Viking science and engineering data. This would be a major undertaking. A first-order correction can be made by altering the altitude scale to which the atmospheric profiles are referenced to compensate for the offset in Figure 7.1.

$$z_{\text{corrected}} = z_{\text{original}} + \text{offset}(z_{\text{original}}) \quad (7.1)$$

The original altitude values, z_{original} , to which the density, pressure, and temperature measurements were matched are offset from their actual values, $z_{\text{corrected}}$. The offset, a function of z_{original} , equals the Viking-derived planetary radius at the corresponding latitudes and longitudes subtracted from the MOLA planetary radius at the same locations. This correction is not complete because the atmospheric properties derived from the accelerometer measurements depend on the trajectory. However, the additional corrections that are needed should be smaller than this initial correction and so I neglect them here. Using the archived values for the spacecraft's trajectory (altitude, latitude, and longitude) and the two profiles in Figure 7.1, I find that the offset is effectively linear with altitude.

$$\text{offset}(z_{\text{original}}) = z_{\text{original}} \times (-0.012) - 1.00\text{km} \quad (7.2)$$

The Viking Lander 1 atmospheric profiles are tabulated in Seiff and Kirk (1977b) at 4 km intervals. I reproduce them here in Table 7.1 with the addition of my corrected altitude scale.

7.8 Conclusions

A kilometre-scale offset in the altitude of the Viking Lander 1 reconstructed entry trajectory has been identified by comparison between MOLA topography and data from the Viking Lander 1 radar altimeter. This causes the results for atmospheric

Original Altitude (km)	Corrected Altitude (km)	Atmospheric Density (kg m ⁻³)	Atmospheric Pressure (mbar)	Atmospheric Temperature (K)
120.00	117.61	1.60E-8	4.14E-6	136.3
116.00	113.65	2.42E-8	6.91E-6	149.2
112.00	109.70	3.95E-8	1.12E-5	148.6
108.00	105.75	6.59E-8	1.84E-5	146.4
104.00	101.79	1.06E-7	3.03E-5	149.4
100.00	97.84	1.67E-7	4.94E-5	154.8
96.00	93.89	2.88E-7	8.02E-5	145.9
92.00	89.93	5.39E-7	1.38E-4	133.6
88.00	85.98	8.33E-7	2.33E-4	146.7
84.00	82.03	1.40E-6	3.87E-4	144.2
80.00	78.07	2.57E-6	6.70E-4	136.6
76.00	74.12	4.66E-6	1.16E-3	130.5
72.00	70.17	7.70E-6	2.05E-3	139.1
68.00	66.21	1.17E-5	3.43E-3	152.9
64.00	62.26	1.88E-5	5.55E-3	154.6
60.00	58.31	3.19E-5	9.11E-3	149.5
56.00	54.35	5.96E-5	1.56E-2	136.8
52.00	50.40	9.56E-5	2.67E-2	146.3
48.00	46.44	1.57E-4	4.45E-2	148.6
44.00	42.49	2.65E-4	7.46E-2	147.5
40.00	38.54	4.10E-4	1.23E-1	157.4
36.00	34.58	6.25E-4	1.98E-1	166.1
32.00	30.63	9.32E-4	3.12E-1	175.1
28.00	26.68	1.38E-3	4.83E-1	183.8

Table 7.1: Viking Lander 1 Atmospheric Profiles with Original and Corrected Altitude Scales. Read 1.60E-8 as 1.60×10^{-8} . These altitudes are radial distances above the landing site.

density and pressure at a given altitude that were derived from the Viking Lander 1 entry to be 10 – 20% too large. This is a significant source of error for the Mars Reference Atmosphere. This error can now, in principle, be corrected using MOLA topographic data and I have made a first-order correction to the atmospheric profiles. There is also the possibility of evaluating the performance of the Viking radar altimeter, which has interesting engineering implications.

A topographic profile from the Viking 2 entry, which is not discussed in this chapter, can be found on page 285 of Euler et al. (1979). This work shows topographic elevation above a reference areoid, so comparison against MOLA data requires knowledge of what that reference areoid was. Since Viking 2 landed on flat Utopia, far from the rugged outflow channel terrain of Viking 1, a smaller error is likely.

CHAPTER 8

ENIGMATIC NORTHERN PLAINS OF MARS

Although the northern plains of Mars form the flattest known surface in the Solar System, they are crisscrossed by ridge features (Smith et al., 1999). Here I test the idea that they might once have been covered by an ocean by examining the topographic profiles of possible shorelines (Head et al., 1999). I conclude that these candidate shorelines were more likely to have been formed by tectonic rather than oceanic processes.

Linear slope changes in the northern plains have been identified as possible shorelines of an ocean formed during the middle part of martian history (Head et al., 1999). Figure 8.1 shows topographic profiles, generated from Mars Orbiter Laser Altimeter (MOLA) data, across two such groups of shorelines (Smith et al., 1999). Candidate shorelines near the Utopia impact basin are flat terraces with a ridge of higher elevation bounding their landward, or upslope, side (Figure 8.1a). Possible shorelines on the other side of the proposed ocean, near the Alba Patera volcano, are also flat terraces with a ridge of higher elevation bounding their oceanward, or downslope, side (Figure 8.1b).

I believe that this morphology is hard to explain in terms of a shoreline formation process, as is the reversal of shoreline morphology from one side of the ocean to the other. I favour the idea that these candidate shorelines were created by tectonic activity, on the basis of recent MOLA digital terrain models of kilometre-scale horizontal resolution of the northern plains of Mars.

As seen from early images recorded by Viking (Figure 8.1c), these plains

are essentially flat and featureless, but MOLA data (Figure 8.1d) reveal a network of ridges spanning the northern plains, some of which are the candidate shorelines of the proposed ancient ocean (Head et al., 1999). Most ridges appear related to obvious stress centres, such as the volcanic Tharsis Rise, the Utopia impact basin, and the Alba Patera volcano. These ridges are generally perpendicular to predicted directions of maximum compressive stress, which suggests that the ridges have a tectonic origin (Banerdt et al., 1992). They also have the characteristic profile of wrinkle ridges formed by compressive tectonism (Schultz, 2000). Some ridges are close to known wrinkle ridge provinces, such as Lunae Planum, and have similar strikes; clearly, these formed with the known wrinkle ridges. Both groups of candidate shorelines have orientations consistent with their formation by compressive tectonism.

The causes of the youth and smoothness of the northern plains are still debated. This network of ridges is the only tectonic feature in this enigmatic region and their discovery opens a new tectonic window into Mars.

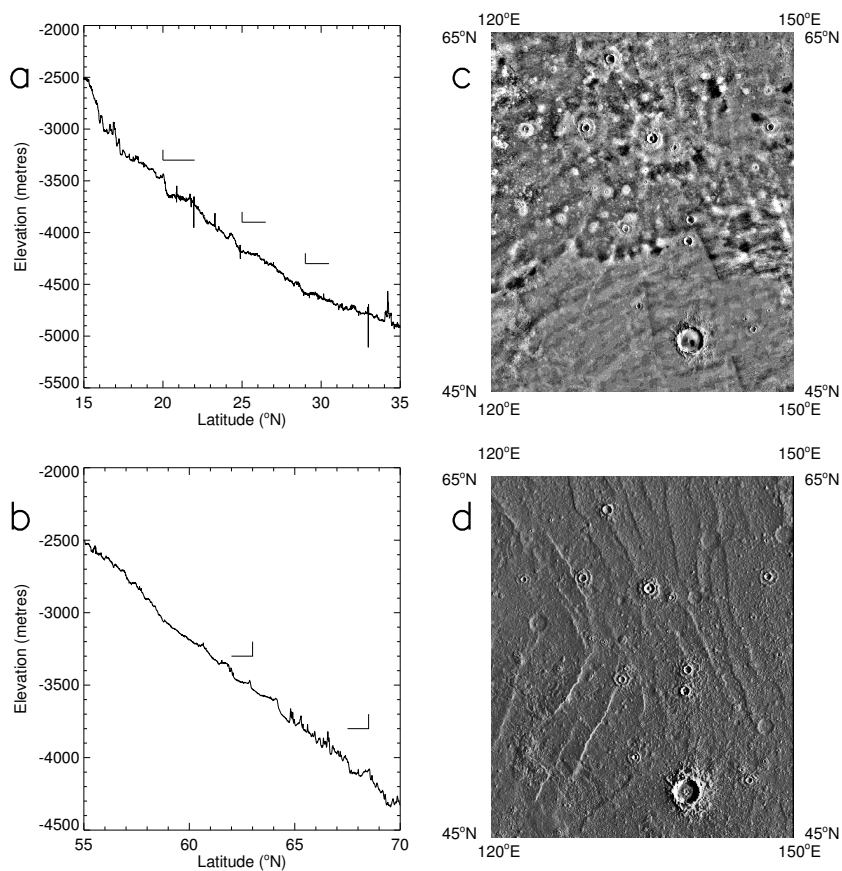


Figure 8.1: Martian topography. a, MOLA profile 10190 near the Utopia impact basin. Terraces and ridges are marked by horizontal and vertical lines, respectively. Vertical exaggeration ~ 400 . b, MOLA profile 10929 near the Alba Patera volcano. Terraces and ridges are marked by horizontal and vertical lines, respectively. Vertical exaggeration ~ 400 . c, Viking photomosaic near the Utopia impact basin, Mercator projection. d, Shaded relief map generated from MOLA digital terrain model of the same region with the same projection. Many ridges are visible in the MOLA image, but not in the Viking image.

CHAPTER 9

AGE OF LUNAR CRATER GIORDANO BRUNO

9.1 Abstract

It has been suggested that the formation of 22 km diameter lunar crater Giordano Bruno was witnessed in June 1178 AD. To date, this hypothesis has not been well tested. Such an impact on the Earth would be “civilization threatening.” Previous studies have shown that the formation of Giordano Bruno would lead to the arrival of 10 million tonnes of ejecta in the Earth’s atmosphere in the following week. I calculate that this would cause a week-long meteor storm potentially comparable to the peak of the 1966 Leonids storm. The lack of any known historical records of such a storm is evidence against the recent formation of Giordano Bruno. Other tests of the hypothesis are also discussed, with emphasis on the lack of corroborating evidence for a very recent formation of the crater.

9.2 Introduction

It has been suggested that the formation of the 22 km diameter lunar crater Giordano Bruno, located just beyond the north-eastern limb of the Moon at 36°N , 103°E and shown in Figure 9.1, was witnessed and recorded around an hour after sunset on 18th June, 1178 AD in the Julian calendar (Hartung, 1976). The date in Hartung (1976) was corrected in Calame and Mulholland (1978). A dramatic passage in the medieval chronicles of Gervase of Canterbury speaks of the crescent Moon “spewing out fire, hot coals, and sparks,” a potentially plausible description of an impact on

the Moon. An English translation of the relevant passage can be found in Hartung (1976) and the original Latin in Stubbs (1879). The chronicle itself resides in the library of Trinity College, Cambridge, Great Britain, with catalogue number MS R.4.11. Based on its extensive pattern of bright rays and uneroded morphology, Giordano Bruno is the youngest lunar crater of its size or larger (Hartung, 1976). Its position close to the north-eastern limb of the Moon is consistent with some details in the passage, and this and its youth led Hartung to suggest it as the impact site.

Following Holsapple (1993), the impactor would have been of size 1 – 3 km, assuming impact velocities of 70 – 5 km s⁻¹ respectively. Such an impact on the Earth would be “civilization threatening” and have a value on the Torino Scale of 9 – 10, corresponding to regional devastation to global climatic catastrophe (Lissauer, 1999; Binzel, 1999). The Torino Scale gauges the potential damage that may occur in the event of an impact of an asteroid, or other object from space, on the Earth, just as the Richter Scale gauges earthquake damage. Therefore it is important to test Hartung’s hypothesis that such an event happened on the Moon less than a millenium ago.

This hypothesis was strongly opposed by Nininger and Huss (1977), who offered a careful rebuttal of many of Hartung’s lines of evidence. They concluded that the passage was inconsistent with a lunar impact and suggested that it was a report of a meteor in transit of the Moon. Apart from turbulence in the atmosphere, no other interpretations of the passage have been suggested in the scientific literature (Hartung, 1976).

Nininger and Huss’s rebuttal failed to completely disprove Hartung’s hypothesis in the eyes of many. As an intriguing, improbable idea, Hartung’s hypothesis has appeared in the peer-reviewed scientific literature (including Hughes (1976), Nininger and Huss (1977), Calame and Mulholland (1978), Baldwin (1981), Hughes (1981), Yoder (1981), Hartung (1987), Oberst (1989), Gault and Schultz (1991), Harris (1993), Hartung (1993a), Hartung (1993b), Pieters et al. (1994),



Figure 9.1: Portion of Apollo 16 metric frame 3008 showing Giordano Bruno. The view is to the northwest. Giordano Bruno has a diameter of approximately $1/30$ of the width of the figure, appears to be uneroded, and is located within the bright region in the upper centre of the figure. A bright ray originates from Giordano Bruno, heads down towards the bottom of the figure, and crosses the crater Szilard. The Szilard-sized crater to the upper right of the bright region is Fabry.

and Saul and Lawniczak (1996)) and well-known popular science literature such as *Cosmos* and *Rain of Iron and Ice* (Sagan, 1980; Lewis, 1996). The hypothesis has also been connected to the Tunguska event of 1908 and the decline of certain Pacific civilizations (Hartung, 1993b; Spedicato, 1998).

Hartung's hypothesis has proven difficult to test over the years, as data from the region of the Moon surrounding Giordano Bruno are of low quality (Pieters et al., 1994). In an attempt to explain unexpectedly large amplitudes of free libration of the Moon, a partial lunar laser ranging dataset was interpreted to be consistent with Hartung's hypothesis and was published on the front cover of *Science* (Calame and Mulholland, 1978). A later analysis of a more complete dataset suggested that Hartung's hypothesis could not explain the large free librations and proposed turbulent core-mantle friction as their source (Yoder, 1981).

9.3 Meteor Storm

The general fate of the ejecta from lunar impacts has been discussed in the literature (Gault, 1983; Gladman et al., 1995; Gladman et al., 1996) — as has the specific case of Giordano Bruno ejecta (Hartung, 1981; Mims and James, 1982; Gault and Schultz, 1991; Harris, 1993; Hartung, 1993a; Hartung, 1993b), but the resultant meteor storm has not been described in the peer-reviewed literature. In a conference abstract, Mims and James (1982) sketch a single direct trajectory, with a daytime arrival at the Earth. They do not appear to have calculated terrestrial arrival times for general direct trajectories, and have not published the work described in the conference abstract in the peer-reviewed literature. Gault and Schultz (1991) state that the Earth would have accreted 10^{13} grams of ejecta, travelling on direct trajectories with a characteristic entry speed of at least the Earth's escape velocity (11.2 km s^{-1}), in the week after the formation of Giordano Bruno. Gault's work on the dynamics of lunar impact ejecta is consistent with currently authoritative work (Gladman et al., 1995). No statements are made about local day or night-time

arrivals of the ejecta on the Earth, but, given the large range in initial speed and direction of the ejecta, it seems reasonable that at least a portion of the subsequent meteor storm would have been visible during night-time. This work calculates the properties of that meteor storm.

The size distribution of the ejecta is uncertain. Power-law distributions for ejecta sizes, with the cumulative number of fragments of mass greater than m approximately inversely proportional to m , have been used in discussions of ejecta deposits. However, such a distribution is not necessarily appropriate here. As discussed by Melosh (1989), it applies to the ejecta deposits taken as a whole, whereas the current problem is concerned only with that fraction of the ejecta that reaches lunar escape velocity. Ejecta from the Ries Crater in Germany clearly shows a dependence of ejecta size on distance from the crater, and hence on ejection speed (Horz et al., 1983). In a study of secondary craters on the Moon, Mercury, and Mars, Vickery (1987) showed that the size of the largest fragment ejected at a given speed is approximately inversely proportional to the square of that speed. The constant of proportionality may depend on impactor size, velocity, and material. For the Giordano Bruno case, it is not directly predictable from Vickery's work. However, a value of $10^6 \text{ m}^{-1} \text{ s}^2$ is consistent with her work. This suggests that no fragments larger in radius than 10 cm reach lunar escape velocity. A minimum fragment radius of 0.1 cm is suggested by Melosh and Vickery (1991). Rather than compounding uncertainties by requiring a range of sizes according to some distribution, I shall assume that all fragments reaching Earth are the same size. I shall later show that this assumption does not affect my conclusions.

Mass-velocity-magnitude relations for meteors are uncertain (Jenniskens et al., 1998). Jenniskens et al. (1998) use a relationship from Jacchia et al. (1967):

$$\log M(\text{g}) = 6.06 - 0.62m_{\text{vis}} - 3.89 \log V^\circ(\text{kms}^{-1}) - 0.67 \log(\sin(\text{hr})) \quad (9.1)$$

with M the mass, hr the radiant altitude, V° the apparent velocity, and

m_{vis} the visible magnitude of the meteor. Consider fragments with a characteristic radius of 1 cm and a typical silicate density of 2.5 g cm^{-3} , giving a characteristic mass of 10 g. Taking hr as 45° , V° as 11.2 km s^{-1} , and M as 10 g results in a visible magnitude of 1.7 and total number of meteors of 10^{12} , where the total mass has been constrained by Gault and Schultz (1991) to be 10^{13} g. A uniform distribution over the surface of the Earth and the week-long interval corresponds to a rate of $10^3 \text{ meteors km}^{-2} \text{ hr}^{-1}$. Taking the meteors to be visible at an altitude of 70 km or above (Greenhow and Hall, 1960), an observer viewing within 30° of zenith would see 5×10^4 meteors per hour. For comparison, the greatest meteor storm in living memory, the 1966 Leonids, had a zenith hourly rate of $\sim 1.5 \times 10^5$ for 20 minutes over the western United States (Kronk, 1988) and typical background rates are a few per hour, with seasonal and diurnal variability of factors of a few (Shirley, 1997). If the characteristic radius of the ejecta is allowed to vary between the extremes of 0.1 and 10 cm, the magnitudes and numbers of meteors changes correspondingly, as shown in Figure 9.2.

The predicted range of meteor fluxes and magnitudes is large, but is not a critical problem for visibility of the meteor storm. At one extreme, the meteor storm is composed of very many faint meteors, and at the other, of many bright meteors. For the smallest reasonable characteristic ejecta radius, a hourly rate of 10^8 and some allowance for variability about the characteristic radius may be invoked to ensure that some of the meteors are brighter than magnitude 6. For any reasonable characteristic ejecta radius, the meteor storm is exceptional. It is apparent that any reasonable size distribution between the two extremes of 0.1 and 10 cm produces an exceptional meteor storm. A meteor storm as impressive as this and lasting for a week would have been considered apocalyptic by all medieval observers. Any historical source from this time that mentions any astronomical phenomena whatsoever would have recorded this event. Neither European (Dall'olmo, 1978), Arab (Rada and Stephenson, 1992), Chinese (Zhaung, 1977; Imoto and Hasegawa, 1958), Korean (Imoto and Hasegawa, 1958), nor Japanese (Imoto and Hasegawa, 1958) sources record a storm at this time, though they do qualitatively describe many

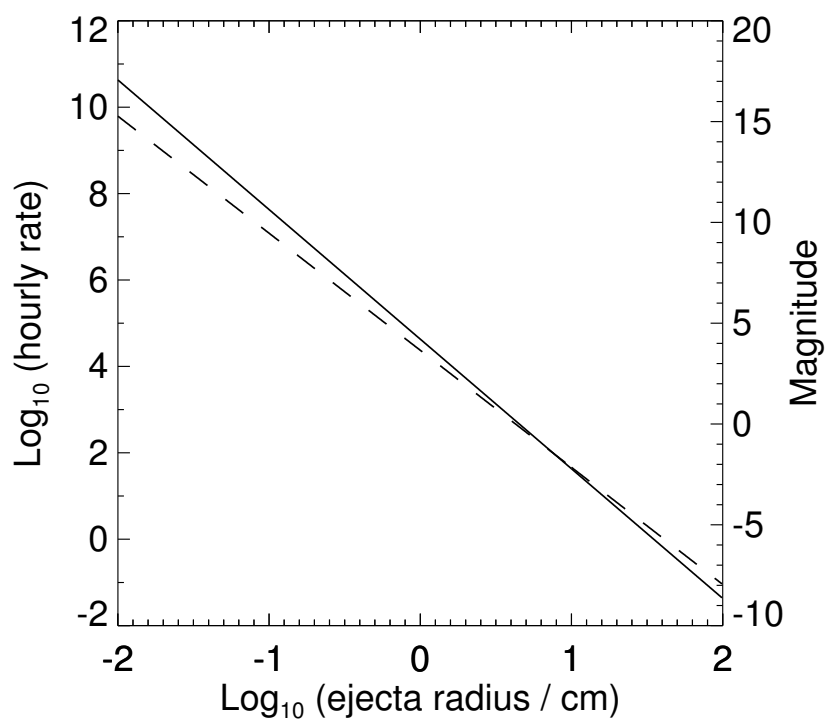


Figure 9.2: Variation in hourly rate (solid line) and visible magnitude (dashed line) of meteor storm with characteristic ejecta radius. Reasonable values for characteristic ejecta radius are 0.1 – 10 cm, as discussed in Section 9.3.

others. In such reports, large numbers of meteors are typically described as “many” or “countless”, and bright meteors as “great stars” or “balls of fire.” The qualitative nature of these descriptions makes estimates of hourly rates or magnitudes difficult, and hence quantitative comparison between the recorded storms of antiquity and the predicted Giordano Bruno storm is also difficult. There is room for debate on the precise size of the meteor storm created by the hypothesized formation of Giordano Bruno 800 years ago. However, as shown in Figure 9.2, it seems clear that it would have been a magnificent spectacle, worthy of chroniclers’ attention, visible over much of the world. The lack of records of such a meteor storm is strong evidence against Hartung’s hypothesis.

Only one record of a meteor storm has ever been suggested as being the arrival of Giordano Bruno ejecta. This is a Korean report stating that “countless stars flew west” a few months after the proposed formation of Giordano Bruno (Mims and James, 1982).

9.4 Other Tests of Hartung’s Hypothesis

There are other ways in which Hartung’s hypothesis can be tested. Analysis of the best current imagery, such as Apollo 16 metric frame 3008, shown in Figure 9.3, reveals only that there are no craters of 1 km diameter or larger on the floor or ejecta blanket of Giordano Bruno out to one crater diameter from the rim, an area of approximately 3400 km².

The lunar cratering rate as a function of time is given by Neukum and Ivanov (1994):

$$N(1) = 5.44 \times 10^{-14} \times [\exp(6.93 \times t) - 1] + 8.38 \times 10^{-4} \times t \quad (9.2)$$

where $N(1)$ is the cumulative crater frequency per km² at a crater diameter



Figure 9.3: Enlarged portion of Apollo 16 metric frame 3008 showing Giordano Bruno.

of 1 km and t is the age in billions of years. This constrains Giordano Bruno to be less than 350 million years old, which in itself does not prove or disprove Hartung's hypothesis. However, assuming that cumulative crater frequency scales inversely with the square of crater diameter, Equation 9.2 predicts the expected interval between Giordano Bruno-like cratering events on the Moon to be ~ 15 million years, making the formation of Giordano Bruno in historical times an extremely unlikely event (Neukum and Ivanov, 1994).

According to Hartung's hypothesis, this event should have been visible over a sizeable fraction of Western Europe, full of scholars ready to note such celestial happenings (Hartung, 1976). For example, in the English records, both a chronicler in nearby London and Gervase note a solar eclipse a mere three months later. The London chronicle has no mention of any impacts on the Moon. A number of French records also note the solar eclipse but not any impacts on the Moon (Newton, 1972). Maybe only Canterbury had clear skies that night. However, Gervase mentions only five witnesses, seated together, to the event. It is improbable that a lunar impact, as described in the passage, would be witnessed by only five people in the Canterbury region. However, for an observer to see a meteor appear directly in front of the Moon requires the observer to be in a 1 kilometre diameter footprint on the Earth. Such a small footprint may help explain the paucity of witnesses so soon after sunset on a summer's evening. A more serious problem is found in the reported date of the event, 18th June, 1178 AD in the Julian calendar. Contrary to earlier expectations, the 1.3 day old Moon would not have been visible on this date (Meeus, 1990; Schaefer and Bagnall, 1990). It would have been visible on the next and later days. It is possible that Gervase or his witnesses are in error about the date, but Gervase gives the correct date for the solar eclipse three months later (Newton, 1972) and the passage refers to the date as "the Sunday before the Feast of St. John the Baptist." In an era of regular Sunday church attendance, it may be assumed that a witness would not confuse Sunday and any other day of the week. It seems to be generally agreed that this Sunday was the 18th June. According to Waddington (Hartung, 1993b) "Hoc anno, die Dominica ante Nativitatem Sancti Johannis Baptistae" may

actually translate as the day after the Sunday in question, or 19th June, thus fixing all date-related problems. I have not yet seen any evidence to support this unusual assertion. This date problem also poses problems for the meteor interpretation of the passage, and is probably best used as evidence for unreliability in the source.

The search for a surface temperature anomaly suggested by Hartung (1976) seems unrealistic in view of the observed rapid cooling and solidification of the surface of terrestrial kilometre-thick lava lake, Kilauea-Iki (Hardee, 1980). A simple terrestrial cooling model, adapted for the Moon, suggests that no surface temperature anomaly would remain after a decade (Kesthelyi and Denlinger, 1996).

Radiometric studies of Giordano Bruno material would definitively date its formation. The Soviet Luna 24 sample return mission landed close to a Giordano Bruno ray but unfortunately is not believed to have returned any Giordano Bruno ejecta (Maxwell and El-Baz, 1978). It has been suggested that a lunar meteorite, ALHA 81005, may originate from Giordano Bruno, though the evidence supporting this claim is not strong (Ryder and Ostertag, 1983). ALHA 81005 was ejected from the Moon approximately 10,000 years ago (Warren, 1994).

Studies of the spectral maturation of lunar crater ejecta have been used to constrain crater ages with respect to radiometrically dated large craters and suggest that Giordano Bruno is younger than 100 million years old (Grier, 1999). Work is proceeding to include radiometrically dated smaller, younger craters in the calibration, which may drive down this upper age limit (Grier et al., 2000).

High resolution Clementine images show evidence of weathering in Giordano Bruno suggesting “that either Giordano Bruno is substantially older than 800 years old, or that the weathering process on the Moon is far more rapid than currently expected.” (Pieters et al., 1994).

There are also a number of reasons why Gervase’s chronicle should not be interpreted as describing a lunar impact, many of which are detailed in Nininger and Huss (1977). Briefly summarized, Nininger and Huss considered the dynamic

and repeatable events described in Gervase's chronicle, including the differentiation of "fire, hot coals, and sparks" near the Moon from one another by witnesses on the surface of the Earth, to be inconsistent with Hartung's hypothesis.

9.5 Conclusions

It has been suggested that the formation of 22 km diameter lunar crater Giordano Bruno was witnessed in June 1178 AD. There is no strong evidence to support this hypothesis. Strong evidence against this hypothesis is provided by Nininger and Huss (1977) and by the current Chapter. Nininger and Huss suggest that the medieval text upon which the hypothesis is based is inconsistent with the hypothesis. The current Chapter predicts a superlative meteor storm in the week after Giordano Bruno's formation. No records of such a storm have been found, suggesting that no such storm occurred in June 1178 AD, and hence that Giordano Bruno did not form at this time.

CHAPTER 10

SIMPLE CLIMATE MODELS

10.1 Abstract

Simple, one dimensional climate models are commonly used in the first studies of a planet's climate. While planets in our solar system are nowadays usually modelled by general circulation models, simple climate models, which require minimal observational constraints on the nature of an atmosphere, will be useful in studies of extra-solar planets.

This Chapter has two distinct parts. In Section 10.2 I investigate a two-box model of an atmosphere which uses a variational principle to predict heat transport within the atmosphere. I derive an analytical expression that relates the efficiency with which energy is radiated to space to that with which it is transported within the atmosphere. This expression has a surprisingly simple form in most cases. It can be used to make predictions which can then be compared with observations to test the simple atmospheric model. I do not compare predictions with observations because investigating the validity of the model is not the purpose of this work. This work is an investigation of some properties of the previously proposed model, not a test of the model.

In Section 10.3 I investigate three other simple climate models that have been proposed in the literature and show that their predictions are almost identical in most cases. This demonstrates that testing one of them is almost equivalent to testing all of them and that it will be very difficult for other workers to prove that one model is true and the other two are false.

10.2 Two-Box Model

Lorenz et al. (2001) discussed a two-box model for climate controlled by a variational principle. Variational principles (*e. g.* the principle of least action in mechanics or Fermat's principle of least time in optics) are a well-established part of physics, though their discoveries are often serendipitous (Paltridge, 1975; Yourgrau and Mandelstam, 1960).

The model of Lorenz et al. (2001) is shown in Figure 10.1. Energy balance requires:

$$I_0 - F - E_0 = 0 \quad (10.1)$$

$$I_1 + F - E_1 = 0 \quad (10.2)$$

In this model, I_0 and I_1 are assumed to be known from the planet's orbital properties and albedo. E is assumed to be a known linear function of temperature. F , T_0 , and T_1 are unknowns to be solved for.

$$E_0 = A + BT_0 \quad (10.3)$$

$$E_1 = A + BT_1$$

10.2.1 Variational Principle

The model currently has one fewer equations (10.1 and 10.2) than unknowns (F, T_0, T_1). The hypothesized variational principle provides the final constraint. It is hypothesized that the rate of entropy production ($F/T_1 - F/T_0$) within the

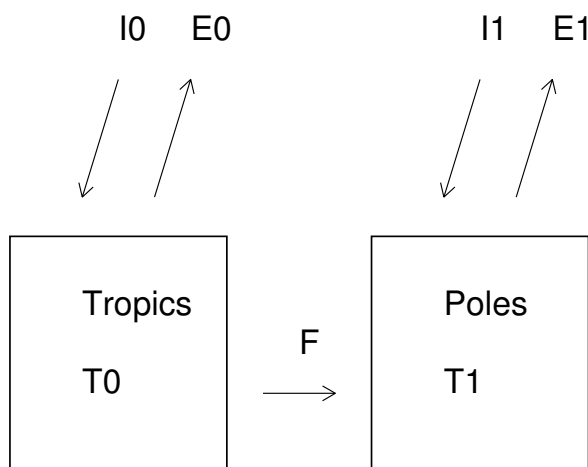


Figure 10.1: Simple two-box climate model. The boxes are of equal surface area, the left (subscript “0”) corresponding to regions equatorward of 30° latitude and the right (subscript “1”) to regions poleward of 30° latitude. I is absorbed solar flux, E is outgoing thermal flux, and F is the rate of latitudinal heat flow per unit area. T is temperature.

system is extremized subject to the energy balance constraints. The extremization proceeds as follows:

$$\frac{\partial}{\partial T_0} (F/T_1 - F/T_0) = 0 \quad (10.4)$$

Using Equations 10.1, 10.2, and 10.3 this becomes:

$$\frac{\partial}{\partial T_0} \left(\frac{I_0 - A - BT_0}{T_1} - \frac{I_0 - A - BT_0}{T_0} \right) = 0 \quad (10.5)$$

The sum of Equations 10.1 and 10.2 is:

$$I_0 + I_1 = 2A + B(T_0 + T_1) \quad (10.6)$$

Using Equation 10.6 to eliminate T_1 , Equation 10.5 becomes:

$$\frac{\partial}{\partial T_0} \left(\frac{I_0 - A - BT_0}{\frac{I_0 + I_1 - 2A}{B} - T_0} - \frac{I_0 - A - BT_0}{T_0} \right) = 0 \quad (10.7)$$

After differentiation, Equation 10.7 becomes:

$$\frac{-B}{\frac{I_0 + I_1 - 2A}{B} - T_0} + \frac{I_0 - A - BT_0}{\left(\frac{I_0 + I_1 - 2A}{B} - T_0 \right)^2} + \frac{I_0 - A}{T_0^2} = 0 \quad (10.8)$$

Using Equation 10.6 to reintroduce T_1 , Equation 10.8 becomes:

$$\frac{-B}{T_1} + \frac{I_0 - A - BT_0}{T_1^2} + \frac{I_0 - A}{T_0^2} = 0 \quad (10.9)$$

Using Equation 10.6 again to reintroduce I_1 , this becomes:

$$\frac{-B}{T_1} - \frac{I_1 - A - BT_1}{T_1^2} + \frac{I_0 - A}{T_0^2} = 0 \quad (10.10)$$

Rearranging:

$$\frac{I_0 - A}{T_0^2} = \frac{I_1 - A}{T_1^2} \quad (10.11)$$

Solving for T_0 :

$$T_0 = T_1 \left(\frac{I_0 - A}{I_1 - A} \right)^{1/2} \quad (10.12)$$

This result can be used with Equation 10.6 to solve for T_0 and T_1 using the known I_0 , I_1 , A , and B .

10.2.2 Solution for F

Simple climate models often try to predict F and the following work investigates this model's predictions. F is often parameterized as being proportional to the temperature difference between the two boxes.

$$F = 2D(T_0 - T_1) \quad (10.13)$$

D is a coefficient of heat transport, taken as an unknown to be solved for. Predicting D is equivalent to predicting F . The factor of two is included for consistency with other models (Lorenz et al., 2001).

I use Equations 10.13 and 10.3 to replace F and E_i in Equations 10.1 and 10.2, then substitute the result of Equation 10.12 for T_0 into Equations 10.1 and 10.2:

$$I_0 - 2DT_1 \left(\left(\frac{I_0 - A}{I_1 - A} \right)^{1/2} - 1 \right) - A - BT_1 \left(\frac{I_0 - A}{I_1 - A} \right)^{1/2} = 0 \quad (10.14)$$

$$I_1 + 2DT_1 \left(\left(\frac{I_0 - A}{I_1 - A} \right)^{1/2} - 1 \right) - A - BT_1 = 0 \quad (10.15)$$

Rearranged, Equation 10.14 becomes:

$$(I_0 - A) = T_1 \left(2D \left(\left(\frac{I_0 - A}{I_1 - A} \right)^{1/2} - 1 \right) + B \left(\frac{I_0 - A}{I_1 - A} \right)^{1/2} \right) \quad (10.16)$$

Using Equation 10.16 to eliminate T_1 from Equation 10.15 shows that:

$$(I_1 - A) + \frac{2D(I_0 - A) \left(\left(\frac{I_0 - A}{I_1 - A} \right)^{1/2} - 1 \right)}{2D \left(\left(\frac{I_0 - A}{I_1 - A} \right)^{1/2} - 1 \right) + B \left(\frac{I_0 - A}{I_1 - A} \right)^{1/2}} - \frac{B(I_0 - A)}{2D \left(\left(\frac{I_0 - A}{I_1 - A} \right)^{1/2} - 1 \right) + B \left(\frac{I_0 - A}{I_1 - A} \right)^{1/2}} = 0 \quad (10.17)$$

Rearranging:

$$(I_1 - A) 2D \left(\left(\frac{I_0 - A}{I_1 - A} \right)^{1/2} - 1 \right) + B(I_0 - A)^{1/2} (I_1 - A)^{1/2} + (I_0 - A) 2D \left(\left(\frac{I_0 - A}{I_1 - A} \right)^{1/2} - 1 \right) - B(I_0 - A) = 0 \quad (10.18)$$

Rearranging to group together like terms:

$$2D((I_0 - A) + (I_1 - A)) \left(\left(\frac{I_0 - A}{I_1 - A} \right)^{1/2} - 1 \right) = B(I_0 - A)^{1/2} \left((I_0 - A)^{1/2} - (I_1 - A)^{1/2} \right) \quad (10.19)$$

Multiplying by $(I_1 - A)^{1/2}$:

$$2D((I_0 - A) + (I_1 - A)) \left((I_0 - A)^{1/2} - (I_1 - A)^{1/2} \right) = \quad (10.20)$$

$$B(I_0 - A)^{1/2} (I_1 - A)^{1/2} \left((I_0 - A)^{1/2} - (I_1 - A)^{1/2} \right)$$

Finally solving for D :

$$\frac{2D}{B} = \frac{(I_0 - A)^{1/2} (I_1 - A)^{1/2}}{(I_0 - A) + (I_1 - A)} \quad (10.21)$$

For the special case where $I_0 = I_1$, Equation 10.21 states that $4D = B$. If $I_0 = I - \delta/2$ and $I_1 = I + \delta/2$, then Equation 10.21 becomes:

$$\frac{4D}{B} = \frac{(I - A + \delta/2)^{1/2} (I - A - \delta/2)^{1/2}}{(I - A)} \quad (10.22)$$

Rearranging:

$$\frac{4D}{B} = \left(1 - \frac{\delta^2}{4(I - A)^2} \right)^{1/2} \quad (10.23)$$

As long as $I - A$ is not much smaller than I , the value of this expression is close to unity. If I use a linearized Stefan-Boltzman law for E , then:

$$-3\sigma T^4 + 4\sigma T^3 T_i = E_i \quad (10.24)$$

$$A + BT_i = E_i$$

Where T is a characteristic temperature at the centre of the linear expansion. If T_0 and T_1 are not too dissimilar from T , then $A \sim -3 \times E_i$. $I - A$ is not much

smaller than I , in fact it is significantly larger than I . If $E(T)$ is any polynomial function of greater than first order that monotonically increases with T , then its linearized form has A negative. This leads to a value for Equation 10.23 that is not too far from unity. As an example, if $A = 0$ and $\delta = I$, then Equation 10.23 has a value of 0.87. Smaller values of δ are closer to unity. To a reasonable approximation:

$$4D = B \quad (10.25)$$

In investigating this simple climate model, I have discovered a conserved quantity that has the same value in each box (Equation 10.11) and a relationship between the coefficient of heat transport within the atmosphere (D) and the derivative of outgoing radiation flux with respect to temperature (B) (Equation 10.25). These properties can be used to make predictions and test the model.

10.3 Other Simple Climate Models

In Section 10.3 I investigate three other simple climate models that have been proposed in the literature (Paltridge, 1975; Rodgers, 1976; Lin, 1982). These three models all use different variational principles to predict the annually-averaged variation of temperature with latitude. I show that their predictions are almost identical in most cases.

Steady state, one dimensional climate models are generally of the form:

$$F(x) = I(x) - E(x) \quad (10.26)$$

where x is the sine of latitude, F is the meridional heat flux, I is the absorbed solar radiation, and E is the emitted thermal radiation. The effective temperature, T , is defined by:

$$E = \sigma T^4 \quad (10.27)$$

All temperatures discussed in Section 10.3 are effective temperatures, so I have dropped the usual subscript-e for convenience. I depends on planetary orbital parameters and Bond albedo and F or E is to be predicted by a climate model. Energy balance requires that:

$$\int_{-1}^1 I(x) - E(x) dx = 0 \quad (10.28)$$

In the trivial case where there is no heat transport, $E(x) = I(x)$ and $T(x)$ is easily predicted. In the trivial case where there is infinite ability to transport heat, $E(x)$ is constant and equal to the mean of $I(x)$; $T(x)$ is again easily predicted.

I now introduce some useful notation:

$$\begin{aligned} \langle y \rangle &= \frac{\int_{-1}^1 y(x) dx}{\int_{-1}^1 dx} \\ \langle y \rangle &= \frac{\int_{-1}^1 y(x) dx}{2} \end{aligned} \quad (10.29)$$

10.3.1 Rodgers's Model

Rodgers (1976), in response to Paltridge (1975), discussed a simple model in which $E(x)$ is that which extremizes:

$$\int_{-1}^1 \frac{I(x) - E(x)}{E(x)} dx \quad (10.30)$$

Using the calculus of variations and the energy balance constraint of Equation 10.28, the solution to this model is given by (Arfken and Weber, 1995):

$$\frac{\partial}{\partial E} (I(x)/E(x) - 1 - \lambda I(x) + \lambda E(x)) = 0 \quad (10.31)$$

Where λ is a Lagrange multiplier. Performing the differentiation in Equation 10.31 shows that:

$$\frac{-I(x)}{E(x)^2} + \lambda = 0 \quad (10.32)$$

The solution of Equation 10.32 for $E(x)$ is:

$$\left(\frac{I(x)}{\lambda}\right)^{1/2} = E(x) \quad (10.33)$$

Substituting the result of Equation 10.33 into Equation 10.28 provides a solution for λ :

$$\int_{-1}^1 I(x) dx = \int_{-1}^1 \left(\frac{I(x)}{\lambda}\right)^{1/2} dx \quad (10.34)$$

Using Equation 10.29, Equation 10.34 becomes:

$$\langle I \rangle = \frac{\langle I^{1/2} \rangle}{\lambda^{1/2}} \quad (10.35)$$

Using Equation 10.35 to eliminate λ from Equation 10.33 gives the following solution for $E(x)$:

$$\sigma T(x)^4 = E(x) = I(x)^{1/2} \times \frac{\langle I \rangle}{\langle I^{1/2} \rangle} \quad (10.36)$$

10.3.2 Paltridge's Model

Paltridge (1975) proposed a simple model in which $T(x)$ is that which extremizes:

$$\int_{-1}^1 \frac{I(x) - \sigma T^4(x)}{T(x)} dx \quad (10.37)$$

Subject to the energy balance constraint of Equation 10.28. Using the calculus of variations, the solution of Equation 10.37 is:

$$\frac{\partial}{\partial T} \left(I(x)/T(x) - \sigma T(x)^3 - \lambda I(x) + \lambda \sigma T(x)^4 \right) = 0 \quad (10.38)$$

Performing the differentiation in Equation 10.38 shows that:

$$\frac{-I(x)}{T(x)^2} - 3\sigma T(x)^2 + 4\lambda\sigma T(x)^3 = 0 \quad (10.39)$$

Rearranging:

$$I(x) + 3\sigma T(x)^4 = 4\lambda\sigma T(x)^5 \quad (10.40)$$

Integrating Equation 10.40 and using Equation 10.28 to replace the σT^4 term, I find:

$$4 \langle I \rangle = 4\lambda\sigma \langle T^5 \rangle \quad (10.41)$$

Substituting this solution for λ into Equation 10.40 shows that:

$$I(x) + 3\sigma T(x)^4 = 4 \frac{\langle I \rangle}{\langle T^5 \rangle} T(x)^5 \quad (10.42)$$

I have not found a simple solution for $T(x)$, so I leave the solution in this form and move on.

10.3.3 Lin's Model

Lin (1982) proposed a simple model in which the generation of available potential energy is maximized. I adapt his model by replacing his use of surface temperature with effective temperature. This makes it possible for his model to be compared with those of Rodgers and Paltridge. In my adaption of Lin's model $T(x)$ is that which extremizes:

$$\int_{-1}^1 (I(x) - \sigma T(x)^4) (T(x) - \langle T \rangle) dx \quad (10.43)$$

Subject to the energy balance constraint of Equation 10.28.

Using the calculus of variations, the solution of Equation 10.43 is:

$$\begin{aligned} \frac{\partial}{\partial T} (I(x)T(x) - \sigma T(x)^5 - I(x) \langle T \rangle) + \\ \frac{\partial}{\partial T} (\sigma \langle T \rangle T(x)^4 - \lambda I(x) + \lambda \sigma T(x)^4) = 0 \end{aligned} \quad (10.44)$$

Performing the differentiation in Equation 10.44 shows that:

$$I(x) - 5\sigma T(x)^4 + 4\sigma \langle T \rangle T(x)^3 + 4\lambda \sigma T(x)^3 = 0 \quad (10.45)$$

Integrating Equation 10.45 and using Equation 10.28 to replace the σT^4 term, I find:

$$\langle I \rangle - 5 \langle I \rangle + 4\sigma \langle T \rangle \langle T^3 \rangle + 4\lambda\sigma \langle T^3 \rangle = 0 \quad (10.46)$$

Rearranging:

$$\sigma \langle T \rangle \langle T^3 \rangle + \lambda\sigma \langle T^3 \rangle = \langle I \rangle \quad (10.47)$$

Rearranging to solve for λ :

$$\lambda = \frac{\langle I \rangle}{\sigma \langle T^3 \rangle} - \langle T \rangle \quad (10.48)$$

Substituting the solution for λ from Equation 10.48 into Equation 10.45, I find:

$$I(x) - 5\sigma T(x)^4 + 4\sigma \langle T \rangle T(x)^3 - 4\sigma \langle T \rangle T(x)^3 + \frac{4\sigma T(x)^3 \langle I \rangle}{\sigma \langle T^3 \rangle} = 0 \quad (10.49)$$

Rearranging:

$$I(x) - 5\sigma T(x)^4 + \frac{4\sigma T(x)^3 \langle I \rangle}{\sigma \langle T^3 \rangle} = 0 \quad (10.50)$$

I have not found a simple solution for $T(x)$, so I leave the solution in this form and move on.

10.3.4 Restricted Solution

To investigate the similarity of this three models, I assume that $I(x)$ is symmetrical about the equator and close to uniform:

$$I(x) = I_0 + ax^2 \quad (10.51)$$

Where $a/I_0 \ll 1$. This could be rewritten to use Legendre polynomials if desired. The omission of a term linear in x is equivalent to assuming a circular orbit and hemispherically symmetric albedo. Using Equation 10.51, $\langle I \rangle$ becomes:

$$\begin{aligned} \langle I \rangle &= \frac{1}{2} \int_{-1}^1 I_0 + ax^2 dx \\ \langle I \rangle &= I_0 + \frac{a}{3} \end{aligned} \quad (10.52)$$

I now find the solution for $E(x)$ for each of the three models using this $I(x)$.

10.3.5 Restricted Solution to Rodgers's Model

Equation 10.36 relates $E(x)$ to $I(x)$ in Rodgers's model. To find $E(x)$ using $I(x)$ from Equation 10.51, I first find $I(x)^{1/2}$ and then $\langle I^{1/2} \rangle$.

$$\begin{aligned} I(x)^{1/2} &= (I_0 + ax^2)^{1/2} \\ I(x)^{1/2} &= I_0^{1/2} \left(1 + \frac{ax^2}{2I_0} \right) \end{aligned} \quad (10.53)$$

$$\begin{aligned} \langle I^{1/2} \rangle &= \frac{1}{2} \int_{-1}^1 I_0^{1/2} \left(1 + \frac{ax^2}{2I_0} \right) dx \\ \langle I^{1/2} \rangle &= I_0^{1/2} \left(1 + \frac{a}{6I_0} \right) \end{aligned} \quad (10.54)$$

Substituting the results of Equations 10.53 and 10.54 into Equation 10.36 I find:

$$E(x) = I_0^{1/2} \left(1 + \frac{ax^2}{2I_0} \right) \frac{\left(I_0 + \frac{a}{3} \right)}{I_0^{1/2} \left(1 + \frac{a}{6I_0} \right)} \quad (10.55)$$

Rearranging:

$$E(x) = I_0 \left(1 + \frac{ax^2}{2I_0} \right) \left(1 + \frac{a}{3I_0} \right) \left(1 - \frac{a}{6I_0} \right) \quad (10.56)$$

Rearranging:

$$E(x) = I_0 \left(1 + \frac{ax^2}{2I_0} + \frac{a}{3I_0} - \frac{a}{6I_0} \right) \quad (10.57)$$

Rearranging:

$$\sigma T(x)^4 = E(x) = I_0 + \frac{ax^2}{2} + \frac{a}{6} \quad (10.58)$$

10.3.6 Restricted Solution to Paltridge's Model

Equation 10.42 is not a simple solution for $E(x)$. Following the form of the restricted solution to Rodgers's model, Equation 10.58, I search for a solution of the form:

$$T(x) = T_0 + bx^2 + c \quad (10.59)$$

Where $b/T_0 \ll 1$ and $c/T_0 \ll 1$. Using Equation 10.59, I have:

$$T(x)^4 = T_0^4 + 4bx^2T_0^3 + 4cT_0^3 \quad (10.60)$$

$$T(x)^5 = T_0^5 + 5bx^2T_0^4 + 5cT_0^4 \quad (10.61)$$

$$\langle T^5 \rangle = T_0^5 + \frac{5bT_0^4}{3} + 5cT_0^4 \quad (10.62)$$

Taking Equation 10.42 and substituting for $I(x)$ using Equation 10.51, for $\langle I \rangle$ using Equation 10.52, for $T(x)^4$ using Equation 10.60, for $T(x)^5$ using Equation 10.61, and for $\langle T^5 \rangle$ using Equation 10.62 I find:

$$I_0 + ax^2 + 3\sigma \left(T_0^4 + 4bx^2T_0^3 + 4cT_0^3 \right) = \quad (10.63)$$

$$4 \left(I_0 + \frac{a}{3} \right) \frac{T_0^5 + 5bx^2T_0^4 + 5cT_0^4}{T_0^5 + \frac{5bT_0^4}{3} + 5cT_0^4}$$

Rearranging:

$$I_0 + ax^2 + 3\sigma \left(T_0^4 + 4bx^2T_0^3 + 4cT_0^3 \right) = \quad (10.64)$$

$$4I_0 \left(1 + \frac{a}{3I_0} \right) \frac{1 + \frac{5bx^2}{T_0} + \frac{5c}{T_0}}{1 + \frac{5b}{3T_0} + \frac{5c}{T_0}}$$

Rearranging:

$$I_0 + ax^2 + 3\sigma T_0^4 + 12\sigma bx^2T_0^3 + 12\sigma cT_0^3 = \quad (10.65)$$

$$4I_0 \left(1 + \frac{a}{3I_0} + \frac{5bx^2}{T_0} + \frac{5c}{T_0} - \frac{5b}{3T_0} - \frac{5c}{T_0} \right)$$

Rearranging:

$$I_0 + ax^2 + 3\sigma T_0^4 + 12\sigma bx^2 T_0^3 + 12\sigma c T_0^3 = \quad (10.66)$$

$$4I_0 + \frac{4a}{3} + \frac{20bx^2 I_0}{T_0} - \frac{20bI_0}{3T_0}$$

Grouping together large and uniform terms, small and non-uniform terms, and small and uniform terms, I have the following three equations:

$$I_0 + 3\sigma T_0^4 = 4I_0 \quad (10.67)$$

$$ax^2 + 12\sigma bx^2 T_0^3 = \frac{20bx^2 I_0}{T_0} \quad (10.68)$$

$$12\sigma c T_0^3 = \frac{4a}{3} - \frac{20bI_0}{3T_0} \quad (10.69)$$

Equation 10.67 shows that:

$$\sigma T_0^4 = I_0 \quad (10.70)$$

Using the result of Equation 10.70 to eliminate I_0 from Equations 10.68 and 10.69, I have the following two equations:

$$ax^2 + 12\sigma bx^2 T_0^3 = 20\sigma bx^2 T_0^3 \quad (10.71)$$

$$12\sigma cT_0^3 = \frac{4a}{3} - \frac{20\sigma bx^2T_0^3}{3} \quad (10.72)$$

Equation 10.71 shows that the solution for b is:

$$a/8 = \sigma bT_0^3 \quad (10.73)$$

Substituting the solution of Equation 10.73 for b into Equation 10.72, I have:

$$\begin{aligned} 12\sigma cT_0^3 &= \frac{4a}{3} - \frac{20a}{3 \times 8} = \frac{a}{2} \\ \sigma cT_0^3 &= \frac{a}{24} \end{aligned} \quad (10.74)$$

Substituting the results of Equations 10.70, 10.73 and 10.74 into Equation 10.60 and multiplying by σ , I have:

$$\begin{aligned} E(x) = \sigma T(x)^4 &= \sigma T_0^4 + 4\sigma bx^2T_0^3 + 4\sigma cT_0^3 \\ E(x) &= I_0 + \frac{ax^2}{2} + \frac{a}{6} \end{aligned} \quad (10.75)$$

This restricted solution for $E(x)$ in Paltridge's model is the same as in Rodgers's model (Equation 10.58).

10.3.7 Restricted Solution to Lin's Model

Equation 10.50 is not a simple solution for $E(x)$. Following the form of the restricted solution to Rodgers's model, Equation 10.58, I search for a solution of the form:

$$T(x) = T_0 + bx^2 + c \quad (10.76)$$

Where $b/T_0 \ll 1$ and $c/T_0 \ll 1$. Using Equation 10.76, I have:

$$T(x)^4 = T_0^4 + 4bx^2T_0^3 + 4cT_0^3 \quad (10.77)$$

$$T(x)^3 = T_0^3 + 3bx^2T_0^2 + 3cT_0^2 \quad (10.78)$$

$$\langle T^3 \rangle = T_0^3 + bT_0^2 + 3cT_0^2 \quad (10.79)$$

Taking Equation 10.50 and substituting for $I(x)$ using Equation 10.51, for $\langle I \rangle$ using Equation 10.52, for $T(x)^4$ using Equation 10.77, for $T(x)^3$ using Equation 10.78, and for $\langle T^3 \rangle$ using Equation 10.79 I find:

$$I_0 + ax^2 - 5\sigma \left(T_0^4 + 4bx^2T_0^3 + 4cT_0^3 \right) + \quad (10.80)$$

$$4 \left(I_0 + \frac{a}{3} \right) \frac{T_0^3 + 3bx^2T_0^2 + 3cT_0^2}{T_0^3 + bT_0^2 + 3cT_0^2} = 0$$

Rearranging:

$$I_0 + ax^2 - 5\sigma T_0^4 - 20\sigma bx^2T_0^3 - 20\sigma cT_0^3 + \quad (10.81)$$

$$4I_0 \left(1 + \frac{a}{3I_0} \right) \frac{1 + \frac{3bx^2}{T_0} + \frac{3c}{T_0}}{1 + \frac{b}{T_0} + \frac{3c}{T_0}} = 0$$

Rearranging:

$$I_0 + ax^2 - 5\sigma T_0^4 - 20\sigma bx^2 T_0^3 - 20\sigma c T_0^3 + 4I_0 \left(1 + \frac{a}{3I_0} + \frac{3bx^2}{T_0} + \frac{3c}{T_0} - \frac{b}{T_0} - \frac{3c}{T_0} \right) = 0 \quad (10.82)$$

Rearranging:

$$I_0 + ax^2 - 5\sigma T_0^4 - 20\sigma bx^2 T_0^3 - 20\sigma c T_0^3 + 4I_0 + \frac{4a}{3} + \frac{12bx^2 I_0}{T_0} - \frac{4bI_0}{T_0} = 0 \quad (10.83)$$

Grouping together large and uniform terms, small and non-uniform terms, and small and uniform terms, I have the following three equations:

$$I_0 - 5\sigma T_0^4 + 4I_0 = 0 \quad (10.84)$$

$$\sigma T_0^4 = I_0$$

$$ax^2 - 20\sigma bx^2 T_0^3 + \frac{12bx^2 I_0}{T_0} = 0 \quad (10.85)$$

$$-20\sigma c T_0^3 + \frac{4a}{3} - \frac{4bI_0}{T_0} = 0 \quad (10.86)$$

Using the result of Equation 10.84 to eliminate I_0 from Equations 10.85 and 10.86, I have the following two equations:

$$ax^2 - 20\sigma bx^2 T_0^3 + 12\sigma bx^2 T_0^3 = 0 \quad (10.87)$$

$$a/8 = \sigma b T_0^3$$

$$-20\sigma cT_0^3 + \frac{4a}{3} - 4\sigma bx^2T_0^3 = 0 \quad (10.88)$$

Substituting the solution of Equation 10.87 for b into Equation 10.88, I have:

$$\begin{aligned} -20\sigma cT_0^3 + \frac{4a}{3} - \frac{a}{2} &= 0 & (10.89) \\ \frac{5a}{6} &= 20\sigma cT_0^3 \\ \sigma cT_0^3 &= \frac{a}{24} \end{aligned}$$

Substituting the results of Equations 10.84, 10.87 and 10.90 into Equation 10.77 and multiplying by σ , I have:

$$\begin{aligned} E(x) = \sigma T(x)^4 &= \sigma T_0^4 + 4\sigma bx^2T_0^3 + 4\sigma cT_0^3 & (10.90) \\ E(x) &= I_0 + \frac{ax^2}{2} + \frac{a}{6} \end{aligned}$$

This restricted solution for $E(x)$ in Lin's model is the same as in Rodgers's model (Equation 10.58).

10.3.8 Restricted Solution to Zero and Infinite Heat Transport Models

In the limit in which there is no heat transport within the atmosphere, $E(x) = I(x)$ and Equation 10.51 shows that:

$$E(x) = I_0 + ax^2 \quad (10.91)$$

In the limit in which there is infinite ability to transport heat within the atmosphere, $E(x) = \langle I \rangle$ and Equation 10.52 shows that:

$$E(x) = I_0 + \frac{a}{3} \quad (10.92)$$

The mean of these two limits for $E(x)$ is:

$$E(x) = I_0 + \frac{ax^2}{2} + \frac{a}{6} \quad (10.93)$$

This expression for $E(x)$ is *also* the same as the restricted solution for $E(x)$ in Rodgers's model (Equation 10.58).

10.3.9 Conclusions

In the limit $I_0 + ax^2$, where $a/I_0 \ll 1$, Rodgers's, Paltridge's, and Lin's models all have the same solution for $E(x)$. This solution is also the mean of models with zero and infinite ability to transport heat. I have not found the solutions of next highest order in x^2 for $E(x)$ for the three models. I have not experimented with numerical values in these equations to see how large the x^4 term in $I(x)$ can be before these three models make predictions for $E(x)$ that differ by, say, 50%. Since $T(x) \propto E(x)^{1/4}$, this corresponds to predictions for $T(x)$ that differ by only 10%. It can be seen that these three models give very similar predictions for $T(x)$ for quite large deviations of $I(x)$ from being uniform in x .

Since these three models make nearly-identical predictions, testing one of them is almost equivalent to testing all of them. It will be very difficult to prove that one is true and the other two are false.

CHAPTER 11

CONCLUSIONS

Each Chapter of this dissertation ends with its main conclusions. I summarize those here and then try to draw together some common threads that link the diverse research questions that I have studied during my five years at LPL.

In Chapter 2 I studied the sol-to-sol variability in the martian upper atmosphere at fixed latitude, altitude, longitude, times of day, and season. This variability is not due solely to solar flux variations, and further modelling and studies of lower atmospheric observations are needed to understand its cause and make useful predictions about it.

In Chapter 2 I also looked at zonal structure in the martian upper atmosphere due to thermal tides. These observations, together with classical tidal theory and observations from other instruments, have been analysed to identify the dominant tidal modes. A simple explanation has been outlined for why topography is the most likely cause of the thermal tides.

The density profiles remain almost unexamined (Keating et al., 2001a). Every bump and wiggle on them has a story to tell about the small-scale dynamics in the upper atmosphere and there are many hints of significant changes in density over very short distances that seem to defy reason. Comparison of data with general circulation models is also at an early stage. Models provide a way of filling the gap in time and space between measurements, so if the models do an adequate job of reproducing the data then it is possible to examine the model's results and determine which physical mechanisms are most important.

Dust storms on Mars are unique in their planetary scale. Their effects on the upper atmosphere are not well-known. Further analysis of this dataset will let us watch the upper atmosphere during the rapid rise and slow decay of a dust storm.

The upper atmosphere sits atop the lower atmosphere. Many phenomena in the upper atmosphere are influenced by the state of the lower atmosphere. As models progress and become able to reproduce upper atmospheric observations reliably, it may be possible to infer information about the state of the lower atmosphere from upper atmospheric measurements alone. For example, some tidal modes require specific wind conditions in the lower atmosphere to propagate to the upper atmosphere and be detected there. The ability to indirectly study the lower atmosphere during aerobraking would greatly extend the scientific usefulness of accelerometer data.

Chapters 3 and 4 have possibly the most important conclusions of this dissertation: Accelerometer data from aerobraking or neutral mass spectrometer data from orbit can be used to measure winds. A novel “Balanced Arch” technique for deriving winds from aerobraking data has been derived and applied to MGS data. These are the first measurements of winds in the martian upper atmosphere. This technique also provides a way of deriving consistent pressure and temperature profiles from the MGS data. Neither the archived dataset nor other workers have yet derived pressure or temperature profiles from the data. Coupled density, pressure, and temperature data are much more useful than density data alone and permit the study of a wider range of phenomena. This technique could be applied to several other existing and anticipated datasets from Venus and Titan.

Winds are one of the most difficult atmospheric properties to measure, yet they play a huge role in determining a planet’s weather and climate. It is unfortunate that I have not been able to test my “Balanced Arch” technique against GCM simulations. It is important that the technique is tested as much as possible to determine what its limits of applicability are. There are several assumptions in the derivation of the technique that warrant careful scrutiny. In the text, I have tried to

emphasize the preliminary nature of the results for the martian upper atmosphere. However, there should be some way to use the combination of inbound and outbound profiles to constrain horizontal gradients in the atmosphere. Separating vertical and horizontal gradients in the density profiles would make them much more useful. The relatively poor agreement between my results and GCM simulations is interesting. Either my results are incorrect, which means that the technique is flawed, or the simulations are incorrect. A combination of those two failures is also possible. There are several possible causes of problems with the simulations. The upper atmospheric simulations are linked to lower atmospheric simulations. These lower atmospheric simulations are well-constrained by data at their lowest altitude levels, but not at the highest levels where they are coupled to the upper atmospheric model. The current coupling is one-way only and does not allow the upper atmosphere to influence the lower. The upper atmosphere is also zonally-averaged and much of this dissertation has discussed longitudinal variability in the upper atmosphere. In the traditional words of graduating students, “more work in this area is needed.”

Chapter 5 represents work whose main usefulness will come after I graduate and use it analyse Beagle 2 and MER entry accelerometer data. By developing techniques to process entry accelerometer data, I have gained a better understanding of what hidden problems and assumptions exist in the processed MGS accelerometer dataset. Section 5.7.3 presents what I believe is a new idea that could radically simplify the first analysis of entry accelerometer data when management and public alike are clamouring for results. Deriving an atmospheric temperature profile without needing an aerodynamic information about the spacecraft is potentially a powerful technique. The problems that have been discovered in the PDS archive are probably not important for the atmospheric structure results or their interpretation. Spencer et al. (1999), using what I believe is a valid entry state, derived essentially identical atmospheric results as Magalhães et al. (1999), whom I believe quoted an invalid entry state. It is not clear that the entry state quoted by Magalhães et al. (1999) was actually used to derive their results.

Chapter 6 is also something of an investment for the future when I am able to analyse entry accelerometer data. It will not provide ground-breaking scientific results, but it offers the chance to obtain very rapid, yet crude, characterizations of atmospheric structure even before the entry is complete. The ability to make a robust estimate of atmospheric temperature at peak acceleration without being overwhelmed by the uncertainties in transmitted frequency is potentially useful. The ability to derive any scientific results from a failed mission might help maintain public support of NASA's exploration program.

Chapter 7 presents a way to improve the atmospheric profiles measured during the entry of the two Viking landers. Errors of 10 – 20% in density and pressure at a given altitude were found and preliminarily corrected for. A topographic profile from the Viking 2 entry, which is not discussed in this chapter, can be found on page 285 of Euler et al. (1979). This work shows topographic elevation above a reference areoid, so comparison against MOLA data requires knowledge of what that reference areoid was. Since Viking 2 landed on flat Utopia, far from the rugged outflow channel terrain of Viking 1, a smaller error is likely.

This is another example of scientifically useful information coming from what might be considered an engineering instrument. Comparing the Viking radar altimeter topographic profiles with MOLA data provides a test of an established dataset that could not have been foreseen in the Viking era. The possibility of someone reanalysing the entire Viking entry with the additional constraint of MOLA data is, I think, slim. Many different instruments were used to derive the Viking entry trajectories and the chance that all the necessary data and documentation can be found and understood in the JPL archives is small. Since martian surface atmospheric pressure varies so much, the Viking-derived standard atmosphere is primarily temperature based (Seiff, 1982). Temperature as a function of altitude is specified from the Viking entry data, but pressure and density profiles are derived from the temperature profile, an assumed surface pressure, hydrostatic equilibrium, and the equation of state. Consequently, the likely impact of errors in the original

Viking density and pressure profiles on other work is relatively small.

Chapter 8 continues the theme of martian topography with a concise discussion of the discovery of a network of tectonic features in the otherwise bland northern plains of Mars and their implications for a possible ocean in that area.

This project has received an undeservedly small amount of attention in this dissertation. I began this project in the summer of 2000 after my second year as a graduate student. My orals kept me away from it for much of the subsequent semester. I continued working on it in the spring of 2001 and wrote a funding proposal to support my work. My involvement in entry accelerometer work from the summer of 2001 onwards pushed this project further into the background and the rejection of the funding proposal did not help my motivation either. It has been two years since I worked on this project and my notes are simply not adequate for writing a substantial chapter on this without more work than is justified at this time. I would like to continue with this project in the future. Projects important enough to get published in *Nature* are unlikely to be a steady occurrence in my career and I should take full advantage of them when I have them. To make a significant contribution with this project in the future I need to develop a robust technique for mapping these ridges and measuring their characteristics. I am dissatisfied with the subjectivity of my previous mapping work and think that I would benefit from working closely with someone experienced in this area to develop a more objective and repeatable technique, preferably one that can be automated. The nature of the northern plains is, as *Nature's* editors phrased it, enigmatic. Neither sedimentation in an ocean nor steady influx of material from localized volcanic or fluvial sources as championed in current models seems to explain either the flatness or smoothness of this region or its veneer-like covering of older craters and ridges. Why the plains are closer to level with the pole-to-pole slope than with respect to an equipotential is also perplexing.

Chapter 9 investigates whether the formation of lunar crater Giordano Bruno was witnessed in 1178 AD. The formation of this crater would have caused

great meteor storms in Earth's atmosphere that would have merited recording in the many chronicles of the era. Since no such records are known, I concluded that Giordano Bruno did not form in 1178 AD. This means that there is not a large, pristine crater on the Moon that can be studied to give more insight into the important geological process of impact cratering than weathered terrestrial examples.

Chapter 10 presents some studies of simple climate models. Simple, one dimensional climate models are commonly used in the first studies of a planet's climate. While planets in our solar system are nowadays usually modelled by general circulation models, simple climate models, which require minimal observational constraints on the nature of an atmosphere, will be useful in studies of extra-solar planets.

The common thread that runs through this dissertation is the analysis of accelerometer data to derive atmospheric properties. Accelerometer data seem relatively simple to me, just a single scalar measurement as a function of time, when compared to, for example, gas chromatograph measurements or the millions of spectra that TES has measured. I have used two different approaches in this analysis. One approach aims for back-of-the-envelope, order-of-magnitude analysis leading to rapid generalizations about the phenomena present in the data. Chapter 6 and Section 5.7.3 are examples of this. The other approach aims for long-term, methodical, and in-depth analysis to extract every last piece of information from the data. Chapters 2 and 4 are examples of this. The rapid approach favours analytical tools with sweeping simplifications and limited predictive power, whereas the detailed approach favours comparison to other observations and theoretical models to build a comprehensive picture of what is happening. Both styles have their advantages and disadvantages. I believe that the most useful progress can be made by switching back and forth between them.

The datasets that I have analysed or prepared to analyse in this dissertation are not directly concerned with the most pressing scientific questions that drive current programmatic and mission priorities. However, they are in a sense "free data."

Since the measurements are made for engineering purposes anyway, subsequent scientific analysis of them is relatively cheap. The dynamics of the martian upper atmosphere are almost unconstrained by data in comparison with the lower atmosphere. That means that connections to the major questions pertaining to the study of the better-studied martian lower atmosphere or of upper atmospheres in general are weak. Only after collecting new and broad-based observations, such as the Mars Global Surveyor accelerometer data, and surveying and characterizing those data can specific, focused questions be posed that address these issues.

Exploring such a *terra incognita* will always lead to discoveries, even if it is not known in advance what they will be. In the final analysis, the reason why I have spent five years studying these data is for the stimulation of making unexpected discoveries that will influence scientific priorities in the future.

APPENDIX A

CHARACTERIZING THE ZONAL STRUCTURE WITH AN HARMONIC FIT

Having selected a subset of density measurements in some way, I fit a function to it to quantify the variation in density with longitude. A linear combination of harmonic functions is a natural choice as the fitted function. I fit:

$$\rho = a_0 + a_1 \cos(\lambda) + b_1 \sin(\lambda) + \cdots + a_k \cos(k\lambda) + b_k \sin(k\lambda) \quad (\text{A.1})$$

Where ρ is density, λ is east longitude, and the a_i and b_i are model parameters. This is a wave- k model. There must be enough data points in the subset to constrain the fit, so there must be at least $2k + 1$ data points. It is not possible to fit fewer data points with a wave- k model. If k is smaller than an optimal value, then the model does not capture all the information present in the data. If k is larger than an optimal value, then the model parameters are poorly constrained. I shall discuss the optimal value of k later in this section.

In general, when fitting a model to data, one should incorporate measurement uncertainties directly into the fitting procedure. However, as I now outline, that is not appropriate here. The uncertainties quoted for each density measurement in the PDS archive are not formal uncertainties in the strictest sense (Tolson et al., 2000; Keating et al., 2001a). As described in Tolson et al. (2000), these uncertainties include contributions from an empirical “quality indicator”. However, one might still consider using them as if they were formal 1σ uncertainties. There

is a problem with this approach. The quoted uncertainties each refer to the uncertainty of an individual measurement. Should a later measurement at exactly the same longitude obtain the same density within the quoted uncertainty? Not necessarily. The conditions within the experiment, the martian upper atmosphere, are beyond our control. They vary, due to weather, between measurements. The quoted uncertainties are very relevant to each individual measurement. They are less relevant to the repeatability of each measurement at some later time. The repeatability of measurements on a timescale of one sol is addressed in Section 2.4. I find that sol-to-sol variability is five times greater than the few percent measurement uncertainties at 130 km altitude.

The measurement uncertainties are simply inappropriate for direct incorporation into the fitting procedure in the manner of page 162 of Bevington (1969). The appropriate uncertainties are those between repeat measurements taken over the duration of the experiment. These uncertainties cannot be calculated *a priori* using only knowledge of the measurement instrument and measurements from a single aerobraking pass. I must use the mean square error between the measurements and model predictions as a proxy for the uncertainty in the repeatability of each measurement following Equation 8.29 of Bevington (1969). The individual measurement uncertainties do not become comparable to the sol-to-sol variabilities until altitudes greater than 150 km. Since measurements at altitudes above 150 km are rarely used in this chapter, I neglect the measurement uncertainties throughout this chapter.

With the above assumption about dealing with uncertainties, m density measurements, and n model parameters, the basic model follows Equation 7.18 of Neter and Wasserman (1974):

$$\underline{Y} = \underline{X} \underline{p} + \epsilon \tag{A.2}$$

Where \underline{Y} is an m -element vector of density observations, \underline{X} is an m -by- n

matrix, \underline{p} is an n -element vector of model parameters, and $\underline{\epsilon}$ is an n -element vector of uncorrelated random variables of mean 0 and standard deviation σ .

Using the model outlined in Equation A.1:

$$\begin{aligned}
 X_{i0} &= 1 & (A.3) \\
 X_{i1} &= \cos(\lambda_i) \\
 X_{i2} &= \sin(\lambda_i) \\
 &\vdots \\
 X_{in-2} &= \cos\left(\frac{(n-1)\lambda_i}{2}\right) \\
 X_{in-1} &= \sin\left(\frac{(n-1)\lambda_i}{2}\right)
 \end{aligned}$$

$$\begin{aligned}
 p_0 &= a_0 & (A.4) \\
 p_1 &= a_1 \\
 p_2 &= b_1 \\
 &\vdots \\
 p_{n-2} &= a_{\frac{n-1}{2}} \\
 p_{n-1} &= b_{\frac{n-1}{2}}
 \end{aligned}$$

The index i labels an individual density measurement. The n variables $(1, \cos(\lambda), \sin(\lambda), \dots)$ being fitted are linearly independent. The least squares solution for the model parameters, \underline{p} , follows Equation 7.21 of Neter and Wasserman (1974):

$$\underline{p} = \left(\underline{\underline{X}}^T \underline{\underline{X}} \right)^{-1} \underline{\underline{X}}^T \underline{Y} \quad (A.5)$$

Where a superscript T indicates the transpose of a matrix and the superscript -1 indicates the inverse of a matrix. Note that the constant density term, a_0 or p_0 , is not formally identical to the mean density. Hence I refer to it as the constant density term rather than as the zonal mean term. However, the two are usually similar.

The model predictions, $\hat{\underline{Y}}$, for atmospheric densities at the longitudes at which measurements have been made follow Equation 7.23 of Neter and Wasserman (1974):

$$\hat{\underline{Y}} = \underline{\underline{X}} \underline{\underline{p}} \quad (\text{A.6})$$

The covariance matrix for $\underline{\underline{p}}$ follows Equation 7.39 of Neter and Wasserman (1974):

$$\underline{\underline{Cov}}(\underline{\underline{p}}) = \frac{(\hat{\underline{Y}} - \underline{\underline{Y}})^T (\hat{\underline{Y}} - \underline{\underline{Y}})}{m - n} (\underline{\underline{X}}^T \underline{\underline{X}})^{-1} \quad (\text{A.7})$$

1 σ uncertainties in the model parameters are given by:

$$\sigma_{p_j} = \underline{\underline{Cov}}_{jj} \quad (\text{A.8})$$

Using sine and cosine terms is useful for forming a linear model. However, it is more useful to interpret paired sine and cosine terms as being a single sinusoid with an amplitude and a phase. I define the phase of a given harmonic as the longitude of its first peak east of 0° . Thus the phase of the wave- q harmonic must lie between 0° and $360^\circ\text{E}/q$. q labels a certain harmonic.

$$a_q \cos(q\lambda) + b_q \sin(q\lambda) = R_q \cos(q[\lambda - \alpha_q]) \quad (\text{A.9})$$

Where R_q is the amplitude of the q th harmonic and $q\alpha_q$ is the phase of the q th harmonic. Trigonometry yields the following solutions for R_q and α_q in terms of a_q and b_q .

$$R_q = (a_q^2 + b_q^2)^{1/2} \quad (\text{A.10})$$

$$\alpha_q = \frac{1}{q} \tan^{-1} (b_q/a_q) \quad (\text{A.11})$$

Using the usual formula, Equation 4.9 of Bevington (1969), for transforming uncertainties of uncorrelated variables:

$$\sigma_{R_q}^2 = \sigma_{a_q}^2 \left(\frac{\partial R_q}{\partial a_q} \right)^2 + \sigma_{b_q}^2 \left(\frac{\partial R_q}{\partial b_q} \right)^2 \quad (\text{A.12})$$

$$\sigma_{\alpha_q}^2 = \sigma_{a_q}^2 \left(\frac{\partial \alpha_q}{\partial a_q} \right)^2 + \sigma_{b_q}^2 \left(\frac{\partial \alpha_q}{\partial b_q} \right)^2 \quad (\text{A.13})$$

$$\sigma_{R_q}^2 = \sigma_{a_q}^2 \left(\frac{a_q}{R_q} \right)^2 + \sigma_{b_q}^2 \left(\frac{b_q}{R_q} \right)^2 \quad (\text{A.14})$$

$$\sigma_{\alpha_q}^2 = \frac{b_q^2 \sigma_{a_q}^2 + a_q^2 \sigma_{b_q}^2}{q^2 (a_q^2 + b_q^2)^2} \quad (\text{A.15})$$

A phase of $3^\circ \pm 15^\circ$ is a perfectly reasonable and meaningful result. An amplitude of $3 \text{ kg km}^{-3} \pm 15 \text{ kg km}^{-3}$ means that the harmonic is not present in any statistically significant sense and that its corresponding phase is meaningless.

I generally normalized the zonally-varying terms in each wavefit (R_q) by their constant density term (R_0). This facilitates a comparison of the strength of the zonal structure between different seasons or altitudes. I use the symbol R_q^N to label normalized harmonic amplitudes.

$$R_q^N = \frac{R_q}{R_0} \quad (\text{A.16})$$

$$\sigma_{R_q^N}^2 = \sigma_{R_q}^2 \left(\frac{\partial R_q^N}{\partial R_q} \right)^2 + \sigma_{R_0}^2 \left(\frac{\partial R_q^N}{\partial R_0} \right)^2 \quad (\text{A.17})$$

$$\sigma_{R_q^N}^2 = \frac{R_q^2 \sigma_{R_0}^2}{R_0^4} + \frac{\sigma_{R_q}^2}{R_0^2} \quad (\text{A.18})$$

A 1σ uncertainty about the fitted function can be calculated at any given longitude following Equation 7.54a of Neter and Wasserman (1974):

$$\sigma_{fit}^2 = \left(1 + \underline{X}_{new}^T (\underline{X}^T \underline{X})^{-1} \underline{X}_{new} \right) \frac{(\hat{\underline{Y}} - \underline{Y})^T (\hat{\underline{Y}} - \underline{Y})}{m - n} \quad (\text{A.19})$$

where \underline{X}_{new} is an n -element vector whose elements are calculated identically to those of a single column of \underline{X} , as in Equation A.3. The longitude used to calculate \underline{X}_{new} is that at which the 1σ uncertainty is desired. Formally, this is the 1σ uncertainty on what a new observation at that longitude might be. The predicted value of that observation is as in Equation A.6.

Finally, I must quantify the goodness (or otherwise) of the fit. Well-characterized model parameters are useless in any predictive sense if the fit is poor. Since I do not know the appropriate uncertainties I cannot use a χ^2 test. This problem is discussed on page 192 of Bevington (1969).

I used an F-test instead and followed Equation 7.30 in Neter and Wasserman (1974). If there were at least a minimum number of data points, defined later in this section, used in the fit *and* this F-test showed a probability of 90% or greater that not all model parameters beyond the constant density term should be zero, then I accepted the fit as good. If not, then I concluded that there was no justification for modelling the density with anything beyond a constant density term. Bad fits generally occurred in regions where there were significantly fewer data points than usual, which might be due to data dropouts or a high rate of periapsis precession through a given latitude range. Since so many of the bad fits were due to insufficient data rather than the zonal structure being well-characterized as merely a constant density term, bad fits are generally ignored in the Figures either by omission or by interpolating nearby good fits into that region to estimate what the fit would be like if there were more data. If fewer than the minimum number of data points were available, then I did not attempt a fit.

To perform an F-test, I calculated:

$$F = \frac{(\overline{Y} \underline{I} - \underline{Y})^T (\overline{Y} \underline{I} - \underline{Y}) - (\hat{\underline{Y}} - \underline{Y})^T (\hat{\underline{Y}} - \underline{Y})}{(\hat{\underline{Y}} - \underline{Y})^T (\hat{\underline{Y}} - \underline{Y})} \frac{m - n}{n - 1} \quad (\text{A.20})$$

Where the scalar \overline{Y} is the mean of \underline{Y} and \underline{I} is an n -element vector with all elements equal to 1. This result for F is then compared against the requisite statistical distribution, using IDL's F_PDF function, to find the probability that all model parameters beyond the constant density term are zero. If this probability exceeds 10%, then I declare that the fit is bad.

An F-test can, in theory, be used to determine whether to include any higher-order terms in the fitting function as discussed on page 200 of Bevington (1969). One might consider beginning with a constant density model, then adding progressively higher harmonics until the latest addition failed to provide significant improvement. However, if the zonal structure is dominated, say, by wave-3 and

wave-4 terms and has only small contributions from wave-1 and wave-2 terms, then this approach would recommend truncating the fitting function before reaching the dominant harmonics.

For consistency, the same basic model has to be applied to all subsets of the data to which I attempt to fit a harmonic model. It is inconsistent to fit, say, a full wave-4 model to one portion of the data and, say, a constant density term plus wave-3 and wave-4 terms to another portion of the data. I chose to truncate my fits at wave-4 throughout Chapter 2. I chose to use a wave-4 model after extensive experimentation on subsets of data from the Daytime Precession and Polar Crossing parts of Phase 2. Models with fewer harmonics seemed to me to have significantly worse fits, on the whole. Models with more harmonics did not have significantly better fits, though the increase in the number of free parameters without a corresponding increase in the number of data points to control them led to increased uncertainties in the solution for the model parameters. Lacking a formal technique for arriving at this conclusion, I acknowledge that other choices are valid.

A wave-4 model has 9 free parameters and so cannot be fitted to less than 9 data points. If there are only slightly more than 9 data points in a data subset, then all model parameters are predicted with such large uncertainties as to be useless. I did not attempt any fits to data subsets with less than 15 data points. If the model is fit with only slightly more data points than free parameters, then the model parameters have large uncertainties regardless of whether the model is good or not. If more data points are used, then large uncertainties in model parameters mean that the data are more complicated than the simple model. Thus using many data points increases the meaningfulness of the uncertainties on the model parameters.

APPENDIX B

GENERATING CONSTANT ALTITUDE DATA FROM THE PDS PROFILES

Whilst analysing the MGS Accelerometer data archived with the PDS (Keating et al., 2001a; Keating et al., 2001b), I discovered an interesting complication in how the constant altitude data are generated. Although this is not of direct importance to the conclusions I present in the main body of this dissertation, I would like to document it here. The motivation for this investigation was an attempt to extract constant altitude data at 120 km since, as Figure B.1 shows, periapsis is below 120 km for nearly all of Phase 2 of aerobraking.

The constant altitude data in the PDS archive are generated from the profile data in the same archive (Keating et al., 2001a; Keating et al., 2001b). File catalog/altds.cat in the archive details the extraction of the constant altitude data at 130, 140, 150, and 160 km (Tolson et al., 2000). The PDS profile data contain two tables of densities and altitudes for each orbit. One is based on 7-second (or 6.7 second, the documentation contains some inconsistencies) averaging of accelerometer counts. The other is based on 40-second averaging.

I have generated constant altitude data at 120 km for all orbits where periapsis was below that altitude. I attempted to verify my technique for doing so by reproducing the PDS data at higher constant altitudes from the profile data. I was initially unable to get a good match. After discussions with Jill Hanna, who participated in the generation of the archive at NASA-Langley, I found that I could reproduce the PDS results by fitting 7-s densities to the 40-s altitudes and not incorporating the measurement uncertainties into the analysis.

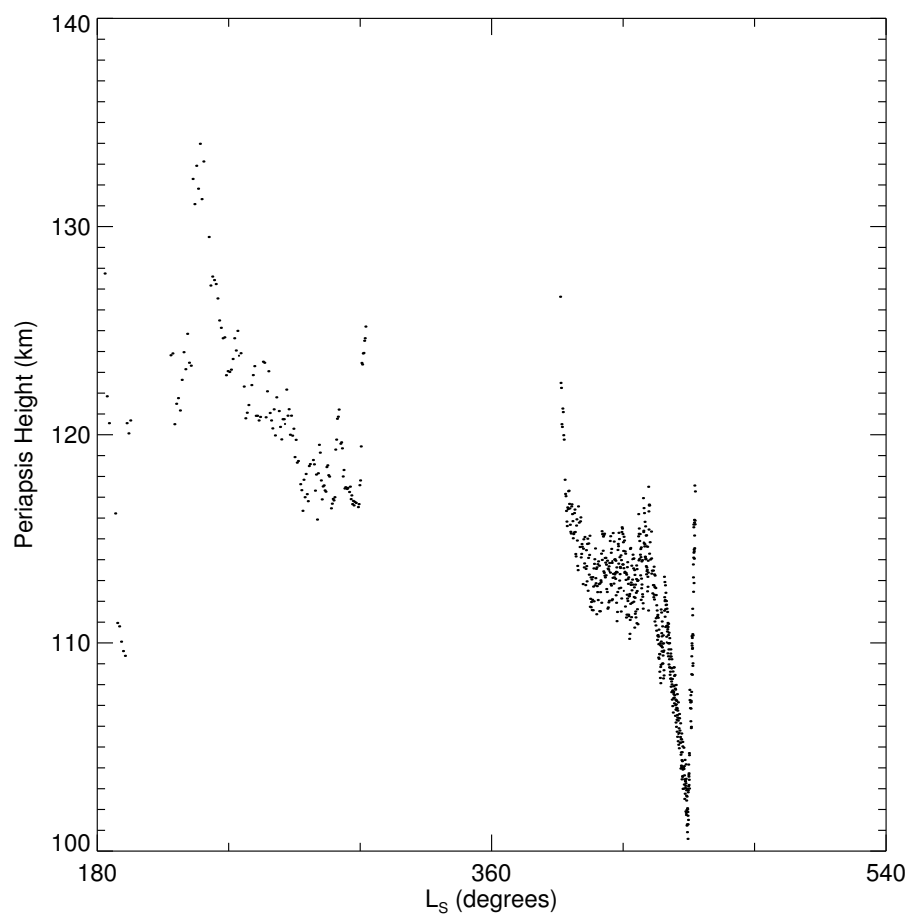


Figure B.1: Periapsis altitude versus L_S

It is unclear why different time averages are used for density and for altitude. I am unable to reproduce the results of some orbits where the 7-s density is not given, but the 40-s altitude is, at high altitude due to low signal to noise. On these occasions, I believe that data not given in the PDS profile data were used to generate the PDS constant altitude data. Since the measurement uncertainties are empirical, as discussed in Appendix A, it is not surprising that they have been ignored in the fitting procedure.

APPENDIX C

CURVATURE TERMS IN EQUATIONS 3.6 – 3.7

Most of the terms in Equation 3.1 have an obvious, one-to-one correspondence with terms in Equations 3.6 – 3.8. The exceptions are the non-linear advective terms.

$$\begin{aligned}
 (\underline{v} \cdot \underline{\nabla}) \underline{v} = & \hat{r} (\underline{v} \cdot \underline{\nabla}) v_r + v_r (\underline{v} \cdot \underline{\nabla}) \hat{r} + \hat{\theta} (\underline{v} \cdot \underline{\nabla}) v_\theta + \\
 & v_\theta (\underline{v} \cdot \underline{\nabla}) \hat{\theta} + \hat{\phi} (\underline{v} \cdot \underline{\nabla}) v_\phi + v_\phi (\underline{v} \cdot \underline{\nabla}) \hat{\phi}
 \end{aligned} \tag{C.1}$$

Equation 3.9 defines $(\underline{v} \cdot \underline{\nabla})$. Using Arfken and Weber (1995), I have:

$$\frac{\partial \hat{r}}{\partial r} = 0 \tag{C.2}$$

$$\frac{\partial \hat{r}}{\partial \theta} = \hat{\theta} \tag{C.3}$$

$$\frac{\partial \hat{r}}{\partial \phi} = \sin \theta \hat{\phi} \tag{C.4}$$

$$\frac{\partial \hat{\theta}}{\partial r} = 0 \tag{C.5}$$

$$\frac{\partial \hat{\theta}}{\partial \theta} = -\hat{r} \quad (\text{C.6})$$

$$\frac{\partial \hat{\theta}}{\partial \phi} = \cos \theta \hat{\phi} \quad (\text{C.7})$$

$$\frac{\partial \hat{\phi}}{\partial r} = 0 \quad (\text{C.8})$$

$$\frac{\partial \hat{\phi}}{\partial \theta} = 0 \quad (\text{C.9})$$

$$\frac{\partial \hat{\phi}}{\partial \phi} = -\hat{r} \sin \theta - \cos \theta \hat{\theta} \quad (\text{C.10})$$

Using Equations C.2 – C.10 to differentiate the unit vectors, the advective terms become:

$$\begin{aligned} (\underline{v} \cdot \nabla) \underline{v} = & \hat{r} (\underline{v} \cdot \nabla) v_r + \hat{\theta} (\underline{v} \cdot \nabla) v_\theta + \hat{\phi} (\underline{v} \cdot \nabla) v_\phi + \frac{v_r v_\theta \hat{\theta}}{r} + \frac{v_r v_\phi \hat{\phi}}{r} + \\ & \frac{-v_\theta^2 \hat{r}}{r} + \frac{v_\theta v_\phi \cos \theta \hat{\phi}}{r \sin \theta} + \frac{v_\phi^2}{r \sin \theta} \left(-\hat{r} \sin \theta - \cos \theta \hat{\theta} \right) \end{aligned} \quad (\text{C.11})$$

Rearranging:

$$\begin{aligned} (\underline{v} \cdot \nabla) \underline{v} = & \hat{r} (\underline{v} \cdot \nabla) v_r + \hat{\theta} (\underline{v} \cdot \nabla) v_\theta + \hat{\phi} (\underline{v} \cdot \nabla) v_\phi + \left(\frac{-(v_\theta^2 + v_\phi^2)}{r} \right) \hat{r} + \\ & \left(\frac{v_r v_\theta}{r} - \frac{v_\phi^2}{r \tan \theta} \right) \hat{\theta} + \left(\frac{v_r v_\theta}{r} + \frac{v_\theta v_\phi}{r \tan \theta} \right) \hat{\phi} \end{aligned} \quad (\text{C.12})$$

The terms containing derivatives continue to be called the advective terms, the others are called curvature terms.

APPENDIX D

SIMPLIFYING THE VISCOUS TERMS IN EQUATIONS 3.6 – 3.7

In Equation 3.1 the viscous term is $\underline{\nabla} \times (\eta \underline{\nabla} \times \underline{v}) / \rho$. This is too complicated to include directly in the scale analysis of Section 3.2.2. Since η is molecular, not eddy, viscosity, I assume that it is uniform and bring it outside the spatial derivatives. I need to find a reasonable approximation for $\underline{\nabla} \times (\underline{\nabla} \times \underline{v})$ in spherical polar coordinates:

$$\begin{aligned} \underline{\nabla} \times \underline{v} = & \frac{1}{r^2 \sin \theta} \hat{r} \left(\frac{\partial}{\partial \theta} (rv_\phi \sin \theta) - \frac{\partial}{\partial \phi} (rv_\theta) \right) - \\ & \frac{1}{r \sin \theta} \hat{\theta} \left(\frac{\partial}{\partial r} (rv_\phi \sin \theta) - \frac{\partial}{\partial \phi} (v_r) \right) + \\ & \frac{1}{r \sin \theta} \hat{\phi} \left(\frac{\partial}{\partial r} (rv_\theta) - \frac{\partial}{\partial \theta} (v_r) \right) \end{aligned} \quad (\text{D.1})$$

The importance of the various terms can be estimated by using Equations 3.14 – 3.16 again:

$$\frac{\partial}{\partial r} \sim \frac{1}{H} \quad (\text{D.2})$$

$$\frac{1}{r} \frac{\partial}{\partial \theta} \sim \frac{1}{R} \quad (\text{D.3})$$

$$\frac{1}{r} \frac{\partial}{\partial \phi} \sim \frac{1}{R} \quad (\text{D.4})$$

Hence:

$$\begin{aligned} \underline{\nabla} \times \underline{v} = & \frac{1}{R} \hat{r} \left(\frac{Rv_\phi}{R} - \frac{Rv_\theta}{R} \right) - \\ & \frac{1}{R} \hat{\theta} \left(\frac{Rv_\phi}{H} - v_r \right) + \\ & \frac{1}{R} \hat{\phi} \left(\frac{Rv_\theta}{H} - v_r \right) \end{aligned} \quad (\text{D.5})$$

Since $H \ll R$:

$$\underline{\nabla} \times \underline{v} = -\frac{\hat{\theta} v_\phi}{H} + \frac{\hat{\phi} v_\theta}{H} \quad (\text{D.6})$$

I use this approximation for $\underline{\nabla} \times \underline{v}$ to find the dominant terms in $\underline{\nabla} \times (\underline{\nabla} \times \underline{v})$:

$$\begin{aligned} \underline{\nabla} \times (\underline{\nabla} \times \underline{v}) = & \frac{1}{r^2 \sin \theta} \hat{r} \left(\frac{\partial}{\partial \theta} \left(\frac{rv_\theta \sin \theta}{H} \right) - \frac{\partial}{\partial \phi} \left(\frac{-rv_\phi}{H} \right) \right) - \\ & \frac{1}{r \sin \theta} \hat{\theta} \left(\frac{\partial}{\partial r} \left(\frac{rv_\theta \sin \theta}{H} \right) - 0 \right) + \\ & \frac{1}{r} \hat{\phi} \left(\frac{\partial}{\partial r} \left(\frac{-rv_\phi}{H} - 0 \right) \right) \end{aligned} \quad (\text{D.7})$$

$$\begin{aligned} \underline{\nabla} \times (\underline{\nabla} \times \underline{v}) = & \frac{1}{R} \hat{r} \left(\frac{Rv_\theta}{HR} + \frac{Rv_\phi}{RH} \right) - \\ & \frac{1}{R} \hat{\theta} \left(\frac{Rv_\theta}{HH} \right) + \\ & \frac{1}{R} \hat{\phi} \left(\frac{-Rv_\phi}{HH} \right) \end{aligned} \quad (\text{D.8})$$

The dominant terms are:

$$\underline{\nabla} \times (\underline{\nabla} \times \underline{v}) = -\frac{\hat{\theta} v_\theta}{HH} - \frac{\hat{\phi} v_\phi}{HH} \quad (\text{D.9})$$

Reintroducing the derivatives in their proper form, I have the following approximation for $\underline{\nabla} \times (\underline{\nabla} \times \underline{v})$:

$$\underline{\nabla} \times (\underline{\nabla} \times \underline{v}) = -\hat{\underline{\theta}} \frac{\partial^2 v_\theta}{\partial r^2} - \hat{\underline{\phi}} \frac{\partial^2 v_\phi}{\partial r^2} \quad (\text{D.10})$$

APPENDIX E

ESTIMATING THE IMPORTANCE OF LATITUDINAL CHANGES IN PRESSURE

It is useful to make a simple estimate of how important the effects of latitude are for influencing derived pressure profiles. Here I outline a technique for doing so.

The conservation of momentum equations for the quasi-cyclostrophic case are, as in Equations 3.40 – 3.41:

$$\frac{1}{\rho} \frac{\partial p}{\partial r} = -\frac{GM}{r^2} \quad (\text{E.1})$$

$$\frac{v_\phi^2}{r \tan \theta} = \frac{1}{\rho r} \frac{\partial p}{\partial \theta} - g_{eff,\theta} \quad (\text{E.2})$$

The ideal gas equation of state is:

$$p = \rho \left(\frac{k_B}{M_{mol}} \right) T \quad (\text{E.3})$$

I assume that $g_{eff,\theta}$ is negligible and that $GM/r^2 = g$ is uniform over the region of interest. I also assume that M_{mol} and T are uniform. Combining Equations E.1 and E.3 and the assumptions gives:

$$\frac{1}{p} \frac{\partial p}{\partial r} = \frac{\partial \ln p}{\partial r} = -\frac{1}{H} \quad (\text{E.4})$$

where $H = k_B T / M_{mol} g$. I also assume that $\tan \theta$ is constant. This is a major assumption that is not always appropriate, but it makes generating a rough estimate for E much easier. I use t for my constant value of $\tan \theta$.

With those assumptions:

$$\ln p = \ln p_0 - \frac{(r - r_0)}{H} + \frac{(\theta - \theta_0) v_\phi^2}{g H t} \quad (\text{E.5})$$

r and θ do not vary independently. The spacecraft must remain on the appropriate flight path through the atmosphere. This is shown in Figure E.1 where r_0 is the value of r at periapsis, θ_0 is the value of θ at periapsis, Δr is the difference between r at the top of the atmosphere and at periapsis, and $\Delta \theta$ is the difference between θ at the top of the atmosphere and at periapsis. The “top” of the atmosphere is where the density profile begins and ends. Since the size of the elliptical orbit is assumed to be much larger than the planet’s radius, the flight path appears linear in this Figure.

$$r_0 = r \cos(\theta - \theta_0) \quad (\text{E.6})$$

$$r - r_0 = r_0 \left(\frac{1}{\cos(\theta - \theta_0)} - 1 \right) \quad (\text{E.7})$$

$$r - r_0 = r_0 \left(\frac{1}{1 - \frac{(\theta - \theta_0)^2}{2}} - 1 \right) \quad (\text{E.8})$$

$$r - r_0 = r_0 \left(1 + \frac{(\theta - \theta_0)^2}{2} - 1 \right) \quad (\text{E.9})$$

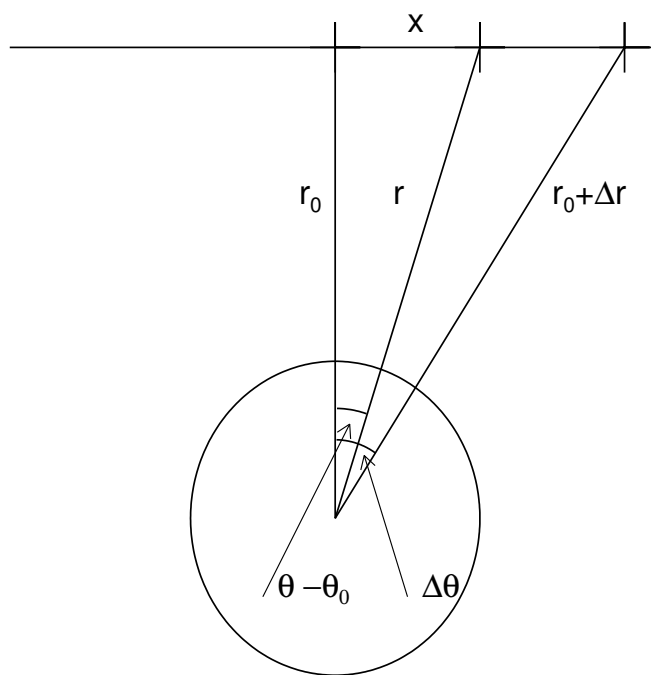


Figure E.1: Aerobraking Geometry

$$r - r_0 = \frac{r_0}{2} (\theta - \theta_0)^2 \quad (\text{E.10})$$

I now introduce the superscript “+” to refer to the leg of the aerobraking pass with $\theta > \theta_0$. I later use the superscript “-” to refer to the other leg. The two legs correspond to the positive and negative square roots in Equation E.10. So flying along the positive leg of the flight path:

$$\ln p^+ = \ln p_0^+ - \frac{(r - r_0)}{H} + \frac{\sqrt{2} (r - r_0)^{1/2} v_\phi^2}{r_0^{1/2} g H t} \quad (\text{E.11})$$

The only difference for the other leg is that the sign of the last term on the right hand side changes. Using gravity as the only force, the usual best estimate for periapsis pressure is:

$$p_{peri^+, est} = p_{top^+} + \int_{r_0}^{r_0 + \Delta r} \rho^+ g dr \quad (\text{E.12})$$

The subscript “est” refers to values that are calculated without any consideration of changes with latitude. The subscript “top” refers to values at the top of the atmosphere, either on inbound or outbound. ρ^+ is density measured along the inbound leg of the flight path. p_{top^+} can be related to the measured change in density with altitude (and latitude) at the top of the flight path.

With the earlier assumptions, density obeys a formula similar to Equation E.11:

$$\ln \rho^+ = \ln \rho_0^+ - \frac{(r - r_0)}{H} + \frac{\sqrt{2} (r - r_0)^{1/2} v_\phi^2}{r_0^{1/2} g H t} \quad (\text{E.13})$$

At the top^+ position on the flight path, $r = r_0 + \Delta r$ and $\theta = \theta_0 + \sqrt{2\Delta r/r_0}$, the density is:

$$\ln \rho = \ln \rho_0 - \frac{\Delta r}{H} + \frac{(2\Delta r)^{1/2} v_\phi^2}{r_0^{1/2} g H t} \quad (\text{E.14})$$

At an altitude H below top^+ and displaced in latitude to remain on the flight path, the density is:

$$\ln \rho = \ln \rho_0 - \frac{\Delta r}{H} + 1 + \frac{\sqrt{2(\Delta r - H)} v_\phi^2}{r_0^{1/2} g H t} \quad (\text{E.15})$$

In practice, a scale height would be estimated from a best fit to all measured densities along the flight path between these two points. Here, I just estimate as if these are the only two data points. If the estimate for the scale height turns out to have a large influence on the results, then I will revise this. The estimated scale height from these two data points is $-\Delta z/\Delta \ln \rho$:

$$\frac{H}{1 - \frac{\sqrt{2\Delta r} v_\phi^2}{r_0^{1/2} g H t} \left(1 - (1 - H/\Delta r)^{1/2}\right)} \quad (\text{E.16})$$

The estimated pressure is the product of ρ_{top^+} , g , and this:

$$\frac{\rho_0 g H \left(\exp\left(\frac{-\Delta r}{H}\right)\right) \left(\exp\left(\frac{\sqrt{2\Delta r} v_\phi^2}{r_0^{1/2} g H t}\right)\right)}{1 - \frac{\sqrt{2\Delta r} v_\phi^2}{r_0^{1/2} g H t} \left(1 - (1 - H/\Delta r)^{1/2}\right)} \quad (\text{E.17})$$

I now return to the other part of Equation E.12 — the integration.

$$p_{peri+,est} = p_{top+} + \int_{r_0}^{r_0+\Delta r} \rho_0 g \left(\exp\left(-\frac{r-r_0}{H}\right) \exp\left(\frac{\sqrt{2}(r-r_0)^{1/2} v_\phi^2}{r_0^{1/2} g H t}\right) \right) dr \quad (\text{E.18})$$

Let:

$$x = \frac{\sqrt{2}(\Delta r)^{1/2} v_\phi^2}{r_0^{1/2} g H t} \quad (\text{E.19})$$

Let:

$$y = \frac{H}{\Delta r} \quad (\text{E.20})$$

Substituting x and y into Equation E.12 and redefining r to remove the $r - r_0$ terms:

$$p_{peri+,est} = p_{top+} + \rho_0 g \int_0^{\Delta r} \exp\left(-\frac{r}{H} + x \left(\frac{r}{\Delta r}\right)^{1/2}\right) dr \quad (\text{E.21})$$

Let:

$$r' = \frac{r}{H} \quad (\text{E.22})$$

Substituting r' into Equation E.21:

$$p_{peri+,est} = p_{top+} + \rho_0 g H \int_0^{\Delta r/H} \exp\left(-r' + x \left(\frac{H r'}{\Delta r}\right)^{1/2}\right) dr' \quad (\text{E.23})$$

Substituting y into Equation E.23:

$$p_{peri+,est} = p_{top+} + \rho_0 g H \int_0^{1/y} \exp(-r' + xy^{1/2}r'^{1/2}) dr' \quad (\text{E.24})$$

Let:

$$q^2 = r' \quad (\text{E.25})$$

Substituting q into Equation E.24:

$$p_{peri+,est} = p_{top+} + \rho_0 g H \int_0^{1/\sqrt{y}} \exp(-q^2 + xy^{1/2}q) 2q dq \quad (\text{E.26})$$

Rearranging by completing the square:

$$p_{peri+,est} = p_{top+} + 2\rho_0 g H \int_0^{1/\sqrt{y}} \exp\left(-\left(q - \frac{xy^{1/2}}{2}\right)^2 + \frac{x^2 y}{4}\right) q dq \quad (\text{E.27})$$

Moving the constant term outside the integration:

$$p_{peri+,est} = p_{top+} + 2\rho_0 g H \exp\left(\frac{x^2 y}{4}\right) \int_0^{1/\sqrt{y}} \exp\left(-\left(q - \frac{xy^{1/2}}{2}\right)^2\right) q dq \quad (\text{E.28})$$

Let:

$$s = q - \frac{xy^{1/2}}{2} \quad (\text{E.29})$$

Substituting s into Equation E.28:

$$p_{peri^+,est} = p_{top^+} + 2\rho_0 g H \exp\left(\frac{x^2 y}{4}\right) \int_{0-\frac{xy^{1/2}}{2}}^{\frac{1}{\sqrt{y}}-\frac{xy^{1/2}}{2}} \exp(-s^2) \left(s + \frac{xy^{1/2}}{2}\right) ds \quad (\text{E.30})$$

Separating the two summed terms comprising the integrand:

$$\begin{aligned} p_{peri^+,est} = p_{top^+} + 2\rho_0 g H \exp\left(\frac{x^2 y}{4}\right) \int_{0-\frac{xy^{1/2}}{2}}^{\frac{1}{\sqrt{y}}-\frac{xy^{1/2}}{2}} s \exp(-s^2) ds + \quad (\text{E.31}) \\ 2\rho_0 g H \exp\left(\frac{x^2 y}{4}\right) \frac{xy^{1/2}}{2} \int_{0-\frac{xy^{1/2}}{2}}^{\frac{1}{\sqrt{y}}-\frac{xy^{1/2}}{2}} \exp(-s^2) ds \end{aligned}$$

Performing the two integrations:

$$\begin{aligned} p_{peri^+,est} = p_{top^+} + \frac{2\rho_0 g H \exp\left(\frac{x^2 y}{4}\right)}{-2} \left[\exp(-s^2)\right]_{0-\frac{xy^{1/2}}{2}}^{\frac{1}{\sqrt{y}}-\frac{xy^{1/2}}{2}} + \quad (\text{E.32}) \\ 2\rho_0 g H \exp\left(\frac{x^2 y}{4}\right) \frac{xy^{1/2}}{2} \frac{\sqrt{\pi}}{2} [erf(s)]_{0-\frac{xy^{1/2}}{2}}^{\frac{1}{\sqrt{y}}-\frac{xy^{1/2}}{2}} \end{aligned}$$

Where I have used:

$$\frac{2}{\sqrt{\pi}} \int_0^s \exp(-f^2) df = erf(s) \quad (\text{E.33})$$

Substituting Equations E.19 and E.20 into Equation E.17 and then substituting that into Equation E.32:

$$p_{peri^+,est} = \rho_0 g H \frac{\exp\left(\frac{-1}{y}\right) \exp(x)}{1-x \left(1-(1-y)^{1/2}\right)} - \quad (\text{E.34})$$

$$\rho_0 g H \exp\left(\frac{x^2 y}{4}\right) \left(\exp\left(-\frac{1}{y} + x - \frac{x^2 y}{4}\right) - \exp\left(-\frac{x^2 y}{4}\right) \right) +$$

$$2\rho_0 g H \exp\left(\frac{x^2 y}{4}\right) \frac{xy^{1/2} \sqrt{\pi}}{2} \left(\operatorname{erf}\left(\frac{1}{\sqrt{y}} - \frac{xy^{1/2}}{2}\right) - \operatorname{erf}\left(-\frac{xy^{1/2}}{2}\right) \right)$$

Cancelling terms:

$$\frac{p_{peri^+,est}}{\rho_0 g H} = \frac{\exp\left(\frac{-1}{y}\right) \exp(x)}{1 - x \left(1 - (1 - y)^{1/2}\right)} - \left(\exp\left(-\frac{1}{y} + x\right) - 1 \right) + \quad (\text{E.35})$$

$$\exp\left(\frac{x^2 y}{4}\right) \frac{xy^{1/2} \sqrt{\pi}}{2} \left(\operatorname{erf}\left(\frac{1}{\sqrt{y}} - \frac{xy^{1/2}}{2}\right) - \operatorname{erf}\left(-\frac{xy^{1/2}}{2}\right) \right)$$

Combining similar terms:

$$\frac{p_{peri^+,est}}{\rho_0 g H} = 1 + \exp\left(\frac{-1}{y}\right) \exp(x) \left(\frac{x \left(1 - (1 - y)^{1/2}\right)}{1 - x \left(1 - (1 - y)^{1/2}\right)} \right) + \quad (\text{E.36})$$

$$\exp\left(\frac{x^2 y}{4}\right) \frac{xy^{1/2} \sqrt{\pi}}{2} \left(\operatorname{erf}\left(\frac{1}{\sqrt{y}} - \frac{xy^{1/2}}{2}\right) - \operatorname{erf}\left(-\frac{xy^{1/2}}{2}\right) \right)$$

Periapsis pressure can be estimated from this equation. By symmetry, the other leg's value of periapsis pressure is the same except for replacing x with $-x$. Using Equation E.35 and its twin for $p_{peri^-,est}$, an expression can be found for:

$$E = 2 \frac{p_{peri^+,est} - p_{peri^-,est}}{p_{peri^+,est} + p_{peri^-,est}} \quad (\text{E.37})$$

E represents how measurable the effects of winds are on a density profile. In the limit that the winds are zero $v_\phi = 0$, $x = 0$, and so $E = 0$. I now simplify by assuming:

$$x \ll 1 \quad (\text{E.38})$$

$$y \ll 1 \tag{E.39}$$

Which leads to:

$$\exp\left(\frac{-1}{y}\right) \rightarrow \exp\left(\frac{-1}{y}\right) \tag{E.40}$$

$$\exp(x) \rightarrow 1 + x \tag{E.41}$$

$$(1 - y)^{1/2} \rightarrow 1 - \frac{y}{2} \tag{E.42}$$

$$\exp\left(\frac{x^2 y}{4}\right) \rightarrow 1 + \frac{x^2 y}{4} \tag{E.43}$$

Since:

$$erf(s + \delta s) = erf(s) + \delta s \frac{\partial erf(s)}{\partial s} \tag{E.44}$$

And:

$$\frac{\partial erf(s)}{\partial s} = \frac{2}{\sqrt{\pi}} \exp(-s^2) \tag{E.45}$$

$$erf\left(\frac{1}{\sqrt{y}} - \frac{xy^{1/2}}{2}\right) \rightarrow erf\left(\frac{1}{\sqrt{y}}\right) - \frac{xy^{1/2}}{\sqrt{\pi}} \exp\left(\frac{-1}{y}\right) \tag{E.46}$$

$$\operatorname{erf}\left(\frac{-xy^{1/2}}{2}\right) \rightarrow \frac{-xy^{1/2}}{2} \quad (\text{E.47})$$

Putting all this into Equation E.36:

$$\begin{aligned} \frac{p_{peri^+,est}}{\rho_0 g H} = & 1 + \exp\left(\frac{-1}{y}\right) (1+x) \left(\frac{x(1-(1-y/2))}{1-x(1-(1-y/2))}\right) + \\ & \left(1 + \frac{x^2 y}{4}\right) \frac{xy^{1/2}}{2} \sqrt{\pi} \left(\operatorname{erf}\left(\frac{1}{\sqrt{y}}\right) - \frac{xy^{1/2}}{\sqrt{\pi}} \exp\left(\frac{-1}{y}\right) + \frac{xy^{1/2}}{2}\right) \end{aligned} \quad (\text{E.48})$$

The messy fraction simplifies to $xy/2$:

$$\frac{p_{peri^+,est}}{\rho_0 g H} = 1 + \exp\left(\frac{-1}{y}\right) (1+x) \frac{xy}{2} + \frac{xy^{1/2}}{2} \sqrt{\pi} \left(\operatorname{erf}\left(\frac{1}{\sqrt{y}}\right) + \frac{xy^{1/2}}{2}\right) \quad (\text{E.49})$$

Where I have used $\exp(-1/y) \ll 1$ to eliminate part of the last term on the right hand side. Now, since $\operatorname{erf}(1/\sqrt{y}) \rightarrow 1$:

$$\frac{p_{peri^+,est}}{\rho_0 g H} = 1 + \exp\left(\frac{-1}{y}\right) \frac{xy}{2} + \frac{xy^{1/2}}{2} \sqrt{\pi} \quad (\text{E.50})$$

Since $\exp(-1/y) \ll 1$:

$$\frac{p_{peri^+,est}}{\rho_0 g H} = 1 + \frac{xy^{1/2}}{2} \sqrt{\pi} \quad (\text{E.51})$$

$p_{peri^-,est}$ is given by the same equation with the sign of x reversed. Errors in p_{top+} arising from my crude estimate of the scale height do not influence this result. Using Equation E.37, E is:

$$E = xy^{1/2}\sqrt{\pi} = \frac{\sqrt{2}(\Delta r)^{1/2} v_\phi^2}{r_0^{1/2} gHt} \left(\frac{H}{\Delta r}\right)^{1/2} \sqrt{\pi} \quad (\text{E.52})$$

Rearranging:

$$E = \left(\frac{2\pi}{r_0 H}\right)^{1/2} \frac{v_\phi^2}{gt} \quad (\text{E.53})$$

For this quasi-cyclostrophic case, the latitudinal pressure gradient is given by:

$$\frac{v_\phi^2}{gH \tan \theta} = \frac{\partial \ln p}{\partial \theta} \quad (\text{E.54})$$

For the quasi-geostrophic case, the latitudinal pressure gradient is given by:

$$\frac{2\Omega v_\phi r \cos \theta}{gH} = \frac{\partial \ln p}{\partial \theta} \quad (\text{E.55})$$

Similarly to before, I assume that $\cos \theta$ is constant and label it c . Since $\Delta r \ll r_0$, I can approximate r in Equation E.55 as r_0 and the above derivation remains valid as long as the following transformation is made:

$$\frac{v_\phi^2}{t} \rightarrow 2\Omega v_\phi r_0 c \quad (\text{E.56})$$

This time x and y are given by:

$$x = \frac{\sqrt{2}(\Delta r)^{1/2} 2\Omega v_\phi r_0 c}{r_0^{1/2} gH} \quad (\text{E.57})$$

$$y = \frac{H}{\Delta r} \tag{E.58}$$

$$E = xy^{1/2}\sqrt{\pi} = \left(\frac{2\pi r_0}{H}\right)^{1/2} \frac{2\Omega v_\phi c}{g} \tag{E.59}$$

For Titan, I assume that $\Delta r = 250$ km and $t = 1$ and take all the other parameters from Table 3.1. I find that $E \sim 0.05$.

For Mars, I assume that $\Delta r = 30$ km and $c = 0.7$ and take all the other parameters from Table 3.1. I find that $E \sim 0.2$.

APPENDIX F

UNCERTAINTY ANALYSES FOR SECTION 6.3

F.1 Uncertainties for Section 6.3.1

Using Equation 6.33:

$$\left(\frac{\sigma_{\rho_{n+1/2}}}{\rho_{n+1/2}}\right)^2 = \left(\frac{\sigma_{a_{n+1/2}}}{a_{n+1/2}}\right)^2 + \left(\frac{\sigma_{v_{n+1/2}^2}}{v_{n+1/2}^2}\right)^2 \quad (\text{F.1})$$

$$\left(\frac{\sigma_{\rho_{n+1/2}}}{\rho_{n+1/2}}\right)^2 = \left(\frac{\sigma_{a_{n+1/2}}}{a_{n+1/2}}\right)^2 + \left(\frac{2\sigma_{v_{n+1/2}}}{v_{n+1/2}}\right)^2 \quad (\text{F.2})$$

$$\left(\frac{\sigma_{\rho_{n+1/2}}}{\rho_{n+1/2}}\right)^2 = \frac{\sigma_{a_{n+1/2}}^2}{a_{n+1/2}^2} + \frac{4\sigma_{v_{n+1/2}}^2}{v_{n+1/2}^2} \quad (\text{F.3})$$

Using Equations 6.14, 6.15, 6.16, and 6.17:

$$\left(\frac{\sigma_{\rho_{n+1/2}}}{\rho_{n+1/2}}\right)^2 = \frac{\left(\frac{\sqrt{2}\sigma_v}{\Delta}\right)^2}{\left(\frac{v_{n+1}-v_n}{\Delta}\right)^2} + 4\frac{\left(\frac{\sigma_v}{\sqrt{2}}\right)^2}{\left(\frac{v_n+v_{n+1}}{2}\right)^2} \quad (\text{F.4})$$

$$\left(\frac{\sigma_{\rho_{n+1/2}}}{\rho_{n+1/2}}\right)^2 = \frac{2\sigma_v^2}{(v_{n+1}-v_n)^2} + \frac{8\sigma_v^2}{(v_n+v_{n+1})^2} \quad (\text{F.5})$$

Using Equation 6.34:

$$\sigma_{\rho_{n+1/2}}^2 = \left(\frac{v_{n+1} - v_n}{(v_n + v_{n+1})^2} \frac{4m}{\Delta AC_D} \right)^2 \sigma_v^2 \left(\frac{2}{(v_{n+1} - v_n)^2} + \frac{8}{(v_n + v_{n+1})^2} \right) \quad (\text{F.6})$$

$$\sigma_{\rho_{n+1/2}}^2 = \left(\frac{4m}{\Delta AC_D} \right)^2 \frac{\sigma_v^2}{(v_n + v_{n+1})^6} \left(2(v_n + v_{n+1})^2 + 8(v_{n+1} - v_n)^2 \right) \quad (\text{F.7})$$

$$\sigma_{\rho_{n+1/2}} = \left(\frac{4m}{\Delta AC_D} \right) \frac{\sigma_v}{(v_n + v_{n+1})^3} \left(2(v_n + v_{n+1})^2 + 8(v_{n+1} - v_n)^2 \right)^{1/2} \quad (\text{F.8})$$

F.2 Uncertainties for Section 6.3.2

Using Equation 6.36:

$$\sigma_{p_{n+1}^*}^2 = \sigma_{p_n^*}^2 + g^2 \left((z_n - z_{n+1})^2 \sigma_{\rho_{n+1/2}}^2 + \rho_{n+1/2}^2 \sigma_{z_n - z_{n+1}}^2 \right) \quad (\text{F.9})$$

$\sigma_{\rho_{n+1/2}}$ can be calculated from Equation F.8 and $\sigma_{z_n - z_{n+1}}$ can be calculated from Equation 6.13. $\rho_{n+1/2}$ can be calculated from Equation 6.33 and $(z_n - z_{n+1})$ can be calculated from Equation 6.8.

F.3 Uncertainties for Section 6.3.3

Using Equation 6.38:

$$\left(\sigma_{\rho_n^2} \right)^2 = \rho_n^4 \frac{\sigma_{\rho_{n-1/2}}^2}{\rho_{n-1/2}^2} + \rho_n^4 \frac{\sigma_{\rho_{n+1/2}}^2}{\rho_{n+1/2}^2} \quad (\text{F.10})$$

Using Equation 6.38:

$$\left(\sigma_{\rho_n^2}\right)^2 = \rho_{n+1/2}^2 \sigma_{\rho_{n-1/2}}^2 + \rho_{n-1/2}^2 \sigma_{\rho_{n+1/2}}^2 \quad (\text{F.11})$$

$$\frac{\sigma_{\rho_n}}{\rho_n} = \frac{2\sigma_{\rho_n^2}}{\rho_n^2} \quad (\text{F.12})$$

$$\sigma_{\rho_n} = \frac{2}{\sqrt{\rho_{n-1/2}\rho_{n+1/2}}} \left(\rho_{n+1/2}^2 \sigma_{\rho_{n-1/2}}^2 + \rho_{n-1/2}^2 \sigma_{\rho_{n+1/2}}^2\right)^{1/2} \quad (\text{F.13})$$

This can be calculated using Equations F.8 and 6.34. Using Equation 6.39:

$$\left(\frac{\sigma_{T_n^*}}{T_n^*}\right)^2 = \left(\frac{\sigma_{p_n^*}}{p_n^*}\right)^2 + \left(\frac{\sigma_{\rho_n}}{\rho_n}\right)^2 \quad (\text{F.14})$$

$$\sigma_{T_n^*}^2 = \frac{T_n^{*2}}{p_n^{*2}} \sigma_{p_n^*}^2 + \frac{T_n^{*2}}{\rho_n^2} \sigma_{\rho_n}^2 \quad (\text{F.15})$$

$$\sigma_{T_n^*}^2 = \left(\frac{M_{mol}}{k_B}\right)^2 \left(\frac{\sigma_{p_n^*}^2}{\rho_n^2} + \frac{p_n^{*2} \sigma_{\rho_n}^2}{\rho_n^4}\right) \quad (\text{F.16})$$

$\sigma_{p_n^*}$ can be calculated from Equation F.9 and σ_{ρ_n} can be calculated from Equation F.13. p_n^* can be calculated from Equation 6.36 and ρ_n can be calculated from Equation 6.38.

F.4 Uncertainties for Section 6.3.4

The uncertainty calculation is quite involved. Since I did not find a simple expression for $\sigma_{T_n^\circ}$, I outline a scheme for calculating numerically what $\sigma_{T_n^\circ}$ is:

Define P as:

$$P = v_{n-1} + 6v_n + v_{n+1} \quad (\text{F.17})$$

Define Q as:

$$Q = \ln \left(\frac{v_{n+1} - v_n}{(v_n + v_{n+1})^2} \frac{(v_{n-1} + v_n)^2}{v_n - v_{n-1}} \right) \quad (\text{F.18})$$

Using Equation 6.45:

$$T_n^\circ = \frac{M_{mol}g}{8k_B} \Delta \frac{P}{Q} \quad (\text{F.19})$$

$$\left(\frac{\sigma_{T_n^\circ}}{T_n^\circ} \right)^2 = \left(\frac{\sigma_P}{P} \right)^2 + \left(\frac{\sigma_Q}{Q} \right)^2 \quad (\text{F.20})$$

$$\sigma_P^2 = \sigma_v^2 + 36\sigma_v^2 + \sigma_v^2 \quad (\text{F.21})$$

$$\sigma_P = \sigma_v \sqrt{38} \quad (\text{F.22})$$

Define R as:

$$R = \left(\frac{v_{n+1} - v_n}{(v_n + v_{n+1})^2} \frac{(v_{n-1} + v_n)^2}{v_n - v_{n-1}} \right) \quad (\text{F.23})$$

Hence:

$$Q = \ln R \quad (\text{F.24})$$

$$\sigma_Q = \frac{\sigma_R}{R} \quad (\text{F.25})$$

Define S as:

$$S = v_{n+1} - v_n \quad (\text{F.26})$$

Define Z as:

$$Z = (v_n + v_{n+1})^2 \quad (\text{F.27})$$

Define U as:

$$U = (v_{n-1} + v_n)^2 \quad (\text{F.28})$$

Define W as:

$$W = v_n - v_{n-1} \quad (\text{F.29})$$

Hence:

$$R = \frac{S U}{Z W} \quad (\text{F.30})$$

$$\left(\frac{\sigma_R}{R}\right)^2 = \left(\frac{\sigma_S}{S}\right)^2 + \left(\frac{\sigma_Z}{Z}\right)^2 + \left(\frac{\sigma_U}{U}\right)^2 + \left(\frac{\sigma_W}{W}\right)^2 \quad (\text{F.31})$$

$$\sigma_S^2 = \sigma_W^2 = 2\sigma_v^2 \quad (\text{F.32})$$

Define X as:

$$X = (v_n + v_{n+1}) \quad (\text{F.33})$$

Hence:

$$Z = X^2 \quad (\text{F.34})$$

$$\frac{\sigma_Z}{Z} = \frac{2\sigma_X}{X} \quad (\text{F.35})$$

$$\sigma_X = \sqrt{2}\sigma_v \quad (\text{F.36})$$

Define Y as:

$$Y = (v_{n-1} + v_n) \quad (\text{F.37})$$

Hence:

$$U = Y^2 \quad (\text{F.38})$$

$$\frac{\sigma_U}{U} = \frac{2\sigma_Y}{Y} \quad (\text{F.39})$$

$$\sigma_Y = \sqrt{2}\sigma_v \quad (\text{F.40})$$

F.5 Uncertainties for Section 6.3.5

Using Equation 6.46:

$$\frac{\sigma_{p_n^{\text{a}}}}{p_n^{\text{a}2}} = \frac{\sigma_{\rho_n}^2}{\rho_n^2} + \frac{\sigma_{T_n^{\text{a}}}}{T_n^{\text{a}2}} \quad (\text{F.41})$$

σ_{ρ_n} can be calculated using Equation F.13 and $\sigma_{T_n^{\text{a}}}$ can be calculated using Equation F.20. T_n^{a} can be calculated using Equation 6.45 and ρ_n can be calculated from Equation 6.38.

F.6 Uncertainties for Section 6.3.6

Using Equation 6.51:

$$\left(\frac{\sigma_{T_n^{\#}}}{T_n^{\#}}\right)^2 = \left(\frac{\sigma_{v^2}}{v_n^2}\right)^2 + \left(\frac{\sigma_{v_{n-1}-v_{n+1}}}{v_{n-1} - v_{n+1}}\right)^2 \quad (\text{F.42})$$

$$\left(\frac{\sigma_{T_n^\#}}{T_n^\#}\right)^2 = \left(\frac{2\sigma_v}{v_n}\right)^2 + \left(\frac{\sqrt{2}\sigma_v}{v_{n-1} - v_{n+1}}\right)^2 \quad (\text{F.43})$$

$$\left(\frac{\sigma_{T_n^\#}}{T_n^\#}\right)^2 = \frac{4\sigma_v^2}{v_n^2} + \frac{2\sigma_v^2}{(v_{n-1} - v_{n+1})^2} \quad (\text{F.44})$$

Using Equation 6.51:

$$\sigma_{T_n^\#}^2 = \left(\frac{M_{mol}g\Delta}{k_B}\right)^2 \left(\frac{v_n^2}{v_{n-1} - v_{n+1}}\right)^2 \sigma_v^2 \left(\frac{4}{v_n^2} + \frac{2}{(v_{n-1} - v_{n+1})^2}\right) \quad (\text{F.45})$$

$$\sigma_{T_n^\#}^2 = \left(\frac{M_{mol}g\Delta}{k_B}\right)^2 \frac{v_n^2}{(v_{n-1} - v_{n+1})^4} \sigma_v^2 (4(v_{n-1} - v_{n+1})^2 + 2v_n^2) \quad (\text{F.46})$$

This uncertainty is less than before (Equation F.20) since the expression for calculating T_n (Equation 6.51) is so much simpler than before (Equation 6.45). However, there are only restricted circumstances in which it can be used.

F.7 Uncertainties for Section 6.3.7

Using Equation 6.56:

$$\sigma_{p_n^\#} = \frac{mg}{C_D A} \frac{\sigma_v}{v_n} \quad (\text{F.47})$$

F.8 Uncertainties for Section 6.3.8

The uncertainty calculation is quite involved. Since I did not find a simple expression for $\sigma_{T_n^\$}$, I outline a scheme for calculating numerically what $\sigma_{T_n^\$}$ is. Neglecting p_0 and using Equation 6.56:

$$\frac{p_{n+1}^{\#}}{p_n^{\#}} = \frac{\ln v_{n+1} - \ln v_x}{\ln v_n - \ln v_x} \quad (\text{F.48})$$

Define B as:

$$B = v_n + v_{n+1} \quad (\text{F.49})$$

Define C as:

$$C = \ln \left(\frac{p_{n+1}^{\#}}{p_n^{\#}} \right) \quad (\text{F.50})$$

Hence:

$$T_{n+1/2}^{\$} = \frac{M_{mol} g \Delta B}{2k_B C} \quad (\text{F.51})$$

$$\left(\frac{\sigma_{T_{n+1/2}^{\$}}}{T_{n+1/2}^{\$}} \right)^2 = \left(\frac{\sigma_B}{B} \right)^2 + \left(\frac{\sigma_C}{C} \right)^2 \quad (\text{F.52})$$

$$\sigma_B^2 = 2\sigma_v^2 \quad (\text{F.53})$$

Using Equation F.48, I define D as:

$$D = \frac{p_{n+1}^{\#}}{p_n^{\#}} = \frac{\ln v_{n+1} - \ln v_x}{\ln v_n - \ln v_x} \quad (\text{F.54})$$

Hence:

$$C = \ln D \quad (\text{F.55})$$

$$\sigma_C = \frac{\sigma_D}{D} \quad (\text{F.56})$$

Define E as:

$$E = \ln v_{n+1} - \ln v_x \quad (\text{F.57})$$

Define F as:

$$F = \ln v_n - \ln v_x \quad (\text{F.58})$$

Hence:

$$D = \frac{E}{F} \quad (\text{F.59})$$

$$\left(\frac{\sigma_D}{D}\right)^2 = \left(\frac{\sigma_E}{E}\right)^2 + \left(\frac{\sigma_F}{F}\right)^2 \quad (\text{F.60})$$

$$\sigma_E = \frac{\sigma_v}{v_{n+1}} \quad (\text{F.61})$$

$$\sigma_F = \frac{\sigma_v}{v_n} \quad (\text{F.62})$$

REFERENCES

- Albee, A. L., R. E. Arvidson, F. Palluconi, and T. Thorpe (2001). Overview of the Mars Global Surveyor mission. *J. Geophys. Res.* **106**, 23291–23316.
- Albee, A. L., F. D. Palluconi, and R. E. Arvidson (1998). Mars Global Surveyor Mission: Overview and Status. *Science* **279**, 1671–1672.
- Angelats i Coll, M., F. Forget, F. Hourdin, O. Talagrand, J. Wanherdrick, S. R. Lewis, P. L. Read, and M. A. Lopez-Valverde (2001). Waves in the Martian upper atmosphere: A study with the LMD General Circulation Model, #44.06. *Bull. Am. Astron. Soc.* **33**.
- Angelats i Coll, M., F. Forget, F. Hourdin, J. Wanherdrick, M. A. Lopez-Valverde, S. R. Lewis, and P. L. Read (2002). First results with the Mars thermospheric LMD general circulation model. In *EGS General Assembly #27*, #EGS02-A-04418.
- Arfken, G. B. and H. J. Weber (1995). *Mathematical methods for physicists*. Academic Press, 4th ed.
- Avduevskii, V. S., A. G. Godnev, V. V. Semenchenko, G. R. Uspenskii, and Z. P. Cheremukhina (1983). Investigation of the characteristics of the Venus stratosphere from acceleration measurements during the braking of the Venera-13 and Venera-14 probes. *Cosmic Research* **21**, 205–210.
- Avduevskii, V. S., M. I. Marov, I. N. Kulikov, V. P. Shari, A. I. Gorbachevskii, G. R. Uspenskii, and Z. P. Cheremukhina (1983). Structure and parameters of the Venus atmosphere according to Venera probe data. In D. M. Hunten, L. Colin, T. M. Donahue, and V. I. Moroz (Eds.), *Venus*, pp. 280–298. Tucson: University of Arizona Press.
- Baldwin, R. B. (1981). Tektites — Size estimates of their source craters and implications for their origin. *Icarus* **45**, 554–563.
- Banerdt, W. B., M. P. Golombek, and K. L. Tanaka (1992). Stress and tectonics on Mars. In H. H. Kieffer, B. M. Jakosky, C. W. Snyder, and M. S. Matthews (Eds.), *Mars*, pp. 249–297. Tucson: University of Arizona Press.
- Banfield, D., B. Conrath, J. C. Pearl, M. D. Smith, and P. Christensen (2000). Thermal tides and stationary waves on Mars as revealed by Mars Global Surveyor thermal emission spectrometer. *J. Geophys. Res.* **105**, 9521–9538.
- Banfield, D., B. J. Conrath, M. D. Smith, P. Christensen, and R. J. Wilson (2003). Forced waves in the Martian Atmosphere from MGS TES Nadir Data. *Icarus* **161**, 319–345.

- Barth, C. A., A. I. F. Stewart, S. W. Bougher, D. M. Hunten, S. J. Bauer, and A. F. Nagy (1992). Aeronomy of the current Martian atmosphere. In H. H. Kieffer, B. M. Jakosky, C. W. Snyder, and M. S. Matthews (Eds.), *Mars*, pp. 1054–1089. Tucson: University of Arizona Press.
- Belton, M. J. S. (2002). *New Frontiers in the Solar System: An Integrated Exploration Strategy*. National Academy of Science, Washington, USA.
- Bendura, R. J., R. R. Lundstrom, and P. G. Renfro (1974). *Flight tests of Viking parachute system in three Mach number regimes. 2: Parachute test results*. NASA-TN-D-7734, Langley Research Center, Virginia.
- Bertin, J. J. and M. L. Smith (1979). *Aerodynamics for Engineers*. Prentice Hall, New Jersey, USA.
- Bevington, P. R. (1969). *Data reduction and error analysis for the physical sciences*. McGraw-Hill, New York, USA.
- Binzel, R. P. (1999). Assessing the hazard: The development of the Torino Impact Scale. *The Planetary Report* **19**, 6–10.
- Bird, G. A. (1994). *Molecular Gas Dynamics*. Clarendon Press, Oxford, Great Britain.
- Blanchard, R. C., E. W. Hinson, and J. Y. Nicholson (1989). Shuttle High-Resolution accelerometer package experiment results — Atmospheric density measurements between 60 and 160 km. *Journal of Spacecraft and Rockets* **26(3)**, 173–180.
- Blanchard, R. C., R. G. Wilmoth, and J. N. Moss (1997). Aerodynamic Flight Measurements and Rarefied-Flow Simulations of Mars Entry Vehicles. *Journal of Spacecraft and Rockets* **34(5)**, 687–690.
- Bougher, S., G. Keating, R. Zurek, J. Murphy, R. Haberle, J. Hollingsworth, and R. T. Clancy (1999). Mars global surveyor aerobraking : atmospheric trends and model interpretation. *Advances in Space Research* **23**, 1887–1897.
- Bougher, S. W. and R. E. Dickinson (1988). Mars mesosphere and thermosphere. I — Global mean heat budget and thermal structure. *J. Geophys. Res.* **93**, 7325–7337.
- Bougher, S. W., S. Engel, and D. P. Hinson (2000). Mars Global Surveyor Radio Science Electron Density Profiles and Implications for the Neutral Atmosphere. In *American Astronomical Society, DPS meeting #32, #51.22*.
- Bougher, S. W., S. Engel, D. P. Hinson, and J. M. Forbes (2001). Mars Global Surveyor Radio Science electron density profiles: Neutral atmosphere implications. *Geophys. Res. Lett.* **28**, 3091–3094.
- Bougher, S. W., S. Engel, R. G. Roble, and B. Foster (2000). Comparative terrestrial planet thermospheres 3. Solar cycle variation of global structure and winds at solstices. *J. Geophys. Res.* **105**, 17669–17692.

- Bougher, S. W. and G. M. Keating (1999). Structure of the Mars Upper Atmosphere: MGS Aerobraking Data and Model Interpretation. In *The Fifth International Conference on Mars, July 19-24, Pasadena, California, abstract no. 6010*.
- Bougher, S. W., G. M. Keating, J. M. Forbes, J. R. Murphy, J. L. Hollingsworth, R. J. Wilson, and P. G. Withers (2001). The Upper Atmospheric Wave Structure of Mars as Determined by Mars Global Surveyor. In *American Geophysical Union, Fall Meeting, abstract #P32E-12*.
- Bougher, S. W., J. R. Murphy, and S. Engel (2002). Coupling processes and model simulations linking the Mars lower and upper atmospheres. In *COSPAR Scientific Assembly #34, #A-00132*.
- Bougher, S. W., J. R. Murphy, J. L. Hollingsworth, R. M. Haberle, G. M. Justus, C. G. and Keating, and R. W. Zurek (1997). MGS Aerobraking and Monitoring of Mars's Atmospheric Structure. In *American Geophysical Union, Fall Meeting, abstract #P21B-10*.
- Bougher, S. W., R. G. Roble, E. C. Ridley, and R. E. Dickinson (1990). The Mars thermosphere. II — General circulation with coupled dynamics and composition. *J. Geophys. Res.* **95**, 14811–14827.
- Bougher, S. W., P. Withers, J. R. Murphy, R. C. Roble, and G. M. Keating (2000). Longitude Structure in the Mars Upper Atmosphere: Characterization and Model Simulations. In *COSPAR Scientific Assembly #33, #C3.2-0011*.
- Braun, R. D., D. A. Spencer, P. H. Kallemeyn, and R. M. Vaughan (1999). Mars Pathfinder atmospheric entry navigation operations. *Journal of Spacecraft and Rockets* **36(3)**, 348–356.
- Calame, O. and J. D. Mulholland (1978). Lunar crater Giordano Bruno — A.D. 1178 impact observations consistent with laser ranging results. *Science* **199**, 875–877.
- Cancro, G. J., G. M. Keating, and R. H. Tolson (1998). Operational Data Reduction Procedure for Determining Density and Vertical Structure of the Martian Upper Atmosphere from Mars Global Surveyor Accelerometer Measurements, also NASA/CR-998-208721. Master's thesis, Joint Institute for Advanced Flight Studies, George Washington University and NASA Langley Research Centre.
- Chamberlain, J. W. and D. M. Hunten (1987). *Theory of planetary atmospheres: an introduction to their physics and chemistry, 2nd revised and enlarged edition*. Academic Press, New York, USA.
- Chapman, S. and R. Lindzen (1970). *Atmospheric tides. Thermal and gravitational*. Reidel, Dordrecht, Germany.
- Conrath, B. J. (1976). Influence of planetary-scale topography on the diurnal thermal tide during the 1971 Martian dust storm. *Journal of Atmospheric Sciences* **33**, 2430–2439.

- Croom, C. A. and R. H. Tolson (1994). Using Magellan Attitude Control Data to study the Venusian Atmosphere and Various Spacecraft Properties. *Adv. Astronaut. Sci.* **87**, 451–467.
- Dall’olmo, U. (1978). Meteors, meteor showers and meteorites in the Middle Ages: From European medieval sources. *J. History Astron.* **9**, 123–134.
- Eldred, C. H. (1991). Aerobraking for space exploration. In *Mars: Past, present, and future; Proceedings of the Conference, Williamsburg, VA, July 16 – 19, American Institute of Aeronautics and Astronautics*, pp. 307–322.
- Elliot, J. L., R. G. French, E. Dunham, P. J. Gierasch, J. Veverka, C. Church, and C. Sagan (1977). Occultation of Epsilon Geminorum by Mars. II — The structure and extinction of the Martian upper atmosphere. *Astrophys. J.* **217**, 661–679.
- Euler, E. A., G. L. Adams, and F. W. Hopper (1979). Lander Flight Path Analysis. In *Viking Navigation, NASA-CR-162917*, pp. 212–299. Pasadena, California, USA: Jet Propulsion Laboratory.
- Faber, T. E. (1995). *Fluid Dynamics for Physicists*. Cambridge University Press, Great Britain.
- Forbes, J. F. (1995). Tidal and Planetary Waves. In R. M. Johnson and T. L. Killeen (Eds.), *The Upper Mesosphere and Lower Thermosphere: A Review of Experiment and Theory*, pp. 67–87. Washington: American Geophysical Union.
- Forbes, J. M. (1999). Stationary Planetary Waves in the Mars Atmosphere. In *American Astronomical Society, DPS meeting #31, #49.06*.
- Forbes, J. M., R. Gonzalez, F. A. Marcos, D. Revelle, and H. Parish (1996). Magnetic storm response of lower thermosphere density. *J. Geophys. Res.* **101**, 2313–2320.
- Forbes, J. M. and M. E. Hagan (2000). Diurnal Kelvin Wave in the Atmosphere of Mars: Towards an Understanding of “Stationary” Density Structures Observed by the MGS Accelerometer. *Geophys. Res. Lett.* **27**, 3563–3566.
- Forbes, J. M., M. E. Hagan, S. W. Bougher, and J. L. Hollingsworth (2001). Kelvin wave propagation in the upper atmospheres of Mars and Earth. *Advances in Space Research* **27**, 1791–1800.
- Forbes, J. M., N. A. Makarov, and Y. I. Portnyagin (1995). First results from the meteor radar at south pole: A large 12-hour oscillation with zonal wavenumber one. *Geophys. Res. Lett.* **22**, 3247–3250.
- Forbes, J. M., S. E. Palo, and F. A. Marcos (1999). Longitudinal structures in lower thermosphere density. *J. Geophys. Res.* **104**, 4373–4386.
- Forget, F., F. Hourdin, R. Fournier, C. Hourdin, O. Talagrand, M. Collins, S. R. Lewis, P. L. Read, and J. Huot (1999). Improved general circulation models of the Martian atmosphere from the surface to above 80 km. *J. Geophys.*

- Res.* **104**, 24155–24176.
- French, J. R. and C. W. Uphoff (1979). Aerobraking for planetary missions. In *American Astronautical Society paper 79 – 286*.
- French, R. G. and J. L. Elliot (1979). Occultation of Epsilon Geminorum by Mars. III — Temperature structure of the Martian upper atmosphere. *Astrophys. J.* **229**, 828–845.
- Gault, D. E. (1983). The Terrestrial Accretion of Lunar Material. In *Proc. Lunar Planet. Sci. Conf., #14*, pp. 243–244.
- Gault, D. E. and P. H. Schultz (1991). Ejecta from Lunar Impacts: Where is it on Earth? *Meteoritics* **26**, 336–337.
- Gladman, B. J., J. A. Burns, M. Duncan, P. Lee, and H. F. Levison (1996). The exchange of impact ejecta between terrestrial planets. *Science* **271**, 1387–1392.
- Gladman, B. J., J. A. Burns, M. J. Duncan, and H. F. Levison (1995). The dynamical evolution of lunar impact ejecta. *Icarus* **118**, 302–321.
- Gnoffo, P. A., K. J. Weilmuenster, R. D. Braun, and C. I. Cruz (1996). Influence of Sonic-Line Location on Mars Pathfinder Probe Aerothermodynamics. *Journal of Spacecraft and Rockets* **33**(2), 169–177.
- Goldstein, H. (1980). *Classical Mechanics, 2nd edition*. Addison-Wesley Pub. Co., Reading, Massachusetts, USA.
- Golombek, M. (1999). Introduction to the special section: Mars Pathfinder. *J. Geophys. Res.* **104**, 8521–8522.
- Golombek, M. P., R. A. Cook, T. Economou, W. M. Folkner, A. F. C. Haldemann, P. H. Kallemeyn, J. M. Knudsen, R. M. Manning, H. J. Moore, T. J. Parker, R. Rieder, J. T. Schofield, P. H. Smith, and R. M. Vaughan (1997). Overview of the Mars Pathfinder Mission and Assessment of Landing Site Predictions. *Science* **278**, 1743.
- Greeley, R., M. D. Kraft, R. O. Kuzmin, and N. T. Bridges (2000). Mars Pathfinder landing site: Evidence for a change in wind regime from lander and orbiter data. *J. Geophys. Res.* **105**, 1829–1840.
- Greenhow, J. S. and J. E. Hall (1960). The variation of meteor heights with velocity and magnitude. *Mon. Not. R. Astron. Soc.* **121**, 174–182.
- Grier, J. A. (1999). *Determining the ages of impact events: Multidisciplinary studies using remote sensing and sample analysis techniques*. Ph. D. thesis, THE UNIVERSITY OF ARIZONA.
- Grier, J. A., A. S. McEwen, M. Milazzo, J. A. Hester, and P. G. Lucey (2000). The Optical Maturity of the Ejecta of Small Bright Rayed Lunar Craters. In *Proc. Lunar Planet. Sci. Conf., #31, #1950*.
- Gurwell, M. A., D. O. Muhleman, and G. L. Berge (1993). Observations of Middle

- Atmospheric Winds on Mars. In *American Astronomical Society, DPS meeting #25, #11.02*.
- Haberle, R. M. (1997). Mars: Atmosphere. In J. H. Shirley and R. W. Fairbridge (Eds.), *Encyclopedia of Planetary Sciences*, pp. 432–440. Boston: Kluwer Academic Press.
- Haberle, R. M., J. B. Pollack, J. R. Barnes, R. W. Zurek, C. B. Leovy, J. R. Murphy, H. Lee, and J. Schaeffer (1993). Mars atmospheric dynamics as simulated by the NASA AMES General Circulation Model. I - The zonal-mean circulation. *J. Geophys. Res.* **98**, 3093–3123.
- Hardee, H. C. (1980). Solidification in the Kilauea-Iki lava lake. *J. Volcanology Geothermal Res.* **7**, 211–223.
- Harris, A. W. (1993). Corvid meteoroids are not ejecta from the Giordano Bruno impact. *J. Geophys. Res.* **98**, 9145–9149.
- Hartung, J. B. (1976). Was the formation of a 20-km-diameter impact crater on the moon observed on June 18, 1178. *Meteoritics* **11**, 187–194.
- Hartung, J. B. (1981). On the Occurrence of Giordano Bruno Ejecta on the Earth. In *Proc. Lunar Planet. Sci. Conf., #12*, pp. 401–403.
- Hartung, J. B. (1987). The Giordano Bruno myth and other midsummer events. *Meteoritics* **22**, 402.
- Hartung, J. B. (1993a). Corvid meteoroids are ejecta from the Giordano Bruno impact. *J. Geophys. Res.* **98**, 9141–9144.
- Hartung, J. B. (1993b). Giordano Bruno, the June 1975 meteoroid storm, Encke, and other Taurid Complex objects. *Icarus* **104**, 280–290.
- Head, J. W., H. Hiesinger, M. A. Ivanov, M. A. Kreslavsky, S. Pratt, and B. J. Thomson (1999). Possible ancient oceans on Mars: Evidence from Mars Orbiter Laser Altimeter data. *Science* **286**, 2134–2137.
- Hinson, D. P., G. L. Tyler, J. L. Hollingsworth, and R. J. Wilson (2001). Radio occultation measurements of forced atmospheric waves on Mars. *J. Geophys. Res.* **106**, 1463–1480.
- Hollingsworth, J. L. and J. R. Barnes (1996). Forced, stationary planetary waves in Mars' winter atmosphere. *J. Atmos. Sci.* **53**, 428–448.
- Holsapple, K. A. (1993). The scaling of impact processes in planetary sciences. *Annual review of earth and planetary sciences.* **21**, 333–373.
- Holton, J. R. (1992). *An introduction to dynamic meteorology, 3rd ed.* Academic Press, New York, USA.
- Hooke, W. H. (1977). Rossby-Planetary Waves, Tides, and Gravity Waves in the Upper Atmosphere. In *The Upper Atmosphere and Magnetosphere*, pp. 130–140. Washington: National Research Council Studies in Geophysics.

- Horz, F., R. Ostertag, and D. A. Rainey (1983). Bunte Breccia of the Ries — Continuous deposits of large impact craters. *Reviews of Geophysics and Space Physics* **21**, 1667–1725.
- Houghton, J. T. (2002). *The Physics of Atmospheres, 3rd ed.* Cambridge University Press, Great Britain.
- Hubbard, W. B., B. Sicardy, R. Miles, A. J. Hollis, R. W. Forrest, I. K. M. Nicolson, G. Appleby, W. Beisker, C. Bittner, H.-J. Bode, M. Bruns, H. Denzau, M. Nezel, E. Riedel, H. Struckmann, J. E. Arlot, F. Roques, F. Sevre, W. Thuillot, M. Hoffmann, E. H. Geyer, C. Buil, F. Colas, J. Lecacheux, A. Klotz, E. Thouvenot, J. L. Vidal, E. Carreira, F. Rossi, C. Blanco, S. Cristaldi, Y. Nevo, H. J. Reitsema, N. Brosch, K. Cernis, K. Zdanavicius, L. H. Wasserman, D. M. Hunten, D. Gautier, E. Lellouch, R. V. Yelle, B. Rizk, F. M. Flasar, C. C. Porco, D. Toubanc, and G. Corugedo (1993). The occultation of 28 SGR by Titan. *Astronomy and Astrophysics* **269**, 541–563.
- Hughes, D. W. (1976). Giordano Bruno, the Moon's latest large crater. *Nature* **264**, 212–213.
- Hughes, D. W. (1981). The influx of comets and asteroids to the earth. *Philosophical Transactions of the Royal Society, Series A* **303**, 353–368.
- Imoto, S. and I. Hasegawa (1958). Historical records of meteor showers in China, Korea, and Japan. *Smithsonian. Contrib. Astrophys.* **2**, 131–144.
- Intrieri, P. F., C. E. D. Rose, and D. B. Kirk (1977). Flight Characteristics of Probes in the Atmospheres of Mars, Venus, and the Outer Planets. *Acta Astronautica* **4**, 789–799.
- Jacchia, G. J., F. Verniani, and B. R. E. (1967). An analysis of the atmospheric trajectories of 413 precisely reduced photographic meteors. *Smithsonian. Contrib. Astrophys.* **10**, 1–139.
- Jenniskens, P., M. de Lignie, H. Betlem, J. Borovicka, C. O. Laux, D. Packan, and C. H. Kruger (1998). Preparing for the 1998/99 Leonid Storms. In P. Ehrenfreund, K. Krafft, H. Kochan, and V. Pirronello (Eds.), *Laboratory astrophysics and space research*, pp. 425–455. Dordrecht: Kluwer Academic Publishers.
- Joshi, M. M., J. L. Hollingsworth, R. M. Haberle, and A. F. C. Bridger (2000). An interpretation of Martian thermospheric waves based on analysis of a general circulation model. *Geophys. Res. Lett.* **27**, 613–616.
- Kahn, R. (1983). Some observational constraints on the global-scale wind systems of Mars. *J. Geophys. Res.* **88**, 10189–10209.
- Kasprzak, W., H. Niemann, D. Harpold, J. Richards, H. Manning, E. Patrick, and P. Mahaffy (1996). Cassini orbiter ion and neutral mass spectrometer instrument. In L. Horn (Ed.), *Proc. SPIE, volume 2803, Cassini/Huygens: A Mission to the Saturnian Systems*, pp. 129–140.
- Kasprzak, W. T., H. B. Niemann, A. E. Hedin, and S. W. Bougher (1993).

- Wave-like perturbations observed at low altitudes by the Pioneer Venus Orbiter Neutral Mass Spectrometer during orbiter entry. *Geophys. Res. Lett.* **20**, 2755–2758.
- Kaula, W. M. (1966). *Theory of satellite geodesy. Applications of satellites to geodesy*. Blaisdell Pub. Co., Massachusetts, USA.
- Keating, G. M., S. W. Bougher, R. W. Zurek, R. H. Tolson, G. J. Cancro, S. N. Noll, J. S. Parker, T. J. Schellenberg, R. W. Shane, B. L. Wilkerson, J. R. Murphy, J. L. Hollingsworth, R. M. Haberle, M. Joshi, J. C. Pearl, B. J. Conrath, M. D. Smith, R. T. Clancy, R. C. Blanchard, R. G. Wilmoth, D. F. Rault, T. Z. Martin, D. T. Lyons, P. B. Esposito, M. D. Johnston, C. W. Whetzel, C. G. Justus, and J. M. Babicke (1998). The Structure of the Upper Atmosphere of Mars: In Situ Accelerometer Measurements from Mars Global Surveyor. *Science* **279**, 1672–1676.
- Keating, G. M., A. Dwyer, R. J. Wilson, R. H. Tolson, S. W. Bougher, P. G. Withers, and J. M. Forbes (2000). Evidence of Large Global Diurnal Kelvin Wave in Mars Upper Atmosphere. In *American Astronomical Society, DPS meeting #32, #50.02*.
- Keating, G. M., F. W. Taylor, J. Y. Nicholson, and E. W. Hinson (1979). Short-term cyclic variations and diurnal variations of the Venus upper atmosphere. *Science* **205**, 62–64.
- Keating, G. M., R. H. Tolson, A. M. Dwyer, S. W. Bougher, P. G. Withers, and J. M. Forbes (2001). Persistent planetary-scale wave-2 and wave-3 density variations observed in Mars upper atmosphere from MGS accelerometer experiment. In *EGS General Assembly #26, #PS2.02*.
- Keating, G. M., R. H. Tolson, J. L. Hanna, R. F. Beebe, J. R. Murphy, and L. Huber (2001a). *MGS-M-ACCEL-5-PROFILE-V1.1*. NASA Planetary Data System.
- Keating, G. M., R. H. Tolson, J. L. Hanna, R. F. Beebe, J. R. Murphy, and L. Huber (2001b). *MGS-M-ACCEL-5-ALTITUDE-V1.1*. NASA Planetary Data System.
- Keating, G. M., R. H. Tolson, S. N. Noll, T. J. Schellenberg, R. L. Stephens, M. S. Bradford, D. T. Baird, L. J. Ellis, S. W. Bougher, and J. L. Hollingsworth (1999). First In Situ Atmospheric Measurements of Mars Southern Hemisphere. In *American Geophysical Union, Spring Meeting, abstract #P31A-05*.
- Keating, G. M., R. H. Tolson, S. N. Noll, T. J. Schellenberg, R. L. Stephens, M. S. Bradford, S. W. Bougher, and J. L. Hollingsworth (1999). First Global Mapping of the Mars Thermosphere. In *American Astronomical Society, DPS meeting #31, #76.02*.
- Kerzhanovich, V. V. (1977). Mars 6 — Improved analysis of the descent module measurements. *Icarus* **30**, 1–25.
- Kerzhanovich, V. V. and M. I. Marov (1983). The atmospheric dynamics of Venus according to Doppler measurements by the Venera entry probes. In D. M.

- Hunten, L. Colin, T. M. Donahue, and V. I. Moroz (Eds.), *Venus*, pp. 766–778. Tucson: University of Arizona Press.
- Kesthelyi, L. and R. Denlinger (1996). The initial cooling of pahoehoe flow lobes. *Bull. Volcanol.* **58**, 5–18.
- Kieffer, H. H., B. M. Jakosky, C. W. Snyder, and M. S. Matthews (1992). *Mars*. University of Arizona Press, Tucson, USA.
- Krasnopolsky, V. A., O. B. Likin, F. Farnik, and B. Valnicek (1991). Solar occultation observations of the Martian atmosphere in the ranges of 2-4 and 4-8 keV measured by PHOBOS 2. *Icarus* **89**, 147–151.
- Kronk, G. W. (1988). *Meteor Showers: A Descriptive Catalogue*. Enslow Publishers, New Jersey, USA.
- Lammer, H., W. Stumptner, and S. J. Bauer (2000). Upper limits for the Martian exospheric number density during the Planet B/Nozomi mission. *Planetary and Space Science* **48**, 1473–1478.
- Landau, L. D. and E. M. Lifshitz (1959). *Fluid mechanics*. Pergamon Press, Oxford, Great Britain.
- Landau, L. D. and E. M. Lifshitz (1969a). *Mechanics*. Pergamon Press, Oxford, Great Britain.
- Landau, L. D. and E. M. Lifshitz (1969b). *Statistical physics*. Pergamon Press, Oxford, Great Britain.
- Lang, K. R. (1999). *Astrophysical formulae*. Springer, New York, USA.
- Lebreton, J.-P., M. Verdant, and R. D. Wills (1994). Huygens — The Science, Payload and Mission Profile. *ESA Bulletin* **77**, 31–41.
- Lellouch, E., J. Rosenqvist, J. J. Goldstein, S. W. Bougher, and G. Paubert (1991). First absolute wind measurements in the middle atmosphere of Mars. *Astrophys. J.* **383**, 401–406.
- Lemoine, F. G., D. E. Smith, D. D. Rowlands, M. T. Zuber, G. A. Neumann, D. S. Chinn, and D. E. Pavlis (2001). An improved solution of the gravity field of Mars (GMM-2B) from Mars Global Surveyor. *J. Geophys. Res.* **106**, 23359–23376.
- Leovy, C. B. (1982). Martian meteorological variability. *Advances in Space Research* **2**, 19–44.
- Leovy, C. B. (2001). Weather and climate on Mars. *Nature* **412**, 245–249.
- Leovy, C. B. and Y. Mintz (1969). Numerical simulation of the atmospheric circulation and climate of Mars. *J. Atmos. Sci.* **26**, 1167–1190.
- Lewis, J. S. (1996). *Rain of Iron and Ice*. Addison-Wesley, Reading, Massachusetts, USA.

- Lide, D. R. (1994). *CRC Handbook of chemistry and physics. A ready-reference book of chemical and physical data*. CRC Press, Boca Raton, Florida.
- Lin, C. A. (1982). An Extremal Principle for a One-Dimensional Climate Model. *Geophys. Res. Lett.* **9**, 716–718.
- Lissauer, J. J. (1999). How common are habitable planets? *Nature* **402**, C11–C14.
- Lodders, K. and B. Fegley (1998). *The planetary scientist's companion*. Oxford University Press, Great Britain.
- Lorenz, R. D., J. I. Lunine, P. G. Withers, and C. P. McKay (2001). Titan, Mars and Earth: Entropy Production by Latitudinal Heat Transport. *Geophys. Res. Lett.* **28**, 415–418.
- Lyons, D. T. (1996). Aerobraking: The Key to Affordable Mars Exploration. In *International Academy of Astronautics IAA Paper L-0512 presented at 2nd International Low-Cost Spacecraft Conference, Laurel, Maryland, April, 1996*.
- Lyons, D. T. (1999). Aerobraking at Venus and Mars: A Comparison of the Magellan and Mars Global Surveyor Aerobraking Phases. In *American Astronomical Society paper 99 – 358*.
- Lyons, D. T., R. S. Saunders, and D. G. Griffith (1995). The Magellan Venus Mapping Mission: Aerobraking Operations. *Acta Astronautica* **35**, 669–676.
- Magalhães, J. A., J. T. Schofield, and A. Seiff (1999). Results of the Mars Pathfinder atmospheric structure investigation. *J. Geophys. Res.* **104**, 8943–8955.
- Marcos, F. A., H. B. Garrett, K. S. W. Champion, and J. M. Forbes (1977). Density variations in lower thermosphere from analysis of AE-C accelerometer measurements. *Planet. Space Sci.* **25**(5), 499–507.
- Martin, T. Z. and J. R. Murphy (2001). A Martian Year of Mapping by the MGS Horizon Science Experiment. In *American Astronomical Society, DPS meeting #33, #19.24*.
- Maxwell, T. A. and F. El-Baz (1978). The nature of rays and sources of highland material in Mare Crisium. In R. B. Merrill and J. J. Papike (Eds.), *Mare Crisium: The view from Luna 24*, pp. 89–103.
- Mayo, A. P., W. T. Blackshear, R. H. Tolson, W. H. Michael, G. M. Kelly, J. P. Brenkle, and T. A. Komarek (1977). Lander locations, Mars physical ephemeris, and solar system parameters Determination from Viking lander tracking data. *J. Geophys. Res.* **82**, 4297–4303.
- Meeus, J. (1990). The “lunar event” of AD 1178. *J. Br. Astron. Assoc.* **100**, 59.
- Melosh, H. J. (1989). *Impact cratering: A geologic process*. Oxford University Press, Great Britain.

- Melosh, H. J. and A. M. Vickery (1991). Melt droplet formation in energetic impact events. *Nature* **350**, 494–497.
- Mims, S. S. and R. W. James (1982). Meteors from Giordano Bruno Ejecta. In *Proc. Lunar Planet. Sci. Conf.*, #13, pp. 520–521.
- Mischna, M. A., J. F. Bell, P. B. James, and D. Crisp (1998). Synoptic measurements of Martian winds using the Hubble Space Telescope. *Geophys. Res. Lett.* **25**, 611–614.
- Moreno, R., S. Guilloteau, E. Lellouch, T. Encrenaz, F. Forget, E. Chassefiere, F. Jegou, and F. Hourdin (2001). Mars' wind measurements at Equinox : IRAM PdB Interferometric CO observations. In *American Astronomical Society, DPS meeting #33*, #19.21.
- Moss, J. N., R. C. Blanchard, R. G. Wilmoth, and R. D. Braun (1998). Mars Pathfinder Rarefied Aerodynamics: Computations and Measurements. In *American Institute of Aeronautics and Astronautics paper 98-0298*. 36th AIAA Aerospace Science Meeting in Reno, Nevada, USA.
- Müller-Wodarg, I. C. F., R. V. Yelle, M. Mendillo, L. A. Young, and A. D. Aylward (2000). The thermosphere of Titan simulated by a global three-dimensional time-dependent model. *J. Geophys. Res.* **105**, 20833–20856.
- Murphy, J. R., S. Larsen, H. Joergensen, and J. T. Schofield (2002). Derivation and Analyses of Martian Surface Winds from Mars Pathfinder. In *American Astronomical Society, DPS meeting #34*, #15.06.
- Murphy, J. R., T. Z. Martin, M. Blackmon, and S. Nelli (2001). Quantification of high frequency thermal waves in the martian atmosphere: Analysis of MGS Horizon Sensor atmospheric temperatures. In *American Astronomical Society, DPS meeting #33*, #19.23.
- Murphy, J. R., J. B. Pollack, R. M. Haberle, C. B. Leovy, O. B. Toon, and J. Schaeffer (1995). Three-dimensional numerical simulation of Martian global dust storms. *J. Geophys. Res.* **100**, 26357–26376.
- Murray, C. D. and S. F. Dermott (1999). *Solar System Dynamics*. Cambridge University Press, Great Britain.
- Nakamura, Y. and D. L. Anderson (1979). Martian wind activity detected by a seismometer at Viking lander 2 site. *Geophys. Res. Lett.* **6**, 499–502.
- National Space Science Data Center (2003). <http://nssdc.gsfc.nasa.gov/>.
- Neter, J. and W. Wasserman (1974). *Applied Linear Statistical Models*. Richard D. Irwin, Homewood, Illinois, USA.
- Neubauer, F. M., D. A. Gurnett, J. D. Scudder, and R. E. Hartle (1984). Titan's magnetospheric interaction. In T. Gehrels and M. S. Matthews (Eds.), *Saturn*, pp. 760–787. Tucson: University of Arizona Press.
- Neukum, G. and B. A. Ivanov (1994). Crater Size Distributions and Impact

- Probabilities on Earth from Lunar, Terrestrial-planet, and Asteroid Cratering Data. In T. Gehrels, M. S. Matthews, and A. Schumann (Eds.), *Hazards Due to Comets and Asteroids*, pp. 359–416. Tucson: University of Arizona Press.
- Newton, R. R. (1972). *Medieval Chronicles and the Rotation of the Earth*. Johns Hopkins University Press, USA.
- Niemann, H. B., W. T. Kasprzak, A. E. Hedin, D. M. Hunten, and N. W. Spencer (1980). Mass spectrometric measurements of the neutral gas composition of the thermosphere and exosphere of Venus. *J. Geophys. Res.* **85**, 7817–7827.
- Nier, A. O. and M. B. McElroy (1977). Composition and structure of Mars' upper atmosphere — Results from the neutral mass spectrometers on Viking 1 and 2. *J. Geophys. Res.* **82**, 4341–4349.
- Nininger, H. H. and G. I. Huss (1977). Was the Formation of Lunar Crater Giordano Bruno Witnessed in 1178? Look Again. *Meteoritics* **12**, 21–25.
- Nockolds, P. and P. Withers (2002). Comment and reply on “Meteor storm evidence against the recent formation of lunar crater Giordano Bruno” by Paul Withers. *Meteoritics and Planetary Science* **37**, 465–466.
- Oberst, J. (1989). Possible relationship between the Farmington meteorite and a seismically detected swarm of meteoroids impacting the moon. *Meteoritics* **24**, 23–28.
- Owczarek, J. A. (1964). *Fundamentals of Gas Dynamics*. International Textbook Company, Pennsylvania, USA.
- Paltridge, G. W. (1975). Global dynamics and climate — a system of minimum entropy exchange. *Quart. J. R. Met. Soc.* **101**, 475–484.
- Peterson, V. L. (1965a). *Analysis of the errors associated with the determination of planetary atmosphere structure from measured accelerations of an entry vehicle*. NASA-TR-R-225. Ames Research Center, California.
- Peterson, V. L. (1965b). *A technique for determining planetary atmosphere structure from measured accelerations of an entry vehicle*. NASA TN D-2669. Ames Research Center, California.
- Pieters, C. M., M. I. Staid, E. M. Fischer, S. Tompkins, and G. He (1994). A Sharper View of Impact Craters from Clementine Data. *Science* **266**, 1844–1848.
- Purucker, M., D. Ravat, H. Frey, C. Voorhies, T. Sabaka, and M. Acuña (2000). An altitude-normalized magnetic map of Mars and its interpretation. *Geophys. Res. Lett.* **27**, 2449–2452.
- Rada, W. S. and F. R. Stephenson (1992). A Catalogue of Meteor Showers in Mediaeval Arab Chronicles. *Q. J. R. Astron. Soc.* **33**, 5–16.
- Rees, M. H. (1989). *Physics and chemistry of the upper atmosphere*. Cambridge University Press, Great Britain.

- Rishbeth, H., R. V. Yelle, and M. Mendillo (2000). Dynamics of Titan's thermosphere. *Planetary and Space Science* **48**, 51–58.
- Rodgers, C. D. (1976). Comments on Paltridge's "Minimum Entropy Exchange" Principle. *Quart. J. R. Met. Soc.* **102**, 455–458.
- Ryder, G. and R. Ostertag (1983). ALHA 81005 — Moon, Mars, petrography, and Giordano Bruno. *Geophys. Res. Lett.* **10**, 791–794.
- Sagan, C. (1980). *Cosmos*. Random House, New York, USA.
- Saul, J. M. and A. C. Lawniczak (1996). Meteorite falls in June: Two sets of observations. *J. Geophys. Res.* **101**, 16905–16908.
- Schaefer, B. E. and P. M. Bagnall (1990). Lunar Event of 1178 A .D. — a Canterbury tale. *J. Br. Astron. Assoc.* **100**, 211.
- Schmülling, F., T. Kostiuk, D. Buhl, P. Rozmarynowski, K. Segal, T. Livengood, and T. Hewagama (1999). A new Infrared Heterodyne Instrument for measurements of Planetary Wind and Composition. In *American Astronomical Society, DPS meeting #31, #08.03*.
- Schubert, G. (1983). General circulation and the dynamical state of the Venus atmosphere. In D. M. Hunten, L. Colin, T. M. Donahue, and V. I. Moroz (Eds.), *Venus*, pp. 681–765. Tucson: University of Arizona Press.
- Schultz, R. A. (2000). Localization of bedding plane slip and backthrust faults above blind thrust faults: Keys to wrinkle ridge structure. *J. Geophys. Res.* **105**, 12035–12052.
- Seiff, A. (1963). *Some Possibilities For Determining the Characteristics of the Atmospheres of Mars and Venus From Gas-Dynamic Behavior of a Probe Vehicle*. NASA TN D-1770. Ames Research Center, California.
- Seiff, A. (1982). Post-Viking models for the structure of the summer atmosphere of Mars. *Advances in Space Research* **2**, 3–17.
- Seiff, A. (1993). Mars atmospheric winds indicated by motion of the Viking landers during parachute descent. *J. Geophys. Res.* **98**, 7461–7474.
- Seiff, A. and D. B. Kirk (1977a). Structure of the atmosphere of Mars in summer at mid-latitudes. *J. Geophys. Res.* **82**, 4364–4378.
- Seiff, A. and D. B. Kirk (1977b). Structure of the atmosphere of Mars in summer at mid-latitudes. *J. Geophys. Res.* **82**, 4364–4378.
- Seiff, A. and D. B. Kirk (1977c). Viking Lander Altimeter update. *Minutes of the second meeting of the Viking Mars Physical Properties Working Group (assembled by J. W. Meredith at JPL)*, 26–30.
- Seiff, A., D. B. Kirk, T. C. D. Knight, R. E. Young, J. D. Mihalov, L. A. Young, F. S. Milos, G. Schubert, R. C. Blanchard, and D. Atkinson (1998). Thermal

- structure of Jupiter's atmosphere near the edge of a 5- μm hot spot in the north equatorial belt. *J. Geophys. Res.* **103**, 22857–22890.
- Seiff, A., D. B. Kirk, R. E. Young, R. C. Blanchard, J. T. Findlay, G. M. Kelly, and S. C. Sommer (1980). Measurements of thermal structure and thermal contrasts in the atmosphere of Venus and related dynamical observations — Results from the four Pioneer Venus probes. *J. Geophys. Res.* **85**, 7903–7933.
- Seiff, A., D. B. Kirk, R. E. Young, S. C. Sommer, R. C. Blanchard, J. T. Findlay, and G. M. Kelly (1979). Thermal contrast in the atmosphere of Venus — Initial appraisal from Pioneer Venus probe data. *Science* **205**, 46–49.
- Seiff, A., D. E. Reese, S. C. Sommer, D. B. Kirk, E. E. Whiting, and H. B. Niemann (1973). PAET: An Entry Probe Experiment in the Earth's Atmosphere. *Icarus* **18**, 525–563.
- Shirley, J. H. (1997). Meteor. In J. H. Shirley and R. W. Fairbridge (Eds.), *Encyclopedia of Planetary Sciences*, pp. 479–480. Boston: Kluwer Academic Press.
- Sims, M. R., C. T. Pillinger, I. P. Wright, J. Dowson, S. Whitehead, A. Wells, J. E. Spragg, G. Fraser, L. Richter, H. Hamacher, A. Johnstone, N. P. Meredith, C. de La Nougerede, B. Hancock, R. Turner, S. Peskett, A. Brack, J. Hobbs, M. Newns, A. Senior, M. Humphries, H. U. Keller, N. Thomas, J. S. Lingard, J. C. Underwood, N. M. Sale, M. F. Neal, G. Klingelhofer, and T. C. Ng (1999). Beagle 2: a proposed exobiology lander for ESA's 2003 Mars express mission. *Advances in Space Research* **23**, 1925–1928.
- Slipher, E. C. (1962). *The photographic story of Mars*. Sky Pub. Corp., Cambridge, Massachusetts, USA.
- Smith, D. E., F. J. Lerch, R. S. Nerem, M. T. Zuber, G. B. Patel, S. K. Fricke, and F. G. Lemoine (1993). An improved gravity model for Mars: Goddard Mars Model 1. *J. Geophys. Res.* **98**, 20871–20889.
- Smith, D. E., G. A. Neumann, P. Ford, R. E. Arvidson, E. A. Guinness, and S. Slavney (1999). Mars Global Surveyor Laser Altimeter Initial Experiment Gridded Data Record. *NASA Planetary Data System*, MGS–M–MOLA–5–IEGDR–L3–V1.0.
- Smith, D. E., M. T. Zuber, H. V. Frey, J. B. Garvin, J. W. Head, D. O. Muhleman, G. H. Pettengill, R. J. Phillips, S. C. Solomon, H. J. Zwally, W. B. Banerdt, T. C. Duxbury, M. P. Golombek, F. G. Lemoine, G. A. Neumann, and et al. (2001b). Mars Orbiter Laser Altimeter: Experiment summary after the first year of global mapping of Mars. *J. Geophys. Res.* **106**, 23689–23722.
- Smith, D. E., M. T. Zuber, H. V. Frey, J. B. Garvin, J. W. Head, D. O. Muhleman, G. H. Pettengill, R. J. Phillips, S. C. Solomon, H. J. Zwally, W. B. Banerdt, and T. C. Duxbury (1998a). Topography of the Northern Hemisphere of Mars from the Mars Orbiter Laser Altimeter. *Science* **279**, 1686–1690.
- Smith, D. E., M. T. Zuber, S. C. Solomon, R. J. Phillips, J. W. Head, J. B.

- Garvin, W. B. Banerdt, D. O. Muhleman, G. H. Pettengill, G. A. Neumann, F. G. Lemoine, J. B. Abshire, O. Aharonson, D. C. Brown, S. A. Hauck, A. B. Ivanov, P. J. McGovern, H. J. Zwally, and T. C. Duxbury (1999). The Global Topography of Mars and Implications for Surface Evolution. *Science* **284**, 1495–1503.
- Smith, M. D., J. C. Pearl, B. J. Conrath, and P. R. Christensen (2000). Mars Global Surveyor Thermal Emission Spectrometer (TES) observations of dust opacity during aerobraking and science phasing. *J. Geophys. Res.* **105**, 9539–9552.
- Smith, M. D., J. C. Pearl, B. J. Conrath, and P. R. Christensen (2001). Thermal Emission Spectrometer results: Mars atmospheric thermal structure and aerosol distribution. *J. Geophys. Res.* **106**, 23929–23946.
- Snyder, C. W. and V. I. Moroz (1992). Spacecraft Exploration of Mars. In H. H. Kieffer, B. M. Jakosky, C. W. Snyder, and M. S. Matthews (Eds.), *Mars*, pp. 71–119. Tucson: University of Arizona Press.
- Sommer, S. C. and L. Yee (1969). An experiment to determine the structure of a planetary atmosphere. *Journal of Spacecraft and Rockets* **6(6)**, 704–710.
- Spedicato, E. (1998). Tunguska-type impacts over the Pacific Basin around the year 1178 AD: Chronology and catastrophism review. *J. Soc. Interdisciplinary Studies* **1**, 8–12.
- Spencer, D. A., R. C. Blanchard, R. D. Braun, P. H. Kалlemeyn, and S. W. Thurman (1999). Mars Pathfinder entry, descent, and landing reconstruction. *Journal of Spacecraft and Rockets* **36(3)**, 357–366.
- Squyres, S. W. (2001). The Mars Exploration Rover Project. In *American Geophysical Union, Fall Meeting, abstract #P41A-09*.
- Stewart, A. I. F. (1987). *Revised time dependent model of the martian atmosphere for use in orbit lifetime and sustenance studies*. LASP-JPL Internal Report, PO# NQ-802429, Pasadena, California.
- Strangeway, R. J. (1993). The Pioneer Venus Orbiter entry phase. *Geophys. Res. Lett.* **20**, 2715–2717.
- Stubbs, W. (1879). *The historical works of Gervase of Canterbury, Vol. 1*. Her Majesty's Stationery Office, London, Great Britain.
- Thomas, P. (1981). North-south asymmetry of eolian features in Martian polar regions — Analysis based on crater-related wind markers. *Icarus* **48**, 76–90.
- Tolson, R. H., G. M. Keating, G. J. Cancro, J. S. Parker, S. N. Noll, and B. L. Wilkerson (1999). Application of Accelerometer Data to Mars Global Surveyor Aerobraking Operations. *Journal of Spacecraft and Rockets* **36**, 323–329.
- Tolson, R. H., G. M. Keating, S. N. Noll, D. T. Baird, and T. J. Shellenberg

- (2000). Utilization of Mars Global Surveyor Accelerometer Data for Atmospheric Modeling. *Advances in the Astronautical Sciences* **103**, 1329–1346.
- Tracadas, P. W., M. T. Zuber, D. E. Smith, and F. G. Lemoine (2001). Density structure of the upper thermosphere of Mars from measurements of air drag on the Mars Global Surveyor spacecraft. *J. Geophys. Res.* **106**, 23349–23358.
- Tu, K. Y., M. S. Munir, K. D. Mease, and D. S. Bayard (2000). Drag-based predictive tracking guidance for Mars precision landing. *Journal of Guidance Control and Dynamics* **23**(4), 620–628.
- Tyler, G. L., G. Balmino, D. P. Hinson, W. L. Sjogren, D. E. Smith, R. A. Simpson, S. W. Asmar, P. Priest, and J. D. Twicken (2001). Radio science observations with Mars Global Surveyor: Orbit insertion through one Mars year in mapping orbit. *J. Geophys. Res.* **106**, 23327–23348.
- Vickery, A. M. (1987). Variation in ejecta size with ejection velocity. *Geophys. Res. Lett.* **14**, 726–729.
- Vinh, N. X., A. Busemann, and R. D. Culp (1980). *Hypersonic and Planetary Entry Flight Mechanics*. University of Michigan Press, USA.
- Warren, P. H. (1994). Lunar and martian meteorite delivery services. *Icarus* **111**, 338–363.
- Wercinski, P. F. and J. E. Lyne (1994). Mars aerocapture — extension and refinement. *Journal of Spacecraft and Rockets* **31**(4), 703–705.
- Wilson, R. J. (2000a). Evidence for Diurnal Period Kelvin Waves in the Martian Atmosphere from Mars Global Surveyor TES Data. *Geophys. Res. Lett.* **27**, 3889–3892.
- Wilson, R. J. (2000b). Topographically Modulated Thermal Tides in the Martian Atmosphere. In *American Astronomical Society, DPS meeting #32, #50.03*.
- Wilson, R. J. (2002). Evidence for nonmigrating thermal tides in the Mars upper atmosphere from the Mars Global Surveyor Accelerometer Experiment. *Geophys. Res. Lett.* **29**(7), 10.1029/2001GL013975.
- Wilson, R. J. and K. Hamilton (1996). Comprehensive model simulation of thermal tides in the Martian atmosphere. *J. Atmos. Sci.* **43**, 1290–1326.
- Withers, P. (2001, April). Meteor storm evidence against the recent formation of lunar crater Giordano Bruno. *Meteoritics and Planetary Science* **36**, 525–529.
- Withers, P., S. W. Bougher, and G. M. Keating (2000). New Results from Mars Global Surveyor Accelerometer. In *Proc. Lunar Planet. Sci. Conf., #31, #1268*.
- Withers, P., S. W. Bougher, and G. M. Keating (2001a). Harmonic Analysis of Zonal Density Structures in Martian Upper Atmosphere. In *American Geophysical Union, Spring Meeting, abstract #P41A-05*.

- Withers, P., S. W. Bougher, and G. M. Keating (2001b). Unpredictable day-to-day variability in the martian upper atmosphere. In *American Astronomical Society, DPS meeting #33, #19.29*.
- Withers, P., S. W. Bougher, and G. M. Keating (2002a). Measurements of Winds in the Martian Upper Atmosphere from the MGS Accelerometer. In *American Astronomical Society, DPS meeting #34, #05.05*.
- Withers, P., S. W. Bougher, and G. M. Keating (2002b). MGS Accelerometer-derived profiles of Upper Atmospheric Pressures and Temperatures: Similarities, Differences, and Winds. In *American Geophysical Union, Spring Meeting, abstract #P41A-10*.
- Withers, P., S. W. Bougher, and G. M. Keating (2002c). Winds in the martian upper atmosphere from MGS aerobraking density profiles. In *American Geophysical Union, Fall Meeting, abstract #P61C-0353*.
- Withers, P., S. W. Bougher, and G. M. Keating (2003). The effects of topographically-controlled thermal tides in the martian upper atmosphere as seen by the MGS accelerometer. *Icarus*, under review.
- Withers, P., R. D. Lorenz, and G. A. Neumann (2002, September). Comparison of Viking Lander Descent Data and MOLA Topography Reveals Kilometer-Scale Offset in Mars Atmosphere Profiles. *Icarus* **159**, 259–261.
- Withers, P. and G. A. Neumann (2001). Enigmatic northern plains of Mars. *Nature* **410**, 651.
- Withers, P., M. C. Towner, B. Hathi, and J. C. Zarnecki (2003). Analysis of entry accelerometer data: A case study of Mars Pathfinder. *Planetary and Space Science*, under review.
- Withers, P. G., S. W. Bougher, and G. M. Keating (1999). The Martian Upper Atmosphere During Phase 2 of Mars Global Surveyor Aerobraking: Comparison to Predictions. In *The Fifth International Conference on Mars, July 19-24, Pasadena, California, abstract no. 6073*.
- Yoder, C. F. (1981). The free librations of a dissipative moon. *Philosophical Transactions of the Royal Society, Series A* **303**, 327–338.
- Young, R. E. and J. A. Magalhães (2001). Alvin Seiff (1922-2000). *Icarus* **152**, 1–3.
- Yourgrau, W. and S. Mandelstam (1960). *Variational principles in dynamics and quantum theory*. Page 154, Pittman and Sons, London, Great Britain.
- Zhaung, T. (1977). Ancient Chinese Records of Meteor Showers. *Chinese Astronomy* **1**, 197–220.
- Zurek, R. W., J. R. Barnes, R. M. Haberle, J. B. Pollack, J. E. Tillman, and C. B. Leovy (1992). Dynamics of the atmosphere of Mars. In H. H. Kieffer, B. M. Jakosky, C. W. Snyder, and M. S. Matthews (Eds.), *Mars*, pp. 835–933. Tucson: University of Arizona Press.